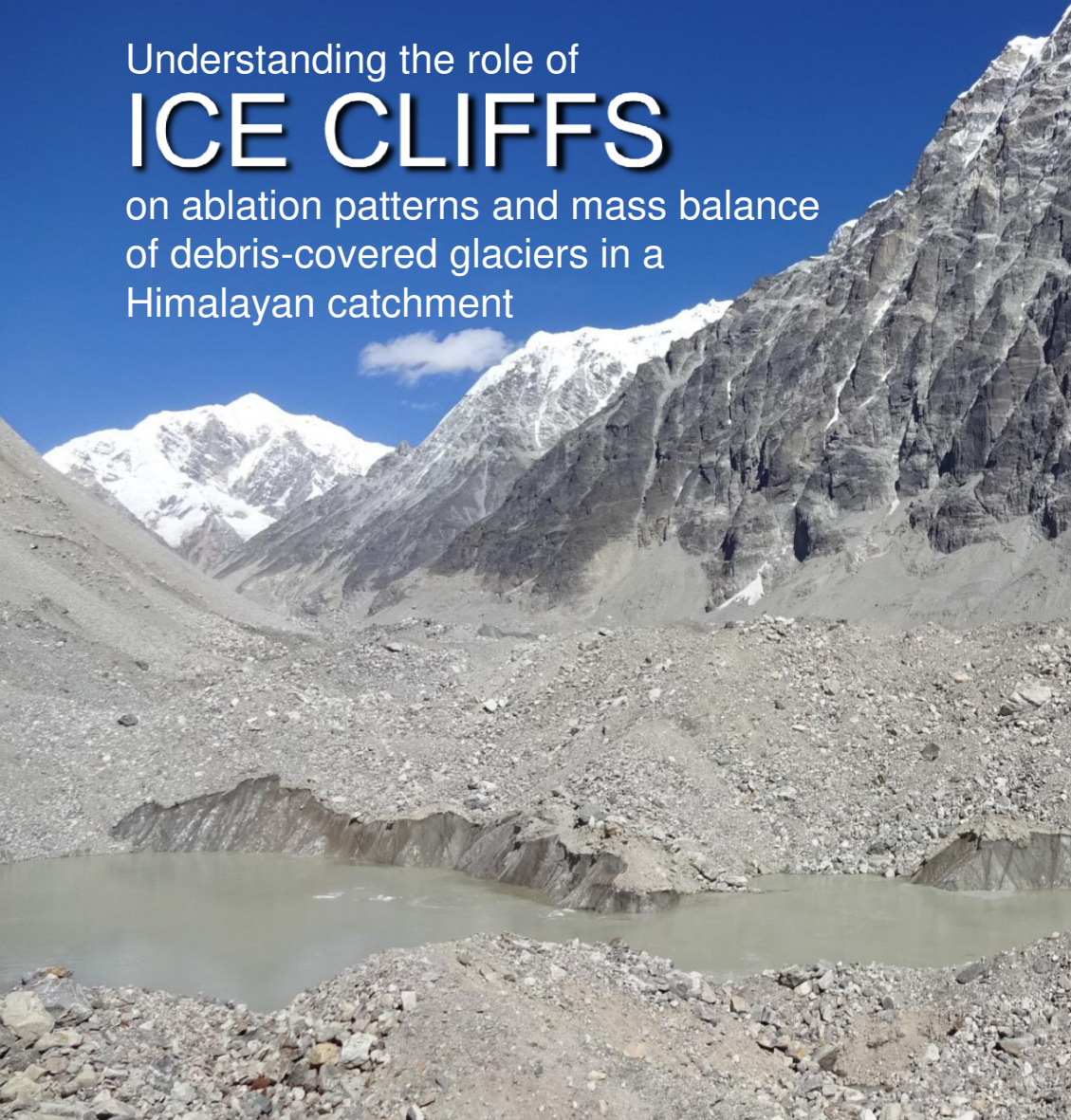


Pascal Buri

Understanding the role of **ICE CLIFFS**

on ablation patterns and mass balance
of debris-covered glaciers in a
Himalayan catchment



Diss. ETH No. 24731

**Understanding the role of ice cliffs on ablation
patterns and mass balance of debris-covered
glaciers in a Himalayan catchment**

A thesis submitted to attain the degree of
DOCTOR OF SCIENCES of ETH ZURICH
(Dr. sc. ETH Zurich)

presented by
PASCAL BURI
MSc in Physical Geography,
University of Zurich
born on 12 February 1988,
citizen of Rapperswil (BE), Switzerland

accepted on the recommendation of:
Prof. Dr. Paolo Burlando, examiner
Prof. Dr. Francesca Pellicciotti, co-examiner
Prof. Dr. Walter Immerzeel, co-examiner
Dr. Martin Kirkbride, co-examiner
Prof. Dr. Konrad Steffen, co-examiner

2017

Abstract

The past, present and future retreat of glaciers around the globe affects societies through sea level rise, increase in natural hazards and unambiguous impacts on water resources for drinking, agriculture, hydropower and other economic activities. Glaciers located in the arc of High Mountain Asia (HMA, spanning 3000 km across continental Asia) builds the headwaters of densely-populated regions and feed the major rivers of Asia, and are thus highly relevant as water sources for millions of people downstream. As in other regions of the world, glaciers in HMA are on average losing mass due to retreat and downwasting caused by anthropogenic climate change, with heterogeneous patterns of mass losses across HMA. A warming atmosphere affects these high-altitude zones more strongly than lower land masses. With very few studies focusing on HMA until recently, the last decade has seen an exponential increase in research efforts in the region, because of the large mass of ice it contains and the crucial role glaciers have for water supply to large populations. While much effort has gone into the monitoring and modelling of clean ice glaciers, little attention has been given to debris-type glaciers, although roughly one fifth of all glaciers are debris-covered in High Mountain Asia. These glaciers pose a complication in assessments of glacier change under future climate scenarios, as their response to climate is not yet fully understood. It is commonly understood from point scale observations, theory and numerical studies that a continuous, thick supra-glacial debris mantle suppresses ice melt. However, recent evidence from large-scale studies has suggested that debris-covered glaciers show similar rates of mass losses as debris-free glaciers, a counter-intuitive finding that is not supported by small scale studies. Despite their large extension and assumed importance, their actual role on glacier mass balance is thus still not understood.

Supraglacial ice cliffs are typical surface features of debris-covered glaciers worldwide, affecting surface evolution and mass balance by providing a direct ice-atmosphere interface with low albedo and high longwave emissions from surrounding debris, causing very high melt rates accounting for a significant portion of total glacier mass loss. Their role as windows of energy transfer suggests they may explain the anomalously high mass losses of debris-covered glaciers observed in HMA despite the insulating effect of debris. A recent work has shown that

recent accelerations in volume losses of debris-covered glaciers correlate with the presence of supraglacial ice cliffs and ponds, but no modelling evidence has been provided to date beside the satellite based studies or conceptual arguments. In contrast to the debris-covered ice, high melt at cliffs turns them into dynamic features, directly affecting glacier surface evolution. However, despite their importance as melt hot spots little is known about cliffs' and ponds' life cycle and evolution due to lack of direct measurements and adequate numerical models and their contribution to glacier mass balance has never been quantified at the glacier scale. So far all inference has been obtained from extrapolating point-scale model results, neglecting complex geometries and backwasting processes of ice cliffs located in heavily rugged surface topography of debris-covered glaciers.

The main objective of this work is to quantify the contribution of supraglacial ice cliffs to the mass balance of debris-covered glaciers and thus assess whether ice cliffs are responsible for the so-called “debris cover anomaly” and assumed higher than expected mass losses of debris-covered glaciers. This thesis adopts a sequential process to evaluate the impact of ice cliffs on the mass loss of debris-type glaciers: i) in a first step, a major effort has been on the collection of novel field data of cliff geometry, evolution and backwasting, ii) in a second step, we have developed a grid-based energy-balance model to investigate melt patterns on selected ice cliffs; iii) in a third step, the model has been improved from the insights gained from a second field campaign and developed to simulate cliff backwasting; the newly developed physically-based 3D-backwasting model has then been used to investigate the evolution of a selected population of ice cliffs using high-resolution topographical observations as initial conditions and for model validation; iv) in a fourth step, we have investigated the main controls of cliffs temporal evolution, persistence and reburial by applying the model established in (iii) to artificially rotated cliff-systems; and finally, v) in a fifth step, we have applied the model developed in (iii) and (iv) to the entire cliff population of the four debris-covered glaciers of the Langtang catchment and simulated the contribution of ice cliffs to total glacier mass balance calculated by the hydrological model TOPKAPI-ETH for the entire catchment.

The study area for this thesis is the Upper Langtang Valley (Nepalese Himalayas), a high-elevation catchment ($\sim 4000\text{--}7000$ m a.s.l.) in the central Himalaya of Nepal, with four heavily debris-covered glaciers (Lirung-, Shalbachum-,

Langshisha- and Langtang Glacier). In this catchment, ongoing research projects of the Chair of Hydrology, lead by PI Dr Francesca Pellicciotti, have provided the framework for the field activities and research carried out in this thesis.

The energy-balance, physically based numerical modelling, based on a high-resolution digital elevation model (DEM) and on-glacier meteorological data, has allowed calculation of the distributed energy balance at the complex ice cliff surfaces. We have established that, because of the high spatial variability of single energy fluxes acting on the steep surfaces, ice cliff melt rates vary considerably in space. This implies that ice cliffs undergo a distinct geometrical transformation over time.

The physically-based 3D dynamic model developed in step ii) was able to capture the main cliff dynamics and geometry changes over one melt season, simulating the progressive backwasting through interaction with the surrounding topography, and allowing the cliffs to grow and to shrink over time. Atmospheric melt, pond contact ablation enhancement for the cliff base and reburial by surrounding debris have been identified as the main mechanisms controlling the observed evolution patterns of ice cliffs.

Simulations with the 3D dynamic model provided the first evidence that southerly-oriented supraglacial ice cliffs disappear within few weeks to a few months over debris-covered glaciers, as conceptually suggested previously. This improves the understanding of spatial and temporal distribution of ice cliffs on debris-covered glaciers.

Finally, applied to four glaciers in the Upper Langtang Catchment, the results from the ice cliff backwasting model present the first estimate of the importance of supraglacial ice-cliffs to total glacier mass-balance and reveals that the volume lost by backwasting of ice cliffs is, contributing by 1.4–5.5%, a non-negligible term in total glacier downwasting of debris-covered glaciers, especially when considering debris-covered tongues only (9.1–36.4%).

Previous estimates of the influence of ice cliffs on glacier melt were either based on point-scale models or differencing DEMs, either neglecting topographical variability of ice cliffs or superimposing signals of (en)glacial dynamics, which in turn also greatly affect glacier mass balance. The results obtained through a combination of novel, rare datasets from the field and a new numerical model of cliff

backwasting presented in this thesis provide a key advancement in the understanding of the influence and importance of ice cliffs on glacier melt. This study has shown that ice cliffs, acting as hot spots of melt, can partially explain the higher-than-expected mass losses of debris-covered glaciers of HMA.

Sommario

Il passato, il presente e il futuro ritiro dei ghiacciai in tutto il mondo influenza la società inducendo l'innalzamento del livello del mare, l'aumento dei disastri naturali ed inequivocabili effetti sulle risorse idriche per l'acqua potabile, l'agricoltura, la produzione di energia idroelettrica ed altre attività economiche. I ghiacciai collocati nell'arco delle cime montuose asiatiche (High Mountain Asia, HMA, che si estende per oltre 3000 chilometri in Asia continentale) fungono da sorgenti d'acqua per regioni densamente popolate e alimentano i principali fiumi dell'Asia, e pertanto costituiscono le fonti di risorse idriche per milioni di persone a valle. Come in altre regioni del mondo, i ghiacciai collocati in HMA si stanno mediamente riducendo, con perdite di massa distribuite eterogeneamente, a causa del ritiro e dei processi di downwasting causati dai cambiamenti climatici di origine antropica. Gli effetti del riscaldamento dell'atmosfera sono più evidenti a queste quote elevate che in aree a più basse elevazioni. Mentre in precedenza pochi studi si sono focalizzati sull' HMA, l'ultimo decennio ha visto un aumento esponenziale delle attività di ricerca nella regione, a causa della grande massa di ghiaccio presente e del ruolo cruciale che i ghiacciai hanno per l'approvvigionamento idrico di larghe popolazioni. Molte risorse sono state investite nel monitoraggio e nella modellazione di ghiacciai non coperti da detriti, ma poca attenzione è stata finora prestata ai ghiacciai coperti da detriti, nonostante costituiscano circa un quinto di tutti i ghiacciai della catena montuosa asiatica dell'HMA. Questi ghiacciai costituiscono una complessità nella valutazione delle dinamiche dei ghiacciai sotto futuri scenari climatici, poiché la loro risposta al clima non è ancora stata compresa completamente. È generalmente appurato, sia da osservazioni puntuali, sia dalla teoria, che da studi numerici, che un continuo e spesso strato di detriti attenua lo scioglimento del ghiaccio. Tuttavia, studi su larga scala hanno recentemente suggerito che i ghiacciai coperti da detriti presentino perdite di massa simili ai ghiacciai privi di detriti, una conclusione contro intuitiva che non è supportata da studi su piccola scala. Nonostante la loro importanza e la loro grande estensione, il ruolo effettivo di questi ghiacciai sul bilancio di massa totale non è ancora chiaro.

In tutto il mondo, le falesie di ghiaccio rappresentano elementi caratteristici delle superfici dei ghiacciai coperti da detriti. Le falesie di ghiaccio influen-

zano l'evoluzione della superficie del ghiacciaio e il bilancio di massa. Fornendo un'interfaccia diretta ghiaccio-atmosfera caratterizzata da bassa albedo ed essendo circondate da detriti, fonti di alte emissioni ad onde lunghe, sono soggette ad elevate velocità di scioglimento che contribuiscono in maniera significativa alla perdita di massa totale del ghiacciaio. Il loro ruolo di finestre di trasferimento di energia, suggerisce che possano rappresentare la spiegazione delle elevate perdite di massa osservate nei ghiacciai ricoperti da detriti in HMA, nonostante l'effetto isolante dei detriti. Una recente ricerca ha dimostrato che l'accelerazione della perdita di volume dei ghiacciai ricoperti da detriti è correlata con la presenza di falesie e pozze di ghiaccio sopragliaciali. Tuttavia, oltre a studi basati su dati satellitari o argomentazioni concettuali, non sono ancora state fornite conferme da modelli. Contrariamente al ghiaccio coperto da detriti, grazie all'elevato scioglimento, le falesie di ghiaccio rappresentano elementi dinamici che influenzano in maniera diretta l'evoluzione della superficie del ghiacciaio. Tuttavia, nonostante la loro importanza come zone di elevato scioglimento, si conosce ancora poco sul loro ciclo di vita e sulla loro evoluzione, per mancanza sia di misure dirette che di modelli numerici adeguati. Di conseguenza, il loro contributo al bilancio di massa non è mai stato quantificato a scala di ghiacciaio. Le informazioni dedotte finora, derivano da estrapolazioni di risultati di modelli a scala puntuale, ricavate trascurando sia i processi di backwasting, che le complesse geometrie che caratterizzano i ghiacciai coperti da detriti.

L'obiettivo principale di questo lavoro è quello di quantificare il contributo delle falesie di ghiaccio al bilancio di massa totale dei ghiacciai coperti da detriti, e quindi valutare se esse siano responsabili della cosiddetta "anomalia della copertura dei detriti", ovvero del fatto che la perdita di massa dei ghiacciai ricoperti da detriti sia superiore a quella prevista. In questa tesi è stato adottato un processo sequenziale per valutare l'impatto delle falesie di ghiaccio sulla perdita di massa dei ghiacciai coperti da detriti: i) in una fase iniziale, è stato fatto uno sforzo importante per la raccolta di nuovi dati di campo sulla geometria delle falesie, sulla loro evoluzione e backwasting; ii) in una seconda fase, un modello del bilancio energetico, basato su griglia, è stato sviluppato per analizzare schemi di scioglimento del ghiaccio su falesie di ghiaccio selezionate; iii) nella terza fase, il modello è stato migliorato sulla base delle conoscenze acquisite durante una seconda campagna di misure, ed è stata sviluppata la modellazione del backwasting delle falesie; il nuovo modello di backwasting-3D fisicamente basato è stato

poi utilizzato per investigare l'evoluzione di una serie selezionata di falesie di ghiaccio, utilizzando osservazioni topografiche ad alta risoluzione sia come condizioni iniziali sia in fase di validazione; iv) in una quarta fase, i principali fattori che controllano l'evoluzione temporale delle falesie, la loro persistenza o scomparsa, sono stati esaminati applicando il modello stabilito in fase (iii) a falesie ruotate artificialmente; infine v) nella quinta fase, abbiamo applicato il modello sviluppato in (iii) e (iv) sull'intera popolazione di falesie dei quattro ghiacciai coperti da detriti del bacino di Langtang ed abbiamo simulato il contributo delle falesie di ghiaccio al bilancio totale di massa dei ghiacciai calcolato col modello idrologico TOPKAPI-ETH sull'intero bacino idrografico.

L'area di studio di questa tesi è l'Alta Valle del Langtang (Himalaya Nepalese), un bacino a quota elevata ($\sim 4000\text{--}7000$ m slm) nell'Himalaya centrale in Nepal, che ospita quattro ghiacciai caratterizzati da notevole copertura di detriti (ghiacciaio Lirung, Shalbachum, Langshisha e Langtang). In questo bacino idrografico, i progetti di ricerca in corso, gestiti dal gruppo di Idrologia e guidati dal ricercatore principale Dr. Francesca Pellicciotti, hanno fornito il quadro per le attività di campo e la ricerca descritta in questa tesi.

Il modello numerico, su base fisica, del bilancio energetico, basato su un modello di elevazione digitale ad alta risoluzione e su dati meteorologici misurati sul ghiacciaio, ha permesso il calcolo del bilancio energetico sulle complesse superfici delle falesie. Queste analisi hanno mostrato che, a causa dell'elevata variabilità spaziale dei singoli flussi di energia che agiscono sulle superfici, i tassi di scioglimento del ghiaccio variano notevolmente nello spazio. Questo implica che le falesie di ghiaccio subiscono una distinta trasformazione geometrica nel tempo.

Il modello dinamico 3D sviluppato al punto (ii) è stato in grado di simulare le principali dinamiche delle falesie e le variazioni geometriche durante una stagione di scioglimento, simulando il progressivo backwasting attraverso l'interazione con la topografia circostante e permettendo alle falesie di crescere e di ridursi nel tempo. Lo scioglimento in atmosfera, l'aumento dell'ablazione nella parte basale delle falesie dovuto al contatto con le pozze ed il ri-sotterramento delle falesie da detriti circostanti, sono stati identificati come i principali meccanismi che controllano l'evoluzione osservata delle falesie di ghiaccio.

Le simulazioni con il modello dinamico 3D hanno fornito per la prima volta la prova che, sui ghiacciai coperti dai detriti, le falesie di ghiaccio orientate a sud scompaiono in un periodo che va da poche settimane a pochi mesi, come suggerito da precedenti deduzioni concettuali. Questa informazione facilita la comprensione della distribuzione spaziale e temporale delle falesie di ghiaccio sui ghiacciai coperti da detriti.

Infine, i risultati del modello di backwasting delle falesie di ghiaccio, applicato a quattro ghiacciai nel bacino dell'Alto Langtang, rappresentano la prima stima dell'importanza delle falesie sopragliaciali nel bilancio di massa totale del ghiacciaio. I risultati rivelano che la perdita di volume dovuta al backwasting delle falesie è un termine non trascurabile nella perdita totale di ghiaccio nei ghiacciai coperti da detriti, contribuendo per il 1,4 - 5,5% (9,1 - 36,4% per le lingue dei ghiacciai coperte da detriti).

Stime precedenti dell'influenza delle falesie di ghiaccio sullo scioglimento dei ghiacciai sono state basate su modelli a scala puntuale o sulla differenziazione di modelli di elevazione digitale, trascurando, quindi, la variabilità topografica delle falesie di ghiaccio o sovrapponendo i diversi segnali di dinamica glaciale, che a loro volta influenzano notevolmente il bilancio di massa del ghiacciaio.

I risultati ottenuti attraverso la combinazione di nuove misure di campo, raramente disponibili, e di un nuovo modello numerico per le falesie, presentato in questa tesi, forniscono un importante progresso nella comprensione dell'influenza e dell'importanza delle falesie di ghiaccio sullo scioglimento dei ghiacciai. Questo studio ha dimostrato che le falesie di ghiaccio, che agiscono come zone ad elevato scioglimento, possono parzialmente spiegare le perdite di massa superiori a quelle previste osservate sui ghiacciai ricoperti da detriti delle cime montuose asiatiche (HMA).

Acknowledgements

I would like to express my deep gratitude to my PhD advisor Paolo Burlando for giving me the opportunity to conduct my research in his Hydrology Group at ETH Zurich. He provided me with wise advices whenever we met for discussions and paved the way for a successful completion of my PhD studies. My deepest gratitude goes to my supervisor Francesca Pellicciotti, thank you for all your catching enthusiasm, motivation and energy for our research, for guiding me through this PhD and thank you for making me part of your family in Newcastle upon Tyne so many times. Thank you also Markus, Federica and Jonas for always welcoming me in your home. My PhD wouldn't have been as joyful as it was without the collaboration with two very fine persons, Jakob Steiner and Evan Miles, which became invaluable friends. I really enjoyed our regular and inspiring discussions about all possible aspects of glaciology and beyond, and will never forget our common time in the Himalayas.

I deeply appreciate all the support I received from my glaciology colleagues in our group at ETH, Alvaro, Silvan, Ilaria and Marco. I also wish to thank all other past and present PhDs and Postdocs in the Hydrology Group: Chris, Daniela, Elena, Fede, Gianluca, Giulia, Martina, Matteo, Nadav and Seba. Thank you also Fanny Brun and Fionna Heuff for being inspiring and great office mates. This group as a whole kept me motivated to come to ETH every day! Special thanks goes to our secretary Manuela, without whom I would have been stuck in many bureaucratic situations. We are both now specialists in shipping freight to Nepal and back. The help in setting up, repair and maintain a variety of instruments for the field by the technicians Walter Jäger (*waljag*), Karl Schroff (*IAC*), Cornelius Senn and Ernst Bleiker (*IfU*) is greatly acknowledged. I also want to thank my predecessors in organizing the ETH field campaigns to Langtang Valley, Lene Petersen and Martin Heynen, who provided me invaluable suggestions for my own field trips there. These field trips were also greatly supported by Anna Chesnokova, Ibai Rico, Peter Hill and Simon Wicki, who helped us with countless measurements in the field and were at every point in time trustful company. A special thanks goes to Pascal Egli, a great and especially strong person with whom I spent our post-earthquake field trip to Langtang Valley.

The laborious field expeditions to the various glaciers in Langtang Valley would not have been possible without the over-arching support of Tek Rai and his

helpers from Himalaya Trekking Dreams, with assistant guides Moti Rai and Vishnu Rai. This great team pulled all the important strings behind the scenes in order to let us do our research, but let us always feeling welcome in their community.

I want to thank Walter Immerzeel and Patrick Wagnon for a fruitful collaboration, helpful advices, good company in the field. Joe Shea's help with shipping and clearance in Nepal is also greatly acknowledged, and it was always a pleasure to run over him and the rest of his ICIMOD team, including Inka, Maxime and Susan, in the valley. I also wish to thank Walter Immerzeel, Koni Steffen and Martin Kirkbride being my PhD co-examiners and being willing to review my work.

Big thanks go to Roger Rüegg, who is the best flat mate I can imagine for more than seven years, and who celebrated every intermediate and other steps of my PhD with me.

Last but not least, I am extremely thankful to my parents, Nelly and Willi, who always supported me with their love and joy in walking the line and following my passion, together with my two brothers, Roman and Michi. And my deepest gratitude goes to my big love, Anna!

Contents

List of Figures	XV
List of Tables	XXV
1. Introduction	1
1.1. Motivation and aim	2
1.2. Scientific background	6
1.2.1. Knowledge on glaciers and snow in High Mountain Asia	6
1.2.2. Debris-covered glaciers	8
1.2.3. Ice cliffs	10
1.2.4. Glacio-hydrological modelling	14
2. Study site: The Upper Langtang Valley, Nepal	17
2.1. Geography and geology	18
2.2. Climate	21
2.3. Glaciology	21
3. Data	23
3.1. Major field campaigns: April–May 2014, October–November 2014	24
3.2. Data used for ice cliff modelling	25
4. Modelling radiative fluxes over complex cliff geometries	27
4.1. Background computations	28
4.2. Geometry driven computation of radiative forcing	31
5. A grid-based model of backwasting of ice cliffs	37
5.1. Introduction	38
5.2. Study site	40
5.3. Data	43
5.3.1. Meteorological data	43

5.3.2.	Topographic data	43
5.3.3.	Cliff ablation and surface topography	45
5.4.	Model	47
5.4.1.	Sky and debris view factors	47
5.4.2.	Shortwave radiation flux	48
5.4.3.	Longwave radiation flux	50
5.4.4.	Turbulent fluxes	52
5.4.5.	Optimal model parameters	52
5.5.	Results and discussion	53
5.5.1.	Energy fluxes	53
5.5.2.	Melt	58
5.5.3.	Model strengths, limitations and outlook	61
5.6.	Conclusions	66
6.	A physically-based 3D-model of ice cliff evolution	69
6.1.	Introduction	70
6.2.	Study Site and Data	72
6.3.	Field Observations of Cliff Changes	75
6.3.1.	Reclining Cliffs	75
6.3.2.	Persistent Cliffs	78
6.3.3.	Expanding Cliff	79
6.3.4.	Summary of Observed Cliff Types	79
6.4.	Modeling Cliff Evolution	80
6.4.1.	Model	82
6.4.2.	Validation Metrics	89
6.4.3.	Model Sensitivity	91
6.5.	Results	91
6.5.1.	Dimensions, Slope, and Aspect	91
6.5.2.	Radiative Fluxes	95
6.5.3.	Area, Volume Loss and Melt Rate	95
6.5.4.	Model Sensitivity	99
6.6.	Discussion	102
6.6.1.	Observations of Cliff Evolution	102
6.6.2.	Model Simulations	104
6.6.3.	Model Limitations	107

6.6.4. Comparison with Other Studies	109
6.7. Conclusions	110
7. Aspect controls the survival of ice cliffs	113
7.1. Introduction	114
7.2. Backwasting of south-facing cliffs	115
7.3. Radiative forcing at the cliff surface	120
7.4. Discussion	123
7.5. Methods	124
7.6. Supplementary Information	125
7.6.1. Study site	125
7.6.2. Initial conditions and model inputs	126
7.6.3. Dynamic 3D-backwasting model	128
7.6.4. Extended results	135
8. Modelling the contribution of ice cliffs to mass-balance	145
8.1. Overview	146
8.2. Data	146
8.2.1. Model application and testing	157
8.3. Results and discussion	161
8.4. Conclusions	168
9. Concluding remarks	171
9.1. Knowledge advancements	172
9.2. Outlook	175
10. Bibliography	177
Appendix A. Modelling radiative fluxes over complex cliff geometries: Results	195
Appendix B. Ice cliff modelling at the glacier scale: Partitioning	203
Appendix C. Ice cliff modelling at the glacier scale: Meteorological forcing	205
C.1. Air temperature	208

C.2. Surface temperature	217
C.2.1. Comparison of surface temperatures on Langtang- and Shalbachum Glaciers	219
C.2.2. Surface temperature measured and related to measured or lapsed air temperatures on Lirung- and Shalbachum Glacier	221
C.2.3. Surface temperature related to lapsed air temperatures on all four study glaciers	225
C.3. Shortwave radiation	226
C.4. Longwave radiation	229
C.5. Relative humidity of the air	231
Appendix D. Ice cliff modelling at the glacier scale: Testing of model parameters	233
D.1. Test on spatial resolution	233
D.2. Test on DEMs	238
D.3. Test on negative buffers	242
D.4. Test on slope thresholds	249
Appendix E. Ice cliff modelling at the glacier scale: Results	257

List of Figures

1.1.	Supraglacial ice cliff on debris-covered Langtang Glacier. Note the person at the very top of the cliff for scale (12 May 2014).	1
1.2.	Scheme of the iterative framework on which the methodology presented in this thesis to quantify the impact of ice cliffs on the mass balance of debris-covered glaciers, is based on.	5
1.3.	Different ice cliff types described in Chapter 1.2.3. The dashed line on the marginal ice wall (top right panel) indicates the sample cliff of Winkler et al. (2010), encircled the corresponding meteorological station.	12
2.1.	Langtang Valley, located in the middle of the picture, as seen from space (ca. 300 km above the earth, looking north). The tie-shaped lake is Peko Tso on the Tibetan Plateau (China; picture: NASA, ISS Mission 8, E6230, 26 Nov. 2003).	17
2.2.	Overview map of the upper Langtang Valley catchment with glacierized areas, debris covered tongues and mapped supraglacial ice cliffs	19
2.3.	Overview upstream and downstream basin boundaries of the Indus, Ganges, Brahmaputra, Salween and Mekong river basins. . .	20
3.1.	Approaching the debris-covered tongue of Langtang Glacier, bringing down equipment for the automatic weather station (Picture: E. Miles, 12 May 2014)	23
4.1.	Tilted sensor (CNR1) installed on Cliff 1 on Lirung Glacier to measure short- and longwave radiation (24 Oct. 2014).	27
4.2.	Scheme of the earth's declination angle (δ), hour angle (ω) and the latitude (ϕ) at a certain point P on the earth's surface. . . .	29
4.3.	Scheme of the solar zenith angle (θ_z) and the elevation angle (here: α) which is its summand to 90°	30

4.4.	Scheme of the angle of incidence (θ_i) which indicates the angular difference between the solar incidence angle and the vector normal to the surface with a specific slope (β) and azimuth (A_{ZS}).	31
4.5.	Scheme of the radiation conversion from a horizontal plane (here: <i>Plane A</i>) to a plane normal to the solar beam (here: <i>Plane C</i>).	33
5.1.	Ablation measurements on Cliff 2 with a supraglacial pond attached to its base (6 May 2014)	37
5.2.	Overview of Langtang region, the tongue of Lirung Glacier and the two investigated cliffs	41
5.3.	3D-view of Cliff 1 and Cliff 2	42
5.4.	UAV-DEMs showing the maximum area of influence for the calculations of longwave radiation for the entire Cliff 1 and Cliff 2	44
5.5.	Calculation of the individual horizon angles for shortwave and longwave radiation, respectively, and of the debris view angle for a single azimuth direction	49
5.6.	Hourly energy fluxes averaged across each cliff for the three seasons separately	55
5.7.	Distribution of incoming direct shortwave radiation at Cliff 1 at 8:00, 11:00 and 14:00 in pre-Monsoon, Monsoon and post-Monsoon	57
5.8.	Distribution of incoming direct shortwave radiation at Cliff 2 at 8:00, 11:00 and 14:00 in pre-Monsoon, Monsoon and post-Monsoon	58
5.9.	Distribution of longwave radiation from debris at Cliff 2 at 8:00, 11:00 and 14:00 in pre-Monsoon, Monsoon and post-Monsoon	62
5.10.	Distribution of daily melt rate for Cliff 1 and Cliff 2 in pre-Monsoon, Monsoon and post-Monsoon	63
5.11.	Mean observed daily melt rates at Cliff 1 and Cliff 2	64
6.1.	Supraglacial pond (frozen) attached to an ice cliff with an approximately 5m high undercut on Lirung Glacier (26 Oct. 2014).	69
6.2.	Overview of the tongue of Lirung Glacier, in the upper Langtang Valley, Central Nepalese Himalayas	74
6.3.	Aspect and elevation within 200 m x 200 m area of interest for each cliff based on the May 2013 UAV-DEM	76
6.4.	Slopes derived from the UAV-DEM and manually delineated outlines of the four cliffs in May and October	78

6.5. Modelled (S-Model) aspect and slope for Cliff 2 for October 2013 without considering intermediate geometry updates	81
6.6. Modeling chain within the dynamic ice cliff backwasting model (D-Model)	83
6.7. Schematic cross section of cliff backwasting from left to right . .	88
6.8. Modeled debris view factors for each cliff calculated from the initial UAV-DEM in May	90
6.9. Model results of slope and aspect for October 2013 for each cliff, simulated cliff evolution based on the monthly updated outlines (D-Model) and the October cliff outlines simulated with the D-Model and the S-Model	92
6.10. Daily mean values of modeled (D-Model) radiative fluxes averaged over each cliff and measured temperatures at AWS Lirung	96
6.11. Modeled cliff volume losses from May to October, modeled daily melt rates and May to October mean cliff melt rates per cliff . .	97
6.12. Orthoimages showing the glacier surface in May and October 2013, with observed and modelled final Cliff 2 outlines, and elevation profiles across Cliff 2 as observed in May and October and modelled from May to October	103
6.13. Observed slopes at and around Cliff 3 in May and October, observed cliff outlines in May and October and the D-Model result	106
7.1. Cliff 2 on Lirung Glacier, showing the high spatial variability of incoming radiation and shadows. Note the person at the top ridge of the cliff for scale (20 Oct. 2015).	113
7.2. Observed cliffs on Lirung Glacier, Langtang Valley, Nepalese Himalaya	117
7.3. Simulated outlines and elevation profiles of south-facing cliffs . .	118
7.4. Modelled surface energy fluxes for Cliff 2 rotated to various aspects	119
7.5. Distributed energy fluxes modelled over Cliff 2 rotated to various aspects	121
7.6. Slopes of south-facing cliffs 1 and 2	127
7.7. Aspects of cliffs 1 and 2	129
7.8. Viewing angles for an ice cliff surface	132

7.9. Modelled surface energy fluxes averaged for cliffs 1 and 2 rotated to various aspects	136
7.10. Modelled seasonal direct shortwave radiation averaged for cliffs 1 and 2 rotated to various aspects	137
7.11. Distributed energy fluxes for Cliff 1 rotated to various aspects . .	139
7.12. Distributed energy fluxes for cliffs 1 and 2 rotated to various aspects	140
7.13. Map of view factors for cliffs 1 and 2 rotated to a southern aspect	143
8.1. Heterogeneous debris-covered surface of the lower part of Langtang Glacier, with its lowest tributary in the background. Peak of Gangchempo (6387m a.s.l.) on the right (Oct. 2015).	145
8.2. Catchment-scale map of upper Langtang Valley (central map) and glacier-scale maps (marginally aligned) of four debris-covered glaciers as observed in April 2014.	149
8.3. Timeseries of daily minimum, mean and maximum air temperature as measured at Kyanjing AWS (KYA) and Langshisha T-Logger (LSH) in 2014 (top) and as measured at LSH and lapsed to LSH from KYA (bottom).	151
8.4. Diurnal cycle of hourly air temperature as measured at Kyanjing AWS (KYA) and Langshisha T-Logger (LSH) in 2014 (top) and as measured at LSH and lapsed to LSH from KYA (bottom). . .	152
8.5. 2014-timeseries of daily minimum, mean and maximum surface temperature as derived from lapsed air temperature from Kyanjing AWS (KYA).	153
8.6. All year (top) and seasonal diurnal cycles (bottom) for pre-monsoon (PRM), monsoon (M) and post-monsoon (POM) of hourly incoming shortwave radiation as measured at AWSs Kyanjing (KYA), Lirung (LIR) and Langtang AWS (LGT) in 2014.	155
8.7. Timeseries of daily minimum, mean and maximum incoming longwave radiation as modelled at Langtang AWS (LGT) and measured at Lirung AWS (LIR).	156
8.8. All year (top) and seasonal diurnal cycles (bottom) for pre-monsoon (PRM), monsoon (M) and post-monsoon (POM) of hourly relative air humidity as measured at AWSs Kyanjing (KYA), Lirung (LIR) and Langtang (LGT) in 2014.	158

8.9. Averages over time of characterising ice cliff variables: slope, inclined area, melt rate and cumulative ice volume loss.	162
8.10. Ice cliff model results showing the contribution in percentages of all ice cliffs per elevation band of the two debris-covered glacier tongues of Lirung- (LIR) and Shalbachum Glacier (SHA), in terms of area and mass balance.	165
8.11. Ice cliff model results showing the contribution in percentages of all ice cliffs per elevation band of the two debris-covered glacier tongues of Langshisha- (LSH) and Langtang Glacier (LGT), in terms of area and mass balance.	166
9.1. Lower part of Langtang Glacier and its lowest tributary, peak of Gurkarpo Ri (6889m a.s.l.) in the background. In the foreground the so-called Morimoto Basecamp (Oct. 2015).	171
A.1. Time series of calculated sun-relevant angles according to Han et al. (2010) and Reid and Brock (2014) for Cliff 1 on Lirung Glacier at the position of the CNR1-instrument.	196
A.2. Time series of calculated direct and diffuse irradiance and two relevant angles for the direct solar radiation.	197
A.3. Time series of the elevation angle (green), incidence angle (red) as well as the cosine of the latter.	198
A.4. Time series of calculated direct and diffuse irradiance for a cliff slope as well as measured incoming and longwave radiation at the AWS and directly on the cliff.	199
A.5. Top: diurnal cycle of modelled shortwave radiation along the central profile at Cliff 1. Middle: topographical characteristics from profile derived from UAV-DEM. Bottom: Skyview and debrisview factors along the cliff profile.	200
A.6. Top: diurnal cycle of modelled shortwave radiation along the east profile at Cliff 1. Middle: topographical characteristics from profile derived from UAV-DEM. Bottom: Skyview and debrisview factors along the cliff profile.	201

A.7. Top: diurnal cycle of modelled shortwave radiation along the central profile at Cliff 2. Middle: topographical characteristics from profile derived from UAV-DEM. Bottom: Skyview and debrisview factors along the cliff profile. 202

B.1. Left: Partitioning (red lines and labels) of Langshisha Glacier using an algorithm following cliff pixel distribution on the glacier. Right: Fine-scale partitioning on Langtang Glacier of cliffs (violet) or lakes (not shown) if cut by a sector boundary line (black). . . 204

C.1. T-Logger structure. 206

C.2. Timeseries of daily minimum, mean and maximum air temperature as measured at Kyanjing AWS (KYA) and Jathang T-Logger (JAT) in 2014 (left) and as measured at KYA and lapsed to KYA from JAT (right). 210

C.3. Diurnal cycle of hourly air temperature as measured at Kyanjing AWS (KYA) and Jathang T-Logger (JAT) in 2014 (left) and as measured at KYA and lapsed to KYS from JAT (right). 210

C.4. Seasonal diurnal cycles (pre-monsoon, monsoon and post-monsoon) of hourly air temperature as measured at Kyanjing AWS (KYA) and Jathang T-Logger (JAT) in 2014 (left) and as measured at KYA and lapsed to KYA from JAT (right). 211

C.5. Timeseries of daily minimum, mean and maximum air temperature as measured at Kyanjing AWS (KYA) and Lirung AWS (LIR) in 2014 (left) and as measured at LGT and lapsed to LIR from KYA (right). 211

C.6. Timeseries of daily minimum, mean and maximum air temperature as measured at Kyanjing AWS (KYA) and Shalbachum T-Logger (SHA) in 2014 (left) and as measured at SHA and lapsed to SHA from KYA (right). 212

C.7. Timeseries of daily minimum, mean and maximum air temperature as measured at Kyanjing AWS (KYA) and Langtang AWS (LGT) in 2014 (left) and as measured at LGT and lapsed to LGT from KYA (right). 212

C.8. Diurnal cycle of hourly air temperature as measured at Kyanjing AWS (KYA) and Lirung AWS (LIR) in 2014 (left) and as measured at LIR and lapsed to LIR from KYA (right).	213
C.9. Diurnal cycle of hourly air temperature as measured at Kyanjing AWS (KYA) and Shalbachum T-Logger (SHA) in 2014 (left) and as measured at SHA and lapsed to SHA from KYA (right). . . .	213
C.10. Diurnal cycle of hourly air temperature as measured at Kyanjing AWS (KYA) and Langtang AWS (LGT) in 2014 (left) and as measured at LGT and lapsed to LGT from KYA (right).	214
C.11. Seasonal diurnal cycles (pre-monsoon, monsoon and post-monsoon) of hourly air temperature as measured at Kyanjing AWS (KYA) and Lirung AWS (LIR) in 2014 (left) and as measured at LIR and lapsed to LIR from KYA (right).	214
C.12. Seasonal diurnal cycles (pre-monsoon, monsoon and post-monsoon) of hourly air temperature as measured at Kyanjing AWS (KYA) and Shalbachum T-Logger (SHA) in 2014 (left) and as measured at SHA and lapsed to SHA from KYA (right).	215
C.13. Seasonal diurnal cycles (pre-monsoon, monsoon and post-monsoon) of hourly air temperature as measured at Kyanjing AWS (KYA) and Langshisha T-Logger (LSH) in 2014 (left) and as measured at LSH and lapsed to LSH from KYA (right).	215
C.14. Seasonal diurnal cycles (pre-monsoon, monsoon and post-monsoon) of hourly air temperature as measured at Kyanjing AWS (KYA) and Langshisha AWS (LGT) in 2014 (left) and as measured at LGT and lapsed to LGT from KYA (right).	216
C.15. Example of determination of the piece-wise regressions for T-Logger 5 on Lirung Glacier in pre-monsoon 2013 from Steiner and Pellicciotti (2016) (Fig. 12).	218
C.16. Timeseries of daily minimum, mean and maximum surface temperature as measured at Langtang (LGT) and Shalbachum (SHA) T-Loggers in 2013.	219
C.17. All year (left) and seasonal diurnal cycles (right) for pre-monsoon (PRM), monsoon (M) and post-monsoon (POM) of hourly surface temperature as measured at Langtang (LGT) and Shalbachum (SHA) T-Loggers in 2013.	220

C.18. Timeseries of daily minimum, mean and maximum surface temperature as measured at Lirung AWS (LIR) in 2014 and related to measured air temperature (left), and surface temperature as measured at LIR and related to lapsed air temperature (right). 221

C.19. Diurnal cycle of hourly surface temperature as measured at Lirung AWS (LIR) in 2014 and related to measured air temperature (left), and surface temperature as measured at LIR and related to lapsed air temperature (right). 222

C.20. Seasonal diurnal cycle of hourly surface temperature as measured at Lirung AWS (LIR) in 2014 and related to measured air temperature (left), and surface temperature as measured at LIR and related to lapsed air temperature (right). 222

C.21. Timeseries of daily minimum, mean and maximum surface temperature as measured at Shalbachum T-Logger (SHA) in 2014 and related to measured air temperature (left), and surface temperature as measured at SHA and related to lapsed air temperature (right). 223

C.22. Diurnal cycle of hourly surface temperature as measured at Shalbachum T-Logger (SHA) in 2014 and related to measured air temperature (left), and surface temperature as measured at SHA and related to lapsed air temperature (right). 223

C.23. Seasonal diurnal cycle of hourly surface temperature as measured at Shalbachum T-Logger (SHA) in 2014 and related to measured air temperature (left), and surface temperature as measured at SHA and related to lapsed air temperature (right). 224

C.24. Diurnal cycles of hourly surface temperature during 2014 (left) and separated into subseasons (right) as derived from lapsed air temperature from Kyanjing AWS (KYA) to the specific station locations on Lirung-, Shalbachum-, Langhshisha- and Langtang Glacier (LIR, SHA, LSH, LGT). 225

C.25. Timeseries of daily mean and maximum incoming shortwave radiation as measured at AWSs Kyanjing (KYA), Lirung (LIR) and Langtang AWS (LGT) in 2014. 227

C.26. Timeseries of daily mean cloud-factors derived for AWSs Kyanjing (KYA), Lirung (LIR) and Langtang AWS (LGT) in 2014. 228

C.27. All year (left) and seasonal diurnal cycles (right) for pre-monsoon (PRM), monsoon (M) and post-monsoon (POM) of hourly incoming longwave radiation as modelled at Langtang AWS (LGT) and measured at Lirung AWS (LIR) in 2014. 230

C.28. Timeseries of daily minimum, mean and maximum relative air humidity as measured at AWSs Kyanjing (KYA), Lirung (LIR) and Langtang (LGT) in 2014. 232

List of Tables

5.1. Characteristics of the two supraglacial ice cliffs on Lirung Glacier investigated in this study	46
5.2. Optimized model parameters for May and October 2013 averaged across all stakes at Cliff 1 and Cliff 2	53
5.3. Hourly mean, standard deviation (sd) and coefficient of variation (cv=sd/mean) of the energy fluxes, averaged spatially over the entire cliff, separated for pre-Monsoon, Monsoon and post-Monsoon	56
5.4. Slope and aspect values at stake locations in May 2013, measured manually on the ice surface and derived from the UAV-DEM . .	62
6.1. Cliff characteristics derived from the UAV-DEM and orthoimage, shown as mean values for 18 May and 22 October 2013	77
6.2. Ice cliff volume loss and mean backwasting rate from May to October 2013 for the four cliffs	98
6.3. Validation metrics and results of the sensitivity analysis for different model runs	100
6.4. Cliff characteristics derived from the UAV-DEM and modeled with the D-Model	101
7.1. Coefficients of variation for all positive fluxes of entire Cliff 2 per aspect from diurnal cycles averaged from May to October 2013 .	141
7.2. Total positive fluxes of entire Cliff 2 per aspect as sum from diurnal cycles averaged from May to October 2013	142
7.3. Survival period of cliffs 1 and 2 rotated to various target aspects	144
8.1. Stations used to force the cliff model with meteorological data (AWSs) and for testing environmental lapse rates (T-Loggers). .	148
8.2. Numerical experiments (Chapter D) using the ice cliff melt model	159

8.3.	Overview of the spatial domain and model outputs for the cliff model used in this Chapter compared to the hydrological model used to estimate the glacier-scale mass balance for the four glaciers in the catchment.	160
8.4.	Observed and simulated ice cliff area and melt, respectively, related to the glacier scale for each study glacier (Gla).	167
C.1.	Characteristics of the studied upper Langtang catchment.	206
C.2.	Definition of seasons used in this study, based on Heynen et al. (2016).	207
C.3.	Air temperature lapse rates derived for Langtang Valley for the 2013 season (Heynen et al., 2016) and for debris-covered Lirung Glacier for the 2014 season (Steiner and Pellicciotti, 2016).	209
C.4.	Median slopes (a_1 and a_2) and intercepts (b_1 and b_2) of the piecewise regression for the $T_{air}-T_{surf}$ -relation in all three seasons in 2014 from Steiner and Pellicciotti (2016) (Tab. 3).	217
C.5.	Parameter sets for alternatives ‘A’ and ‘B’	230
E.1.	Model results for melt of supraglacial ice cliffs (ice cliff model) only and total melt glacier melt (TOPKAPI-ETH), including cliffs and ponds, for the debris-covered glacier tongues of Lirung Glacier	258
E.2.	Model results for melt of supraglacial ice cliffs (ice cliff model) only and total melt glacier melt (TOPKAPI-ETH), including cliffs and ponds, for the debris-covered glacier tongues of Shalbachum Glacier	259
E.3.	Model results for melt of supraglacial ice cliffs (ice cliff model) only and total melt glacier melt (TOPKAPI-ETH), including cliffs and ponds, for the debris-covered glacier tongue of Langshisha Glacier	260
E.4.	Model results for melt of supraglacial ice cliffs (ice cliff model) only and total melt glacier melt (TOPKAPI-ETH), including cliffs and ponds, for the debris-covered glacier tongue of Langtang Glacier	261

Chapter 1.

Introduction



Figure 1.1.: Supraglacial ice cliff on debris-covered Langtang Glacier. Note the person at the very top of the cliff for scale (12 May 2014).

1.1. Motivation and aim

Debris-covered glaciers are a common feature in high mountain ranges and constitute a significant share of the total glacierized area in the Hindukush-Karakoram-Himalaya (HKH; Benn et al., 2012; Nuimura et al., 2012; Bolch et al., 2012). Debris cover is generally understood to act as an insulation to the ice mass of the glacier, inhibiting ablation rates (Østrem, 1959). Recent remote sensing studies have however failed to identify diminished rates of recession compared to debris-free glaciers (Kääb et al., 2012; Basnett et al., 2013; Gardelle et al., 2013) and have suggested an anomalous behaviour of debris-covered glaciers in the HKH-region, that has been termed as a “debris cover anomaly”. Despite the fact that these studies refer only to a very recent period of data and are based on remote sensed observations only, they have triggered investigations of the behaviour of debris-covered glaciers at scales larger than that of the numerous point scale numerical studies carried out until recently. An explanation for high ablation rates at the glacier scale has been attributed to the occurrence of ice cliffs and supra-glacial lakes on debris-covered glaciers (Gardelle et al., 2012; Pellicciotti et al., 2015; Ragetti et al., 2016a). Although cliffs can cover only small portions of the total debris cover area (less than 2 % for cliffs on Lirung Glacier, Sakai et al., 2000), melt rates larger than 5 cm day⁻¹ during the melt season have been reported and could hence contribute a significant amount of mass loss when extended to the scale of the entire glacier (Sakai et al., 1998; Han et al., 2010; Reid and Brock, 2014).

The assumed increase of melt on sloped cliffs is likely caused by a combination of different factors: i) the exposure to a high amount of (often direct) solar radiation during a certain period of the day, especially when facing east- to south (on the Northern Hemisphere); ii) assumed high longwave radiation receipts emanating from the surrounding debris-covered glacier surface, which unlike debris-free ice reaches very high temperatures during the day and thus emits a large amount of longwave radiation; and iii) the low albedo of the cliff ice due to dust or very fine debris or originating from the surrounding debris on top and around the cliffs and deposited by aeolian processes or meltwater funnels. While each of these assumptions has been variously suggested in previous studies, none has been tested systematically or in combination with the others. More importantly, all evidence has been provided by field observations at few stake locations and

point scale energy balance melt models also applied to few locations on single accessible cliffs. Models that calculate the energy balance and melt over entire cliffs are lacking, but seem important to develop as debris-covered glaciers are characterized by a rough topography (Benn et al., 2012; Pellicciotti et al., 2015) and cliffs exhibit complex geometries, with strong variability in extension, size, aspect, slope, and shape of the vertical profiles (Immerzeel et al., 2014a). These manifold surfaces and their interaction with the surrounding glacier thus need to be modelled accurately using a grid based, distributed approach to calculate the energy fluxes resulting from the complex cliff topography, in order to properly quantify backwasting rates and their controls. Measurements of backwasting at single locations on cliffs (inferred from measurements at stakes or at the cliff top) have been useful to provide quantitative estimates of backwasting rates and to qualitatively suggest possible dominant controls (Sakai et al., 1998; Han et al., 2010), (Reid and Brock, 2014). However, it is clear that more advanced models are needed to understand the actual contribution of total cliffs areas to ice melt, their formation, development and decay and their interaction with supraglacial ponds.

The few estimates of total contribution of cliff backwasting to total melt of a debris-covered glacier have until now been provided by extrapolating measured- or modelled melt at single locations to the entire cliff surface (Sakai et al., 1998; Han et al., 2010; Reid and Brock, 2014; Anderson, 2014). Estimates of the contribution of cliffs to the total mass loss of debris-covered glaciers vary widely within a very large range from 7.3 and 7.4% (Reid and Brock, 2014; Han et al., 2010), respectively, up to 69% (Sakai et al., 1998). This method however seems prone to errors given the high variability in cliff topography, energy fluxes and ablation (Reid and Brock, 2014; Steiner et al., 2015) and none of the estimates above seems particularly reliable given the simplistic approaches used to infer them or the limited areas considered (Immerzeel et al., 2014b). An accurate quantification of the actual backwasting of a single cliff is still missing and as a result, despite the high melting rates observed at few stakes locations, it is difficult to establish without ambiguity the importance of cliffs for the mass balance and runoff of debris-covered glaciers.

Little is known about the evolution and changes in space and time of cliffs, and their mechanisms of formation and decay. While hypotheses have been advanced (Reid and Brock, 2014; Sakai et al., 2002, 2000) none has been substantiated

through modelling or systematic, detailed observations in the field, which are difficult and very onerous. Given this lack of knowledge about cliffs' evolution in time and space, no ablation or mass balance model exists that includes temporal changes in cliffs geometry and characteristics. None of the models applied to date to simulate the mass balance or hydrological response of debris-covered glaciers in the HKH-region includes cliffs. As a result, all current model predictions of glacier mass balance and runoff in the region are neglecting key processes and might therefore be affected by errors the magnitude of which is difficult to estimate but which might be large, if the results of the remote sensing studies (Kääb et al., 2012; Basnett et al., 2013; Gardelle et al., 2013) are reliable. The only hydrological model that incorporates in a conceptual way the role of cliffs on the glacier ablation, mass balance and runoff is the one by Ragettli et al. (2015) (TOPKAPI-ETH), in the upper Langtang River basin, in Nepal.

The main motivation for this thesis is to assess how supraglacial ice cliffs affect debris-covered glaciers and establish whether ice cliffs, in their role as hot spots of melt, are indeed responsible for higher than expected mass losses and thus an anomalous behaviour of debris-covered glaciers, as recently observed in remote sensing studies in HMA.

The high-resolution DEM, derived from unmanned aerial vehicle surveys (UAV, Immerzeel et al., 2014a), is a key element of this research and crucial for the assessment of small scale phenomena like ice cliffs, as the lack of detailed topographic data is often the limiting factor on other glaciers. The UAV-DEM provides a high-resolution, high quality, DEM of the debris-covered tongue of Lirung Glacier, by using a Structure from Motion approach (SfM, Agisoft, 2013). The main goal of this thesis is to establish the impact of supraglacial ice cliffs on the total ablation of the debris-covered glaciers of the upper Langtang Valley, as a case study for their general importance for debris-covered glaciers in the HKH-region. Our main research question is:

Are supraglacial ice cliffs responsible for high mass losses and thus for the so-called “debris cover anomaly”?

To meet the above stated goal to assess how ice cliffs affect debris-covered glaciers, we defined the following three research aims:

(i) Assessing the distributed energy-balance and melt pattern of supraglacial ice cliffs

Knowledge about the energy fluxes and the resulting melt pattern on the entire

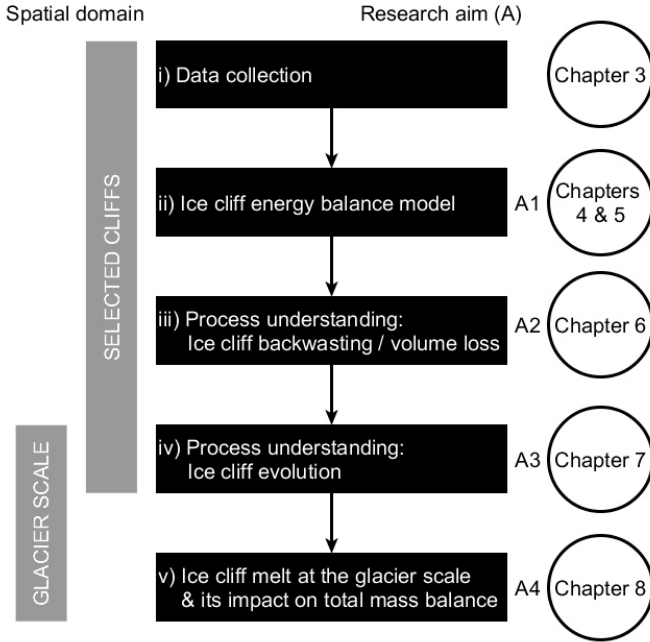


Figure 1.2.: Scheme of the iterative framework on which the methodology presented in this thesis to quantify the impact of ice cliffs on the mass balance of debris-covered glaciers, is based on. The individual research aims (A) are indicated with their corresponding number.

surface of ice cliffs at a distributed scale, considering their varying slopes and aspects, is unknown. We will be asking the following questions of these process: How does the surrounding topography influence the energy balance on the ice cliff surface? Which energy fluxes contribute how much to total ice cliff melt? How do energy fluxes and hence melt rates vary in space across an ice cliff surface? How effective is ice cliff melt compared to melt under debris in terms of melt per area?

(ii) Investigating the backwasting evolution and associated volume loss of supraglacial ice cliffs

Although the importance of supraglacial ice cliffs for glacier-scale ablation is now widely recognized (Ragettli et al., 2016a; Watson et al., 2017), their evolution in

time and space is still unknown. We will improve the understanding of the cliffs' behaviour in terms of geometry change, through a combination of a numerical model based on the findings of research aim i) and detailed observations based on high-resolution DEMs, by asking the following questions: How do ice cliff geometries change over time and how much ice volume gets lost through this process? How does adjacent ponded water affect ice cliff melt? How is the melting ice cliff interacting with the surrounding debris-covered glacier surface?

(iii) Understanding the controlling factors of ice cliff's persistence and demise

So far only theoretical assumptions explaining the processes of reburial and disappearance of supraglacial ice cliffs exist. We want to test the hypothesis about the prevalence of northerly-facing ice cliffs and the short life-span of southerly-oriented ice cliffs (Northern Hemisphere) controlled by aspect, which has been suggested previously (Sakai et al., 2002) and observed on several debris-covered glaciers in the Himalayas (Watson et al., 2017). Knowledge about the expected persistence time of ice cliffs with different aspects is needed to estimate longer-term evolution of the surface of debris-covered glaciers.

(iv) Estimating the contribution of supraglacial ice cliffs to total ablation of debris-covered glaciers

Calculations of volume loss from cliff melt alone, as partly derived in (ii), do not resolve the question of how much ice cliffs contribute to the total mass balance of glaciers, even when cliff melt is simulated at the glacier scale. What is needed is a comparison of cliff volume losses to total mass losses of debris-covered glaciers. To get total mass balance values simulations with physically-based models are required, as DEM-differencing methods do not separate the signals of glacier melt and glacier dynamics including glacier flow and emergence processes.

We use a combination of ground observations and long-term ground monitoring, optical remote-sensing and physically based model approaches to understand the dynamic processes acting at the surface of debris-covered glaciers.

1.2. Scientific background

1.2.1. Knowledge on glaciers and snow in High Mountain Asia

The past, present and future retreat of glaciers around the globe has implications for sea level, water resources and natural hazards (IPCC, 2013). Although

glaciers outside Greenland and Antarctica contain less than 1% of the total land ice, they are major contributors to sea-level rise (Kaser et al., 2006; Meier et al., 2007; Gardner et al., 2013). A warming atmosphere affects the high-altitude-zones more strongly than land masses at lower elevations through feedback of temperature and surface albedo (Pepin et al., 2015).

Central Asia holds the largest volume of ice outside the polar regions and subpolar Greenland and Alaska (Grinsted, 2013), and is thus one of the world's largest supplies of fresh water, given the large number of people living in the region and potentially affected by changes in those resources (Bandyopadhyay and Gyawali, 1994). The role of runoff from glaciers and snow cover has received increasing attention as climate change is expected to have widespread consequences on snow melt and glacier runoff across the region (Immerzeel et al., 2010, 2013; Pritchard, 2017). Fresh water in mountainous regions is predominantly stored as ice (long term) and snow (short term) and the amount and timing of its release towards regions further downstream directly impacts societies in terms of drinking water or irrigation in agriculture, and electricity (hydropower generates e.g. 90% of Nepal's electricity Pritchard, 2017).

Quantitative estimates of the past and current state of glaciers over High Mountain Asia are few and mostly based on satellite images, as only a very limited amount of in-situ data exists, and modelling studies are seriously limited by lack of in-situ data. In the Himalayan region, fieldwork is very difficult to conduct due to the remoteness of glaciers as well as logistical, financial and political barriers (Ragettli et al., 2015). For this reason, in recent years the focus has been on remote sensing approaches that are used to reconstruct snow cover, frontal and areal changes of glaciers and ice volumetric changes (Kääb et al., 2012; Gardelle et al., 2013; Shangguan et al., 2014). Remote sensing techniques have been applied widely to estimate glacier mass balances in the Indian (Berthier et al., 2007) and Nepalese Himalaya (Bolch et al., 2008, 2011), in the Karakoram (Gardelle et al., 2012) and at the large regional scale over selected regions of the entire Pamir-Karakoram-Himalaya-mountain range (Gardelle et al., 2013). Although satellite images provide evidence of changes in glaciers and the cryosphere at large spatial scale and without the need for labour-intensive fieldwork, their main disadvantage is the integration of observed changes over several years, which does not allow insights into seasonally driven processes, as well as the fact that they cannot provide any causal explanation for the observed changes (Cogley, 2012).

A general overview on the present state of the glaciers in High Mountain Asia has been provided by Bolch et al. (2012) based on satellite imagery works. The study played down the wrongly assumed perspectives of a very dramatic and fast change in runoff in the Himalaya (Cruz et al., 2007) but also pointed to a dramatic lack of understanding of the main processes controlling these changes. They also emphasized strong differences in climatic conditions and drivers of changes over the entire region.

1.2.2. Debris-covered glaciers

If the thickness of a debris rock layer on a glacier exceeds several centimeters, it is assumed to have an insulation effect on the underlying ice, reducing melt considerably (Østrem, 1959; Brock et al., 2010; Collier et al., 2014; Evatt et al., 2015).

Although melt under a homogenous debris mantle is relatively well understood and can be simulated with some confidence at the point-scale (Mattson and Gardner, 1993; Takeuchi et al., 2000; Nicholson and Benn, 2006; Suzuki et al., 2007; Lambrecht et al., 2011; Reid et al., 2012; Nicholson and Benn, 2013; Lejeune et al., 2013), all other aspects of debris influence on mass balance are relatively poorly known.

Studies on distributed debris thickness estimates (Zhang et al., 2011; Foster et al., 2012; Rounce et al., 2015; Schauwecker et al., 2015), aerodynamic surface roughness (Miles et al., 2017a), debris cover formation and supply (Kirkbride and Deline, 2013), evolution of debris cover extent (Herreid et al., 2015) and the dynamics of debris-covered glaciers (Rowan et al., 2015) are still very limited and affected by large uncertainties. However, a better understanding of the current and future state of debris-covered glaciers and their surface characteristics in particular is crucial for estimates of water resources and global scale estimates of ice contribution to the oceans. In fact, all studies that predicted global glacier mass balances and hence make estimates about the glacial contribution to sea level rise so far (Raper and Braithwaite, 2006; Kaser et al., 2006; Meier et al., 2007; Radić and Hock, 2011; Marzeion et al., 2012; Gardner et al., 2013; Marzeion et al., 2014; Huss and Hock, 2015) neglect debris cover.

Many glacier tongues in High Mountain Asia are covered by a mantle of more or less continuous debris. Despite their large extension and assumed importance, their actual role on glacier mass balance is still not understood.

Scherler et al. (2011) investigated frontal variations of 255 Himalayan glaciers from 2000–2008 and detected no uniform response to climate change. Debris-covered glaciers showed little snout variations within the investigated period. The authors estimated the relative area of debris-covered glaciers to 18.3% of the total glacier area and highlighted the importance of debris-covered glaciers to understand glacier retreat in this region.

The influence of debris cover and supraglacial lakes on glacier area change was investigated in Basnett et al. (2013) at the regional scale of the Sikkim Himalaya, between Nepal and Bhutan. They detected an increase in debris cover area and in the number of glaciers with debris and supraglacial lakes for the period 1990–2010, and suggested this could contribute to further mass loss. Herreid et al. (2015) investigated the area debris covers on 93 glaciers in the Karakoram from 1977–2014 and detected no significant change over that period, most probably affected by the stable mass balances observed in this region. The analysis of the debris cover evolution in space and time also suggest that the Karakoram anomaly extends further back than previously known (Herreid et al., 2015).

Although located in the same altitude ranges, clean ice glaciers, debris-covered glaciers and glaciers with supraglacial lakes on their debris covered portions showed different responses to the rising air temperatures estimated for this region, with debris-covered glaciers showing retreats at a faster rate than debris-free glaciers, if associated with lakes.

Kääb et al. (2012) derived glacier volume losses over the eastern, southern and southwestern part of the HKH-mountain range during 2003–2008, but a contrasting pattern in the Karakoram with very low thinning rates over the same time span. Additionally, they observed similar trends of thinning rates for clean ice and debris-covered glaciers, and suggested to reassess the role of debris cover in glacier mass balance in order to better understand future glacier feedback to climate change.

By investigating nine study sites over the entire Pamir-Karakoram-Himalaya region (Gardelle et al., 2013) confirmed the slight gain or equilibrium mass balance in the Karakoram and found the same for the Pamir. The most negative mass balances were detected in the monsoon-arid transition study site in the western Himalaya. They also observed similar thinning rates of debris-covered and clean-ice glaciers for four study sites and assumed supraglacial lakes and ice cliffs to be responsible for the enhanced ablation of debris-covered glaciers in combination

with a thin debris layer. Gardelle et al. (2013) suggested that intensified glaciological and meteorological recordings in the vicinity of high-altitude glaciers are needed to understand the mechanisms behind the contrasted mass budgets in the study region.

While the remote sensing studies described above only covered 5–20 years of the two most recent decades, Pellicciotti et al. (2015) derived mass balance changes within the Langtang catchment for the end of the 20th century from 1979–1999 and obtained thinning rates similar to the previous studies. Looking at variations within single glaciers they observed highly non-linear mass balance profiles with elevation, caused by highest thinning rates at shallow and semi-stagnant sections of debris-covered glaciers. On these glacier sections, supraglacial lakes and cliffs, which offer surfaces where high melt rates can occur, are typically present to a high degree. Ragettli et al. (2016a) could extend this analysis until 2015 and observed highest thinning rates in glacier zones on the debris-covered tongue with a high occurrence of ice cliffs and ponds.

1.2.3. Ice cliffs

Observations of the ablation and meteorological conditions on ice cliffs on debris-free glaciers have been conducted in different regions in the world. Fig. 1.3 gives an overview on the different ice cliff types described below. Goldthwait (1971) was the first to survey a 500m by 40m frontal ice cliff (“Red Rock ice cliff” at North Ice Cap, West Greenland), a feature seen as a barrier to vehicle access and to communication and fuel lines to the ice sheet, using terrestrial photogrammetry. He derived a high resolution DEM (0.25m) to estimate volume losses and area changes for one decade (1955–1965) to better understand their evolution in space and time. Chinn (1987) studied a marginal ice cliff at Wright Lower Glacier, a cold glacier in Victoria Land (Antarctica). He measured meteorological conditions in terms of radiation, temperature and wind speed measurements near the ice wall and suggested that the cliff is acting as a radiation trap, especially close to adjacent rocky slopes through longwave emittance. Ablation at the terminal ice cliff of Tasman Glacier (Southern Alps, New Zealand) was measured by Purdie and Fitzharris (1999). They observed that ice loss at the glacier terminus is largely decoupled from climatic influences through calving processes into a proglacial lake. Additionally to measurements on the flat glacier surface, Lewis et al. (1999) measured meteorological variables in front of the ter-

minal ice cliffs of Canada Glacier (Taylor Valley, Antarctica) for two summers (1995–1997) both vertically and horizontally in order to investigate the processes acting at the steep ice faces. Ice cliff ablation was found to be driven primarily by melt (shortwave radiation), in contrast to the glacier surface mainly affected by sublimation (Lewis et al., 1999). They suggested melt at terminus ice cliffs being important in maintaining streamflow during cool periods, particularly in the beginning and end of summer. Levy et al. (2013) studied thermokarst erosion rates on debris-covered Garwood Glacier (McMurdo Dry Valleys, Antarctica) by monitoring a terminal ice cliff with the help of an airborne LiDAR, terrestrial time lapse imagery and meteorological data recorded in front of the ice wall. Air temperature has not been a primary driver of the observed ice cliff melt, instead net radiation was suggested to be the main physical factor controlling ice cliff retreat (Levy et al., 2013). On the summit plateau of Kibo (Kilimanjaro massif, Tanzania), a tropical glacier, Mölg (2003) analyzed the solar-radiation pattern in combination with glacier retreat of the marginal ice walls. Winkler et al. (2010, 2012) showed that the vertical ice faces on Kibo show a tendency towards an ideal orientation and slope depending on the annual solar cycle.

Supraglacial ice cliffs found on debris-covered glacier tongues have been suggested to act as hot spots for melt, potentially increasing by a substantial amount glacier mass losses (Sakai et al., 1998; Han et al., 2010; Reid and Brock, 2014; Immerzeel et al., 2014b; Thompson et al., 2016; Ragetti et al., 2016a; Watson et al., 2017). By providing a direct ice-atmosphere interface at steep ice faces steep enough to maintain a relatively clean surface, ice cliffs represent spots of high melt rates within debris-covered surfaces where the insulating effect of the glacier-wide debris mantle does not operate. A detailed description of the solar radiation calculation on complex geometries is shown in Chapter A.

Supraglacial ice cliffs (or “ice faces” as they were called) on debris-covered glaciers were studied for the first time on Wolf Creek Glacier in the Canadian St. Elias Range (Sharp, 1947, 1949) in 1941 as distributed debris thickness could be measured at the cliffs’ ridges. In the Himalayas the first field observations in which supraglacial ice cliffs were investigated specifically were conducted during the Japanese ‘Glaciological Expedition of Nepal’ (GEN) 1978 to Khumbu Glacier, Solokhumbu region, Nepalese Himalayas, with several publications in the *Journal of the Japanese Society of Snow and Ice* (Seppy) 1980. Watanabe et al. (1980) described ice cliffs and ponds as typical surface features on debris-

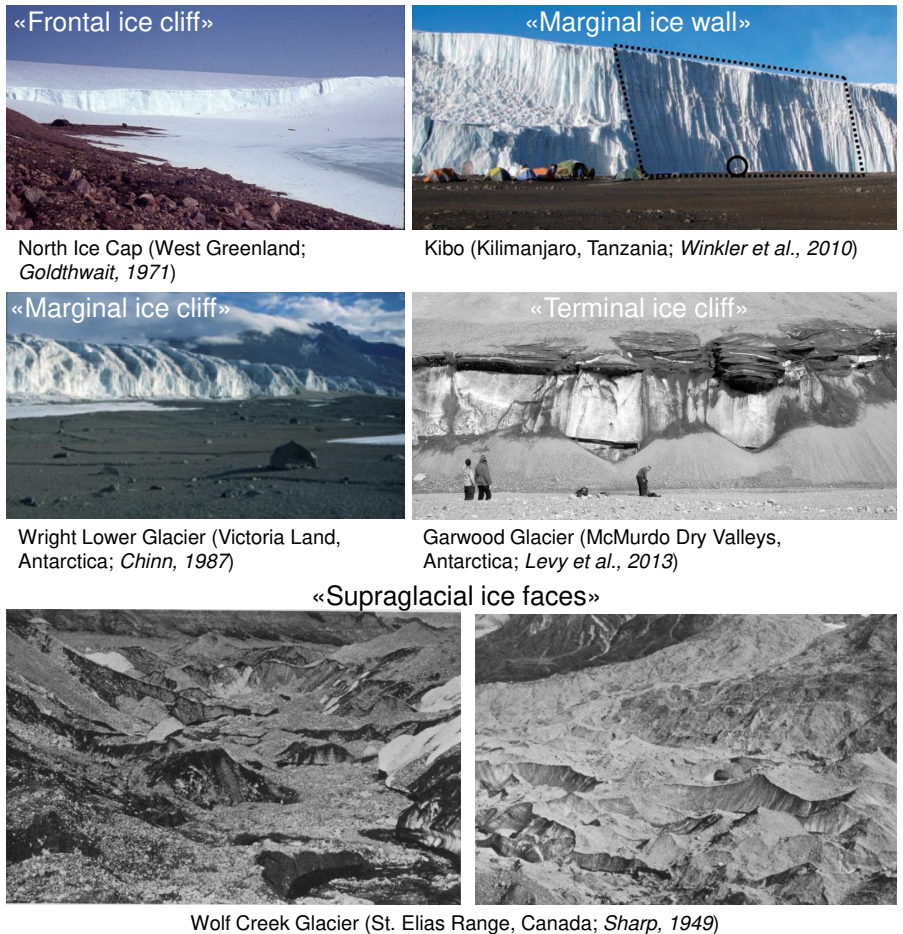


Figure 1.3.: Different ice cliff types described in Chapter 1.2.3. The dashed line on the marginal ice wall (top right panel) indicates the sample cliff of Winkler et al. (2010), encircled the corresponding meteor station.

covered glaciers, Iwata et al. (1980) mapped the morphological characteristics on Khumbu Glacier, during 1978 summer monsoon season. They described ponds, cliffs, streams and debris thickness using terrestrial photogrammetry from the moraine ridges, supported by aerial photographs (Fushimi et al., 1980) conducted

at the same time. Iwata et al. (1980), who stressed the similarity between the surface features on the terminus of Khumbu Glacier with an active rock glacier, investigated the distribution of cliffs and lakes. They concluded that cliffs, with their talus-like form, are formed mainly on flanks of debris-covered ridges and on pond banks, but also appear where streams erode debris slopes laterally. In the lowest glacier part only few cliffs were observed, but many scattered in the upper part, showing high and steep bare ice slopes. Inoue and Yoshida (1980) emphasized for the first time that melt from ice cliff retreat plays a crucial role in total glacier ablation, with most of the glacier ice buried under a thick debris layer. They observed (horizontal) backwasting rates at cliffs of various orientations of up to 4.5cm day^{-1} (mean 2.3cm day^{-1}) as well as calving, compared to a lowering of only 0.15cm day^{-1} of the ice surface under 1.2m thick debris. This was measured during one day in September 1978 in the lower ablation zone of Khumbu Glacier, where the area ratio of the ice cliffs was estimated $<15\%$. Inoue and Yoshida (1980) also compared the measured melt of the ice cliffs with a calculated direct solar radiation receipt, assuming a simplified surface topography. They showed a good agreement between cliff melt rates and direct shortwave radiation, indicating the relevance of this energy flux.

Sakai et al. (1998) were the first to address a complete study of supraglacial ice cliffs. They measured horizontal backwasting distances during one melting season at nearly 50 cliffs on Lirung Glacier, Langtang Valley in the Nepalese Himalayas, where the majority of cliffs was found to have a northern aspect. Sakai et al. (1998) also performed energy balance calculations for idealized cliff geometries to simulate cliff melt rates in a simplified way. They estimated the total horizontal area of all cliffs to be 1.8% of the total debris-covered glacier area, but contributing by 69% to the total sub-debris melt on that glacier. In a similar way, Han et al. (2010) calculated backwasting for 38 cliffs over Koxkar Glacier, in the Tien Shan, China, regarding each cliff as a plane with constant slope and aspect and applying a point calculation to each of them. Their model was further improved by Reid and Brock (2014) with inclusion of a term accounting for the effect of close-range local topography. Debris mounds at close distance from the ice cliffs emit longwave radiation that can be high because of the high temperature debris reaches during the day (up to $30\text{--}40^\circ\text{C}$). This effect, in combination with reduced shortwave radiation, has been proposed to be

responsible for the survival of inclined northerly-facing (in the Northern Hemisphere) cliffs and reburial of southerly-facing cliffs (Sakai et al., 2002). Reid and Brock (2014) accounted for the longwave radiation emitted by debris using an empirical debris view factor above the horizontal which they obtained through calibration. They used the model to calculate ablation on five cliffs on Miage Glacier (Italian Alps), which were monitored in two consecutive years, and then extrapolated the results to the glacier scale.

Up to this point, studies of ice cliff ablation over debris-covered glaciers were limited to point models of ice cliff melt (Sakai et al., 1998, 2002; Han et al., 2010; Reid and Brock, 2014). A holistic understanding of cliffs' role at the glacier scale is still missing. The only studies that have assessed ice cliffs at the glacier scale are Watson et al. (2017), who analyzed cliff aspects on several glaciers in the Khumbu region (Nepal) over multiple years, and Thompson et al. (2016), who derived volume losses of ice cliffs from multi-year DEM-differencing and estimated cliff melt accounting for 40% of the ablation of the debris-covered tongue of Ngozumpa Glacier (Nepal). Anderson (2014) documented cliff characteristics on Kennicott Glacier (Wrangell–St. Elias Mountains, Alaska) for one point in time and calculated cliff melt rates by assuming simple cliff shapes and compared to sub-debris melt extrapolated from field measurements. They found that ice cliffs contribute to 30% of glacier melt in the study area.

1.2.4. Glacio-hydrological modelling

In order to understand the impact of ice cliffs on the mass balance of debris-covered glaciers their total ablation has to be quantified. Model simulations are useful to understand the hydrological characteristics of glacierized catchments and their response to climate (Ragettli, 2014). Typically only a numerical approach can resolve the complex glacio-hydrological system in a distributed way, as the interaction between climatic forcing, glacier change and hydrological response depends on many factors (Ragettli, 2014). Current glacio-hydrological models used to simulate the hydrology of glacierized catchments and predict glacier's long-term response do not include an explicit representation of cliffs or only a simplified one (Ragettli et al., 2015). TOPKAPI-ETH is a process-based and fully distributed hydrological model that includes snow and ice melt (Pellicciotti et al., 2005), melt of debris under ice (Carenzo et al., 2016), glacier geometry changes accounting for glacier flow (Huss et al., 2010), snow albedo

evolution (Brock et al., 2000), re-distribution of snow by avalanching (Bernhardt and Schulz, 2010) and melt water routing (Hock and Noetzi, 1997). These modules make the model suitable for water budget analysis of alpine catchments dominated by cryospheric processes (Ayala, 2017). TOPKAPI-ETH has been applied to various glacierized in the Chilean Andes (Ragettli and Pellicciotti, 2012; Ragettli et al., 2013a, 2016b; Ayala et al., 2016), Pakistan Karakoram (Ragettli et al., 2013b) and Nepalese Himalaya (Ragettli et al., 2015, 2016b). Ragettli et al. (2015) presented a comprehensive study of glacier and runoff components in a Himalaya catchment by integrating detailed local information (distributed meteorological data, satellite images of snow cover, spatially varying debris thickness on glaciers, numerous mass balance and ablation observations) into TOPKAPI-ETH. They were able to link all model parameters to observable physical processes. However, melt due to supraglacial cliffs and lakes was only considered conceptually and an effort to integrate melt from these supra-glacial features into the total melt and mass balance of the debris-covered glaciers through a better process understanding was suggested (Ragettli et al., 2015).

Chapter 2.

Study site: The Upper Langtang Valley, Nepal



Figure 2.1.: Langtang Valley, located in the middle of the picture, as seen from space (ca. 300 km above the earth, looking north). The tie-shaped lake is Peko Tso on the Tibetan Plateau (China; picture: NASA, ISS Mission 8, E6230, 26 Nov. 2003).

2.1. Geography and geology

Langtang Valley is located in the Central Nepalese Himalayas, 60 km north of the capital of Nepal, Kathmandu, and 125km West of Mount Everest. As a glaciated high-altitude catchment in HMA with relatively easy access, Langtang Valley has been site of many scientific studies. The valley belongs to the Rasuwa District (Bagmati Zone; Central Development Region of Nepal) and is part of the Langtang National Park (founded in 1976, the oldest in the country), bordering the Tibetan Autonomous Republic (China; Fig. 5.2) in the north (Fig. 5.2).

Langtang Valley is the source of Langtang Khola, the main stream in the valley, which enters Trisuli Khola in Syaphru Besi (1500m) in the Gandaki River Basin, contributing to the Ganges in Northern India (Fig. 2.3). The upper Langtang Valley ranges from 3650 m a.s.l. (former Langtang Village, destroyed by the co-seismic Langtang avalanche in April 2015, triggered by the Gorkha Earthquake Fujita et al., 2017) to the peak of Langtang Lirung (7234 m a.s.l.). The valley shows extremely steep vertical gradients especially at the entrance of the valley, where the distance of the highest point of the entire catchment (Langtang Lirung) to the two main settlements of Langtang Valley, Langtang Village and Kyanjing Gompa (3862 m a.s.l.) is located only 6.2 and 7 km apart, respectively. The steepness of the basin is also underlined by an average mean slope of 31^{circ} (standard deviation 16^{circ} , calculated with a 30m ASTER-DEM) over the entire basin. Moraines attributed to the Little Ice Age, Neoglacial and Late Glacial have been identified along the valley bottom (Heuberger et al., 1984). Geologically, the catchment is located north of the Main Central Thrust and is based on crystalline rock (Weidinger et al., 2002). The valley bottom of Langtang is covered with Quaternary, alluvial sediments, the western- and southern flanks of the valley are dominated by gneisses, the northeastern section consists of migmatites and leucogranites (Weidinger et al., 2002). The northern central part of Langtang Valley is dominated by the remnants of a gigantic pre-historic landslide, with a assumed displaced volume of $>10\text{km}^3$ (Heuberger et al., 1984).

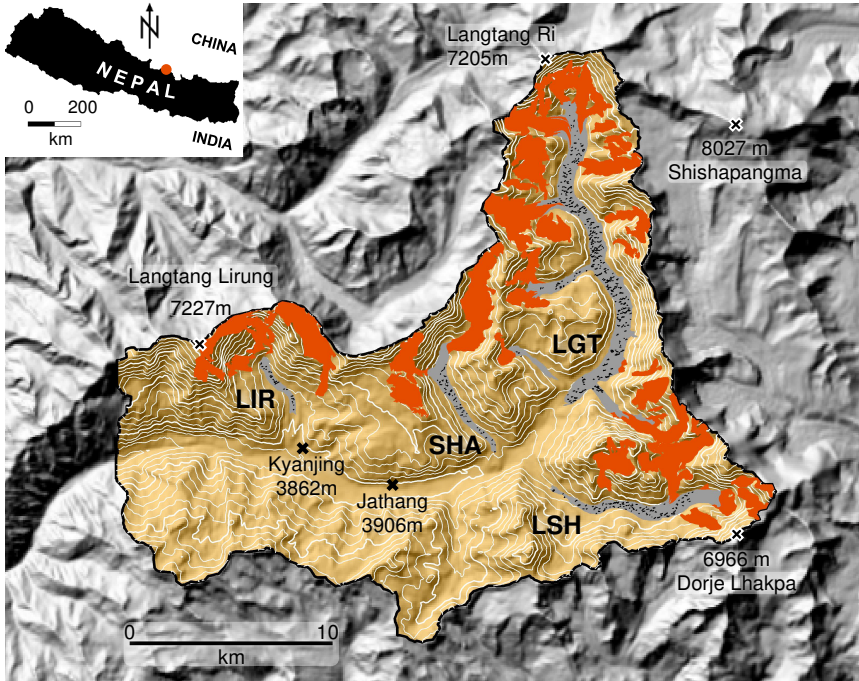


Figure 2.2.: Overview map of the upper Langtang Valley catchment (yellowish) with glaciated areas (orange) and debris covered tongues (grey) including mapped supraglacial ice cliffs (black). The four studied glaciers are Lirung (LIR), Shalbachum (SHA), Langshisha (LSH) and Langtang Glacier (LGT). Also indicated (black crosses) are the automatic weather station in Kyanjing Gompa (KYA), the main settlement in the catchment, and the location of an air temperature logger in Jathang (JAT).

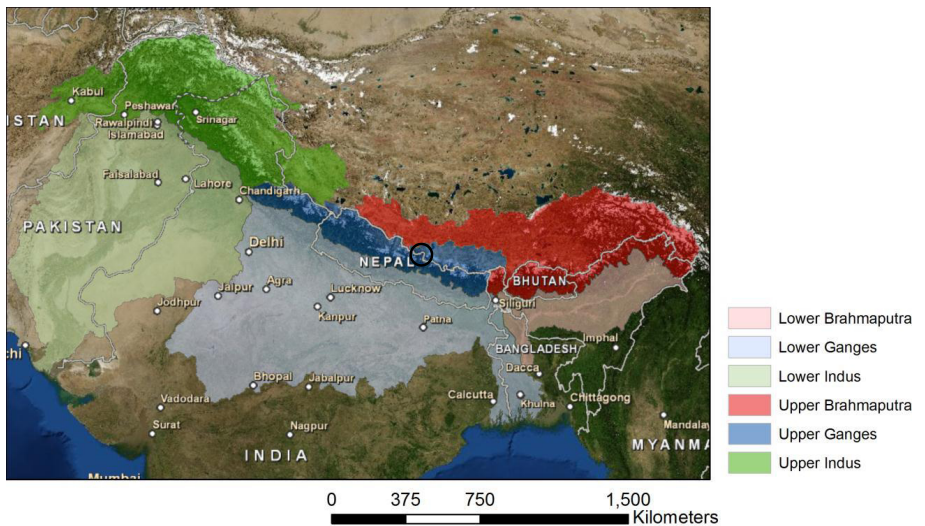


Figure 2.3.: Overview upstream and downstream basin boundaries of the Indus, Ganges, Brahmaputra, Salween and Mekong river basins. Langtang Catchment is in the centre of the black circle. Map modified from Lutz and Immerzeel, (2013).

2.2. Climate

The climatic conditions in the catchment, with its rugged topography directing spatial meteorological variability through relief, illumination, and wind channelization (Miles, 2016), are mainly driven by the South Asian monsoon, affected by dominant easterly winds in summer and westerly winds in winter (Immerzeel et al., 2011). Caused by the typical monsoon circulation, most of the annual precipitation in Langtang Valley (>75%) falls in the monsoon season from mid-June to September (Uppala et al., 2005), with typically consecutive days of moderate rainfall until August and a decreasing number of rainy days but a considerably higher precipitation amount in the second half of the monsoon season (Immerzeel et al., 2011). Precipitation amounts generally increase with elevation both in monsoon- and dry- (winter) seasons (Seko, 1987). Concomitant with the high precipitation rates during the monsoon period with high air temperature, the highest rates of ablation occur during summer (Ragettli et al., 2015). Melting and runoff of snow and ice occurs, especially in the pre-monsoon season (April–June), up to at least 5500 m a.s.l. Steinegger et al. (1993). Transects of air temperature measurements along and across the valley bottom of Langtang Valley have been derived over several years, lapse rates have been analyzed (Immerzeel et al., 2014b; Heynen et al., 2016) and used for high-resolution simulations (WARF) of atmospheric dynamics (Collier and Immerzeel, 2015). On-glacier air temperatures were monitored using a network of loggers across the Lirung Glacier to derive seasonal lapse rates on the debris-covered tongue (Steiner and Pellicciotti, 2016).

2.3. Glaciology

The Langtang Valley catchment has an area of 350km², with a total glacier portion of 33.8%, of which 27% are debris covered, showing varying debris thickness from 0.1 to at least 2.5m (Ragettli et al., 2015). The debris-covered glacier tongues in Langtang Valley are characterized by extremely variable surface topography, with ponds occasionally filling large depressions and by abruptly punctuated ice cliffs (Miles, 2016). The four glaciers studied in this thesis (Lirung, Shalbachum, Langshisha and Langtang Glacier; Fig. 5.2) differ strongly in terms of debris cover, size and hypsometry (Tab. C.1). Lirung Glacier, located at the lowest elevation, is the smallest study glacier with 1.1 km² of debris-cover, which

is 14 times less than the area of the debris-covered tongue of Langtang Glacier. The latter covers the highest elevation range, together with Langshisha Glacier. The contribution of debris on the total glacier area for the four glaciers ranges from 17 (Lirung Glacier) to 33% (Langtang Glacier). All study glaciers show negative mass balances averaged over the entire glacier surface since 1974 with a clear acceleration 2006–2015 with average mass losses of -0.2 (Lirung Glacier) to -0.5m w.e. per year (Langtang Glacier; Ragettli et al., 2016a). Downwasting rates of 0.8 (Langtang Glacier) to 1.4m w.e. per year (Lirung Glacier) were derived for the debris-covered tongues (Ragettli et al., 2016a). While Lirung and Langshisha Glacier slightly retreat from their terminal moraines, Shalbachum and Langtang Glacier downwaste with a stable terminus (Ragettli et al., 2016a). Field observations have noted the pronounced disconnect between the debris-covered tongue and clean-ice upper portion for Lirung Glacier, a process which has recently been noted for Shalbachum Glacier as well (Miles, 2016). Both Langshisha and Langtang Glacier have lost connectivity with minor tributaries since the 1970's (Pellicciotti et al., 2015; Ragettli et al., 2016a) Despite of its small size and advanced decay Immerzeel et al. (2014b), an extensive set of glaciological and meteorological studies has been conducted on Lirung Glacier over the past decades, as it is the most accessible glacier in the valley and its relatively small debris-covered glacier tongue enables investigations of changes across the entire glacier surface (Miles, 2016). Studies on the debris-covered tongue of Lirung Glacier have analyzed surface changes (Aoki and Asahi, 1998; Naito et al., 2002; Immerzeel et al., 2014a; Kraaijenbrink et al., 2016), supraglacial features such as ice cliffs (Sakai et al., 1998, 2002; Steiner et al., 2015) and ponds Sakai et al. (2000); Takeuchi et al. (2012); Miles et al. (2016, 2017a) and serve as an excellent base to further investigate small-scale processes of ice cliffs.

Chapter 3.

Data



Figure 3.1.: Approaching the debris-covered tongue of Langtang Glacier, bringing down equipment for the automatic weather station (Picture: E. Miles, 12 May 2014)

A laborious and time-consuming, but completely necessary part of this PhD-thesis was the organisation and conductance of three field campaigns, which were needed to:

- 1) collect timeseries of on-glacier air- and surface temperature records from all four debris-covered glaciers in the catchment plus altitudinal transects along the valley bottom to gain knowledge about the off-glacier meteorological forcing in the study catchment;
- 2) establish on-glacier automatic weather stations on the debris-covered tongues of Lirung- and Langtang Glacier, serving as fundamental base of all modelling approaches in this thesis;
- 3) conduct extensive mechanical, meteorological and photogrammetric investigations ice cliff melt and backwasting, helping to understand the processes relevant for ice cliff melt and evolution, a knowledge being still in its infancy.

3.1. Major field campaigns: April–May 2014, October–November 2014

The focus of the first two field campaigns conducted during this PhD-project, in pre- and post-monsoon 2014, was the detailed investigation of debris-, pond- and cliff-related processes both on the tongues of Lirung and Langtang Glacier. In each of the lower central parts of the two glaciers we mounted a fully equipped AWS, recording incoming and outgoing short- and longwave radiation, surface and air temperature, surface lowering, as well as wind speed and -direction at 5-minute-intervals. At the site of the station we installed a thermistor chain measuring temperature and moisture at different levels within the debris, reaching from the atmosphere-debris- to the debris-ice interface. Also close to the AWS Lirung we installed a wind tower, measuring wind speed at three different heights (see Miles et al., 2017a) in order to get insights into the atmospheric boundary layer. Distributed over the glacier surface we read out and maintained an existing network of sub-debris-ablation stakes, air- and surface temperature loggers (Fig. C.1, (see Steiner and Pellicciotti, 2016)). In multiple supraglacial ponds we installed shortwave radiometers (CM7B) to derive energy fluxes acting at the water surface (see Miles et al., 2016). Additionally we deployed and maintained pressure transducers and water temperature instruments in various ponds, and tracked supraglacial and sub-debris streams (see Miles et al., 2017c). Using a

differential GPS (dGPS) we surveyed the glacier surface regarding surface motion by tracking dozens of stable boulders at the beginning and at the end of the melting season 2014. Additionally we delineated the outlines of all ice cliffs on Lirung Glacier. The dGPS-surveys were completed by photogrammetric DEMs of selected ice cliffs derived in May and October/November 2014 to derive cliff volume losses (see Brun et al., 2016). Along vertical profiles of various ice cliffs we manually drilled ablation stakes (2–3 measurements per day during pre- and post-monsoon campaigns), monitored the cliff’s topography (slope and aspect) and derived albedo values at multiple points in time, using shortwave radiation instruments (CM7B) or low-cost luxmeters (see Steiner et al., 2015). To investigate different fluxes at the cliff surface we deployed instruments measuring ice surface- or air temperature at different levels above the ice cliff layer, shortwave radiation (CM7B), longwave radiation (CNR1) and wind sensors, all inclined parallel to the cliff slope and placed at different positions along the profile. Regarding the off-glacier meteorology and specifically lapse rates, we read out and maintained an existing network of temperature-logger transects along the valley bottom up to 5450 m a.s.l. (see Heynen et al., 2016).

3.2. Data used for ice cliff modelling

Meteorological data

Meteorological measurements from on-glacier automatic weather stations are available from full automatic weather stations Lirung Glacier (AWS LIR, 4076 m a.s.l.) in 2013 and 2014 (May–Oct), and on Langtang Glacier during in 2014 (May–Oct) (AWS LGT, 4557 m a.s.l.). Both are located on the debris-covered glacier tongue (Fig. 5.2) and recorded (all 2m above ground) air temperature (shielded and ventilated), incoming shortwave radiation (parallel to the surface), relative humidity of the air and wind speed (Steiner et al., 2015). For the 2014-melt season AWS LIR was additionally equipped with an instrument measuring incoming and outgoing longwave radiation. AWS Kyanjing (AWS KYA, 3857 m a.s.l.) was used to extrapolate air temperatures to the two study glaciers without a full on-glacier weather station (SHA and LSH), using valley lapse rates from (Heynen et al., 2016). Further air temperature measurements were recorded using light weight temperature loggers structures (T-loggers) 2m above ground on various sites along the valley bottom (Heynen et al., 2016) and on the four

main debris-covered glaciers in the catchment. Equal temperature sensors were put on the glacier surface to measure debris-temperatures, wrapped in reflective tape to be protected from direct solar radiation (Petersen and Pellicciotti, 2011).

Topographic data

For May and October 2013, and for May 2014 three high-resolution DEMs (0.2 m spatial resolution for May and October 2013 Immerzeel et al., 2014a, and 0.15 m spatial resolution for May 2014 Kraaijenbrink et al., 2016 derived from UAV-based orthomosaics are available. The UAV-DEMs cover the lower part of Lirung Glacier. Additionally, a terrestrial photogrammetry survey from November 2014 on Lirung Glacier (Brun et al., 2016) provided a further high-resolution DEM- and orthoimage dataset, which could be used for validation of ice cliff model results in 2014. The high resolution orthophotos (0.1 m) were used to delineate the outlines of the cliffs. For the modelling approach covering all cliffs in the Langtang Catchment (Chapter 8) we used a high resolution SPOT6-orthoimage and -DEM (1.5 and 3m spatial resolution, tri-stereo mode) from April 2014 (Ragettli et al., 2016a). As due to cloud cover the upper part of Langtang Glacier was not covered by this product, the upper part of Langtang Glacier was replaced by the SPOT7-orthoimage and -DEM (1.5 and 3m spatial resolution, tri-stereo mode) from 6 October 2015 (Ragettli et al., 2016a). Relevant for shortwave and longwave radiative calculations and their interaction with the surrounding topography we used the ASTER-GDEM2 with a resolution of one arc-second (~ 30 m) (Tachikawa et al., 2011).

Chapter 4.

Modelling radiative fluxes over complex cliff geometries



Figure 4.1.: Tilted sensor (CNR1) installed on Cliff 1 on Lirung Glacier to measure short- and longwave radiation (24 Oct. 2014).

The solar radiation income at a cliff is one of the main factors affecting melt. Therefore the understanding of the geometry-radiation-relationship is important. Whereas longwave radiation, which is emitted by the atmosphere (clouds) or surrounding areas (debris, ice), does not have a very strong diurnal cycle, shortwave or solar radiation with the sun as source highly depends on the actual time and the topography which can interrupt the regular solar income.

The distinction between the components of the solar irradiance (direct-, diffuse- and reflected radiation) is important but not easy to manage. Whereas the estimation of the potential direct beam radiation at a slope is theoretically straightforward with the help of an appropriate DEM, the amount of diffuse radiation at a certain time is not easy to calculate.

In this chapter the basic concept of the solar radiation at a non-horizontal surface and hence the way how shortwave radiation at a cliff is calculated in our current cliff models is presented. All these calculations designed for the point-scale had to be transformed into a distributed approach, which we then applied as described in Chapter 5 and all the following studies. Results showing the variability in incoming shortwave radiation along a cliff profile is presented, conducted from in-situ measurements, are shown in the Appendix Chapter A.

4.1. Background computations

With relatively simple empirical but profound equations the position of the sun can be determined for every point in time, assuming a fixed position on any point on the earth surface. First the day angle (Γ [rad]), a continuously increasing value through the year, can be calculated according to Wong and Chow (2001)

$$\Gamma = 2 \cdot \pi(\text{doy} - 79.6764 - 0.2422 \cdot (y - 1985) + \frac{INT[\frac{(y-1985)}{4}]}{65.2422}), \quad (4.1)$$

where *doy* is the day number of the year (*y*). With this angle the eccentricity correction of the earth's orbit (E_0), a factor close to 1, can be derived according to Wong and Chow (2001) from

$$E_0 = 1.00011 + 0.034221 \cdot \cos\Gamma + 0.00128 \cdot \sin\Gamma - 0.000719 \cdot \cos 2\Gamma + 0.000077 \cdot \sin 2\Gamma. \quad (4.2)$$

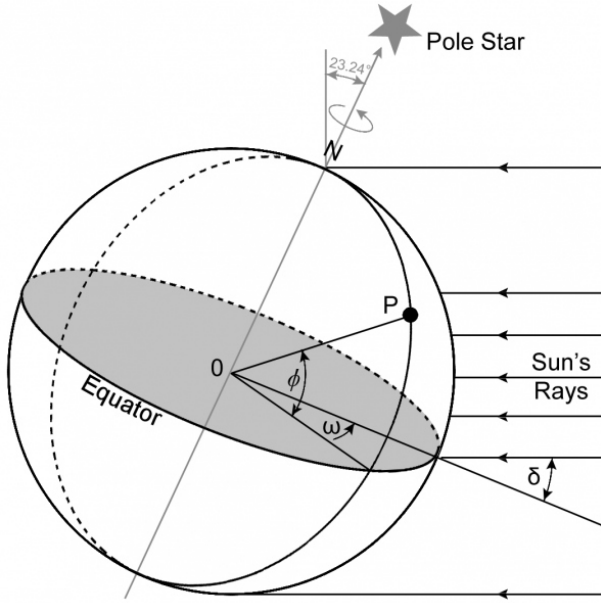


Figure 4.2.: Scheme of the earth's declination angle (δ), hour angle (ω) and the latitude (ϕ) at a certain point P on the earth's surface. Source: <http://www.itacanet.org/the-sun-as-a-source-of-energy/>.

The hour angle (ω [rad]) increases during the day and is negative in the morning and zero during solar noon (Fig. 4.2). As the earth turns once in a day, ω changes by 15° ($360^\circ/24$ hours) every hour. This angle can be calculated as

$$\omega = 15 \cdot \left(\frac{\text{time}}{100} - 12 \right) \cdot \frac{\pi}{180}, \quad (4.3)$$

where time is the time in HHMM format.

The declination angle (δ [rad]) is the same for the whole earth at a the same time/day. δ varies between -23.45° and $+23.45^\circ$ (winter and summer solstice, 0° at autumnal and vernal equinox) and can be calculated according to Cooper (1969) as

$$\delta = 23.45 \cdot \sin\left(\left(\frac{\text{day} + 284}{365}\right) \cdot \frac{\pi}{180}\right) \cdot \frac{\pi}{180}. \quad (4.4)$$

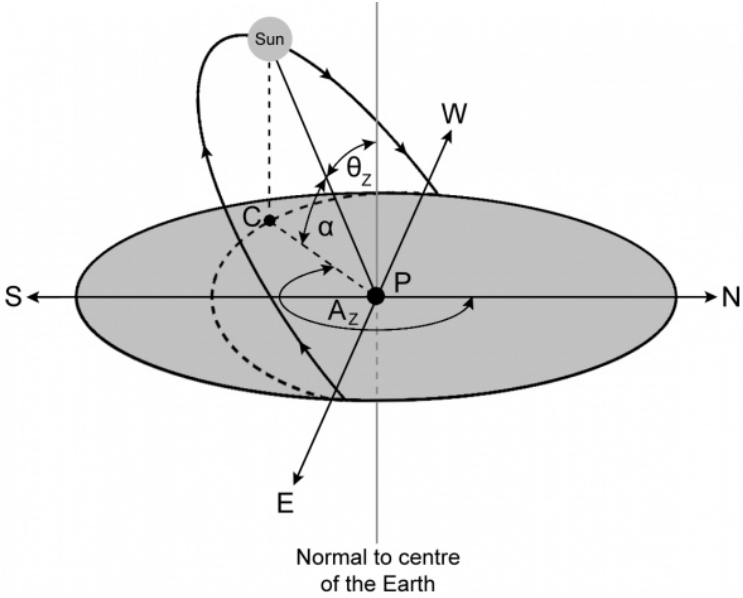


Figure 4.3.: Scheme of the solar zenith angle (θ_z) and the elevation angle (here: α) which is its summand to 90° . A is the solar azimuth which gives the actual compass position of the sun. Note that we are here in a local coordinate system, as in Fig 4.2 we are in a global one. Source: <http://www.itacanet.org/the-sun-as-a-source-of-energy/>.

The solar elevation angle (ϵ [rad]) shows the height of the sun in the sky (Fig. 4.3) and can be determined from

$$\epsilon = \text{asin}(\cos\omega) \cdot \cos\delta \cdot \cos\phi + \sin\delta \cdot \sin\phi, \quad (4.5)$$

where ϕ [rad] is the latitude of a specific point on the earth. From α the solar zenith angle θ_z can be simply derived as the two have to sum up to 90° . The solar azimuth angle (A [rad]) determines the sun's compass position at a certain point in time and can be calculated from

$$A = \pi - \text{asin}(\sin\omega) \cdot \frac{\cos\delta}{\cos\epsilon}. \quad (4.6)$$

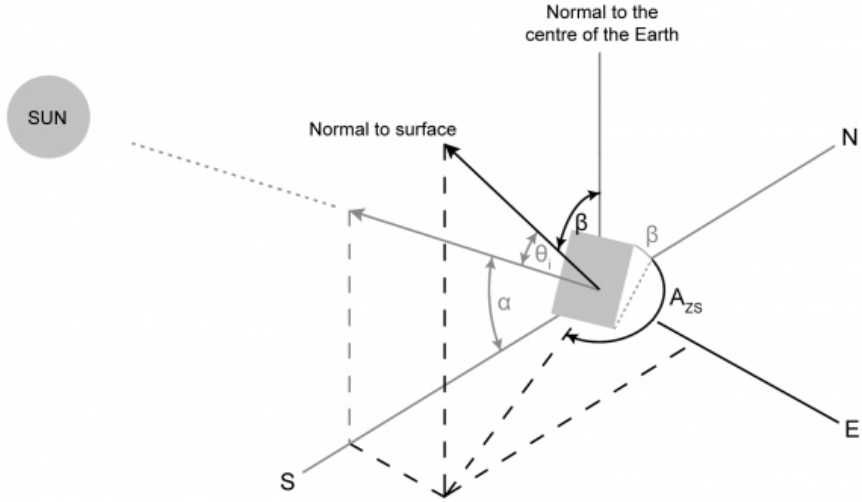


Figure 4.4.: Scheme of the angle of incidence (θ_i) which indicates the angular difference between the solar incidence angle and the vector normal to the surface with a specific slope (β) and azimuth (A_{ZS}). Source: <http://www.itacanet.org/the-sun-as-a-source-of-energy/>.

A comparison of all the relevant angles to determine the sun's position can be seen in Fig. A.1. For later calculations A, the azimuth angle of the sun, is an important value. It can be seen that the sunrise is just below 100° and sunset around 260° (when the elevation angle is above 0°).

Now the extraterrestrial radiation I_E [$W m^{-2}$] can be calculated from

$$I_E = E_0 \cdot I_{SC} \cdot \sin \epsilon, \quad (4.7)$$

where I_{SC} is the solar constant, which is assumed to be constant over time with a value of $1367 W m^{-2}$.

4.2. Geometry driven computation of radiative forcing

With the estimate of the sun's position for every timestep as calculated in 4.1, the geometry of the sun rays can be used. Based on Reindl et al. (1990) and

as used in Han et al. (2010) and Reid and Brock (2014) the clearness of the atmosphere can be described with a clearness index k_t from

$$k_t = \frac{I_0}{I_E}, \quad (4.8)$$

as the amount of solar radiation which reached the (horizontal) surface (I_0 [W m^{-2}], measured at AWS) divided by the potential radiation which would reach the ground in case of a completely clean and dry atmosphere. The diffuse fraction (k_d) depends on k_t the following way:

$$\begin{cases} 1.02 - 0.254 \cdot k_t + 0.0123 \cdot \sin\epsilon & k_t \leq 0.3 \\ 1.4 - 1.749 \cdot k_t + 0.177 \cdot \sin\epsilon & 0.3 < k_t \leq 0.78 \\ 0.486 - 0.182 \cdot \sin\epsilon & k_t \geq 0.78 \end{cases} \quad (4.9)$$

Then the diffuse irradiance to a horizontal surface (D_h [W m^{-2}]) can be expressed as

$$D_h = k_d \cdot I_0, \quad (4.10)$$

and from this the direct normal irradiance (I_b) is then

$$I_b = \frac{(I_0 - D_h)}{\sin\epsilon}. \quad (4.11)$$

Whereas I_0 is the measured global shortwave radiation at a horizontal plane on the earth's surface (here at the AWS location), I_b is the amount of direct radiation which can be expected at a plane normal to the sun rays. I_b shows the direct radiation in case a surface is permanently faced exactly towards the sun. The correction with the sinus as a factor is high with low elevation angles and small when the sun is already at a high position. The conversion from a horizontal plane to a normal one as in Eq. 4.11 can also be done with the help of the solar zenith angle θ_z :

$$I_b = \frac{(I_0 - D_h)}{\cos\theta_z}. \quad (4.12)$$

The equation for estimating I_b is a function of ϵ , I_0 and D_h . The former two are given from the basic calculations and from the observations respectively, thus the uncertainty lies in the diffuse component.

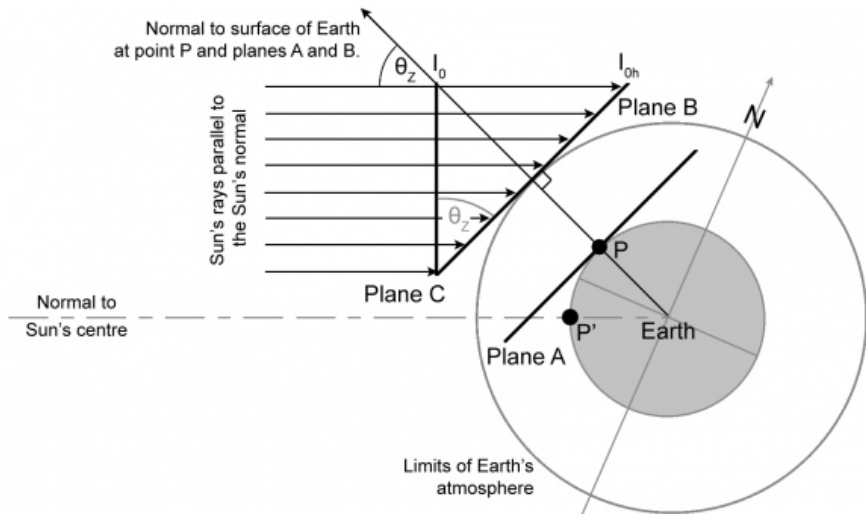


Figure 4.5.: Scheme of the radiation conversion from a horizontal plane (here: *Plane A*) to a plane normal to the solar beam (here: *Plane C*). A similar calculation is done in Eqs. 4.11 and 4.12, respectively. Source: <http://www.itacanet.org/the-sun-as-a-source-of-energy/>.

In Han et al. (2010) and Reid and Brock (2014) the direct solar irradiance from sky on a slope (I_s [W m^{-2}]) is calculated following the approach of Garnier and Ohmura (1968). In the following Eq. 4.13 the cosine of the angle between the solar incidence and the normal vector of the given sloped surface is determined:

$$\begin{aligned}
 \cos\theta_i = & \sin\phi \cdot \cos\omega \cdot (-\cos\gamma \cdot \sin\beta) \\
 & -\sin\omega \cdot \sin\gamma \cdot \sin\beta \\
 & +\cos\phi \cdot \cos(\omega \cdot \cos\beta) \cdot \cos\beta \\
 & +(\cos\phi \cdot \cos(\gamma \cdot \sin\beta) \\
 & +\sin\phi \cdot \cos\beta) \cdot \sin\beta,
 \end{aligned} \tag{4.13}$$

where γ [rad] is the azimuth of the slope and β [rad] the slope's inclination. This relationship between the direction of the sun rays and the normal of the slope is now multiplied with the direct solar radiation normal to the solar beam to make the conversion to the real sloped surface:

$$I_s = I_b \cdot \cos\theta_i, \tag{4.14}$$

where I_s is the simulated direct solar irradiance the slope receives at every timestep. It can be seen that a small deviation of the slope's normal vector to the solar incidence gives a high $\cos\theta_i$ -value (as the minimum deviation angle is 0° , which results in a cosine of 1), thus in that case the (maximal) direct radiation normal to the solar beam is only slightly reduced. Additionally the input of direct solar radiation should be set to zero in cases the sun does not reach the sloped surface due to the local horizon. For that the horizon angle in every direction looking from one point has to be known. This can be derived from a DEM. As a result from these topography analysis a value for sky (V_s) and debris view (V_d) for a point on the surface can be calculated. Applying the horizon angle to the direct component mainly affects the skinniness of the daily solar radiation curves as after the sun's elevation angle exceeds the local horizon in the correspondent azimuth direction, the direct beam radiation can contribute to the total solar income. Once the sun is above the horizon, the topography normally does not affect the direct solar radiation anymore. The shape of the solar radiation curve is therefore dependent on another parameter.

The diffuse irradiance from sky, D_s [W m^{-2}], is calculated by multiplying D_h with the corresponding skyview factor. Thus

$$D_s = D_h \cdot V_s \quad (4.15)$$

gives a value for the diffuse sky irradiance already corrected for a certain slope, as the diffuse radiation can be assumed to be isotropic and therefore only the amount of visible sky from a point on the surface is important, the slope and the azimuth are not taken into account. The same for the diffuse irradiance from the surrounding terrain (D_t), which can be determined from

$$D_t = \alpha_t \cdot I_0 \cdot V_d, \quad (4.16)$$

where α_i is an average albedo value for the surrounding terrain. Summing up all single components of the incoming solar radiation results in

$$I_{in} = I_s + D_s + D_t, \quad (4.17)$$

where I_{in} [W m^{-2}] is the total incoming shortwave radiation. In Fig. A.2 the dependency of the solar elevation angle on the local horizon angle is shown in an 3-day time series. As soon as the solar elevation angle exceeds the horizon angle (during these days around 8'clock), the direct solar radiation component can occur, given there is not a dense cloud cover at that time. The diffuse irradiance in contrast can contribute to the total incoming shortwave already before and after that point in time the direct radiation appears.

Chapter 5.

A grid-based model of backwasting of supraglacial ice cliffs on debris-covered glaciers*



Figure 5.1.: Ablation measurements on Cliff 2 with a supraglacial pond attached to its base (6 May 2014)

* Buri P, Pellicciotti F, Steiner JF, Miles ES and Immerzeel WW (2016a) A grid-based model of backwasting of supraglacial ice cliffs on debris-covered glaciers. *Annals of Glaciology*, 57(71), 199–211 (doi: 10.3189/2016AoG71A059)

Abstract Ice cliffs on debris-covered glaciers might be partly responsible for the high mass losses of these glaciers in the Hindukush-Karakoram-Himalaya region. The few existing models of cliff backwasting are point scale models applied at few locations or assuming cliffs to be planes with constant slope and aspect, a strong simplification given the complex surfaces of most cliffs. We develop the first grid-based model of cliff backwasting for two cliffs on the debris-covered Lirung Glacier, Nepal. The model includes an improved representation of shortwave and longwave radiation and their interplay with the glacier topography. Shortwave radiation varies considerably across the two cliffs, mostly due to the direct radiation. Diffuse radiation is the major shortwave component, as the direct component is strongly reduced by the cliffs' aspect and slope through self-shading. Incoming longwave radiation is higher than the total incoming shortwave flux, due to the radiation emitted by the surrounding terrain, which is 25 % of the incoming flux. Melt is highly variable in space, suggesting that simple models provide inaccurate estimates of total melt volumes. Although only representing 0.09 % of the glacier tongue area, the total melt at the two cliffs over the measurement period is 2313 and 8282 m³, 1.23 % of the total melt simulated by a glacio-hydrological model for the glacier's tongue.

5.1. Introduction

Debris-covered glaciers are common in many mountain ranges of the world, and in the Hindukush-Karakoram-Himalaya (HKH) region in particular (e.g. Bolch et al., 2012), but they are hardly studied and poorly understood. Several works have focused on understanding the energy transfer through debris and the melt of the ice underneath. With few exceptions (Reid et al., 2012; Fyffe et al., 2014; Fujita and Sakai, 2014), however, most have been limited to analysis at the point scale, ignoring the complex and dynamic surfaces of many debris-covered glaciers (Benn et al., 2012; Pellicciotti et al., 2015). A number of recent studies based on remote sensing have suggested that, despite the reduction in melt caused by debris thicker than a few centimetres as observed in experiments at single points, debris-covered glaciers in the HKH region are losing mass at rates similar to those of debris-free glaciers (Kääb et al., 2012; Nuimura et al., 2012; Gardelle et al., 2012, 2013). This discrepancy has been referred to as the debris-cover anomaly (Pellicciotti et al., 2015). Those findings have been obtained only for a

very recent period, and are controversial (Kääb et al., 2012), but have prompted research on possible causes of such high rates of mass loss from debris-covered ice. Some authors have suggested that these might be due to the presence of supraglacial lakes and cliffs that offer surfaces where high melt rates can occur (Sakai et al., 1998; Benn et al., 2012; Pellicciotti et al., 2015). These features are commonly observed at low elevations on semi-stagnant tongues covered in thick debris (Benn et al., 2012; Pellicciotti et al., 2015), but there are relatively few quantitative studies of ablation at ice cliffs (Sakai et al., 1998, 2002; Han et al., 2010; Reid and Brock, 2014; Steiner et al., 2015) and all are limited to point models of backwasting. Han et al. (2010) calculated backwasting for 38 cliffs on Koxkar Glacier, in the Tien Shan, China, but regarded each cliff as a plane with constant slope and aspect and applied a point calculation to each of them. Their model was further modified by Reid and Brock (2014) with inclusion of a term accounting for the effect of longwave radiation originating from close-range local topography. Debris mounds near the ice cliffs emit longwave radiation that can be intense because of the high temperature debris reaches during the day (up to 30 – 40°C, Steiner et al., 2015). This effect, in combination with reduced short-wave radiation, has been proposed to be responsible for the survival of inclined poleward-facing cliffs (Sakai et al., 2002). Reid and Brock (2014) accounted for the longwave radiation emitted by debris using an empirical debris view factor above the horizontal which they obtained through calibration. They used the model to calculate ablation at a number of stakes at five cliffs on Miage Glacier, Italy, that were monitored in two years, and then extrapolated the results to the glacier scale by running the model on every cell of cliff surfaces identified from a high resolution DEM. Steiner et al. (2015) replaced the empirically determined debris view factor with a calculation of the debris and sky view factors based on geometric considerations, a radiation model and an accurate DEM of 0.2 m resolution of the glacier.

No previous gridded model of cliff backwasting exists, and previous distributed estimates have all been obtained from extrapolation of point measurements, running multiple point runs (Reid and Brock, 2014) or assuming that the cliff is a plane with constant geometry, slope and aspect (Sakai et al., 1998; Han et al., 2010). In this paper, we build on the point model developed by Steiner et al. (2015) to develop a distributed model of cliff backwasting in which the cliff is represented as a grid-based domain of cells of 0.2 m resolution. In this way, the

real, complex geometry of the cliff can be taken into account in the calculation of energy fluxes and ablation rates. Our aims are i) to understand the spatial patterns of radiative fluxes and melt over two cliffs on one debris covered glacier; and ii) to accurately quantify (and not by extrapolation) the total mass lost by the two cliffs during one ablation season.

We use data collected at two cliffs on the debris-covered tongue of Lirung Glacier in one melt season, from May to October 2013. The data include meteorological observations, measurements of melt at the cliffs (perpendicular to the surface), observations of cliff geometry and a 0.2 m DEM derived from repeated flights with an unmanned aerial vehicle (UAV) equipped with a camera. The data have been used by Steiner et al. (2015) and are described there in detail. We recall the main characteristics of the data set, then describe the model and the shortwave and longwave calculations in particular, and discuss the results at the two study cliffs, which differ in size and shape.

5.2. Study site

The debris-covered Lirung Glacier (28.2325°N , 85.5619°E) is located in the Upper Langtang Valley, Central Nepalese Himalayas (see Figure 5.2). The Langtang catchment has an area of 350 km^2 and contains 72 glaciers (Shiraiwa and Yamada, 1992) which cover 118 km^2 (about one third of the total area) (Shiraiwa and Yamada, 1992; Ragettli et al., 2015). The largest glaciers have debris-covered ablation zones, and 24% of the glacierized area is covered by debris (Pellicciotti et al., 2015). Lirung Glacier has an elevation range of $\sim 4004 - 7234\text{ m a.s.l.}$, and its tongue, which is decoupled from the steep accumulation zone above, ranges between $\sim 4000 - 4450\text{ m a.s.l.}$ and measures 3.5 km in length and 500 m in width (Immerzeel et al., 2014a). The debris is heterogeneous, ranging in size from large boulders to finer sediments, and exceeds 50 cm in thickness for most of the tongue (Ragettli et al., 2015).

Supraglacial cliffs and lakes are common on the glacier tongue (Sakai et al., 1998, 2000; Immerzeel et al., 2014a; Steiner et al., 2015; Miles et al., 2016). In 2013, a total of 13 supraglacial ice cliffs were observed on the glacier tongue, including eight in the UAV survey area. In this paper we focus on two cliffs that were monitored in detail in May and October 2013 during extensive field campaigns. The aim of the field campaigns was to provide the data for a modelling effort to

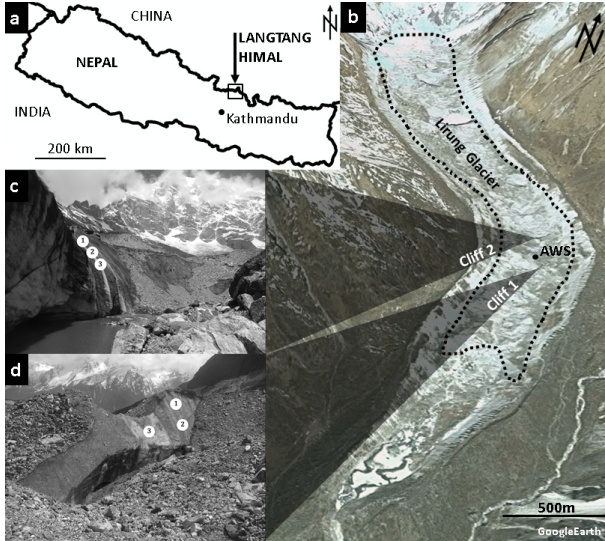


Figure 5.2.: Overview of Langtang region (a); the tongue of Lirung Glacier as it appears on Google Earth (b); and the two investigated cliffs: Cliff 2 (c) and Cliff 1 (d). The on-glacier automatic weather station (AWS in the figure, and indicated as AWS-Lirung in the paper) is marked with a black dot. The approximate extent of the debris-covered tongue is shown with a dashed line. The stake locations on the cliffs in May 2013 are indicated with white dots and their corresponding number in panels (c) and (d).

understand the response of the debris-covered glaciers of the valley to a changing climate (Ragettli et al., 2015). The smaller cliff, Cliff 1 (10 m height, 45 m length), has a NW aspect, while Cliff 2 (25 m height, 95 m length) is mainly facing northeast (Figure 5.3 and Table 5.1).

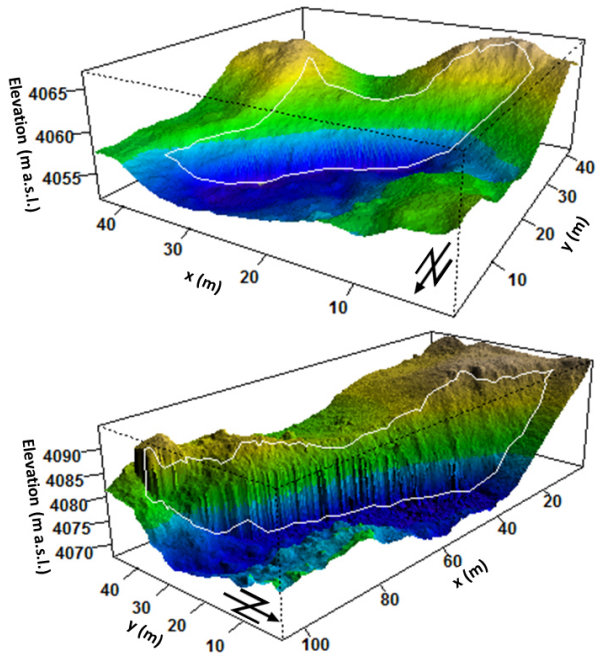


Figure 5.3.: 3D-view of Cliff 1 (top) and Cliff 2 (bottom) based on the UAV-DEM from May 2013, looking from northwest (Cliff 1) and northeast (Cliff 2) and coloured according to elevation. A colour scale is not shown as the elevation scale is provided by the z-axis. The borders of the cliff areas are indicated with white lines.

5.3. Data

5.3.1. Meteorological data

Meteorological data were recorded at a five-minute interval at an automatic weather station (AWS Lirung, 4076 m a.s.l.) located on the tongue of Lirung glacier (see Figure 5.2). The station was installed between the two cliffs in spring 2013 and recorded until autumn 2013 (from 8th of May until 23th of October 2013). The measurement period was divided into three subseasons (following Immerzeel et al., 2014b): i) 'pre-Monsoon' (8th of May to 14th of June), Monsoon (15th of June to 19th of September) and iii) 'post-Monsoon' (20th of September to 23rd of October).

The station recorded the following meteorological variables used for the modelling: air temperature (T_a , shielded and ventilated [$^{\circ}\text{C}$]), incoming shortwave radiation (I_{in} [W m^{-2}], parallel to the gently sloped surface), relative humidity of the air ($h_{r,a}$ [%]) and wind speed (u [m s^{-1}]), all measured at 2 m above ground. The sensor setup and specifications are described in Steiner et al. (2015). Debris surface temperature (T_s [$^{\circ}\text{C}$]) was measured with a temperature logger HOBO TidbiT v2 (UTBI-001) wrapped in reflecting tape and placed on a rock near the station (see Petersen and Pellicciotti (2011) for details of the sensor). Incoming longwave radiation L_{in} [W m^{-2}] was not measured and is therefore modelled (see Section 5.4.3).

5.3.2. Topographic data

In May and October 2013 a UAV collected photos which were processed to generate two high-resolution DEMs (0.2 m) for May and October (Immerzeel et al., 2014a). The two UAV-DEMs cover the lower part of the glacier tongue and include Cliff 1 and Cliff 2 as well as their surroundings. The UAV-DEM from 18th/19th of May is used to prescribe the initial geometry of the cliffs. The high resolution orthophotos (0.1 m) were used to delineate the outlines of the cliffs. For calculation of shortwave and longwave radiative fluxes and their interaction with the nearby topography and more distant mountain ridges we used a combination of the high resolution UAV-DEM and the ASTER-GDEM2 with a resolution of one arc-second (~ 30 m) (Tachikawa et al., 2011).

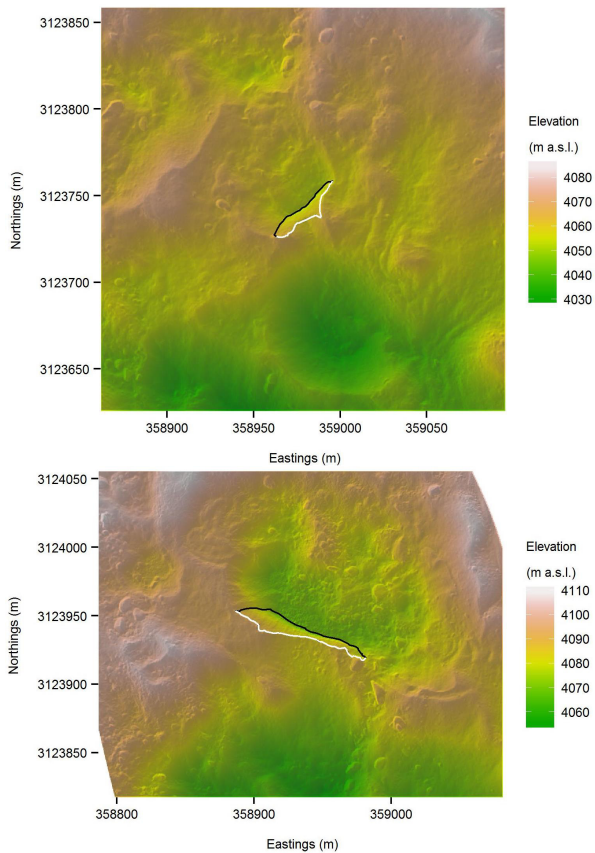


Figure 5.4.: UAV-DEMs (0.4 m resolution) showing the maximum area of influence for the calculations of longwave radiation for the entire Cliff 1 (top) and Cliff 2 (bottom), respectively. The area shown is such that it includes the 200m x 200m area of interest for each of the cliff pixels. The two-dimensional shape of the cliffs is indicated by lines, with the white line marking the crest of the cliffs and the black line their bottom. The reference system of the map is WGS 84 and the projection is UTM 45N.

5.3.3. Cliff ablation and surface topography

Bamboo stakes were drilled across the ice surfaces of both cliffs, seven in May (three on Cliff 1, four on Cliff 2) and eight in October 2013 (five on Cliff 1 and three on Cliff 2) to record cliff melt (see Figure 5.2). Surface backwasting was read during the two field trips of May and October. Surface albedo, slope and aspect were also measured at each stake once in May and once in October 2013. Details of the stake measurements can be found in Steiner et al. (2015). Slope and aspect for every grid cell of 0.2 m resolution were calculated from the UAV DEM. The mean slope of Cliff 1 is 45.6° and of Cliff 2 is 53.2° , with standard deviation of 13.8° and 15.1° respectively (Table 5.1).

Table 5.1.: Characteristics of the two supraglacial ice cliffs on Lirung Glacier investigated in this study: mean, standard deviation (sd), minimum and maximum value (min and max respectively) and coefficient of variation ($cv=sd/mean$). Elevation is in m a.s.l. (and m for sd), slope and aspect are in degrees (with $0/360^\circ$ indicating northern and 180° indicating southern direction). $V_{s,I}$ and $V_{s,L}$ are the skyview factors for shortwave radiation and longwave radiation, respectively; V_d is the debrisview factor. The three viewing factors are dimensionless. The values for the AWS-site are shown for comparison below.

	Variable	mean	sd	min	max	cv
Cliff 1	Elevation	4058	3.10	4052	4066	0.00
	Slope	45.6	13.77	0.37	83.10	0.30
	Aspect	327.70	29.49			
	$V_{s,I}$	0.63	0.05	0.47	0.73	0.08
	$V_{s,L}$	0.75	0.07	0.53	0.93	0.37
	V_d	0.23	0.09	0.11	0.54	0.37
Cliff 2	Elevation	4081	5.55	4068	4093	0.00
	Slope	53.23	15.13	2.23	86.66	0.28
	Aspect	29.37	27.12			
	$V_{s,I}$	0.59	0.07	0.37	0.73	0.11
	$V_{s,L}$	0.72	0.09	0.40	0.93	0.49
	V_d	0.21	0.09	0.08	0.55	0.41
AWS Lirung	Elevation			4062		
	Slope			9.18		
	Aspect			25.53		
	$V_{s,I}$			0.70		
	$V_{s,L}$			0.83		
	V_d			0.17		

5.4. Model

The model used in this study is based on the point model of Steiner et al. (2015), which built on simpler approaches proposed by Han et al. (2010) and Reid and Brock (2014). The point model was coded into a distributed model that calculates each energy flux for every grid cell of a spatial domain describing the cliffs and their surroundings. The model was run for the period of measurements of AWS Lirung, from May to October 2013 (see Section 5.3.1).

The energy balance at the cliff surface is

$$Q_m = I_n + L_n + H + LE \quad (5.1)$$

where Q_m is the energy flux available for melt, I_n and L_n are the net shortwave and longwave radiation fluxes, H is sensible heat and LE is latent heat flux. All fluxes are perpendicular to the surface and in W m^{-2} . The heat from precipitation and conductive heat flux into the ice are neglected (Reid and Brock, 2014). Fluxes are assumed positive when they are directed towards the surface. Ablation normal to the ice surface [m w.e.] was computed as

$$M = \frac{Q_m \Delta t}{\rho_i L_f} \quad (5.2)$$

where Δt is the timestep (here 3600 s), ρ_i the ice density (900 kg m^{-3}) and L_f the latent heat of fusion of ice (334 kJ kg^{-1}).

5.4.1. Sky and debris view factors

The outlines of the two cliffs were derived from the orthophotos and superimposed over the May UAV DEM to determine the initial geometry of the cliff. From the UAV DEM, elevation, slope and aspect for each grid cell were derived. For every grid cell, a sub-section of the UAV DEM of 200 by 200 m was used to represent the nearby topography, and overlaid on the coarser ASTER-GDEM2 for calculations of the effect of the more distant topography. The dimension of the UAV-DEM sub-section was chosen based on tests with different extents which showed that the debris mounds relevant for the cliff were represented relatively well from sub-areas of size 200 x 200 m or greater. Since the size of the sub-area is restricted by computational resources we decided to use 200 m. From the two

DEMs, the topographic and solar parameters needed for the calculation of the radiative fluxes were determined. The horizon angle used for calculation of the shortwave radiation, $h_{\phi,I}$, defines the angle between the zenith and the horizon, for which the sky is visible, as a function of azimuth, ϕ (Figure 5.5). The highest obstacle for each ϕ for both DEMs was taken, either from the UAV or from the coarser ASTER DEM. Together, $h_{\phi,I}$ for the current solar azimuth and the solar elevation angle (θ) define whether a grid cell receives direct sunlight at any given time (see Section 5.4.2). The sky view factor for the solar radiation ($V_{s,I}$) is the mean of all azimuths of $h_{\phi,I}$ divided by 90° , representing the sky fraction which can be seen from a specific point.

The horizon angles used for calculation of the incoming longwave radiation, $h_{\phi,L}$, were calculated from the UAV DEM (see Section 5.4.3), and therefore the corresponding sky view factor ($V_{s,L}$) represents a local sky percentage. A debris view factor (V_d) was determined from the debris portion angle $h_{\phi,d}$ using the UAV-DEM. $h_{\phi,d}$ describes the angular sector of debris seen from a point on the cliff and is limited by the local horizon line (at the top, $h_{\phi,L}$) and the ice of the cliff (at the bottom, Figure 5.5). $V_{s,L}$ and V_d were used to calculate the longwave radiative flux emitted by the sky and terrain, respectively (see Section 5.4.3). The sky and debris view factors are constant in time, as long as the topography is assumed to be stable.

5.4.2. Shortwave radiation flux

The net solar radiation (I_n) for a unit area on an ice cliff with a given slope and aspect was calculated as

$$I_n = (I_s + D_s + D_t) (1 - \alpha_i) \quad (5.3)$$

where I_s is the direct solar radiation, D_s is the diffuse irradiance from the sky and D_t is the incoming radiation reflected from the terrain (all fluxes in W m^{-2}). α_i [no dimension] is the albedo of ice.

Incoming shortwave radiation observed at AWS Lirung (I_0) was separated into direct and diffuse components following Reindl et al. (1990). The direct portion was then converted into the flux incident on a sloped unit area as described in Han et al. (2010), using the approach by Ohmura (1968), which requires

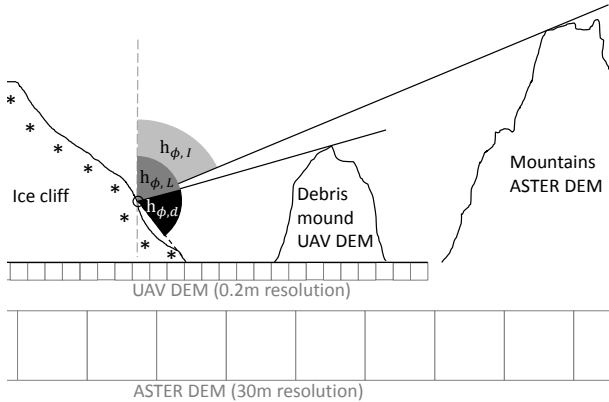


Figure 5.5.: Calculation of the individual horizon angles $h_{\phi, I}$ (light grey) and $h_{\phi, L}$ (dark grey) for shortwave and longwave radiation, respectively, and of the debris view angle $h_{\phi, d}$ (black) for a single azimuth direction. The horizon angles are normalized either by 90° ($h_{\phi, I}$ and $h_{\phi, L}$) or by 180° ($h_{\phi, d}$) and then summed and divided by 360° to determine a single sky view factor for shortwave and longwave radiation ($V_{s, I}$ and $V_{s, L}$) and a debris view factor (V_d , all dimensionless) for each location on the cliff. The grid below the topography indicates which DEM resolution is used for each individual angle (note that the resolution grid is shown only qualitatively and not in the right scale). Where a debris mound is dominating the horizon of a point on the cliff, $h_{\phi, I}$ equals $h_{\phi, L}$.

calculation of the normal vector to the cliff surface and of the solar azimuth. This results in a reduction or enhancement of the direct component measured at AWS Lirung depending on the angle between the two vectors. Calculations were made for each grid cell. Shading was calculated by comparing the position of the sun at each timestep to the corresponding $h_{\phi,I}$.

Diffuse shortwave radiation from the sky was calculated as

$$D_s = V_{s,I} k_d I_0 \quad (5.4)$$

where k_d [no dimension] is the diffuse fraction according to Reindl et al. (1990), depending on the clearness index k_t [no dimension], which is the ratio of I_0 and the theoretical extraterrestrial solar radiation (I_E [W m^{-2}]). k_d was chosen according to the following relation:

$$k_d = \begin{cases} 1.02 - 0.254 k_t + 0.0123 \sin \theta & k_t \leq 0.3 \\ 1.4 - 1.749 k_t + 0.177 \sin \theta & 0.3 < k_t \leq 0.78 \\ 0.486 k_t - 0.182 \sin \theta & k_t > 0.78 \end{cases} \quad (5.5)$$

Diffuse radiation reflected by the terrain was calculated as

$$D_t = \alpha_d I_0 (1 - V_{s,I}) \quad (5.6)$$

where α_d [no dimension] is the albedo of the debris surface.

5.4.3. Longwave radiation flux

The net longwave radiation was calculated as

$$L_n = V_{s,L} L_{in} + V_d L_d - L_o \quad (5.7)$$

where L_{in} is the incoming longwave radiation from the atmosphere for a horizontal, unobstructed location, L_d the longwave radiation emitted by the debris and L_o is the outgoing longwave radiation emitted by the ice surface, all in W m^{-2} . L_{in} was modelled using the Stefan-Boltzmann relation as

$$L_{in} = \epsilon_s \sigma (T_a + 273.15)^4 \quad (5.8)$$

where σ is the Stefan-Boltzmann constant and ϵ_s [no dimension] the effective emissivity of the sky, estimated with the parameterizations of Dille and O'Brien

(1998) for clear sky and of Unsworth and Monteith (1975) for cloudy conditions. This combination was found to give the best results in an evaluation of longwave radiation models (Juszak and Pellicciotti, 2013). The model was calibrated and validated for each season separately using data from an AWS in Kyanjing (3857 m a.s.l.), about 2 km south of Cliff 1 (Steiner et al., 2015).

The longwave radiation emitted by the surrounding debris was calculated as

$$L_d = \epsilon_d \sigma (T_s + 273.15)^4 \quad (5.9)$$

where ϵ_d [no dimension] is the emissivity and T_s [°C] is the temperature of the debris, assumed to be equal to the surface temperature measured with a temperature logger (T-Logger) at the location of the AWS. Assumption of a spatially uniform surface temperature might be a limitation, but no adequate methods exist to model or spatially extrapolate surface temperature to date. In addition, Steiner et al. (2015) showed that cliff ablation rates were little sensitive to changes in surface temperature for the range of variability observed in the field at a number of T-Loggers. Those data also show that the temporal variability in surface temperature is much larger than its spatial variability, and the former is taken into account in the model since the T-Logger provides a time series of hourly T_s values.

The outgoing longwave radiation was also calculated with the Stefan-Boltzmann relation, using the emissivity of ice ϵ_i and the ice surface temperature T_i [°C], assumed to be equal to zero:

$$L_o = \epsilon_i \sigma (T_i + 273.15)^4 \quad (5.10)$$

In Equations 5.7 and 5.9, the sky and debris view factors, $V_{s,L}$ and V_d , control the amount of longwave radiation from the atmosphere and the debris reaching each grid cell. $V_{s,L}$ is derived from the UAV-DEM (Section 5.4.1), using a domain of 200 m. As a result, longwave radiation emitted by the terrain outside of this domain is treated as longwave emitted by the atmosphere. This might result in some inaccuracy in the estimate of the longwave irradiance from the terrain (Plüss and Ohmura, 1997), but we assume this to be small.

5.4.4. Turbulent fluxes

The turbulent sensible (H) and latent heat (LE) fluxes were calculated as described in Steiner et al. (2015) using the bulk aerodynamic method (Han et al., 2010; Reid and Brock, 2014). Aerodynamic surface roughness was estimated (Section 5.4.5).

5.4.5. Optimal model parameters

The following surface variables were not measured in the field: albedo of ice and debris (α_i , α_d), emissivities of ice and debris (ϵ_i , ϵ_d) and the surface roughness length (z_0). They can be regarded as model parameters and are taken from Steiner et al. (2015), who used a Monte Carlo approach to optimise these parameters against measurements at ablation stakes. The parameters were optimised separately at each stake and for the pre-Monsoon and post-Monsoon season (Steiner et al., 2015) and we used the mean values calculated from all stakes on Cliff 1 and all stakes in Cliff 2, averaged over the two seasons (Table 5.2). Optimization of parameters across the entire cliff is impossible as it would require a distributed data set of accurate melt-rate series, and instead we used an average of parameters rigorously calibrated at the single stake locations. We also averaged in time the parameters of Steiner and others (2015) (May and October) to avoid a sudden step change during the season and an arbitrary transition from the May to the October parameters. Use of average parameters in space and time is inevitable in distributed and continuous application of models.

A difference in the ice albedo values between May and October can be observed at Cliff 2 (Table 5.2). The lower ice albedo in May is likely explained by the generally warmer conditions of the pre-Monsoon season, with higher melt and an increase in fine sediment transported down the cliff by the melting water and corresponding darkening of the ice surface. In post-Monsoon, the air temperature is colder and snow remained longer on the cliff surface, leading to a higher reflectance of shortwave radiation. The decrease of debris albedo from May to October is probably a result of the wetter surface due to generally colder weather conditions, with less evaporation leading to a reduced or delayed drying out of the surface during the day in combination with shorter days.

Table 5.2.: Optimized model parameters for May and October 2013 averaged across all stakes at Cliff 1 and Cliff 2, from Steiner et al. (2015), and their mean values used for the distributed cliff model. α_i and α_d are albedo values for ice and debris, respectively, and ϵ_i and ϵ_d are the emissivities of the two surfaces. z_0 , the surface roughness length, is in metres; all other variables are dimensionless.

Variable	Cliff 1			Cliff 2		
	May	Oct	Mean	May	Oct	Mean
α_i	0.278	0.273	0.275	0.057	0.214	0.136
α_d	0.107	0.052	0.080	0.278	0.139	0.208
ϵ_i	0.984	0.982	0.983	0.959	0.970	0.965
ϵ_d	0.951	0.942	0.947	0.949	0.958	0.954
z_0	0.004	0.003	0.003	0.003	0.003	0.003

5.5. Results and discussion

5.5.1. Energy fluxes

Figure 5.6 shows the mean hourly energy fluxes averaged across the cliff surface for each of the three subseasons. Incoming shortwave radiation has a strong diurnal cycle and is in general the highest flux during the day. But in contrast to flat terrain the diffuse component is very high, making up more than half of the total incoming flux at both cliffs. Diffuse radiation varies between 49% (Cliff 1, pre-Monsoon) and 65% (Cliff 2, Monsoon) of the total flux (Table 5.3). It is highest during Monsoon (Table 5.3) because of cloudiness and is high also during post-Monsoon (58 and 65% at Cliff 1 and 2, respectively) because of the low direct radiation in this season. Direct solar radiation is especially low at Cliff 2 (Figure 5.6), likely due to its steeper slope (53.2° average slope compared to 45.6° for Cliff 1). This is a striking difference in comparison to flat or gently sloped surfaces, where the direct component makes up most of the total incoming flux. Radiation reflected by the terrain is quite small, given the low albedo of debris, but it is of some importance at Cliff 2 (Figure 5.6 and Table 5.3).

The total incoming longwave radiation reaching the cliff is high during both day and night (Figure 5.6), but is slightly lower than the outgoing flux (Table 5.3). When averaged over 24 hours it is higher than the total incoming shortwave flux in Monsoon and post-Monsoon season (Table 5.3). Longwave radiation from the sky ($L_s = L_{in} V_{s,L}$) varies between 208 and 240 W m^{-2} at Cliff 1 and between

198 and 229 W m^{-2} at Cliff 2 (Table 5.3). It is slightly lower at Cliff 2 (Table 5.3) likely because of its steeper slope, associated with a relatively high local horizon at the cliff crest. It is a lower flux than at AWS Lirung (with mean L_s between 229 and 265 W m^{-2} for all three seasons), because of the reduction of the visible sky at the two cliffs (the average sky view factor for longwave radiation is 0.75 and 0.72 at Cliff 1 and 2, respectively, and 0.83 at AWS Lirung).

The reduced longwave radiation from the sky is balanced by the additional longwave radiation emitted by the debris. This flux would be very close to zero on a flat surface but contributes about 25% of the total incoming longwave radiation at both cliffs (Figure 5.6 and Table 5.3) and about 15% of the total incoming short and longwave radiation. The longwave from the sky represents between 73 and 75% at Cliff 1 and between 74 and 76% at Cliff 2 of the total incoming longwave radiation for all three seasons (Table 5.3), but the spatial variability in the flux from the debris is considerably higher than that from the sky (Table 5.3). The net longwave radiation remains a negative flux on average at both cliffs, but of much smaller magnitude than if the additional term from the debris were not there (Steiner et al., 2015).

The turbulent fluxes are both positive and small in magnitude at the two cliffs (Table 5.3), and both show an increase in the afternoon, associated with the differential increase in air and debris temperature that results in an increasing temperature deficit. One should notice, however, that these are the fluxes most affected by uncertainties in the spatial distribution of wind speed and surface roughness.

The turbulent fluxes are the same at both cliffs because air temperature and wind speed are assumed constant across the cliff and equal to those measured at AWS Lirung. All other fluxes differ between the two cliffs. The strongest difference between the two cliffs is in the average solar radiation, with Cliff 1 receiving much more direct solar radiation, likely because it is less steep, while incoming longwave radiation is higher at Cliff 1, due to both a higher radiation from the sky and higher flux from the surrounding terrain (Table 5.3).

The direct solar radiation flux has the strongest spatial variability (Table 5.3, Figure 5.7 and 5.8), showing coefficients of variation on the cliff between 53 and 62% for Cliff 1 and 68 and 130% for Cliff 2 (average values over each season) and much higher for individual hours. The flux is higher during the day (Figure 5.7 and 5.8), when it is highly variable also in space, with radiation as high as 600

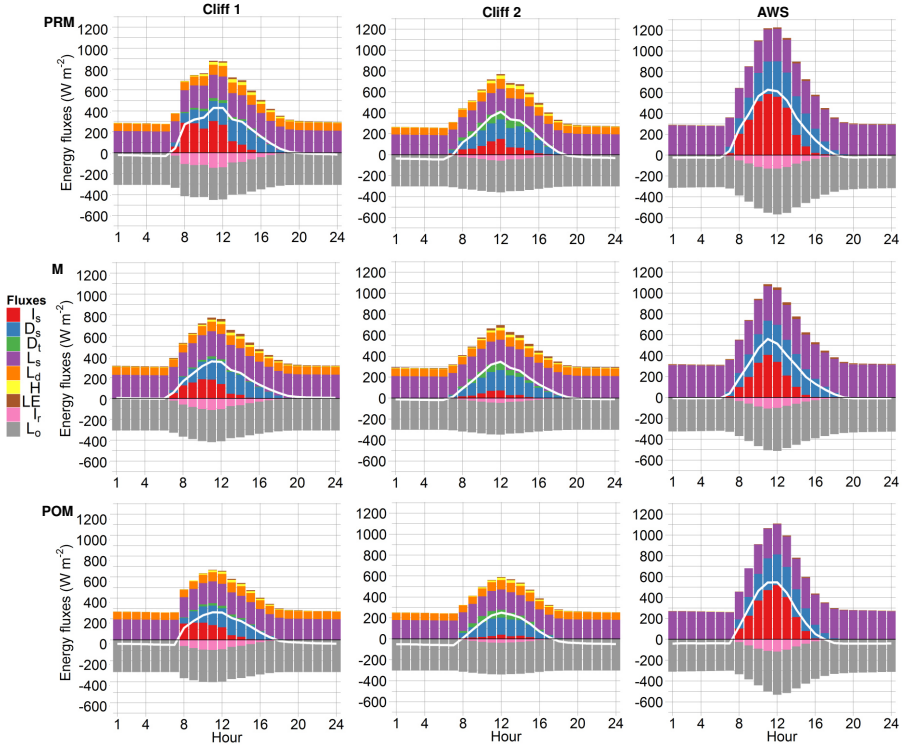


Figure 5.6.: Hourly energy fluxes averaged across each cliff for the three seasons separately (PRM: pre-Monsoon; M: Monsoon; POM: post-Monsoon). For comparison the fluxes at a horizontal site (AWS) are shown as well. Each hourly value is the mean of that hour over the season (in Nepal Time, UTC +5:45). I_s is the direct incoming shortwave radiation, D_s and D_t are diffuse shortwave radiation from sky and from terrain, respectively. I_r is the reflected shortwave radiation, L_o the outgoing longwave radiation. L_s and L_d are incoming longwave radiation coming from sky and from debris, respectively. H and LE are sensible and latent heat fluxes, respectively. The white line represents Q_m .

Table 5.3.: Hourly mean, standard deviation (sd) and coefficient of variation (cv=sd/mean; not calculated for Q_m , H and LE) of the energy fluxes, averaged spatially over the entire cliff, separated for pre-Monsoon, Monsoon and post-Monsoon. I_{in} is the total incoming shortwave radiation, L_{in} the total incoming longwave radiation. The other variables are explained in Fig. 5.6. Mean and sd are in $W m^{-2}$, cv is dimensionless. Also indicated is the mean melt rate, M [mm w.e. hr $^{-1}$]. Statistics for shortwave components are calculated only for hours where mean I_{in} was higher than 10 $W m^{-2}$. The percentage contributions of the single components to I_{in} and L_{in} are indicated in brackets. The mean daily sum of hourly melt rates is shown in brackets [mm w.e. d $^{-1}$].

Variable	pre-Monsoon			Monsoon			post-Monsoon		
	mean	sd	cv	mean	sd	cv	mean	sd	cv
I_{in}	299.5	70.0	0.23	222.7	38.6	0.17	229.7	51.0	0.22
I_s	139.3 (46.5%)	73.3	0.53	77.0 (34.6%)	41.4	0.54	84.6 (36.8%)	52.8	0.62
D_s	146.2 (48.8%)	5.6	0.04	135.3 (60.7%)	5.6	0.04	132.0 (57.5%)	4.4	0.03
D_t	14.0 (4.7%)	1.2	0.09	10.5 (4.7%)	1.0	0.09	13.1 (5.7%)	1.1	0.08
I_r	82.5	19.3	0.23	61.3	10.6	0.17	63.2	14.0	0.22
L_{in}	303.6	3.6	0.01	320.1	2.4	0.01	285.0	2.9	0.01
L_s	223.3 (73.6%)	0.8	0.00	240.3 (75.1%)	0.7	0.00	208.1 (73.0%)	0.7	0.00
L_d	80.3 (26.4%)	3.9	0.05	79.8 (24.9%)	2.6	0.03	76.9 (27.0%)	3.2	0.04
L_o	310.3	0.0	0.00	310.3	0.0	0.00	310.3	0.0	0.00
H	12.9	10.6		10.7	7.0		8.3	7.5	
LE	7.4	5.4		12.1	7.2		3.8	3.6	
Q_m	122.2	27.3		113.5	8.4		56.4	18.2	
M	1.6 (38.8)	0.4	0.25	1.4 (34.2)	0.1	0.10	0.9 (22.6)	0.3	0.33
CHFF 1									
I_{in}	256.8	53.7	0.21	193.5	31.0	0.16	189.4	35.4	0.19
I_s	79.6 (31.0%)	54.1	0.68	36.9 (19.1%)	30.9	0.84	28.2 (14.9%)	36.8	1.30
D_s	136.0 (53.0%)	7.6	0.06	125.9 (65.0%)	7.7	0.06	122.8 (64.8%)	6.1	0.05
D_t	41.2 (16.0%)	4.4	0.11	30.7 (15.9%)	3.5	0.11	38.4 (20.3%)	3.8	0.10
I_r	34.8	7.3	0.21	26.2	4.2	0.16	25.7	4.8	0.19
L_{in}	285.8	3.6	0.01	301.6	2.4	0.01	268.3	3.0	0.01
L_s	212.6 (74.4%)	1.0	0.00	228.8 (75.9%)	0.9	0.00	198.1 (73.8%)	0.9	0.00
L_d	73.3 (25.6%)	4.0	0.05	72.8 (24.2%)	2.6	0.04	70.2 (26.2%)	3.2	0.05
L_o	304.5	0.0	0.00	304.5	0.0	0.00	304.5	0.0	0.00
H	12.9	10.6		10.7	7.0		8.3	7.5	
LE	7.4	5.4		12.1	7.2		3.8	3.6	
Q_m	112.8	35.0		103.7	17.7		44.4	19.8	
M	1.6 (37.4)	0.5	0.33	1.4 (32.5)	0.3	0.20	0.9 (20.7)	0.3	0.40
CHFF 2									

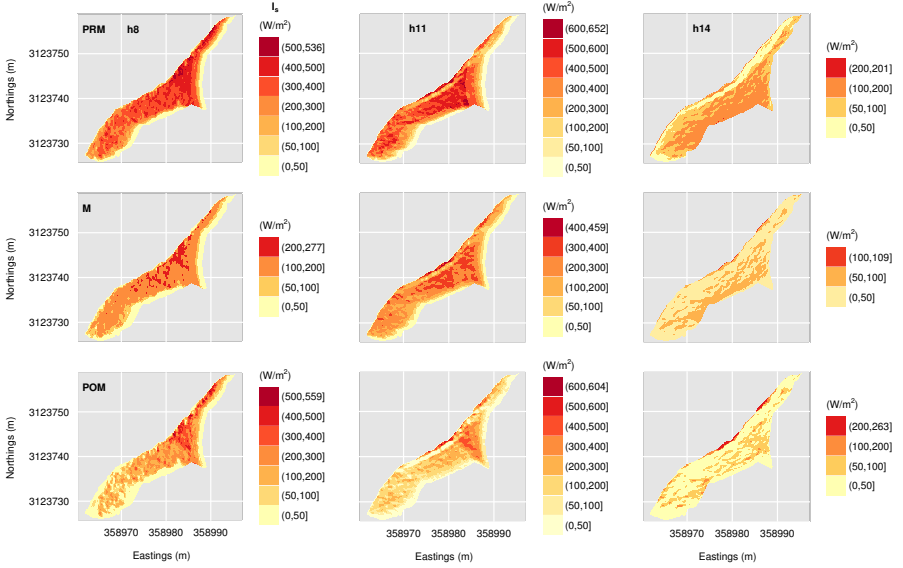


Figure 5.7.: Distribution of incoming direct shortwave radiation (I_s [W m^{-2}]) at Cliff 1 at 8:00, 11:00 and 14:00 (in Nepal Time, UTC +5:45) in pre-Monsoon (PRM), Monsoon (M) and post-Monsoon (POM). The reference system of the map is WGS 84 and the projection is UTM 45N.

W m^{-2} in the upper section of Cliff 2 (Figure 5.8) and in the central part of Cliff 1 (Figure 5.7) and strongly reduced to almost zero in the steeper lower sections. On Cliff 2, at 14:00 the entire surface is already in shade, while in the first part of the day the highest radiation is on the eastern part of the cliff (Figure 5.8). On Cliff 1, radiation is high already at 8:00, in contrast to Cliff 2, which is mostly shaded at the same time. On this cliff, a reduction due to shading is evident on the eastern side at the noon hours (e.g. at 11:00, Figure 5.8).

The longwave radiation is less variable in space (Table 5.3), but the debris component has a strong local variability (Figure 5.9).

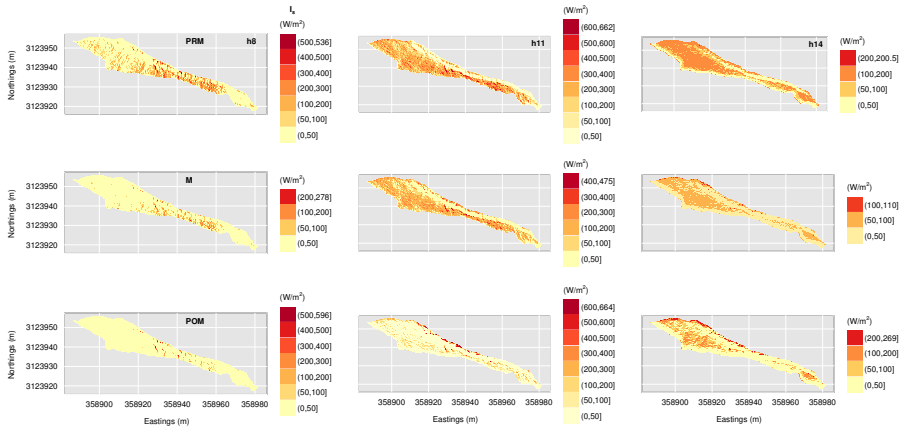


Figure 5.8.: Distribution of incoming direct shortwave radiation (I_s [W m^{-2}]) at Cliff 2 at 8:00, 11:00 and 14:00 (in Nepal Time, UTC +5:45) in pre-Monsoon (PRM), Monsoon (M) and post-Monsoon (POM). The reference system of the DEM is WGS 84 and the projection is UTM 45N.

5.5.2. Melt

As a result of the variability in radiative fluxes, melt is highly variable in space (Figure 5.10), with variations between 10% (for Monsoon) and 33% (for post-Monsoon) in daily melt at Cliff 1 and between 20% (for Monsoon) and 40% (for post-Monsoon) at Cliff 2. Daily melt is higher in pre-Monsoon, followed by Monsoon and post-Monsoon season (Figure 5.10). In all three seasons, melt is higher at the cliff top for both cliffs. Cliff 2 melts most in the middle section of its top (where slopes are shallower, results not shown), whereas at Cliff 1 high melt rates are evident in the entire central section of the cliff almost down to its bottom (Figure 5.10). The pattern on Cliff 1 seems to be explained mostly by direct solar radiation, which is higher in the central section of the cliff during the morning hours in all three seasons but especially in pre-Monsoon (Figure 5.7). The high melt at the crest of the cliffs results from a combination of different fluxes. At Cliff 2, high longwave radiation from the debris compensates the low direct solar radiation (Figure 5.6), and both the diffuse shortwave radiation from the sky and the longwave from the sky are high along the crest. On Cliff 2, the

direct shortwave radiation is very high in the middle of the crest (Figure 5.8), and adds to the longwave radiative flux from the debris which is high along the cliff top (Figure 5.9). This flux is very high at both cliffs along their edges, both on the top and bottom of the cliff. This explains the fact that on both cliffs, but especially on Cliff 2, melt rates are high also along the western bottom part of the cliffs (Figure 5.10), likely due to a combination of reduced shading, evident for Cliff 1 (Figure 5.7), and high longwave radiation from the debris (at both cliffs). Melt rates on the steeper, lower parts of the cliffs are lower, and due mostly to the longwave radiation emitted by the debris and the shortwave radiation reflected by terrain, which, unlike all other fluxes, has a maximum at the cliff bottoms.

Spatially averaged daily melt on the cliff is slightly higher at Cliff 1, with values between $2.3 \text{ cm w.e. day}^{-1}$ (post-Monsoon) and $3.9 \text{ cm w.e. day}^{-1}$ (pre-Monsoon), than at Cliff 2, with mean melt rates between $2.1 \text{ cm w.e. day}^{-1}$ (post-Monsoon) and $3.7 \text{ cm w.e. day}^{-1}$ (pre-Monsoon, see Table 5.3). However, Cliff 2 shows a wider range of melt per day ($1.1 - 7.8$, $0.8 - 7.1$ and $0.5 - 5.3 \text{ cm w.e. day}^{-1}$ in pre-Monsoon, Monsoon and post-Monsoon, respectively) than Cliff 1 ($1.7 - 5.7$, $1.4 - 6.1$ and $0.5 - 4.2 \text{ cm w.e. day}^{-1}$ in pre-Monsoon, Monsoon and post-Monsoon, respectively) in all three seasons.

Although the horizontally projected areas of the cliffs only represent 0.02% (Cliff 1) and 0.07% (Cliff 2) of the debris-covered area, they contribute about 0.27% (Cliff 1) and 0.96% (Cliff 2) of the total melt water estimated for the debris-covered part of Lirung Glacier using a physically-oriented glacio-hydrological model (Ragettli et al., 2015). The total volume lost to melt by the two cliffs is 2313 and 8282 m^3 for Cliff 1 and 2, respectively, for the entire measurement period. The much larger loss of volume of Cliff 2 is mainly due to its larger surface (1786 m^2 for Cliff 2, compared to 431 m^2 for Cliff 1).

Earlier studies estimated the contribution of cliffs on different glaciers to the total ablation of the debris-covered area as 18% (Sakai et al., 2002), 7.3% (Han et al., 2010) and 7.4% (Reid and Brock, 2014). We exclude the extremely high estimate of 69% reported in Sakai et al. (1998). These estimates depend not only on the estimated total melt at the cliffs but also on the total melt from the glacier, which might be problematic to calculate given the large uncertainties in debris thickness and meteorological forcing (e.g. Reid and Brock, 2014). Reid and Brock (2014) calculated total melt from the debris-covered area of Miage

Glacier using an energy balance model but a constant debris thickness, while Han et al. (2010) extrapolated an order of magnitude total meltwater from point mass-balance measurements. Total melt amount from the debris-covered portion of Lirung Glacier was estimated by Sakai et al. (2002) from the simulations of Rana (1997) using a degree-day model forced with input data at Kathmandu.

In our study we have calculated total melt from only two of the cliffs observed on Lirung Glacier in 2013. We therefore derive an estimate of how much melt per unit area of cliff surface (horizontally projected) can be expected compared to a unit area of non-cliff debris-covered glacier surface by dividing the relative melt volume contributed by the two cliffs by the relative area of cliffs (relative compared to the total ablation volume and area, respectively). This represents an index of how effective cliffs are, per unit area, at producing melt and we can use it to compare the contribution of cliff surfaces to total ablation. Melt from ice cliffs in this study is 13.7 times higher than for debris, compared to 5.7 times in Reid and Brock (2014) and 9 times higher in Sakai et al. (2002).

The difference of these ratios can be due to the different methods used to compute the glacier-wide ablation in each of these studies, to the different climate conditions and different debris thickness. However, it might also suggest a tendency to underestimate cliff melt when using simple extrapolation.

A validation with the observed melt rates at different points on Cliff 1 and 2 from 8th to 20th of May 2013 (12 days) is problematic, as the stake location has to be chosen visually from the orthophoto and assigned to a corresponding cell of the DEM and the variability of topography and melt is high in space, so that a small error of a few tens of cm in locating the stake might result in large differences in slope and aspect. We therefore compare measured and modelled melt within a radius of 1.5 m around each assumed stake position. Comparison is good for Cliff 1 (Figure 5.11), for which the slopes and aspects derived from the DEM (and used in the model) and measured in the field are generally very similar (see Table 5.4), apart from the slope at stake 1.3, which is close to an edge where the cliff changes its slope abruptly and distinctly (see Figure 5.2d). At Cliff 2, the model underestimates observations (Figure 5.11). Slopes and aspects measured in the field at the location of the stakes on Cliff 2, however, differ considerably from those derived from the UAV DEM used in the model, especially for the aspect (Table 5.4). Thus, the disagreement between model and observations might be attributed to the differences in topographic parameters, as the model simulates

ablation for surface conditions different from those where ablation was measured. The discrepancies between measured and DEM-derived slopes and aspects can be attributed to the presence on Cliff 2 of pronounced longitudinal bulges and grooves. These features are significantly more marked than on Cliff 1, and can cause strong differences in topographic parameters locally but might not be seen by the DEM due to their small cross section, or might be averaged out at the grid resolution.

An additional validation is provided by comparison of the total melt volume calculated by the model with estimates of volume loss from subtraction of the two DEMs of May and October. Some caution has to be used here, since calculation of the total volume lost by subtraction of the two DEMs is affected by uncertainties, and by the glacier movement in particular. Glacier velocities were estimated to be negligible at Cliff 1 by Immerzeel et al. (2014a), while at Cliff 2 a surface displacement of about 1.5 m over the observed period was derived. We correct for the velocities at Cliff 2 in a simple manner to obtain a first order-of-magnitude estimate of the volume loss, by multiplying the surface movement by the estimated vertical and horizontal extents of the cliff. We obtain volume losses of 2402 and 8453 m³, which are very similar to those calculated with the distributed cliff model (3.8 and 2.1% higher for Cliff 1 and 2, respectively).

While more sophisticated methods should be used for this validation, this first attempt, albeit affected by uncertainties, seems to suggest that our model estimates are in a range of plausible values.

5.5.3. Model strengths, limitations and outlook

The model proposed in this paper is the first fully distributed, grid-based model of ice cliff ablation proposed in the literature, even though the point model by Reid and Brock (2014) was also applied to all the pixels identified as cliffs from the DEM of Miage Glacier. The analysis of the variability of the energy fluxes and resulting ablation across a cliff is the first of its type and has shown large spatial variations in all fluxes, with melt rates resulting from a combination of those spatial patterns. The melt rates obtained are higher near the cliff crests for both cliffs. They are high also at the cliff-debris margin on the western flanks (for both cliffs), because of the debris effect through emission of longwave radiation, and in the central part of the smaller Cliff 1.

Table 5.4.: Slope and aspect values [deg] at stake locations in May 2013, measured manually on the ice surface (left) and derived from the UAV-DEM (right). In the stake column the names of the stakes as used in May 2013 are shown. Point indicates exact point values, where topographic components were measured or where the stakes were assumed to be. Buffer indicates the mean value derived from all pixels in the UAV-DEM within a 1.5 m-buffer around the assumed stake position. In brackets the standard deviation is shown.

Stake	Measured		Derived from UAV-DEM			
	Slope	Aspect	Buffer		Point	
			Slope	Aspect	Slope	Aspect
1.1	40	350	44 (7)	344	51	336
1.2	40	352	40 (7)	1	445	6
1.3	40	330	55 (18)	331	76	328
2.1	43	346	42 (9)	31	43	30
2.2	40	350	46 (5)	36	47	38
2.3	51	345	55 (6)	27	58	21

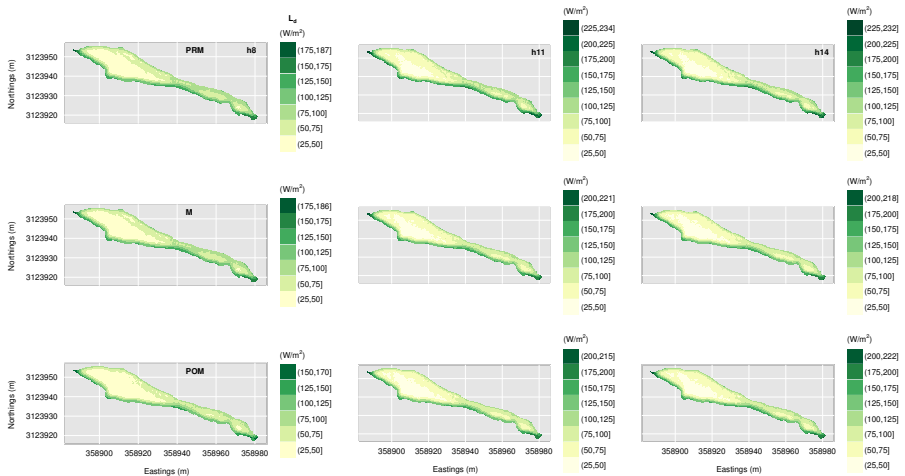


Figure 5.9.: Distribution of longwave radiation from debris (L_d [$W m^{-2}$]) at Cliff 2 at 8:00, 11:00 and 14:00 (in Nepal Time, UTC +5:45) in pre-Monsoon (PRM), Monsoon (M) and post-Monsoon (POM). The reference system of the DEM is WGS 84 and the projection is UTM 45N.

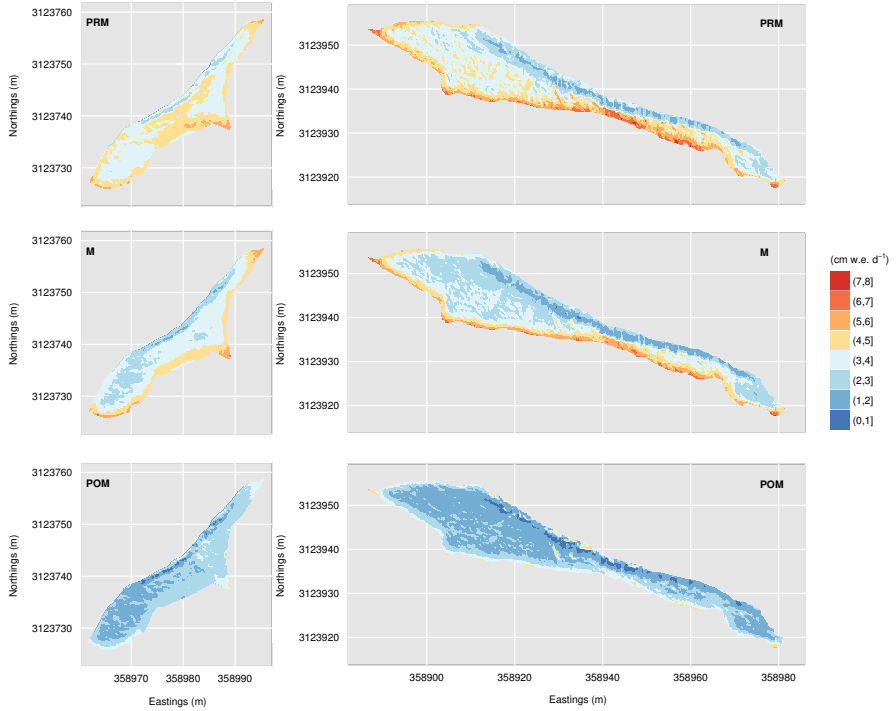


Figure 5.10.: Distribution of daily melt rate for Cliff 1 (left) and Cliff 2 (right) in pre-Monsoon (PRM), Monsoon (M) and post-Monsoon (POM) in cm w.e.. The reference system of the DEM is WGS 84 and the projection is UTM 45N.

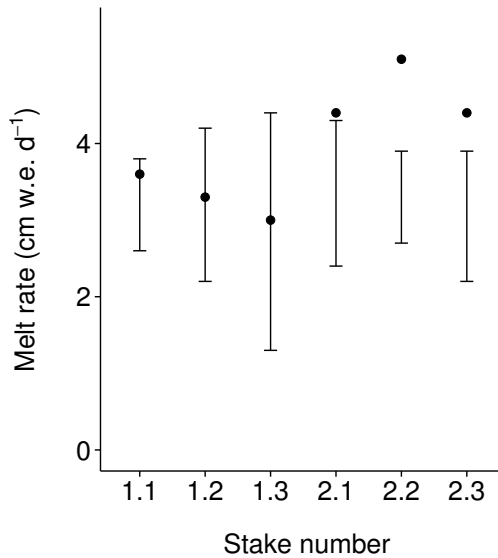


Figure 5.11.: Mean observed daily melt rates [cm w.e. day⁻¹] (dots) at Cliff 1 (stakes 1.1 – 1.3) and Cliff 2 (stakes 2.1 – 2.3) from 8th to 20th of May 2013 (12 days) and range of modelled values (bars) within 1.5 m radius.

These spatial patterns would suggest that a relaxation of the cliff angle would occur. Comparison of the average slope angles obtained from the UAV DEMs in May and October indicates a slight signal of flattening, with slopes decreasing from 45.6° (53.2°) in pre-Monsoon to 41.1° (49.1°) in post-Monsoon for Cliff 1 (Cliff 2). Nevertheless, the observed lowering is small. The relaxation of the cliff angle, if not compensated by similar rates at the steep lower parts, would lead the cliff to degrade. This would imply that cliffs decay and then form again every melt season. This interpretation, however, should be regarded with some caution, since the model does not include an update of the cliff geometry. This seems an important next step in this line of research. Together with this, more work on understanding the evolution of cliffs, their formation and decay, should be carried out. We cannot exclude the hypothesis of a relaxation of the cliff's angle that seems to be implied by our maps of ablation. However, against this hypothesis is the fact that melt rates calculated with the model and shown in Figure 5.10 are calculated perpendicular to the surface. Melt rates per unit horizontally-projected area will therefore be greater at the steep cliff base than on the upper parts of the cliff.

More importantly, our model does not include the effect of lakes, which are often associated with cliffs. The lakes will be responsible for subaqueous melt rates that might add to the ablation rate of the steepest sections of the cliffs in contact with the lake water and thus favour the cliffs backwasting uniformly rather than degrading. Miles et al. (2016) calculated subaqueous melt for Cliff 2 for the same season, and found a rate sufficient to match the horizontally-projected rate on the cliff, thus tending to sustain the cliff-lake system. This might suggest that cliffs coupled with lakes do indeed persist during the melting season, while those without might degrade. This is a very interesting hypothesis that should be further investigated through a coupled cliff and lake model and extension of the analysis to a more numerous sample.

Despite the advances suggested here, the model is still susceptible of improvements. One of these is the inclusion of spatially variable input fields of surface temperature, which is assumed to be uniform in space in our calculations for lack of an appropriate method to extrapolate or model surface temperature. Similarly, inclusion of spatially variable fields of ice albedo might improve model simulations, but also here knowledge is too limited to allow establishing a parameterization. It seems important also to include the overhanging parts of cliffs, which

are not represented in high resolution UAV-DEMs. For this, DEMs obtained from terrestrial photogrammetry or laser scanning could provide an alternative and increase the precision of the cliffs' representation, which is prone to large errors due to steep slopes (Fujita et al., 2008; Nuimura et al., 2012).

5.6. Conclusions

In this paper, we have presented the first distributed, grid-based model of ice cliff backwasting. The model includes a physically-based model of longwave and shortwave radiative fluxes that takes into account the interplay between the inclined cliff surface and the complex topography of the surrounding terrain, which affects the shading of shortwave radiation and the emittance of longwave radiation from sky and terrain. We developed the model using a comprehensive set of data collected on Lirung Glacier during the ablation season 2013 at two cliffs, including meteorological variables, melt at different locations across the cliffs, observations of cliff geometry and a high resolution DEM obtained with a camera placed on a UAV. The model was forced with data from an on-glacier AWS located near the two cliffs. The model parameters not measured in the field (surface albedo, emissivity and surface roughness) had been optimised with a Monte Carlo approach in a previous paper at numerous locations on the two cliffs and we use here the average values.

We use the model to investigate the spatial patterns of energy fluxes and ablation on the two cliffs and quantify the total volume lost during one melt season, from May to October 2013. Our main conclusions are as follows:

- 1) Shortwave radiation at both cliffs is an important component of the energy balance during the day, but mostly due to its diffuse component from the sky, which contributes between 49 and 65% of the total incoming shortwave radiation. This is in contrast to flat or gently sloped areas where the direct component is dominant. The net shortwave radiation varies greatly in space, largely due to the high spatial variability of direct shortwave receipts, which vary by 53 to 62% on Cliff 1 and 68 to 130% on Cliff 2 depending on the season considered.
- 2) Incoming longwave radiation is the highest positive energy flux over the 24h. The radiation from the sky is reduced compared to that on the gently sloped location of the AWS, because of the slope of the cliff and obstruction by the surrounding debris mounds. However, this reduction is compensated by the long-

wave radiation emitted by the debris-covered terrain, which represents about 25% of the total incoming longwave flux averaged across the cliff. Its spatial variability is smaller than that of the shortwave radiation but still high locally. 3) Melt rates vary considerably in space on both cliffs with coefficients of variation between 10 and 40% over the entire season. The total volumes lost to backwasting are 2313 m³ for Cliff 1 and 8282 m³ for Cliff 2, which are about 0.27 and 0.96% of the total melt from the debris-covered part of Lirung glacier estimated with a physically-oriented, advanced glacio-hydrological model that calculates melt under debris as a function of debris thickness. These values are high and confirm the assumed importance of cliffs as contributors to total mass loss of debris-covered glaciers.

The model quality might still be increased by improving calculations of the turbulent fluxes, which are affected by our limited knowledge of air temperature and wind variability at the cliffs. Here, we have used measurements at the AWS as such and assumed they are constant across the cliffs. Spatially variable surface temperature and albedo fields will also be an advance beyond spatially uniform inputs to the models, but parameterizations of these variables are still lacking. Our next steps will be to use this model to evaluate cliff backwasting and evolution over a longer period of time and test hypotheses of cliff formation and decay.

Acknowledgements

We would like to thank Martin Heynen, Tek Rai, Simon Wicki and Peter Hill for their support in the field. Without them, the cliff measurements would not have been possible. All the participants of the two field campaigns of May and October 2013 made this work possible and are gratefully acknowledged, as are all the Nepali helpers who supported our work in a great way. We also would like to thank very much Joe Shea and the International Centre for Integrated Mountain Development (ICIMOD) for their administrative and logistical support in Kathmandu. This study is funded by the SNF project UNCOMUN (Understanding Contrasts in High Mountain Hydrology in Asia) and field work was partially supported by a USAID High Mountain Glacier Watershed Programs Climber-Scientist Grant (CCRDCS0010). Finally, we acknowledge the thorough comments of Lindsey Nicholson and one anonymous reviewer, as well as of Scientific Editor Koji Fujita, which helped to improve the manuscript.

Chapter 6.

A physically-based 3D-model of ice cliff evolution over debris-covered glaciers*



Figure 6.1.: Supraglacial pond (frozen) attached to an ice cliff with an approximately 5m high undercut on Lirung Glacier (26 Oct. 2014).

* Buri P, Miles ES, Steiner JF, Immerzeel WW, Wagnon P and Pellicciotti F (2016b) A physically based 3-D model of ice cliff evolution over debris-covered glaciers. *Journal of Geophysical Research: Earth Surface*, 121(12), 2471–2493 (doi: 10.1002/2016JF004039)

Abstract

We use high resolution digital elevation models (DEMs) from unmanned aerial vehicle (UAV) surveys to document the evolution of four ice cliffs on the debris-covered tongue of Lirung Glacier, Nepal, over one ablation season. Observations show that out of four cliffs, three different patterns of evolution emerge: i) reclining cliffs, that flatten during the ablation season; ii) stable cliffs, that maintain a self-similar geometry; and iii) growing cliffs, expanding laterally. We use the insights from this unique dataset to develop a 3D-model of cliff backwasting and evolution that is validated against observations and an independent dataset of volume losses. The model includes ablation at the cliff surface driven by energy exchange with the atmosphere, reburial of cliff cells by surrounding debris, and the effect of adjacent ponds. The cliff geometry is updated monthly to account for the modifications induced by each of those processes. Model results indicate that a major factor affecting the survival of steep cliffs is the coupling with ponded water at its base, which prevents progressive flattening and possible disappearance of a cliff. The radial growth observed at one cliff is explained by higher receipts of longwave and shortwave radiation, calculated taking into account atmospheric fluxes, shading and the emission of longwave radiation from debris surfaces. The model is a clear step forward compared to existing static approaches that calculate atmospheric melt over an invariant cliff geometry, and can be used for long term simulations of cliff evolution and to test existing hypotheses about cliffs survival.

6.1. Introduction

Debris covers 9-16 % of the total glacier surface in the Hindu Kush-Karakoram-Himalaya region (Kääb et al., 2012), a region where glaciers have undergone mass loss and shrinkage in area during recent decades (e.g. Bolch et al., 2012; Cogley, 2016). Patterns of glacier changes are heterogeneous and controlled by both climate and the varying magnitude and characteristics of debris mantles (Kääb et al., 2012; Scherler et al., 2011). Sustained negative glacier mass balances result in higher relative debris cover, through increased exposure of debris due to the lack of substituting accumulation as well as additional deposits from destabilized moraines or valley flanks (e.g. Kirkbride and Deline, 2013; Herreid et al., 2015)

and it is expected that continued mass losses would lead to an increase in debris cover and thickness (Herreid et al., 2015).

While the effect of a homogeneous layer of debris on the melt of the underlying ice is understood in theory (Østrem, 1959), the general behaviour of debris-covered glaciers is much less well understood (Ragettli et al., 2016a). A supraglacial debris-mantle exceeding a few centimeters in thickness reduces the ablation of the underlying ice through reduced absorption of incoming solar radiation and longer distances for conductive heat (Østrem, 1959; Nicholson and Benn, 2006; Evatt et al., 2015). Nevertheless, recent studies have suggested that thinning rates on debris-covered glacier tongues are similar in magnitude to those of clean ice glaciers (Gardelle et al., 2012; Kääb et al., 2012), even when comparing equal elevation ranges (Gardelle et al., 2013). The issue remains controversial, as evidence has been provided by large scale studies based on satellite images, while more detailed studies at the catchment scale have provided no support for similar thinning rates (Ragettli et al., 2016a). It is however clear that a strong local increase in glacier ablation is associated with both supraglacial ponds (Sakai et al., 2000; Miles et al., 2016) and cliffs (Thompson et al., 2016) forming on the debris-covered tongues of many Himalayan glaciers.

Supraglacial ice cliffs affect the surface evolution, glacier downwasting, and mass balance of debris-covered glaciers (Inoue and Yoshida, 1980; Sakai et al., 1998; Purdie and Fitzharris, 1999; Benn et al., 2012; Pellicciotti et al., 2015; Ragettli et al., 2016a) by providing a direct ice-atmosphere interface, with low albedo because of the dust from the debris slopes, and exposed to high emissions of longwave radiation from the surrounding debris-covered surfaces (Steiner et al., 2015; Buri et al., 2016a). As a result, melt rates can be very high and ice cliffs may account for a significant portion of the total glacier mass loss (Buri et al., 2016a; Thompson et al., 2016). However, their contribution to glacier mass balance has rarely been quantified through physically-based models. Melt on supraglacial ice cliffs has been investigated on Lirung Glacier (Himalaya, Nepal; Sakai et al., 1998; Steiner et al., 2015), Koxkar Glacier (Tian Shan, China; Han et al., 2010) and Glacier du Miage (European Alps, Italy; Reid and Brock, 2014), but the energy-balance models used in those studies are point scale models which calculate energy fluxes at individual cliff locations. Results from the only grid based model to date accurately reflect energy fluxes and short term cliff melt, but are based on a static cliff geometry (Buri et al., 2016a). While the sur-

face energy-balance and its variability in space was correctly reproduced by the model, applying that forcing only (without considering other processes affecting cliff evolution) on an unchanged cliff geometry would lead to the demise and disappearance of most cliffs. This is a perspective that seems unrealistic, although very few studies have extensively documented the evolution, formation and survival cycle of cliffs (Brun et al., 2016). From a multi-temporal dataset of cliff topography and backwasting derived from Structure-from-Motion analysis (SfM) of high-resolution terrestrial and aerial photography on Lirung Glacier, it was apparent that cliffs exhibit a range of behaviours but mostly did not rapidly disappear (Brun et al., 2016).

In this study, we use a unique data set of cliff geometry observations to document distinct patterns of cliff evolution including disappearance, growth and stability, which cannot be explained satisfactorily by atmospheric melt alone. We then use the observations to improve the grid-based energy-balance model described in Buri et al. (2016a) through inclusion of periodic updates of the cliff geometry based on modeled melt. We also include the effect of adjacent supraglacial ponds and ice reburial from marginal debris.

Our main aims in doing so are: 1) to document the evolution of a set of ice cliffs through analysis of rare, high-resolution field observations of cliff outlines and slope patterns, in order to understand the main processes that control the observed evolution; and 2) to incorporate these processes into a dynamic model that can be used to: i) quantify the relative importance of those effects; and ii) simulate cliff evolution over seasonal and annual scales. We apply the new model to simulate cliff evolution over one Himalayan glacier during one melt season to determine the new cliff positions, horizontal and vertical extents, and mean slope and aspect values. Although operating with a dataset of only four cliffs from a single study site, this work sheds light on mechanisms of cliff changes by quantifying them for the first time with a physically-based, dynamic 3D-model, representing many of the key processes controlling ice cliffs evolution.

6.2. Study Site and Data

We investigate four ice cliffs on the debris-covered Lirung Glacier in the upper Langtang Valley, Nepalese Himalaya (28.232° N, 85.562° E; Figure 6.2), using aerial and terrestrial surveys of cliff geometry at the beginning and the end

of the ablation season, which in this monsoon-dominated area approximately corresponds to the monsoon season. The cliffs, indicated as cliffs 1–4, range between ~ 4060 – 4200 m.a.s.l. on the lower tongue of Lirung Glacier (Figure 6.2). Two sets of high resolution orthoimages and DEMs from UAVs were produced by SfM-photogrammetry, covering the lower part of Lirung Glacier (Immerzeel et al., 2014b). The two UAV-DEMs from 19 May and 22 October 2013 were originally produced at 0.2 m resolution and aggregated to 0.6 m because of the model’s computational costs and numerical stability. They were used to derive the initial and final topography of the cliffs and the surrounding glacier surface, respectively. Selected UAV-DEM raster cells near cliffs 2 and 4 had unrealistic increased elevations due to water surface reflection in the May observations, and were corrected manually by considering the local slope.

The outlines of the cliffs and nearby ponds were manually digitized from the UAV-orthoimages, which have a spatial resolution of 0.1 m. Elevation models based on a Triangulated Irregular Network (TIN) derived from UAV-photogrammetry (Brun et al., 2016) are used for validation of modeled volume losses.

An Automatic Weather Station (AWS) located on the tongue of Lirung Glacier (AWS Lirung, 4076 m.a.s.l., Figure 6.2) recorded the following meteorological variables, used as input to the ablation model: incoming shortwave radiation (perpendicular to the surface), relative humidity of the air, wind speed and air temperature (shielded and ventilated), all at a screen level of 2 m. Details about the sensor setup are provided in Steiner et al. (2015). Debris surface temperature was measured, shielded from sunlight, on a rock at the station (Steiner and Pellicciotti, 2016). Incoming longwave radiation was not measured at the AWS on the glacier and was therefore modeled with data from an AWS in Kyanjing (3857 m a.s.l.) about 2 km south of Cliff 1 (see Figure 6.2), following Steiner et al. (2015) and Buri et al. (2016a). Details of the modeling approach are provided in Steiner et al. (2015).

Some of the parameters used in the energy-balance calculations are difficult to measure in the field (albedo for ice and debris, as well as surface roughness length) and were optimized in Steiner et al. (2015) and used as described in Buri et al. (2016a). These parameters were assumed to be uniform across the cliffs and constant in time.

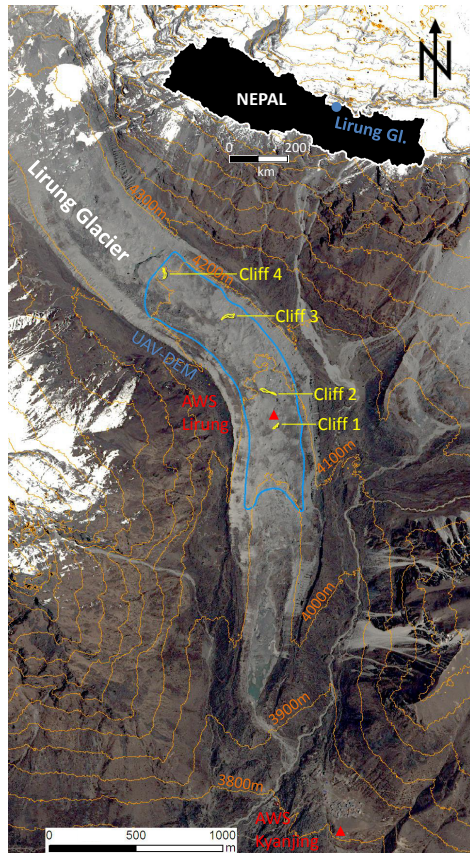


Figure 6.2.: Overview of the tongue of Lirung Glacier, in the upper Langtang Valley, Central Nepalese Himalayas, based on a SPOT6-orthoimage from April 2014. The May UAV-DEM coverage is indicated in blue, and the four investigated cliffs in yellow. The AWS sites are marked by a red triangle.

6.3. Field Observations of Cliff Changes

The purpose of this section is to describe the cliff observations as documented by the UAV and field investigations, to detect patterns of changes between the beginning and end of the monsoon ablation season, and to infer the processes that may be important to the modeling of their evolution. We investigate the slope and aspect distribution and the cliff areas and dimensions (Figures 6.3 and 6.4 and Table 6.1) in May and October as derived from the high resolution UAV-DEM for the four cliffs. We then use them to identify different cliff types in terms of geometry and evolution.

6.3.1. Reclining Cliffs

Cliff 1 is the smallest of the four surveyed cliffs, and presented steep slopes at its base in May 2013 (Figure 6.4). No pond was present in May 2013 (Figure 6.3), although the steep lower section (see slope and orthoimage in Figure 6.4) indicates a probable former pond connection which likely disappeared before the field visit and the UAV-flights in May 2013 (Brun et al., 2016). A small adjacent pond could be identified on two Google Earth satellite images from post-monsoon 2011 (27 September and 5 October, respectively), in contact with the cliff section showing the steepest slopes in May 2013.

Cliff 1 reclined during the 2013 monsoon season, as indicated by markedly lower slope values, especially at the cliff base (Figure 6.4 and Table 6.1). Its area slightly diminished (Table 6.1) and shape changed (Figure 6.4) but the more striking transformation is the flattening of slopes.

A small supraglacial water body, probably only fed by surface melt water, was in contact with Cliff 3 in May but not evident in October. A pattern of slope decline is evident for Cliff 3, similar to the pattern observed at Cliff 1 (Figure 6.4), with the steep slope section at the cliff's base minimized by October, also suggesting that the pond played a negligible role. The area of the cliff decreases slightly (Table 6.1). Cliff 3 is the only cliff which slightly alters its main orientation between May and October, from overall NNW aspect to predominant NNE (Table 6.1).

The flattening of both Cliffs 1 and 3 is not entirely apparent from comparison of their mean slopes between May and October, as changes in area also play a role in the averaging of single cell slopes into a mean cliff value. A clearer signal

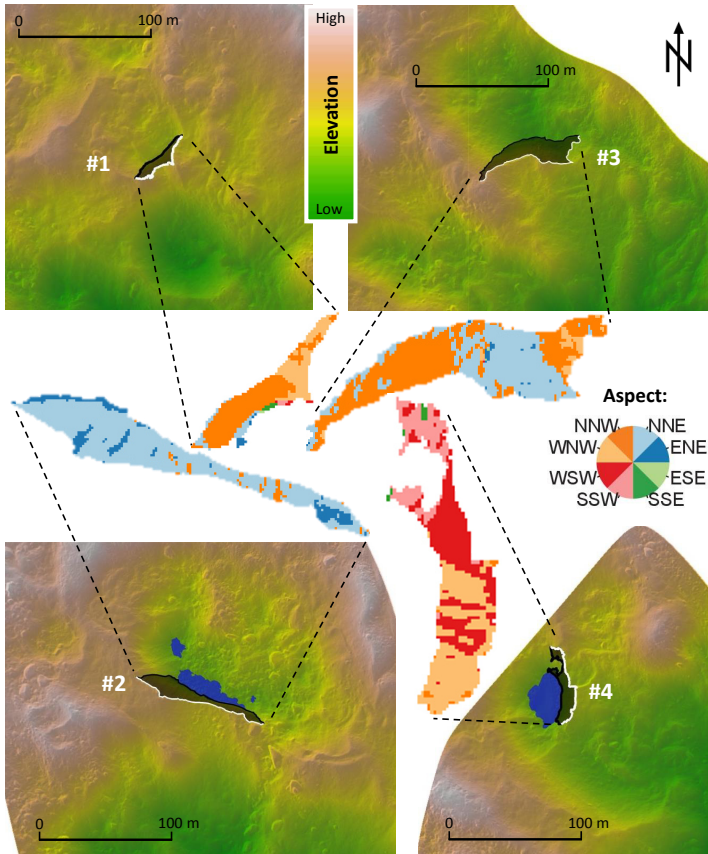


Figure 6.3.: Aspect (insets) and elevation within 200 m x 200 m area of interest (maps) for each cliff (1–4) based on the May 2013 UAV-DEM. On the maps the two-dimensional shape of the cliffs (dark area) is indicated by lines, with the white line marking the crest of the cliffs and the black line their base. Blue areas indicate ponds (pond at Cliff 3 not visible due to small size). The map background shows colors relative to elevation topped by hillshade.

Table 6.1.: Cliff characteristics derived from the UAV-DEM and orthoimage, shown as mean values for 18 May and 22 October 2013, respectively. For elevation, the maximum value within each cliff area is taken. Aspect is defined from 0 to 360°, with North at 0° (vectorial mean). Values of vertical extent indicate the highest difference in elevation within the cliff area, horizontal extent is the manually defined maximum straight distance within the cliff outline. The area represents the real inclined area, calculated considering cell resolution and slope.

Cliff #	Elevation [m a.s.l.]		Aspect [°]		Slope [°]		Vert. Ext. [m]		Hor. Ext. [m]		Area [m ²]	
	May	Oct	May	Oct	May	Oct	May	Oct	May	Oct	May	Oct
1	4066	4062	328 (NNW)	317 (NNW)	47	44	15	11	47	46	298	252
2	4092	4092	30 (NNE)	32 (NNE)	53	48	24	25	100	96	1108	1113
3	4161	4156	359 (NNW)	3 (NNE)	50	49	33	28	82	73	1304	991
4	4202	4205	264 (WSW)	259 (WSW)	42	44	15	24	60	82	505	758

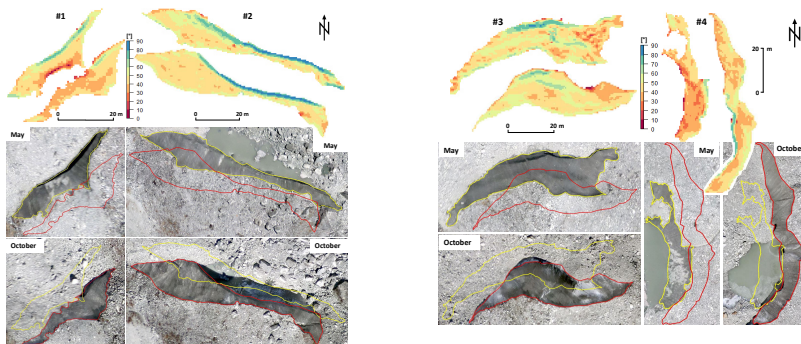


Figure 6.4.: Slopes derived from the UAV-DEM and manually delineated outlines of the four cliffs in May (top or left raster; yellow line on orthoimage) and October (bottom or right raster; red line on orthoimage) 2013, used as initial conditions for the model. Note the different scale bars for different cliffs.

of the general reclining can be found in the reduction of the cliffs vertical extent (Table 6.1) by 25.5 % (Cliff 1) and 16.9 % (Cliff 3), respectively. Both cliffs show a decreased inclined area in October, as a consequence of the removal of steep sections from the cliffs' bases. Additionally, the slopes behind the two cliffs in the direction of backwasting are characterised by a depression downglacier (Figure 6.3) so that the cliff's top ridge is lowered as a result of reduced ice volume for backwasting (Brun et al., 2016). This leads to a slope reduction at the upper portion of the cliff, and progressively decreases the cliff area.

6.3.2. Persistent Cliffs

Cliff 2, the largest of the four cliffs, maintains a remarkably consistent area and self-similar geometry from May to October (Table 6.1 and Figure 6.4). Adjacent to the main section of the cliff a pond is present both in May and October 2013 (see Figure 6.4).

The decrease in mean slope towards October is due to the slight flattening of a steep section at the eastern top part. Through the fall of a large boulder the shading of the uppermost cliff part was stopped at one point in the period between the observations. The vertical extent is very similar between May and October, further suggesting that the cliff geometry has remained self-similar while back-

wasting (Table 6.1 and Figure 6.12). The backwasting pattern is uniform and we know from water-level records that the pond first filled slightly and then drained gradually.

6.3.3. Expanding Cliff

Cliff 4 is the only cliff which increases noticeably in area between the two observations (Table 6.1 and Figure 6.4), mainly due to its initial negative planform curvature in May 2013 (see aspect in Figure 6.3). Both vertical and horizontal extents increase in a pronounced manner from May to October, by 61.2 % and 36.4 %, respectively (Table 6.1). Slopes at the base of the cliff become steeper (Figure 6.4d), and the average slope increases by 1.8° (Table 6.1).

Although a pond is in contact with the cliff in both May and October, the cliff shape changes markedly during the melt season as a result of the draining of the pond, which lowers by about 6 m (calculated as a net change in elevation between the two DEMs). In addition to the increase in area, the most striking change in the geometry of this cliff is the reversal of slope patterns: the base of the cliff in contact with the water has generally shallow slopes in May, while in October the cliff zones at the pond shore are the steepest. In May, on the other hand, the steepest sections were located at the top of the cliff, in its central section. It is possible that steep slopes at the base were also present in May but covered by the higher pond level, and became exposed in October with the lowering of the water level.

6.3.4. Summary of Observed Cliff Types

To summarize, three categories of cliff behaviour can be identified in terms of geometry, evolution and pond-coupling:

1. Absence of pond contact permits flattening of the cliff and causes continuous cliff reclining
2. Consistent pond presence leads to steep sections at the cliff base, enabling a stable cliff geometry
3. Lowering pond water-level reveals steep formerly-submerged ice in a cliff that grew radially in size.

Due to our restricted sample size, these cliff types might not be representative of the full variety observed at larger scales, on different glaciers, or in distinct climatic regimes. Assessing the dominant processes and changes for a larger sample of cliffs and for different locations will be a necessary future step for understanding the dynamics and relevance of ice cliffs.

6.4. Modeling Cliff Evolution

The patterns of cliff evolution observed on Lirung Glacier and described in section 6.3 cannot be explained by considering a static cliff geometry and by applying atmospheric melt alone (Buri et al., 2016a). From field evidence and qualitative results from the pioneering early studies on debris covered-glaciers in the Himalaya (e.g., Iwata et al., 1980; Sakai et al., 1998), as well as from results of very recent works it is evident that cliffs are moderated by the presence of supraglacial ponds at their base (Miles et al., 2016; Roehl, 2008). Ponds were also observed to affect retreat of ice-cored moraines located at glacier termini in St. Elias Mountains (Canada) and in Vestfold Hills (Antarctica) (e.g., Driscoll, 1980; Watson, 1980; Pickard, 1983). Field observations suggest that ice reburial by debris can considerably affect cliff geometry and area (Thompson et al., 2016). The inaccuracy of the static approach is exemplified by calculating only melt due to the interaction with the atmosphere (Figure 6.5). With the grid-based model that considers a static geometry where the cliff geometry is only updated once at the end of the melt season (hereafter referred to in short as ‘static model’ and indicated as ‘S-Model’, Buri et al., 2016a), the patterns of aspect (Figure 6.5a) and slope (Figure 6.5b) after one melt season are not realistic. This is mainly due to the long period before an update to geometry and hence long melt vectors that can intersect each other. Along with evidence from the field, this prompted the development of the new model presented here, which is dynamic in the sense that regular updates of the cliff geometry are conducted on the base of the high resolution ablation calculations. We also represent two key processes observed in the field that seemed to affect cliff geometry and dynamics, a: the presence of ponds and b: reburial of lateral cliff sections by adjacent debris.

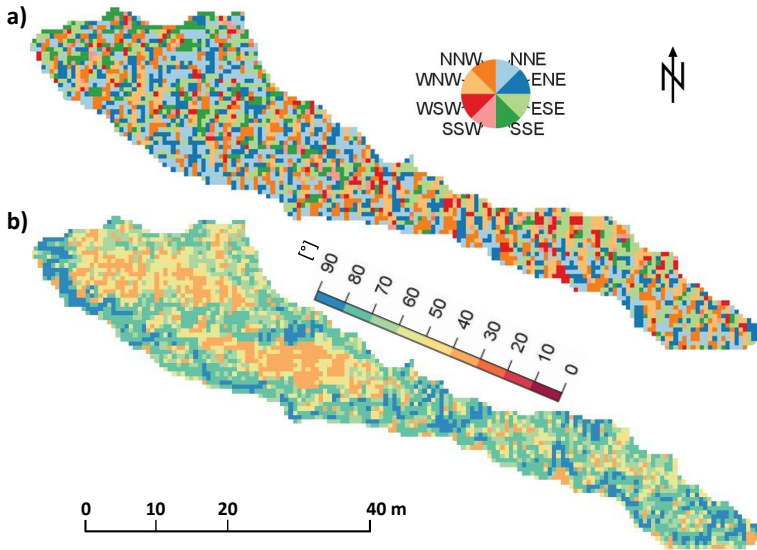


Figure 6.5.: Modelled (S-Model) aspect (a) and slope (b) for Cliff 2 for October 2013 without considering intermediate geometry updates, but only a final melt translation resulting from energy exchange with the atmosphere at the end of the melt season.

6.4.1. Model

With this dynamic approach (hereafter called ‘D-Model’) we simulate cliff evolution by updating the cliff shape in three dimensions considering melt, surface geometry, adjacent ponds and debris slopes. The energy-balance equation is solved at an hourly time-step, all other model steps are performed at monthly intervals. A monthly time step was chosen as a compromise between the computational costs and the need to calculate melt vectors compatible with the cell size.

A daily geometry update was unreasonable for two reasons: computational costs and a geometry update distance less than the grid size, as typical daily melt rates at the cliffs surface are at the order of $< 10^{-1}$ m.

The model is coded in the open-source software R (R Core Team, 2015) and is run separately for each cliff using the UAV-DEM of 0.6 m resolution. In the following, we explain the single modeling steps inside the D-Model (Figure 6.6).

Cliff Outline Derivation (Step 1)

The outline of the ice cliff is needed as input to initialize the model, enabling separation of debris-covered and debris-free area in the calculations. Using the true-color georeferenced UAV-orthoimage from May 2013, supported by terrestrial photography and experience from the field visits, cliff and pond outlines are derived manually. The latter are used to identify the pond-affected zones of a cliff (Step 1c).

After each geometry update (Step 5, section 6.4.1) the new cliff polygon is derived automatically to run the model on the new geometry. As a result of the different aspects (and therefore melt directions) the application of the melt vectors to each cliff cell can lead to voids between the translated cliff raster. The term ‘melt vector’ describes the melt distance in combination with the three-dimensional melt direction per cliff cell. To avoid gaps within the updated cliff, the new outline is based on a convex-hull approximation, the alpha shape method (Edelsbrunner et al., 2006). This approach draws a connected line around the updated cliff raster using a chain of circles approximating the cliff shape as closely as possible. The radius of the alpha shape circles is set to 3 times the resolution, i.e. 1.8m. This size provides the best results in terms of penetrating into gaps between cells and not splitting the cliff into multiple polygons. The model internally increases this radius in case the cliff polygon is split, until a closed shape is reached again.

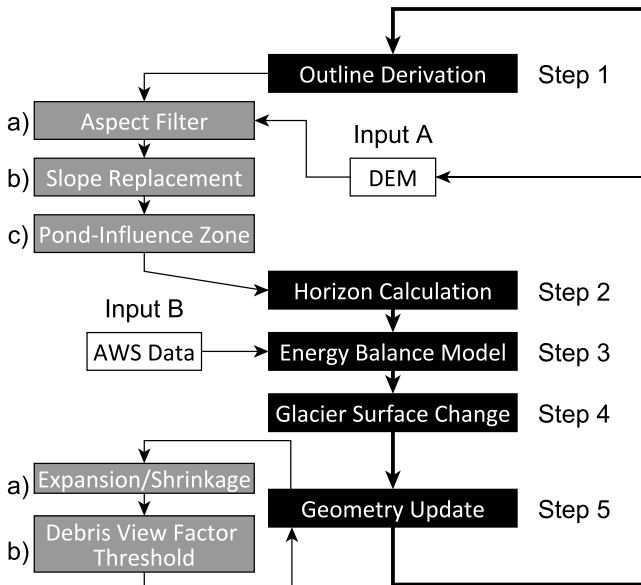


Figure 6.6.: Modeling chain (steps 1 to 5) within the dynamic ice cliff backwasting model (D-Model). Input A is for initialization the UAV-DEM, subsequently the updated DEM based on step 5. Input B is the hourly time series of meteorological data.

In this way the model is avoiding dividing the cliff into multiple areas. As a consequence of the alpha shape method, the new cliff outline can increase in size compared to the previous polygon but can also shrink if transferred cells fall into the same cell after melting. Since these overlaid cells usually do not have the same elevation, a vertical discontinuity can occur with more than one elevation value per cell. If this happens, the minimum of the layered cell elevation values is taken and assigned to the cell.

In this study the DEM which is updated after model step 5 is referred to as the 'active DEM'. By masking it with the cliff polygon, the geometry of the cliff surface can be extracted. In the initial model run, the UAV-DEM from May 2013 serves as input, while in every subsequent interval the active DEM is used. Slope and aspect are derived for every cell together with its elevation from the active DEM based on the algorithm of Horn (1981) for rough topography using eight neighbours with differential weights and excluding the central cell itself. Marginal raster cells can be represented erroneously in terms of slope and aspect, as they can be influenced through the Horn-algorithm by adjacent debris cells. To avoid these edge effects we perform two steps (a and b below) to obtain a stable and realistic initial geometry for the ablation modeling.

a) Aspect Filter (Step 1a)

A median-filter with a window of size 9x9 cell (29.16 m²) is applied to all aspect values within the cliff area in order to 1) remove lateral edge effects at the transition of ice to debris along the cliff outline, and 2) smooth out the high aspect variability of the active DEM, which is partly due to small inaccuracies in steep terrain. The filter is needed to avoid calculation of an incorrect melt direction, as the melt vector depends partly on the aspect of a cliff cell.

b) Slope Replacement (Step 1b)

A threshold of 40° is applied to distinguish between debris-covered (< 40°) and potentially debris-free cells (≥ 40°). The threshold has been determined from field and satellite measurements by Foster (2010) on Miage Glacier. Although maximum angles at which loose material can remain on inclined ice surfaces might vary depending on thickness and shape of debris (Reid and Brock, 2014), ice-exposed slopes < 40° were measured only rarely on supraglacial cliffs on the tongues of both Lirung (Steiner et al.,

2015) and Langtang Glacier in 2013 and 2014. Unrealistically low slopes on the cliff surface, which were apparent especially at the cliff edges, would produce steep melt vectors pointing downward almost vertically. To avoid this effect, all cliff cells below the slope threshold were set to 40° .

c) Pond-Influence Zone (Step 1c)

The presence of supraglacial ponds seems to have an important effect on ice wall evolution (Driscoll, 1980; Watson, 1980; Pickard, 1983; Miles et al., 2016; Buri et al., 2016a; Brun et al., 2016). Two horizontal buffers are applied to define a potential influence zone on the ice cliff surface. The first one is applied to search for all cliff raster cells lying within a 1m band around the pond shore, while the second buffer identifies cliff cells with a slope $\geq 60^\circ$ at a maximum distance of 5m from the pond outline. The two resulting groups of cells are merged to a pond-influenced zone, where an enhanced melt rate is added to the horizontal melt component derived from the atmospheric energy-balance (Step 3). This extra melt accounts for subaqueous melt and is taken equal to 0.033 m d^{-1} . This is the mean value calculated by Miles et al. (2016) in their energy-balance study of a pond (at Cliff 2) on Lirung Glacier during monsoon 2013. Calving, although observed at other field sites (e.g., Inoue and Yoshida, 1980), is unlikely to occur for these cliffs since the ponds are small (Sakai et al., 2009).

Horizon Calculation (Step 2)

The horizon angles and viewing factors for each cliff cell are calculated as described in Buri et al. (2016a). To describe proximal and distal topography and determine view factors for each radiative flux, we use a combination of the active DEM (for proximal topography) and the ASTER-GDEM2 (Advanced Spaceborne Thermal Emission and Reflection Radiometer global DEM 2) (for distal topography) with a resolution of one arc-second ($\sim 30 \text{ m}$) (Tachikawa et al., 2011), following Steiner et al. (2015) and Buri et al. (2016a): the active DEM, adapted after each geometry update, is used to describe the close topography within a 200 by 200 m grid (Figure 6.3), while the ASTER-GDEM2 is used for the rest of the glacier surface and distant mountain ridges for calculation of shading (see Figure 4 in Buri et al., 2016a). Details of all calculations are provided in Buri et al. (2016a).

Energy-Balance (Step 3)

The view factors and horizon angles calculated in Step 2 are used in the surface energy-balance model for a fully distributed calculation of the radiative fluxes. The energy-balance at the cliff surface is

$$Q_m = I_n + L_n + H + LE \quad (6.1)$$

where Q_m is the energy flux available for melt, I_n and L_n are the net shortwave and longwave radiation fluxes, H is sensible heat and LE is latent heat flux. All fluxes are perpendicular to the surface and expressed in W m^{-2} . The heat from precipitation and conductive heat flux into the ice are neglected (Reid and Brock, 2014). The surface energy-balance for each cliff cell is computed using hourly meteorological data following Buri et al. (2016a). The model is run from 19 May to 22 October 2013 (dates of the UAV data-acquisitions).

Glacier Surface Change (Step 4)

While ice cliffs backwaste several meters over a single melt season (Brun et al., 2016), the debris-covered glacier surface also slowly changes due to sub-debris melt and glacier flow. The relevant glacier dynamics are considered in the model by using tie-points, which are detectable objects visible in both UAV-orthoimages in May and October 2013. Large boulders serve as tie-points and define stable references on the glacier during this period. Based on a distributed tie-point approach (Immerzeel et al., 2014b), a thin plate spline interpolated map of displacement was created. Because the tracked boulders lie on the debris-covered parts of the glacier, the differential ablation occurring at ice cliffs does not affect the interpolation. The resulting map provides vertical and horizontal surface changes for every grid cell on the stable glacier surface. The vertical glacier change is applied to the active DEM together with the monthly cliff shape recalculation. The horizontal surface movement is not considered in the model but used to correct the observed October cliff outlines (Figure 6.9) for the glacier surface displacement from May to October 2013. Vertical and horizontal shifts are very small on Lirung Glacier with mean daily changes of -0.0049 and 0.0072 m d^{-1} , respectively.

Geometry Update (Step 5)

In the last model step the cliff geometry is updated according to the melt of ice per cliff cell, d_{melt} [m], resulting from the energy-balance calculations in Step 3 accumulated over each month:

$$d_{xy} = d_{melt} \sin \beta, \quad d_z = d_{melt} \cos \beta, \quad (6.2)$$

$$d_x = d_{xy} \sin \gamma, \quad d_y = d_{xy} \cos \gamma \quad (6.3)$$

where d_z and d_{xy} [m] are the melt distances in vertical and horizontal direction, respectively. The latter is the resulting vector of the horizontal x- and y-components, d_x and d_y , respectively. The angles β and γ indicate slope and backazimuth ($\gamma = \text{azimuth} - 180^\circ$) of the cliff cell, respectively (Figure 6.7).

The new cliff raster cannot be simply embedded into the glacier-wide active DEM, as the updated cells are now located at a different position due to backwasting. The horizontal melt vectors are used to remove relict topography from the former cliff position. The elevation of the cells overlaid by the melt vectors were interpolated linearly between the starting and ending point of the melt vector.

a) Expansion and Shrinkage

Internal and external buffers are applied to the cliff outline once the cliff cells are backwasted and the updated cliff is embedded into the active DEM. The width of both buffers is set to 1m. Shallow cells in the internal buffer with slopes $< 40^\circ$ are assumed to become debris-covered in the next modeling step, consistent with the classification of debris-covered and debris-free surfaces in the outline derivation. The cells selected within the internal buffer allow the cliff to shrink. In the external buffer, steep cells $\geq 40^\circ$ are detected. These are likely to be newly free of debris, and we include these in the new cliff area as a method of expansion. However, we exclude cells that were previously cliff cells but are now outside the cliff outline after applying the melt vectors. These are unlikely to contribute to expanding the cliff area, as the main melt direction in this border area is towards the new cliff and therefore in conflict with cliff expansion.

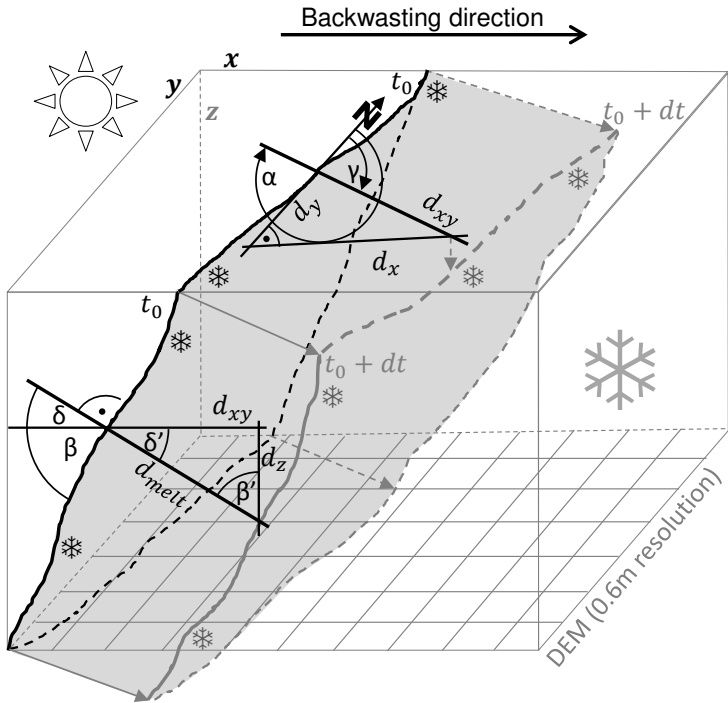


Figure 6.7.: Schematic cross section of cliff backwasting from left to right (Step 5). All cliff edges which are visible from the reader's point of view are shown as solid lines, hidden lines are dashed.

b) Debris View Factor Threshold

Unrealistic cliff outgrowths are limited in the model by the application of a sky view factor threshold. Lateral outgrowths of the cliff surface, unrealistically directed towards and cut into debris slopes are often not automatically removed by the slope threshold described above. To contain these incorrect instances of expansion, cliff cells with high debris-view factors ($V_d > 0.45$) are converted into debris-covered cells. The threshold is assumed to be equal for all cliffs and selected according to test runs with the most realistic results. V_d can be regarded here as a measure of how deep a cliff is cut into a debris ramp. Therefore using V_d as a parameter to control cliff expansion has a clear physical meaning, as above the critical value the portion of debris seen by a cliff cell exceeds 45 % of the total surrounding area (i.e. less than 55 % is defined as sky or ice), which makes reburial by surrounding rocks or melt-out by extra high longwave radiation likely. Figure 6.8 shows the distribution of V_d as modeled for the initial cliff shapes in May 2013. As described above, all cliff cells above the threshold are considered to be covered by debris by the end of each model interval and no volume loss is assigned to these areas.

6.4.2. Validation Metrics

We validate the model by comparing observed and modeled cliff dimensions, slopes and aspects, as well as comparing the calculated volume losses to those derived from a TIN-based calculation in Brun et al. (2016). Direct comparison of the observed and modeled area is not very meaningful, as the same single absolute surface area value could correspond to two different cliff shapes and locations. To take into account the areas that are correctly identified by the model we calculate metrics that are commonly used in image classification and segmentation for binary images. We define three possible outcomes when identifying a cell as belonging to a cliff or not: 1) true positive (TP), when a cell is correctly detected as cliff by the model; 2) false positive (FP), when a cell is erroneously modeled as cliff; and 3) false negative (FN), when a cell is modeled as debris but in reality is part of a cliff. Using TP, FP and FN we then define the following common metrics (e.g., Olson and Delen, 2008; Rittger et al., 2013):

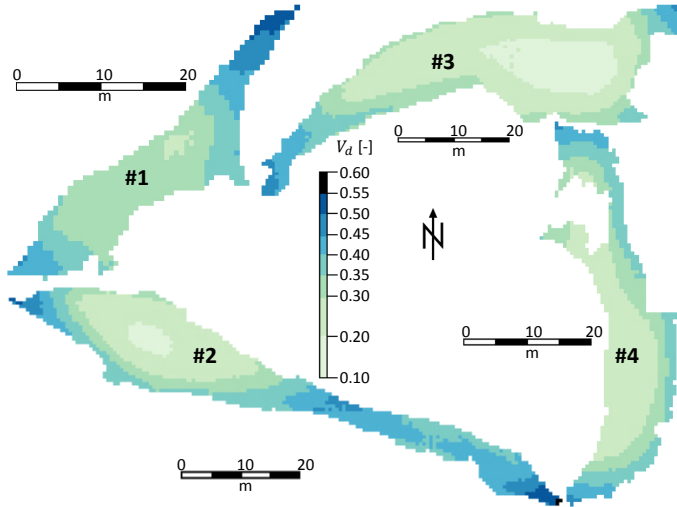


Figure 6.8.: Modeled debris view factors (V_d) for each cliff (1–4) calculated from the initial UAV-DEM in May. Cliff cells with $V_d > 0.45$ are removed from the cliff area and converted into debris cells (Model step 5b).

$$Precision = \frac{TP}{TP + FP} \quad , \quad (6.4)$$

$$Recall = \frac{TP}{TP + FN} \quad , \quad (6.5)$$

$$F = 2 \cdot \frac{Precision \cdot Recall}{Precision + Recall} = \frac{2 \cdot TP}{2 \cdot TP + FP + FN} \quad , \quad (6.6)$$

Precision measures the probability that a cell detected as cliff by the model indeed is cliff (Rittger et al., 2013) and Recall is the fraction of real observed cliff area that was correctly detected in the model and shows the probability of detection (Dong and Peters-Lidard, 2010). F (F-score or Dice coefficient), a measure of segmentation agreement, balances Precision and Recall by penalizing both missing cliff cells and falsely detected debris as cliff (Dice, 1945; Gilani and Rao, 2009; Rittger et al., 2013). It ranges from 0, indicating no spatial overlap

between two sets of binary segmentation results, to 1, indicating complete overlap (Zou et al., 2004).

6.4.3. Model Sensitivity

Since several of the model parameters are evaluated on individual tests, by trial and error or taken from the literature, we perform a sensitivity analysis to evaluate their importance to the model outputs (Table 6.4). Assuming as reference the D-Model run with the setup described in section 6.4, we vary each parameter one at a time (OAT) by a given amount (chosen based on field experience or from the literature) and calculate the corresponding Recall, Precision and F-Score. We also evaluate the metrics for the S-Model run and for a run where the pond-influence is turned off. The varied parameters are spatial resolution of the UAV-DEMs, emissivities of ice and debris, threshold values of slope and debris view factor, as well as ice and debris albedo.

We evaluate the sensitivity of the model to changes in the parameters by calculating the change in F-score per change of parameter unit (i.e. degree or percentage).

6.5. Results

In this section we compare D-Model results to the observed October surface. The S-Model simulations are also presented for comparison. First we focus on cliff dimensions, slope and aspect, then we investigate time series of radiative fluxes for each cliff and recorded meteorological data to explain differential patterns of cliff changes. Finally the calculated volume loss and melt rates per cliff are compared to validation data and model sensitivities are briefly discussed.

6.5.1. Dimensions, Slope, and Aspect

The evolution of the four cliffs in terms of slope, aspect and outline is shown in plan view in Figure 6.9 and as profile for Cliff 2 in Figure 6.12. Cliff geometry and dimensions, modeled and observed, are listed in Table 6.4.

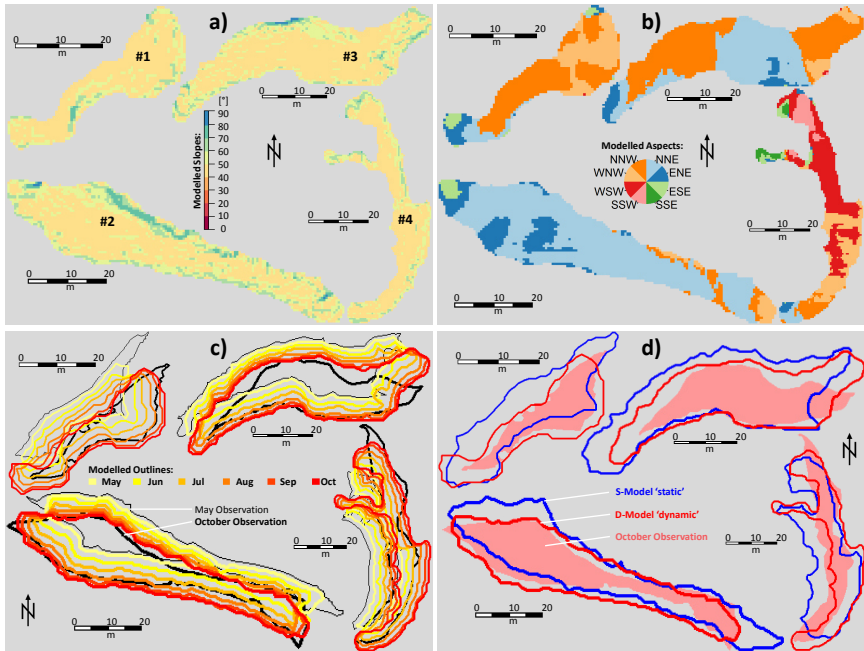


Figure 6.9.: Model results of slope (a) and aspect (b) for October 2013 for each cliff (1–4). Panel c) shows the simulated cliff evolution based on the monthly updated outlines (D-Model), for comparison the May and October observations are shown in the background. Panel d) shows the October cliff outlines simulated with the D-Model (red) and the S-Model (blue), respectively. The rose area in the background indicates the observed cliff area from the October UAV-orthoimages. Model results of slope (a) and aspect (b) for October 2013 for each cliff (1–4). Panel c) shows the simulated cliff evolution based on the monthly updated outlines (D-Model), for comparison the May and October observations are shown in the background. Panel d) shows the October cliff outlines simulated with the D-Model (red) and the S-Model (blue), respectively. The rose area in the background indicates the observed cliff area from the October UAV-orthoimages.

Cliff 1

The geometry of Cliff 1 at the end of the monsoon season is reproduced well by the model. The initial steep section along a large part of the cliff base disappears, in agreement with observations, substituted by a shallower surface continuously sloping into the debris (Figure 6.9a). A small but distinct steep section in the cliff upper area is apparent in the simulations but not in the October UAV-DEM. The modeled average slope (45.3°) is 4.2 % higher than observed (Table 6.1). The modeled vertical and horizontal dimensions show only a small deviation compared to the observations, with 6.8 and 3.3 %, respectively (Table 6.1). The mean simulated aspect deviates by 6.3° towards north.

The cliff outline, and the magnitude of the backwasting, is also reproduced well by the model with the exception of the lateral sections. The modeled outline along the top (south) and base (north) of the cliff agrees well with the observed shape, but the lateral margins are not accurately reproduced. The western corner sees a larger area than observed, whereas the eastern corner is partly removed (Figure 6.9a).

Comparison with the output of the S-Model (Figure 6.9d) shows that for this cliff it is crucial to account for the dynamic processes included in the D-Model, and the S-Model is not able to reproduce the position of the cliff base, with less backwasting at the base but also an overestimation of the cliff area in its topmost sections.

Cliff 2

The agreement between modeled and observed geometry is very good for Cliff 2, and the self-similarity of the May and October geometry (Figures 6.4) is reproduced well by the model in terms of outline and slope distribution (Figures 6.9 and 6.12). The steep lower section, a principal characteristic of Cliff 2 in both May and October, is present also in the modeled cliff shape, even though some discrepancies are evident. The D-Model simulates the average slope (48.6°) with only a deviation of 0.2° , in close agreement with the observations. The modeled cliff dimensions also agree very well, with a small discrepancy of 1.2 m (vertical) and -1.7 m (horizontal), respectively. The average modeled aspect agrees with the average observed aspect (with a difference towards east of 1.9°).

The average backwasting is well reproduced, and the cliff base and its top are simulated in the correct location. This is apparent also for the S-Model in the central section of the cliff, but a main deficiency when using the S-Model is a distinct outgrowth of ice at the eastern margin and a similar remnant in the northwestern section.

Cliff 3

The slope distribution at Cliff 3 was relatively homogenous in pre- and post-monsoon, with a distinct steep part at the central base section which implied the presence of a pond for some period, despite the fact that in May 2013 only a very small frozen pond was observed (Figure 6.4). The conservation of the slope pattern is simulated by the D-Model in a satisfying manner (Figure 6.9), even though the overall deviation in average slope is, at -2.3° or 4.8 %, the highest among all four cliffs.

The overall backwasting of the cliff is reproduced well, with very high agreement at the cliff top and good agreement at the (steep) central basal part (Figure 6.9c). However, discrepancies are evident at the sides, where the ice-debris boundary does not backwaste enough in the model. Both the eastern and western marginal portions of the cliff are preserved in shape by the D-Model, but observations show that they shrank and migrated further south (Figure 6.9c). The model thus results in a overestimation of area. These effects are more pronounced in the S-Model simulations (Figure 6.9c), which overestimate the ice cliff surface considerably at the margins but also in the region along the cliff base. The simulated dimensions (D-Model) exhibit the highest discrepancies to the observations of the four cliffs (23.2 % for the vertical and 18.5 % for the horizontal dimension) because of the errors at the margins. The difference in modeled (D-Model) and observed mean aspect is instead very small (0.6° , Table 6.4), because the bulk of the cliff geometry is preserved.

Cliff 4

The most striking characteristic in the evolution of Cliff 4 was its radial growth from May to October (Figure 6.4) and the D-Model reproduces this pattern correctly in its basic dynamics (Figure 6.9c). The deviations in vertical and horizontal dimensions are low compared to the observed shape (0.1 and 2.1 m, respectively, Table 6.4). The final simulated outline shows in its southern part a

shape congruent to the orthoimage, but a shift eastward can be recognized. In addition, the elongated dent pointing to the West that is evident in the observations in May is maintained by the model during the cliff backwasting, whereas it disappears in reality (Figure 6.9c), likely reburied by debris.

The overall slope simulated by the D-Model deviates by 1.8° from the observation, the average aspect by 12.8° towards west. Another failure of the model is in the steeply sloped lower section of the cliff (section 6.3) which the model cannot replicate.

6.5.2. Radiative Fluxes

Cliff 4 receives the highest amount of direct (SW dir, Figure 6.10) and net (net SW) shortwave radiation of all cliffs throughout the melt season, and in particular in September and October. In this period, the direct solar radiation received by Cliff 4 is more than double the amount for Cliffs 1 to 3. This distinct pattern is also evident in the net shortwave radiation. Differences in longwave radiation from the surrounding debris (LW deb) and the total net longwave income (net LW) are less pronounced but still important. Cliff 1 receives the highest longwave radiation throughout the simulation period, and Cliff 3 the lowest. This can be explained by the debris slopes facing Cliff 1 at close distance, as indicated by high debris view factors in Figure 6.8 (0.35 on average). In contrast, Cliff 3 sees a smaller portion of surrounding debris (0.26 on average).

In general all fluxes shown in Figure 6.10 show a reduced temporal variability during monsoon season (mid June – beginning of September). Measured air and surface temperatures are also reduced in their variability during this period, and differ less compared to pre- and post-monsoon.

6.5.3. Area, Volume Loss and Melt Rate

Simulated volume losses and melt rates from May to October 2013 calculated with the D-Model are shown in Figure 6.11 and Table 6.2. Model results are compared to the volume losses derived from high resolution cliff geometry obtained with SfM as TIN in Brun et al. (2016). Note that the TIN-results of Brun et al. (2016) are provided as volume of ice, but were modified to m^3 w.e. for comparison, using an assumed ice density of 900 kg m^{-3} .

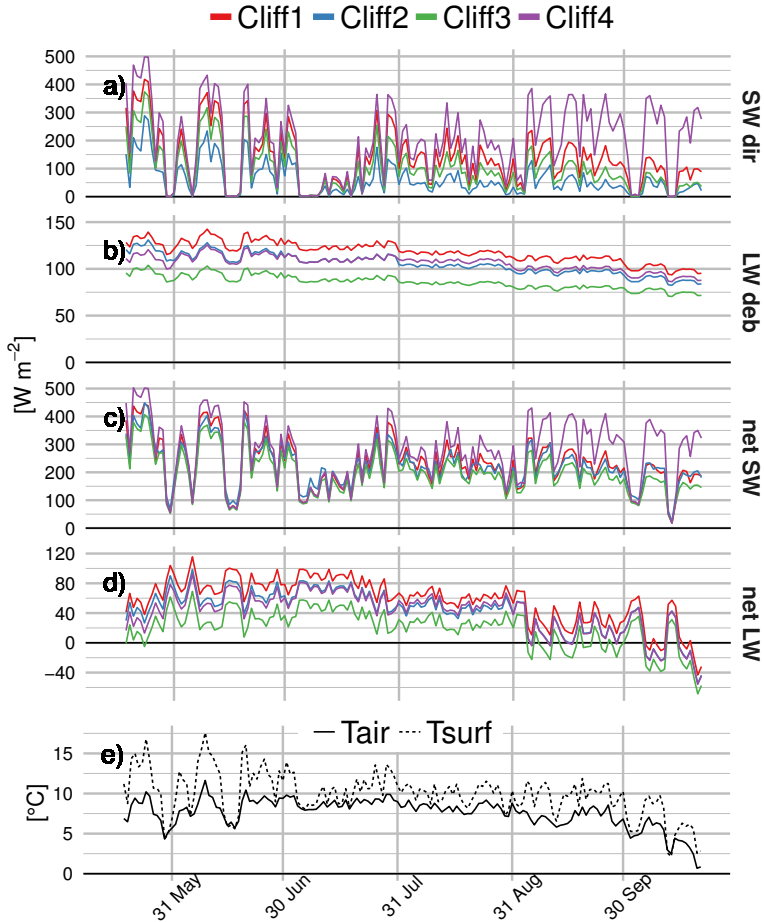


Figure 6.10.: Daily mean values of modeled (D-Model) radiative fluxes [W m^{-2}] averaged over each cliff (a-d) and measured temperatures [$^{\circ}\text{C}$] at AWS Lirung (e). ‘SW dir’ is direct shortwave radiation, ‘LW deb’ is longwave radiation coming from surrounding debris, ‘net SW’ and ‘net LW’ are net short- and longwave radiation (incoming minus outgoing flux). For shortwave fluxes only the hours between 8:00 and 17:00 (in Nepal Time, UTC +5:45) were considered.

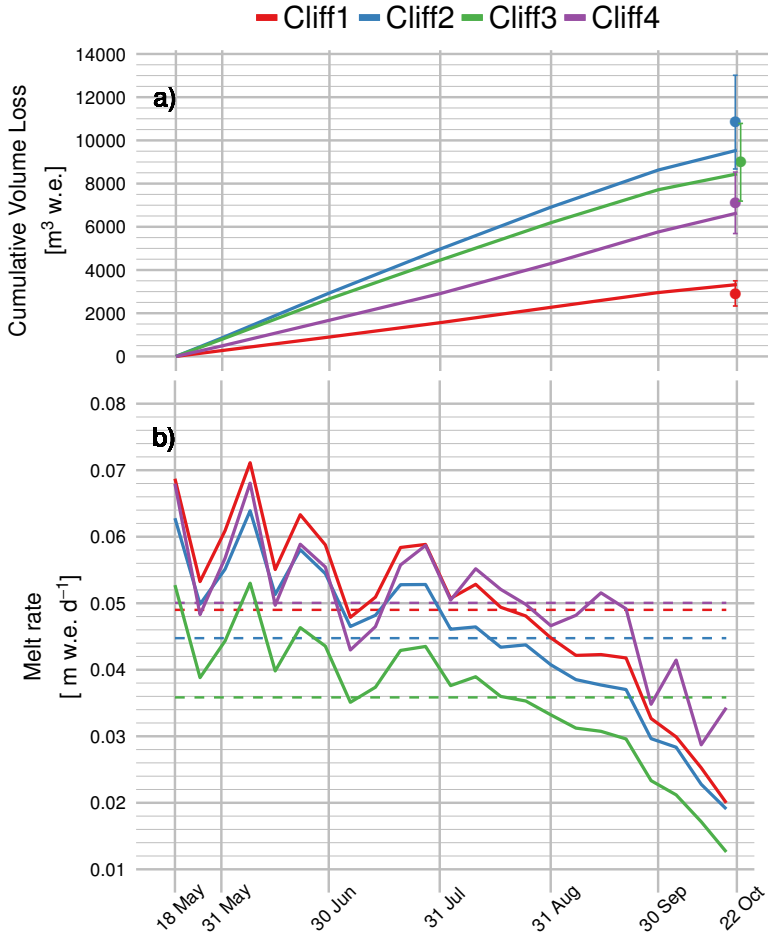


Figure 6.11.: a): Modeled cliff volume losses from May to October shown as lines, compared to the TIN-generated volume losses (points) with their error bar of $\pm 20\%$, as estimated in Brun et al. (2016). b): Modeled daily melt rates (solid lines), averaged per cliff and obtained as the weekly average, and May to October mean cliff melt rates per cliff (dashed lines).

Table 6.2.: Ice cliff volume loss [m^3 w.e.] and mean backwasting rate [m w.e. d^{-1}] from May to October 2013 for the four cliffs. modeled volume losses ('Mod.', D-Model) are compared to the TIN-derived ('Obs', based on Brun et al., 2016) volume loss, together with the relative deviation ('Dev.') between the modeled and observed values. The uncertainty range of $\pm 20\%$ estimated in Brun et al. (2016) is indicated in brackets. Mean backwasting rates obtained as volume loss divided by the corresponding area are also provided.

Cliff #	Volume Loss			Melt Rate
	Obs.	Mod.	Dev.	[m w.e. d^{-1}]
1	2917.3 (2333.8 – 3500.8)	3325.6	14.0	0.048
2	10845.1 (8676.1 – 13014.1)	9544.4	-12.0	0.040
3	8987.0 (7189.6 – 10784.4)	8447.6	-6.0	0.033
4	7110.4 (5688.3 – 8532.5)	6634.9	-6.7	0.051

The cliff outlines in pre- and post-monsoon which serve as base for the TIN-generated volume losses (Brun et al., 2016) are slightly different from the manually delineated cliffs. Therefore the volume losses from the TIN-approach should be used as a reference rather than an exact validation. The uncertainty range of $\pm 20\%$ estimated in Brun et al. (2016) is also indicated in Figure 6.11a.

Simulated volume losses all agree with the TIN-derived values within the given uncertainty ranges (Figure 6.11a and Table 6.2). Estimated volume losses are smaller than the ones of Brun et al. (2016) for all cliffs except Cliff 1 (Table 6.2). Volume losses at the end of the study period are an integrated variable of cliff backwasting processes. The daily melt rates averaged over the entire cliff area and to weekly values, calculated as melt amount multiplied with inclined area per cell, provide a better insight into temporal patterns of changes (Figure 6.11b).

The melt rates at all four cliffs show a clear reduction towards the end of the melt season with distinctly lower values in post-monsoon. Melt rates at Cliff 1, 2 and 4 are similar in magnitude until end of July, when melt at Cliff 4 becomes higher while decreases at Cliff 2. The melt rate at Cliff 3 is remarkably smaller in magnitude (0.036 m w.e. d^{-1} on average with a minimum daily melt rate among all cliffs of 0.013 m w.e. d^{-1} by mid October), indicating that the high volume losses at this cliff (Figure 6.11a) is due to the larger area.

The highest melt rate is at Cliff 1 ($0.071 \text{ m w.e. d}^{-1}$) in early June before monsoon starts, but this cliff also shows the highest variability during the melt season (0.051 m w.e.) as its melt rate goes down to $0.02 \text{ m w.e. d}^{-1}$. The highest mean melt rate over the entire period of record (May to October) is simulated for Cliff 4, with multiple post-monsoonal increases in melt rate (probably related to the exposure of west-oriented cliff sections), whereas melt rates at the other cliffs decrease progressively from mid September on. This behaviour of Cliff 4 results in the lowest variability in melt rate ($0.039 \text{ m w.e. d}^{-1}$) among all cliffs.

From Figures 6.9c and 6.9d, it is apparent that the model overestimates the cliff area. Comparison of areas per se is not entirely meaningful, as the same total area could result from combination of erroneous cells identified as cliffs together with cliff cells wrongly identified as non-cliff. For this reason, we use more sophisticated validation metrics calculated for the projected area that account for the correctly identified cells (section 6.4.2). Table 6.3 shows that the D-Model reference run has, on average over all four cliffs, a high Recall value (0.872), acceptable precision (0.600) and a high F-score (0.708). The latter is higher than in all other runs tested.

6.5.4. Model Sensitivity

The D-Model run has the highest average F-Score value of all models (Table 6.4), which suggests that the chosen parameter values are an appropriate set. The S-Model has the lowest value over the four investigated cliffs, confirming the poor performance of this model version (Figures 6.5 and 6.9). The cliff where the D-Model performance is worst in terms of Recall rate and F-score relative to the S-Model is Cliff 4. This can be seen in Figure 6.9d, where the shift of the D-Model outline towards east is apparent, which reduces prediction of observed cliff area and therefore lowers the Recall value. In turn the precision is higher than with the S-Model. Ignoring the effect of ponds adjacent to a cliff only slightly decreases the F-score value, as the main effect of a pond is on the cliff's slope distribution rather than area.

In general, all additional runs have a higher Recall than the D-Model reference run (0.872), except for the S-Model run and run 'rs+20 cm' (with a spatial resolution of 80 cm) and run ' $\beta_T-20\%$ ' (with a slope threshold of 32°), but very few a higher precision (Table 6.4). As a result, none of the additional runs has a

Table 6.3.: Validation metrics and results of the sensitivity analysis for different model runs (listed in the first column). The values are averaged over the four cliffs from May to October. For D- and S-Model runs the metrics for each cliffs are shown additionally. Standard deviation among cliffs is shown in brackets. Except for the S-Model run, all runs are based on the D-Model with a single parameter changed at a time. In run ‘PondOff’ the pond-influence algorithm was suppressed. In runs ‘rs’ the spatial resolution of the UAV-DEMs was altered, in ϵ_1 and ϵ_d the emissivities of ice and debris, respectively, were changed. ‘ β_T ’ and ‘ V_{dT} ’ indicate the runs where the threshold values for slope and debris view factor, were modified, the α_i and α_d those runs where ice and debris albedo were changed. The second column shows the value corresponding to each specific run. The metrics Recall, Precision and F-score are described in section 4.2. Sensitivity is shown as change in the F-score (ΔF) per unit change of the corresponding parameter.

Run	Tested value	Recall	Precision	F-score	Sensitivity
D-Model		0.872 (0.139)	0.600 (0.068)	0.708 (0.086)	
-Cliff 1		0.965	0.587	0.730	
-Cliff 2		0.933	0.705	0.803	
-Cliff 3		0.957	0.592	0.731	
-Cliff 4		0.633	0.516	0.569	
S-Model		0.807 (0.057)	0.480 (0.079)	0.599 (0.071)	
-Cliff 1		0.726	0.382	0.501	
-Cliff 2		0.846	0.600	0.702	
-Cliff 3		0.873	0.600	0.592	
-Cliff 4		0.784	0.488	0.602	
PondOff		0.874 (0.152)	0.587 (0.075)	0.699 (0.094)	
rs + 20cm	80 cm	0.730 (0.141)	0.627 (0.122)	0.667 (0.104)	0.0006 ΔF /cm rs
$\epsilon_d - 2\%$	0.929	0.872 (0.137)	0.594 (0.082)	0.704 (0.086)	0.0026 ΔF /% ϵ_d
$\epsilon_d + 2\%$	0.967	0.875 (0.131)	0.578 (0.078)	0.693 (0.087)	
$\epsilon_1 - 2\%$	0.959	0.876 (0.125)	0.581 (0.079)	0.698 (0.083)	0.0036 ΔF /% ϵ_1
$\epsilon_1 + 2\%$	0.996	0.880 (0.124)	0.602 (0.074)	0.712 (0.082)	
$\beta_T - 10\%$	0.936	0.905 (0.086)	0.559 (0.077)	0.688 (0.068)	0.0001 ΔF /° β_T
$\beta_T - 20\%$	32°	0.947 (0.029)	0.536 (0.082)	0.681 (0.065)	0.0001 ΔF /° β_T
$\beta_T + 20\%$	48°	0.743 (0.208)	0.632 (0.112)	0.679 (0.153)	
$V_{dT} + 10\%$	0.495	0.881 (0.161)	0.533 (0.069)	0.661 (0.090)	0.0116 ΔF /% V_{dT}
$\alpha_i - 20\%$	0.192	0.885 (0.132)	0.583 (0.088)	0.700 (0.090)	0.0001 ΔF /% α_i
$\alpha_i + 20\%$	0.288	0.874 (0.165)	0.583 (0.063)	0.698 (0.095)	
$\alpha_d - 20\%$	0.089	0.878 (0.139)	0.584 (0.082)	0.698 (0.085)	0.0000 ΔF /% α_d
$\alpha_d + 20\%$	0.134	0.873 (0.127)	0.584 (0.075)	0.697 (0.083)	

Table 6.4.: Cliff characteristics derived from the UAV-DEM ('Obs') and modeled with the D-Model ('Mod'). The mean values are shown together with the respective deviations for 22 October 2013. For elevation the maximum value within the cliff area was taken. Aspect values (vectorial mean) are defined from 0 to 360° with North at 0°. Values for vertical extent indicate the highest difference in elevation within the cliff area, horizontal extent shows the manually defined maximum straight distance within the cliff outline.

Cliff	Elevation		Aspect		Slope		Vertical Ext.		Horizontal Ext.						
	Obs	Mod	Obs	Mod	Obs	Mod	Obs	Mod	Obs	Mod					
1	4061.7	4062.9	1.2	320.2	323.2	3.0	42.0	43.9	4.6	10.8	11.6	6.8	46.1	47.6	3.3
2	4092.2	4093.2	1.0	28.2	30.9	2.7	56.5	51.0	-9.8	24.7	25.9	4.9	95.6	93.9	-1.8
3	4155.5	4161.8	6.3	2.9	0.2	2.7	49.0	46.2	-5.6	27.5	33.9	23.2	72.6	86.0	18.5
4	4204.7	4207.1	2.4	259.6	242.3	17.4	47.0	45.2	-3.9	23.7	23.8	0.4	82.4	80.3	-2.5

higher F-score than the reference run (0.708) except for the run with increased emissivity (0.712), which is only slightly higher.

The factor to which the model seems most sensitive, for the explored ranges, is the debris view factor threshold (V_{dT}) used to rebury cliff cells that are surrounded by a large area of debris. The changes in the F-score ($0.0116 \Delta F/\% V_{dT}$) is at least one order of magnitude higher than the results from all the other runs.

The standard deviations of the scores (values in parantheses in Table 6.3) among the four cliffs are generally homogenous with only a small total range over all model runs. The standard deviations are highest for Recall (0.128) and lowest for Precision (0.082).

6.6. Discussion

6.6.1. Observations of Cliff Evolution

Out of four cliffs for which detailed, high resolution observations were available, we noted three main patterns of evolution over the course of an ablation season, indicating a large variability that makes generalisations of cliff behaviour difficult. It is clear that detailed observations for a longer duration and for a larger sample size of cliffs are needed to shed light with certainty on the principal processes. However, some key results emerge also from the analysis of four cliffs in this study.

The first is the presence and role of supraglacial ponds at the base of a cliff. The presence of supraglacial ponds adjacent to ice cliffs seems to be one of the main factors controlling whether a cliff flattens or is able to preserve a steep face (Figure 6.12). The pond maintains a steep cliff directly through thermo-erosion or subaqueous melt at the pond-cliff interface and indirectly through exposure of the steep sections to increased longwave radiation emitted by the debris surrounding the cliff-pond system. Steep subaqueous ice slopes were observed with use of a sonar transducer on Lirung Glacier in 2013 (unpublished), which identified that maximum pond depth occurred immediately adjacent to the cliff-pond margin. Observations at other study sites have also revealed a steep subaqueous ice face (e.g. Benn et al., 2001), which might not be the case with all pond-cliff systems, but seems to be a frequent characteristic.

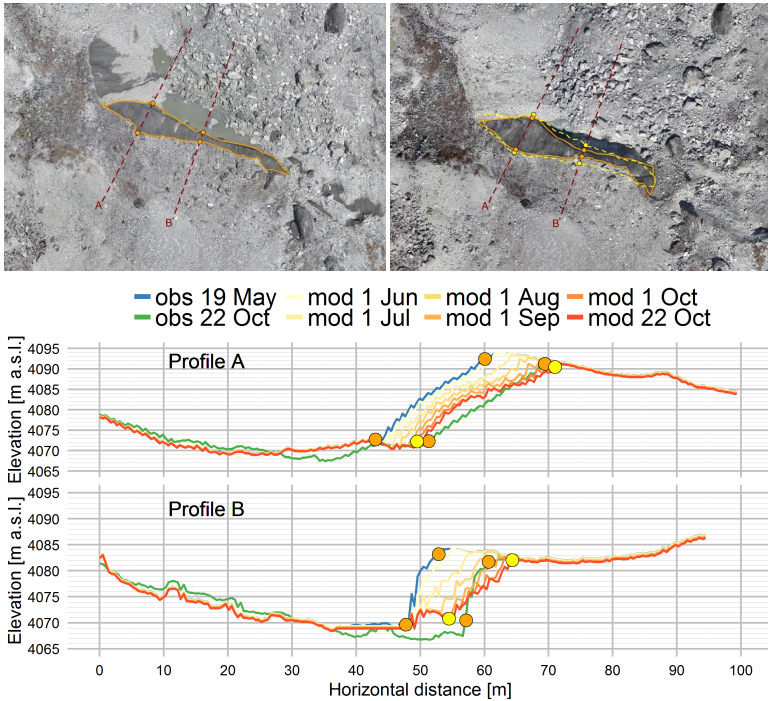


Figure 6.12.: Top: Orthoimages showing the glacier surface in May (left) and October (right) 2013, with observed (orange solid) and modelled (yellow dashed) final Cliff 2 outlines. The corresponding debris-ice contact points are indicated with dots (using the same colour scheme: orange for observations and yellow for model results). The corresponding transects A and B (dark red dashed) are also shown. Bottom: Elevation profiles across Cliff 2 as observed in May and October (blue and green) and modelled from May (yellow) to October (red). The dots indicate the interfaces indicated in the orthoimages above (using the same colour scheme: orange for observations and yellow for model results).

A second important factor controlling cliffs' growth is related to reburial by debris. In the model this is accounted for in a two-fold way, with a threshold slope under which debris-free cells are reburied and by a threshold for the debris-view angle. Despite its simplicity, this approach works satisfactorily. From a combination of model results and observations, this effect seems to be important at the cliff margins, and ignoring it will lead to overestimation of cliffs' areas. However, this should not result in major discrepancies in volume losses as these result mainly from melt occurring in the central section of the cliffs, as indicated by the fact that despite the overestimation of cliff areas by the model, the total volume loss is simulated correctly (Figure 6.11). Nevertheless, for modeling applications aimed at understanding future cliff evolution inclusion of this aspect seems imperative to avoid unlimited areal growth which would translate into erroneous melt and backwasting patterns over the long term.

Observations also show a variety of aspects and shapes, and while none of the cliffs has a south-facing orientation, it is remarkable that the only growing cliff was the West-facing Cliff 4, which received much higher average radiative energy than the other three cliffs (Figure 6.10). We were not able to attribute this growth to aspect alone, but the distributed, high resolution simulation of the radiative fluxes provides a clear indication of higher energy receipts. This also highlights the importance of a grid based, sophisticated model of energy fluxes.

6.6.2. Model Simulations

The dimensions and geometry of the cliffs after one melt season are reproduced by the new model approach (D-Model) in an accurate manner. Simulated mean aspect and slope per cliff deviated only by a few degrees from the observations (Table 6.1). The higher difference in aspect of Cliff 4 (12.8° towards south) is mainly caused by its strong radial expansion from May to October and the resulting generation of a high range of aspects. Modeled vertical and horizontal extents are in close agreement with the observed distances, except for Cliff 3, which shows an overestimation of about 20 % along both dimensions. The penetration of its south-west remnant too far into the debris slope caused overestimation of the maximum elevation and thus of the vertical cliff extent, as the lowest cliff section was modeled correctly. The horizontal excess compared to the observations is due to overestimation of areas in both the south-west and east parts of Cliff 3. Cliff 3 is the one for which discrepancies in the geometric

characteristics are strongest. Nevertheless, the overall pattern of backwasting in the uppermost section of the cliff is reproduced very well by the model, and total volume losses agree with the observed values (Figure 6.11). For Cliffs 1, 2, and 4 simulated dimensions, slope and aspect patterns, and maximum elevations all agree well with the UAV observations, suggesting that the overall backwasting pattern is reproduced well by the model.

Despite the overall good general agreement (F-score > 0.7), discrepancies are still evident when comparing the cliffs outlines and areas. This suggests that additional processes not included in the model may be important, or that a better representation of included processes is needed. In particular, the recovering of marginal cliff cells with debris, implemented with a threshold slope and debris view factor, is not entirely reproduced by the model, and leads to an overestimation of the cliff area especially for Cliff 3 (Figure 6.9c and d). Examination of the surface topography adjacent to the cliff suggests that more complex sourcing of debris contribute to the reburial of sections of cliffs (Figure 6.13). Cliff 3 seems to have backwasted prior to the May 2013 observation along a relatively steep and uniformly inclined debris slope and the debris flank left behind is visible NW of the cliff (white arrows in Figure 6.13a). However, during the 2013 melting season the cliff recedes further down, while the model simulates the cliff to follow the ridge and end up in October at its southern front (Figure 6.13b), similar to the initial position of this cliff's margin in May (Figure 6.13a).

The formation of the debris flank is modeled correctly, but the reburial of the ice surface is not. Inspection of the topography of the debris slopes shows concave crests surrounding the cliff western margin (Figure 6.13c) that are likely to contribute additional debris. This, coming from the sidewardly concave ridge above the southwestern section of the cliff, accumulated in the small cirque at its base (see Figure 6.13c), decreasing the local slope and leading to the disappearance of that section of the cliff. The morphometric characteristics of the ridge and its debris supply are difficult to model without adding increasing complexity and specific parameterisations, despite clearly playing a role in controlling the debris presence or removal through gravitational processes.

In general, the environment surrounding the ice cliffs may explain some of the variability in behaviour and in transitions between cliff types, as much as the processes acting directly on the ice itself. Cliffs retreating into slopes with the same aspects to the cliff would cause a lowering of the ice cliff (Figure 6.12),

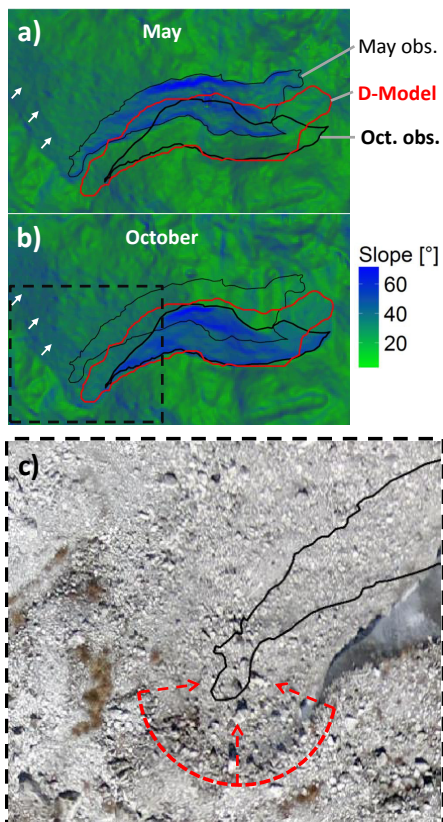


Figure 6.13.: Observed slopes at and around Cliff 3 in May (a) and October (b) are shown in the background. Thin and bold black outlines in the foreground show the observed cliff outlines in May and October, respectively. The red outline is the D-Model result. White arrows indicate the ridge and dip direction of the main debris slope as a trace from cliff backwasting path. A reason for the large overestimation of the modeled cliff area could be convergent accumulation of debris in the cirque sourcing from concave crests (c, red dashed line), which could not be considered in the model.

while retreat into a slope with the opposite aspect to the cliff would result in a heightening. The model reproduces these effects well, given the high resolution and quality of the DEM available (Figure 6.12), suggesting that this effect can be simulated as long as the surrounding topography is correctly represented. However, a mechanism that is not currently included is the effect of varying debris thickness at the top of the cliff. Debris cover thickness varies over short spatial scales, and cliff retreat into a thickening cover at the top of the wall might explain burial of the base. In general the model simulates the top ridge of the cliffs correctly (especially for cliffs 1 and 3), but has some problems in predicting the cliff base position (e.g. Cliff 3), which is likely due to convergent accumulation of debris in the cirque close to the cliff (Figure 6.13). The redistribution of debris from above the ice cliff to its base is only crudely represented in the model by a slope-based control on the area identified as cliff. Physically, the reburial of the base of the cliff and the accumulation of debris mounds depend on the debris thickness above the cliff, retreat rates and ice cliff slope, all controlling the runout and deposition of small rockfall events.

6.6.3. Model Limitations

Some of the approaches implemented in the model presented here are simple, and could be improved towards more physically based formulations. The effect of an adjacent pond is included through prescription of a constant subaqueous melt rate and an affected area that was defined based on sensitivity tests. A more advanced approach could be devised based on the temperature of the pond water, but would require data that are not easily available. Equally, the reburial by debris is parameterised as a function of slope and the amount of debris that is seen by any given cell of the cliff. A more accurate representation could be based on prescription of a source area and debris characteristics, but this also would imply knowledge of the geology of the debris and more burdensome calculations in a model that is already very complex. The main modeling goal that drove the formulation of the model was to incorporate first order controls of cliff changes in a manner that would allow the model to be run for several cliffs and relatively long times without requiring too detailed or specific datasets.

A more stringent limitation related to the effect of ponds is the lack of knowledge about their hydrological variability and water levels. The reversal of slope observed at Cliff 4, with a flat lower cliff section in May turning into a steep one

in October was not reproduced by the model, but could be explained by varying pond levels, which are not considered in the simulations. According to observations the pond adjacent to Cliff 4 lowered substantially towards post-monsoon, exposing a newly steep section at the cliff base, where the pond most probably filled up in early pre-monsoon flooding the lower cliff zone.

The partial disagreement between the observations and modeled cliff geometry for Cliffs 1 and 3 might also be explained by the fact that between the two field visits of May and October 2013 the boundary conditions in the immediate vicinity of the cliffs changed significantly, most likely by the appearance of an ephemeral pond. In general, observations during monsoon and knowledge about pond evolution on debris-covered glaciers are very limited (Watson et al., 2016). Therefore it is difficult to make assumptions about potential inter-seasonal occurrence of supraglacial ponds and prescribe variable pond levels in the model. Nevertheless, it is evident that comparison of model results with field observations can provide insights into processes occurring in the time between observations.

Another model limitation is related to some of the meteorological input data, which were applied in a non-distributed way: unlike the radiative fluxes, air temperature, relative humidity and wind speed were assumed to be uniform in space. The point-scale AWS measurements were taken as such and uniformly applied to each cliff cell, because of lack of better methods for their extrapolation or modeling. Investigations into the micro-meteorology of high elevation debris-covered tongues and Himalayan glaciers is, despite recent progress (e.g. Steiner and Pellicciotti, 2016; Collier and Immerzeel, 2015), a field still in need of sustained focus.

Surface parameters (surface roughness, ice and debris albedo) were also assumed uniform in space. Despite the fact that they can show high spatial and temporal variability, these quantities are difficult to measure in a distributed manner at the cliff scale, for obvious logistic difficulties. Debris albedo depends on radiation patterns and shadow, precipitation determining the wetness of the surface, and debris properties. Ice reflectance additionally depends on preferential melt flow paths and amount of debris sources above the cliff as well as refreezing. Very little is known about surface roughness of cliffs and debris surfaces in general (Brock et al., 2010; Rounce et al., 2015). For both albedo and surface roughness we used values optimized in Steiner et al. (2015) for Cliffs 1 and 2 where comprehensive

survey datasets were available in both pre- and post-monsoon 2013, but it is clear that a better understanding of the spatial and temporal variability of cliffs surface properties could lead to improvements in modeling outputs.

The model seems to have problems in handling very thin, branching cliff segments, as could be seen in the modeled outlines of Cliff 4. This could lead to the development of incorrect cliff remnants with the wrong aspect, a problem that was small for Cliff 4 but could be more significant for other cliffs. As noted above, discrepancies in cliff areas would not necessary result in large errors in simulated volume losses as long as the areas are marginal, but depending on their main aspect they could represent a source of error over the long period.

6.6.4. Comparison with Other Studies

Despite apparent recent advances, models of cliff backwasting are still in their infancy. The three main works that have presented backwasting models (Sakai et al., 1998; Han et al., 2010; Reid and Brock, 2014) are all point scale models that only take into account the effect of atmospheric energy on cliff ablation. The development of the first grid-based model of cliff ablation that considered the cliff surface as a 3-D domain was a significant step forward (Buri et al., 2016a). This work shed considerable light on the spatial variability over a single cliff of the atmospheric forcing and quantified for the first time the relative importance of the various fluxes. However, that model includes only the atmospheric forcing (although in a distributed manner), and does not consider other processes that modulate the backwasting of a cliff and its geometrical changes. Here we show that updating the surface geometry is crucial for realistic calculations of the volume lost by a cliff during one ablation season, and that a gridded representation of the cliff surface is necessary to quantify melt rates appropriately. We also show that accounting for melt at the surface of the cliff exposed to the atmosphere is only one of the processes that drive the dynamics of cliffs, their survival and decay.

Simulations with the new model provide an estimate of May-October mass losses from the four cliffs investigated that range from 3326 (Cliff 1) to 9544 (Cliff 2) m^3 w.e.. The contribution of the four cliffs to total sub-debris melt, estimated with an advanced glacio-hydrological model (Ragettli et al., 2015), is 3.25 %. This value is remarkable, given the small area ice cliffs cover relative to total debris-covered area (0.19 %).

In a recent study on Ngozumpa Glacier, Everest region, Thompson et al. (2016) found that cliffs accounted for 40 % of the volume losses over the stagnant portion of the glacier tongue by differencing of DEMs. It is difficult to compare these values to those obtained in our study, because the method used by Thompson et al. (2016) often also included ponds in the area regarded as cliff, leading to high uncertainty. It would be useful to apply our model to all cliffs over a large glacier and compare those estimates to those of Thompson et al. (2016).

The new model could also be used to understand long term patterns of cliff changes over several ablation seasons and employed to test hypotheses on cliffs survivals such as that only north-facing cliffs (on the northern hemisphere) survive over multiple seasons that have been put forward but never demonstrated. The model, however, given the level of complexity and physical detail included, might not be applicable as such at the glacier-scale, for computational reasons and because it requires high resolution DEMs of the cliffs and their surrounding topography that are rarely available for an entire glacier or catchment. For applications at this spatial scale, for which only coarser resolution DEMs are generally available, the effect of the DEM resolution on the accuracy of the model outputs needs to be tested.

6.7. Conclusions

In this paper, we have used a new dataset of high resolution observations of cliff evolution over one ablation season to identify patterns of changes over four cliffs on the debris-covered tongue of Lirung Glacier. The four cliffs have different shape, dominant orientation and slopes, and different degree and history of coupling to a supraglacial pond. We use the observations to infer the dominant processes controlling the observed evolution based on analysis of backwasting rates and cliffs geometrical properties. We then use the knowledge gained in this way to develop a model of cliff backwasting that takes existing models a step forward by including the cliffs dynamics in response to both atmospheric forcing (included to date), the effect of ponds at the cliff base and reburial by debris. To our knowledge, this is the first model to move beyond theoretical ablation rates for an invariant surface and to represent 3D evolution of cliffs.

Our main conclusions are as follows:

1) Out of four investigated cliffs, three different and contrasting patterns of evolution are evident. We show that cliffs on the same glacier and at short distance within each other can both flatten and recline, remain remarkably self-similar during one ablation season or expand radially in a considerable manner.

2) We were able to identify some of the mechanisms controlling the patterns described above through a combination of high resolution observations and an advanced model. In particular, we developed a model that accounts for the three main processes that seem to be first-order controls on cliff evolution: i) atmospheric melt; ii) pond-contact ablation enhancement for the cliff base; iii) reburial by surrounding debris.

3) The modeling approach suggested is able to simulate the cliff evolution over one melt season in a satisfying way in terms of horizontal and vertical extent as well as mean slope and aspect. The model simulates the progressive backwasting through interaction with the surrounding topography, allowing the cliff shape to grow and to shrink over time. While there is room for further refinement, the model is able to capture the main cliff dynamics and geometric transformation. Importantly, the model application has clearly shown that, for very high resolution studies, neglecting a dynamic update of the cliff geometry would lead to erroneous results in terms of backwasting patterns and volumes. Similarly, ignoring the effect of adjacent ponds or reburial by debris misses major factors affecting cliff evolution

4) Observations and model results suggest a strong dependency of the cliffs' life cycle on supraglacial ponds, as the water body keeps the cliff geometry constant through a combination of subaqueous and atmospheric backwasting as well as calving at the base to maintain steep ice cliff slopes in the lowest sections. The absence of ponds causes the progressive flattening of the cliff, which finally leads to complete disappearance.

Despite the clear advances, several improvements are still possible, and require high-resolution time series datasets of cliff geometry, coupled to pond changes and an understanding of debris local motion, sourcing and redistribution. This calls for increased monitoring efforts from high resolution imagery and field observations to collect a larger sample of cliffs to categorise cliff behaviour based on the insights provided here. These should encompass a variety of sites (others in the Himalaya and in other regions of the world), greater number of cliffs, and a longer duration (e.g. evolution over several years).

Acknowledgments

We thank Lene Petersen and Martin Heynen very much for organising the 2013 field campaigns. Tek Rai was our guide in the field and he and his team proved invaluable assistants to our work and the collection of data in the field. Simon Wicki and Peter Hill also helped carry out cliff measurements. We thank ICI-MOD and Joe Shea for logistical support in Kathmandu. We had interesting conversations with Fanny Brun about some of the initial ideas that went into this paper. This study is funded by the SNF project UNCOMUN (Understanding Contrasts in High Mountain Hydrology in Asia). All model runs and analyses were performed with the R environment (R Core Team, 2015) using the raster (Hijmans, 2015), sp (Bivand et al., 2013) and ggplot2 (Wickham, 2009) packages and we would like to thank the developers for making them freely available. PB thanks Paolo Burlando for support at ETH. We are grateful to M. Kirkbride and G. Evatt and the Scientific Editor B. Hubbard whose constructive and thorough comments improved the manuscript. The data shown in this paper can be available pending an e-mail request to the corresponding author.

Chapter 7.

Aspect controls the survival of ice cliffs on debris-covered glaciers*



Figure 7.1.: Cliff 2 on Lirung Glacier, showing the high spatial variability of incoming radiation and shadows. Note the person at the top ridge of the cliff for scale (20 Oct. 2015).

* *Buri P and Pellicciotti F (in revision) Aspect controls the survival of ice cliffs on debris-covered glaciers. Proceedings of the National Academy of Sciences*

Abstract

Supraglacial ice cliffs exist on debris-covered glaciers worldwide, but despite their importance as melt hot spots their life cycle is little understood, due to lack of direct measurements and adequate numerical models. Early field observations had advanced a hypothesis of survival of north-facing and disappearance of south-facing cliffs which is central for predicting the contribution of cliffs to total glacier mass losses. Their role as windows of energy transfer suggests they may explain the anomalously high mass losses of debris-covered glaciers in High Mountain Asia (HMA) despite the insulating debris, currently at the centre of a debated controversy. We make use of the advancements in modelling these complex features and use a 3D model of cliff evolution coupled to very high resolution topographic data to demonstrate that supraglacial ice cliffs facing south (in the Northern Hemisphere) disappear within few months due to enhanced solar radiation receipts, and that aspect is the key control on cliffs evolution. We reproduce continuous flattening of south-facing cliffs, a result of their vertical gradient of incoming solar radiation and sky view factor. Our results establish that only north-facing cliffs are recurrent features and thus stable contributors to the melting of glaciers. This has major implications for the mass balance of HMA debris-covered glaciers as it defines the population of cliffs contributing to glacier melt, and provides the basis for new parameterisations of cliff evolution and distribution to constrain volume losses in a region where glaciers are highly relevant as water sources for millions of people (Immerzeel et al., 2010; Lutz et al., 2014; Pritchard, 2017).

7.1. Introduction

Many glacier tongues in High Mountain Asia are heavily debris-covered (Scherler et al., 2011; Bolch et al., 2012). Despite the insulating effect of a mantle composed by rock debris on the underlying ice (Østrem, 1959; Evatt et al., 2015), large-scale, satellite-based studies have suggested that thinning rates of debris-covered glaciers are comparable to those of clean ice glaciers (Gardelle et al., 2012; Kääb et al., 2012). Although recent studies at the catchment and glacier scale do not support analogous thinning (Ragettli et al., 2016a; Vincent et al., 2016), it has by now been established that strong local increases in glacier ablation are associated with supraglacial ponds and cliffs (Sakai et al., 2000; Miles et al., 2016; Buri et

al., 2016a; Thompson et al., 2016). Cliffs forming on the surface of debris-covered glaciers contribute to the glacier mass balance through enhanced melt rates, but also affect glacier dynamics, and knowledge about their life cycle and distribution is important to predict future evolution of debris-covered glaciers (Rowan et al., 2015). The understanding of processes acting at the scale of single cliffs has been dramatically improved recently through modelling approaches that have simulated energy fluxes and melt (Buri et al., 2016a,b) and estimated volume losses (Brun et al., 2016) of single cliffs. The rate at which cliffs can affect glacier mass balance and dynamics depends on their distribution and persistence in time, but how cliffs form, evolve and decline is not yet understood, precluding a holistic understanding of their role on longer term mass balance patterns beyond the few observations over a melt season. A hypothesis of persisting north-facing and disappearing south-facing cliffs has been first proposed more than one decade ago (Sakai et al., 2002) based on observations and conceptual assumptions on the importance of solar radiation on ice cliff melt (Inoue and Yoshida, 1980; Sakai et al., 1998). The hypothesis seems to be supported by inventories of cliff distribution from satellite observations of single or selected glaciers in the Khumbu region (Nepalese Himalaya) (Thompson et al., 2016; Watson et al., 2017). Conceptual intuition, supported by sparse observational evidence, has postulated that cliff faces oriented to the south are reburied rapidly and do not persist over debris-covered glaciers, independently of glacier flow direction. No study, however, has been able so far to explain the absence of south-facing cliffs on debris-covered glaciers.

7.2. Backwasting of south-facing cliffs

Here, we simulate the evolution of south-facing ice cliffs to understand the effect of enhanced solar radiation compared to observed north-facing cliffs. Our aim is to establish whether south-facing supraglacial cliffs persist beyond the length of a melt season, as observed northerly-facing cliffs do, or if they disappear more rapidly, and to identify the causes for their behaviour. To test this, we run a 3D numerical model of cliff backwasting that was able to reproduce the evolution of north-facing cliffs (Buri et al., 2016b). We force the model with hourly meteorological data from an on-glacier automatic weather station (AWS) Steiner et al. (2015) and initialised with a digital elevation model (DEM) (Immerzeel et al.,

2014b) of sub-metre resolution over the debris-covered Lirung Glacier (Nepalese Himalaya, Fig. 7.2a).

Initial conditions for our simulations were created by rotating north-facing ice cliff topographies as observed on Lirung Glacier (Fig. 7.2b) towards south, including the surrounding glacier surface and ponds (Fig. 7.2c). Hence, the artificially derived south-facing cliffs were embedded into a realistic cliff-glacier topography and therefore directly comparable to the north-facing cliffs in terms of size, shape and surrounding topography. We applied a dynamic, physically-based backwasting model (Buri et al., 2016b) on the two rotated cliffs over one ablation season (May to October 2013). Cliff melt is derived from distributed surface energy balance calculations and shapes the cliff surface by bi-weekly geometry updates. Melt at water-contact zones is enhanced to account for thermo-erosion by adjacent supraglacial ponds (Miles et al., 2016; Buri et al., 2016a). Depending on the slope at the cliff margins, the cliffs can expand or shrink (because of reburial by debris).

We simulate continuous shrinkage of the south-facing cliffs, resulting in a significant reduction in extent after a few weeks already (Fig. 7.3a). This is a striking difference compared to the evolution of the original north-facing cliffs (observed in the field and confirmed by our simulations Buri et al., 2016b), shown in the background of Fig. 7.3a, which backwaste maintaining a self-similar geometry that allows the cliffs to persist until the end of the ablation season. The reason for the rapid shrinking of the south-facing cliffs is the progressive flattening of their surface (Fig. 7.3b), which allows reburial by debris. The complete reburial of the debris-free cliff areas occur after less than three (Cliff 1) to five months (Cliff 2, Tab. S2). Even when the cliff is not entirely reburied, large sections of its surface disappear, reducing consistently the area available for melt (Fig. 7.4c). In contrast, the north-facing cliffs show stable profiles backwasting with a constant slope (Cliff 2) or only minimal regrading (Cliff 1, Fig. 7.3b).

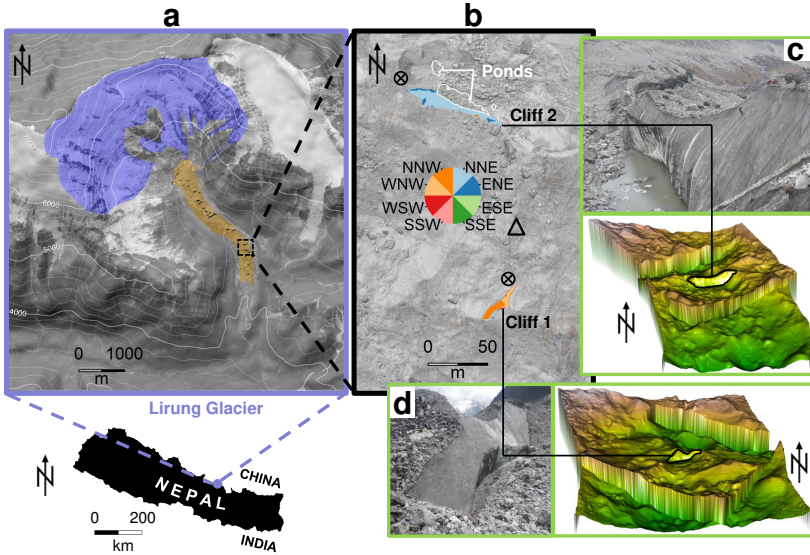


Figure 7.2.: Observed cliffs on Lirung Glacier, Langtang Valley, Nepalese Himalaya. (a) Lirung Glacier with debris covered tongue (orange) and accumulation area (violet). (b) Lirung Glacier surface around cliffs 1 and 2 (marked by colours indicating their aspect, and observed aspect of the cliff faces). Encircled crosses denote position where terrestrial images (c and d) were taken, triangle shows the location of the Automatic Weather Station (AWS). (c) Cliff 2 photographed from the location indicated in (b) (top) in May 2013, and rotated cliff system shown as 3D-elevation model (bottom). (d) Cliff 1 (left) as observed in a photo (taken from the location shown in (b) in May 2013, and rotated cliff system shown as 3D-elevation model (right). Background images: Orthoimage ALOS December 2010 and ASTER GDEM2 hillshade (a); Orthoimage UAV May 2013 and UAV DEM May 2013 hillshade (b); Picture E. Miles May 2013 and partly rotated UAV DEM May 2013 (c and d).

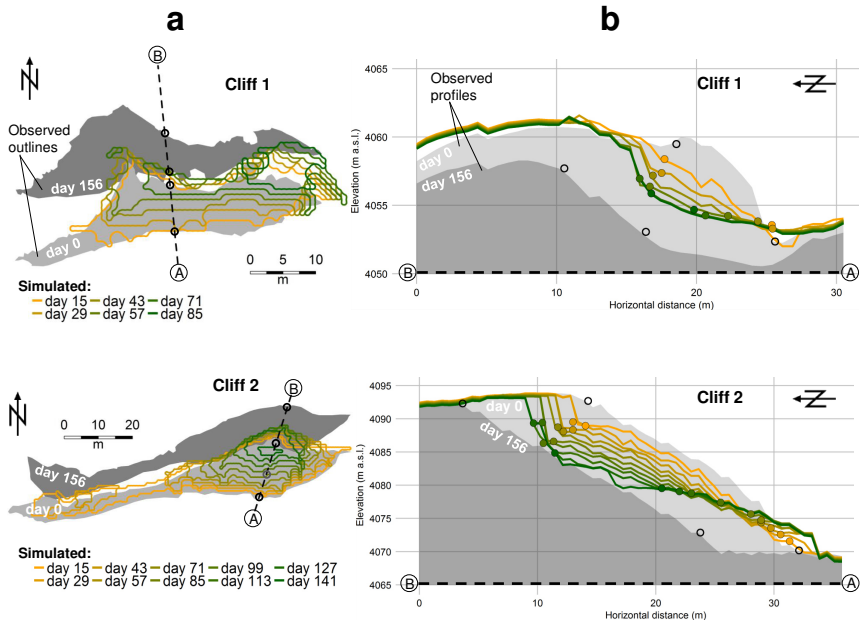


Figure 7.3.: Simulated outlines and elevation profiles of south-facing cliffs. (a) Cliffs 1 (top) and 2 (bottom) outlines simulated by the model with bi-weekly geometry updates (yellow to green lines). For comparison, also the observed shapes of north-facing cliffs are shown (light and dark grey polygons), rotated towards south for consistency (the model was able to simulate the evolution of the original north-facing cliffs; Buri et al., 2016b). Dashed line indicates profile, thick circles the debris-ice transitions. (b) Elevation profiles of rotated cliffs 1 (top) and 2 (bottom) as simulated with bi-weekly geometry updates (yellow to green lines). Profiles of observed north-facing cliffs are also shown (light and dark grey areas), rotated towards south for consistency. Circles indicate debris-ice transitions of modelled (yellow to green) and observed (thick black) cliff profiles. The last of the coloured lines (darkest green) indicates the last cliff profile before the cliffs disappear. None of the two cliffs survives for the duration of the ablation season, disappearing after day 85 (Cliff 1) and day 141 (Cliff 2). Days are counted from the start of the simulations, on 19 May 2013.

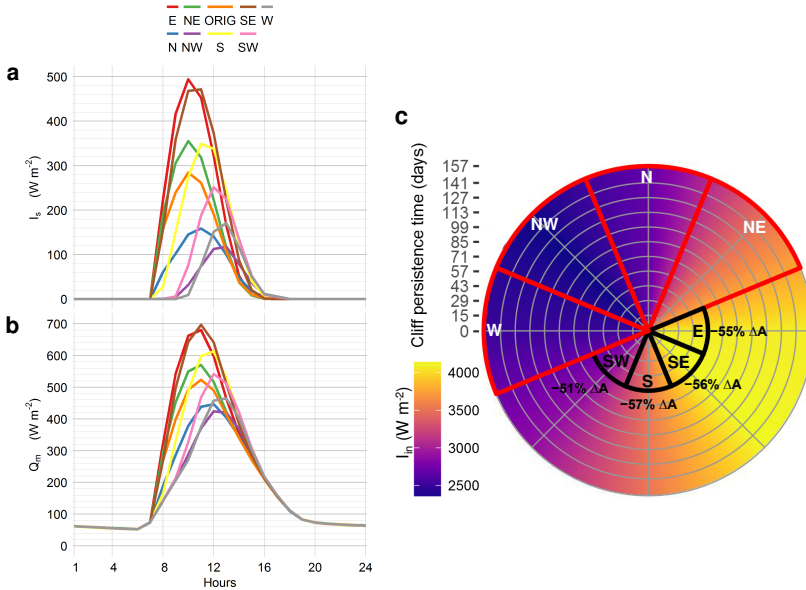


Figure 7.4.: Modelled surface energy fluxes for Cliff 2 rotated to various aspects. (a) Diurnal cycle (May–October 2013) of direct shortwave radiation receipt averaged in space over Cliff 2 rotated to eight different aspects by increments of 45° . (b) Diurnal cycle (May–October 2013) of melt energy averaged for Cliff 2 rotated to eight different aspects by increments of 45° . (c) Cliff persistence per aspect (angular scale in days, counted from the start of the simulations, on 19 May 2013): black lines indicate the time when more than 50% of the initially inclined area has disappeared (with ΔA indicated, providing the percentage of area that has disappeared at that time); red lines indicate the range of directions for which cliffs never reach that threshold (i.e. never loose more than 50% of their inclined area). Cliffs with aspects indicated in white (W, NW, N, NE) persisted for the entire season. In the background, the average daily sum of simulated incoming solar radiation per aspect is shown (blue to yellow).

7.3. Radiative forcing at the cliff surface

To understand what controls the simulated cliffs' evolution, we rotated cliffs 1 and 2 together with their surrounding topography by increments of 45° from north into eight additional directions and modelled the seasonal surface energy balances. We then calculated diurnal cycles of the spatially-averaged energy fluxes for the rotated cliff surfaces (Fig. 7.4a-b and Supplementary information, Fig. S4 and S5) and spatial totals of energy fluxes and melt energy (Fig. 7.5, S6 and S7).

The modelled longwave radiation component, comprised of radiation emitted by the debris surfaces around the cliff and of the longwave radiation emitted by the atmosphere, show no aspect-related differences in amount and timing (Fig. S4e-f and S7a-b). This is not surprising as these fluxes depend on the surface (debris) and air (atmosphere) temperatures, which have no obvious dependence on aspect, and on the local topographical horizons (which are approximately constant for all directions). In contrast, a very high aspect-dependence is evident for the simulated shortwave radiation and its direct component in particular (Fig. 7.4a,c, 7.5a,c). Differences between directions are evident in both the timing and total amount of solar energy received. East-facing cliffs receive direct solar radiation earliest in the day, followed by south- and west-oriented slopes (Fig. 7.4a and 7.5a). The lowest amounts are received by cliffs with aspects in the range north to southwest (Fig. 7.4a,c). East- and southeast-facing cliffs receive the highest direct solar radiation (up to 67% more than the original cliff and exceeding by 3.6 times the energy input at the northwest-facing cliff (Tab. S1), followed by south-facing ones. These cliffs do not survive the duration of the ablation season, but disappear or undergo a substantial loss in area (Fig. 7.4c, Tab. S2). The apparently anomalous behaviour of south- and southwest-facing cliffs, which receive as little radiation as those with a prevalent northerly aspect, is likely due to the presence of cloud cover in the afternoon. During the ablation season, which coincides with the monsoon in this region, in the afternoon, when the south-facing cliffs are theoretically exposed to high solar radiation receipts, thick clouds and rain prevail with regularity and prevent high solar radiation incomes in the Langtang Valley (Fujita et al., 1997; Immerzeel et al., 2014a). This decreases the solar radiation receipt of southwesterly aspects considerably (Sakai et al., 1998) and therefore dampens the all-year average of incoming

7.3. Radiative forcing at the cliff surface

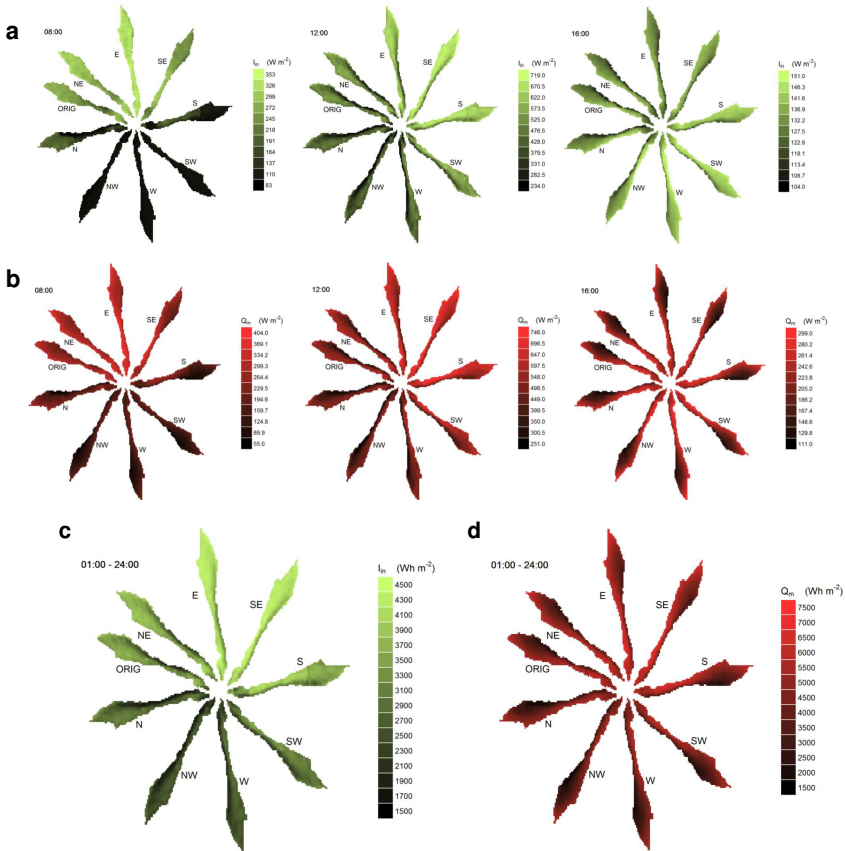


Figure 7.5.: Distributed energy fluxes modelled over Cliff 2 rotated to various aspects. (a) Distributed incoming shortwave radiation averaged over melt season (May–October 2013) rotated to eight different aspects by increments of 45° (indicated by label at crest of each cliff), shown for hours 8 (left), 12 (middle) and 16 (right) of the day, respectively. (b) Map of melt energy per pixel averaged over the melt season (May–October 2013) calculated over Cliff 2 rotated to eight different aspects by increments of 45° , shown for hours 8 (left), 12 (middle) and 16 (right) of the day, respectively. (c) Distributed daily sum (averaged May–October 2013) of incoming shortwave radiation. (d) Map of daily sums (averaged May–October 2013) of melt energy.

shortwave energy (Fig. 7.4). The daily cycle and spatial patterns of melt energy closely reflect those of the solar radiation inputs, with the highest amount of melt energy for east- and southeast-facing cliffs (Fig. 7.4b and 7.5b). As a result of the energy forcing, cliffs with aspect in the range east to southwest do not survive, while cliffs facing northeast to west do (Fig. 7.4c, Tab. S2).

Spatial variability in solar radiation and melt energy is high over a single cliff (coefficients of variation for direct shortwave radiation up to 238% at the west-oriented surface of Cliff 2, Tab. S3). Solar radiation is highest at the top of the cliff, and this effect is stronger at noon because of the high sun angle (Fig. 7.5a). The top sections of the cliffs receive also the highest amount of atmospheric longwave radiation (Fig. S7b), thus amplifying the solar radiation control. This cannot be counterbalanced by the longwave flux emitted by the debris surface surrounding the slopes, which is highest at the cliffs margins (Fig. S7a). Total melt energy results from the interactions of these spatially variable fluxes and their temporal variability: it is highest at the top of the cliff (Fig. 7.5b) for most aspects, and decreases towards the cliffs bottom. This energy gradient is small (with minimum differences between the energy at the top and bottom of the cliff) for cliffs with northwest and western aspects (Fig. 7.5d, Tab. S3). These are those that survive (Fig. 7.4c) because a rather uniform distribution of solar radiation and melt energy allows their backwasting and maintenance of a constant steep slope, rather than downwasting and reburial by debris. The flux of energy emitted by the surrounding debris and received by the cliff margins is not high enough to counterbalance the atmospheric fluxes of shortwave and longwave radiation at south-oriented cliffs. High receipts of solar radiation at the top of these cliffs cause a progressive flattening. The cliff flattening, controlled by the sky view factor and hence the amount of sky that the cliff sections are exposed to, is thus strongly aspect-dependent. Longitudinal profiles of progressively higher solar radiation amounts from base to top will have a much stronger vertical gradient for those aspects that receive much higher solar radiation in the morning hours (northeast to southeast). The upper part of Cliff 2 shows a 20–30% higher sky view factor compared to the base zone (Fig. S8c). The reduction in sky-openness towards the cliff bottom is the combined result of the topography in front of the cliff face and the steep slopes at the cliff bottom. The combination of a very high shortwave radiation income together with a decreasing sky view factor towards the cliff base cause the cliffs with southerly to easterly aspect to flatten progressively

over time, as the upper section recedes at much higher rates than the lower parts, until they reach a slope that can be reburied by debris.

7.4. Discussion

Our model results show that south-facing supraglacial ice cliffs disappear within few weeks to a few months. We thus provide the first evidence for previous conceptual suggestions that (in the Northern Hemisphere) cliffs with a southern aspect are not part of the cliff population on glacier surfaces, as they do not persist on time scales relevant for glacier mass balance considerations. This narrows the knowledge gap concerning distribution and evolution of cliffs as the population of cliff systems can be reduced to northerly- to westerly-facing ones. We can explain this distribution with the enhanced solar radiation received by the cliffs with southern aspects. Southeast- and northwest-oriented cliffs are likely the extremes of cliff life expectancy, as exposure to solar radiation and shadowing, respectively, are highest for these aspects.

We are able to reproduce the flattening of southerly-facing cliffs induced by much higher direct solar radiation, compared to northerly-oriented cliffs, and the increase of the shortwave radiation-relevant sky view factor from cliff base to crest. The increasing debris view factor towards the cliffs base (along a vertical gradient) and boundary zones (along a horizontal gradient from the cliff centre, Fig. S8d) results in a higher longwave radiation receipt from the surrounding debris at these cliff zones. This, however, is not able to counterbalance the extremely high solar radiation receipt of southerly aspects (as it is the case for cliff slopes facing north; Steiner et al., 2015; Buri et al., 2016a,b). Indeed, we show that there is a range of cliff aspects that determine their disappearance as a result of fluxes interaction and a range of aspects within which cliffs over monsoon-dominated central Himalayan glaciers will survive over the melting season: aspects from northeast to west are associated with cliffs persistence, while those from east to southwest with progressing flattening and disappearance (Fig. 7.4c).

The solar radiation received by a cliff and the shadowing of steep cliff surfaces is the first-order control of cliff's melt, evolution and distribution. This underlines the importance of high resolution topographical information of both the cliff and surrounding glacier surface in order to correctly represent cliff backwasting patterns. Importantly, we have shown that the effect of adjacent ponds (which

act on cliffs through enhanced melt through thermo-erosion at the low-lying cliff-pond contact zone) is not sufficient to maintain southerly-facing cliffs steep and thus allow their persistence (Fig. 7.3b), as they are able to do for northerly-oriented cliffs (Buri et al., 2016b).

While radiation seems to ultimately control the evolution and disappearance of supraglacial ice cliffs, their appearance and the mechanisms controlling their formation (subsurface developments such as collapsing of empty melt water channels close to the surface or surface changes induced by glacier dynamics or sub-debris melt; Kirkbride, 1993; Sakai et al., 2002; Benn et al., 2012) are still largely unknown. This is an important field of future investigation that will need to be addressed for detailed studies of cliff dynamics understanding.

7.5. Methods

We mapped two supraglacial ice cliffs on the debris-covered tongue of Lirung Glacier (Langtang Valley, Nepalese Himalaya) using a high-resolution orthoimage and digital elevation model (DEM), which were derived from an unmanned aerial vehicle (UAV) survey in May 2013 Immerzeel et al. (2014b). No south-facing cliffs were observed on Lirung Glacier (nor on the other glaciers of Langtang valley). Therefore we rotated the two cliffs including their surrounding topography and ponds (within 100m in xy-direction) by applying a 2D-matrix rotation around a common center coordinate. The rotation angle is defined as the deviation between the observed mean cliff aspect and the target direction in degrees. For our simulations we selected two observed cliffs of different size (one relatively large and one relatively small), aspect (northeast and northwest) and bottom configuration (in contact with a supraglacial pond and with no water contact). Both were located within 100m from an on-glacier automatic weather station (AWS), which allowed forcing the cliff energy balance and backwasting model with local, high resolution and accurate meteorological input.

A physically-based, dynamic 3D-backwasting model (Buri et al., 2016b), which has previously been tested for four cliffs (of which two are investigated in this study) on the same glacier and for the same period, allowed us to test the behaviour of the south-facing cliffs generated by rotation of the two original cliffs. The model has been validated for the two original cliffs with multiple independent data sets (Buri et al., 2016b), lending confidence to its use for this

experiment. For this study, we further improved the model algorithm for more stable and computationally efficient simulations (Supplementary Information). The use of a high-resolution DEM for initial conditions and hourly meteorological data recorded on-glacier allow the model to calculate radiation and shading at the cliff surface with very high level of detail (Buri et al., 2016a). Simulated melt from calculation of the cliff surface energy balance was accumulated for every cliff cell over two-week intervals, after which the cliff geometry was updated accordingly (Buri et al., 2016b) (Supplementary Information). Enhanced melt rates were applied to cliff sections in direct contact with ponded water Buri et al. (2016b), accounting for thermo-erosion (Miles et al., 2016) (Supplementary Information, Section 3.J). The model algorithm also considered expansion and shrinkage of marginal cliff zones based on slope and debris-view thresholds as described in (Buri et al., 2016b) and in the Supplementary Information (Sections 3.7–3.8).

Acknowledgments This study is funded by the SNF (Swiss National Science Foundation) project UNCOMUN (“Understanding Contrasts in High Mountain Hydrology in Asia”, Grant No. 146761).

7.6. Supplementary Information

7.6.1. Study site

The two cliffs investigated in this work are located on Lirung Glacier (Upper Langtang Valley, Central Nepalese Himalaya), the tongue of which is heavily debris-covered and detached from the accumulation area (Sakai et al., 1998, 2002, 2004; Immerzeel et al., 2014b; Steiner et al., 2015; Miles et al., 2016; Buri et al., 2016a; Kraaijenbrink et al., 2016; Buri et al., 2016b). The glacier elevation ranges from 4004m a.s.l. to 7234m a.s.l., the top of the tongue is at 4400m a.s.l. where a steep bare rock face separates the two glacier zones (Nuimura et al., 2017). Cliff 1 has a northwestern aspect, measures 10m in height and 45m in length (Buri et al., 2016a) and has an average slope of 43.6° . Cliff 2 has a northeastern aspect, measures 25m in height and 95m in length (Buri et al., 2016a) and has an average slope of 54.4° . The study region is influenced by the summer monsoon, with main accumulation and ablation during June–August (Immerzeel et al., 2014a).

7.6.2. Initial conditions and model inputs

Cliff outlines and DEM

Initial cliff outlines were mapped manually from the May 2013 Unmanned Aerial Vehicle (UAV)-orthomosaic (Immerzeel et al., 2014b), supported by in-situ field observations and expert knowledge from the field. The orthoimage was produced using a Structure-from-Motion (SfM) algorithm from Agisoft PhotoScan Professional (Agisoft, 2013) (version 0.9.1). The associated high resolution digital elevation model (Immerzeel et al., 2014b) (DEM), processed from the same UAV survey, served as base for the initial cliff geometry. To reduce computational demands and small inaccuracies in steep terrain in the elevation model we aggregated the original data from 0.2m to 0.8m spatial resolution. Tests on the model accuracy as a function of DEM resolution showed no differences between the runs at the two resolutions. The orthoimage and DEM from May 2013 are available on <http://www.icimod.org/?q=23044> (both at 1m spatial resolution). Distributed slope and aspect for each cell of the cliff surface (Fig. S7.6, S7.7) were derived by applying the Horn algorithm (Horn, 1981), using eight neighboring cells with differential weights and excluding the central cell itself. For the off-glacier topography, relevant for calculation of the shading patterns on the cliff surface, the ASTER-GDEM2 (Advanced Spaceborne Thermal Emission and Reflection Radiometer global DEM 2) (ASTER, 2009) with a spatial resolution of 1 arc second (30m) was used (Buri et al., 2016b).

In order to model the energy receipts and backwasting of cliffs of different aspects, the original cliff polygon, adjacent pond outlines, and the underlying DEM plus 100m of its surrounding topography are rotated in a two-dimensional Euclidean space around the cliff's central coordinate. The rotation angle was defined as the deviation between the vectorial mean aspect of the original cliff and the target aspect.

Meteorological data

The model input variables incoming shortwave radiation, air temperature (shielded and ventilated), wind speed and relative air humidity were all measured at a screen level of 2m at the Lirung on-glacier automatic weather station (AWS) (Steiner et al., 2015; Buri et al., 2016a,b), located between the two investigated cliffs (Fig. 1b). The meteorological data were recorded at 5min intervals, and

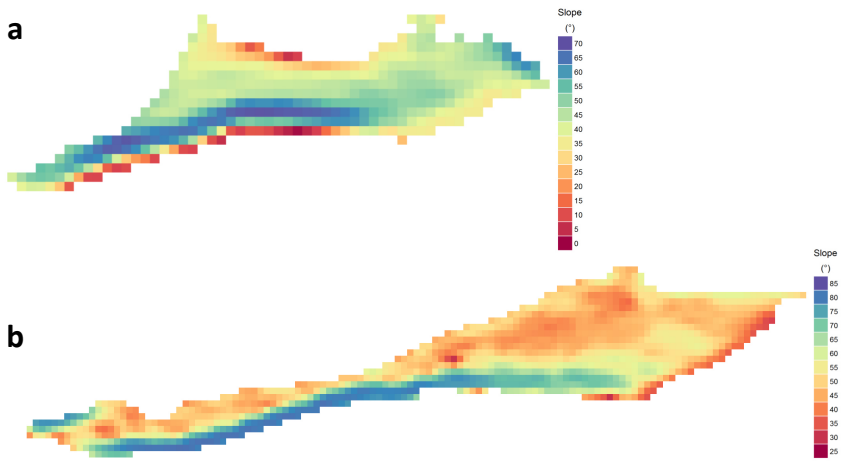


Figure 7.6.: Slopes of south-facing cliffs 1 and 2. (a) Slopes derived from UAV-DEM for Cliff 1 after rotation towards south. (b) Slopes derived from UAV-DEM for Cliff 2 after rotation towards south.

were then aggregated to hourly data for model input. Debris surface temperature was measured at the base of the AWS (Steiner and Pellicciotti, 2016). In the absence of on-glacier observations, incoming longwave radiation was modelled as described in Steiner et al. (2015) using data from AWS Kyanjing, an off-glacier station at 3857m a.s.l. less than 2km south of Lirung Glacier terminus (Buri et al., 2016b).

7.6.3. Dynamic 3D-backwasting model

The model, coded in the open-source software R (R Core Team, 2015), calculates cliff backwasting as a function of ablation for every grid cell of the cliff 3D domain. In addition to ablation caused by atmospheric energy, the model also includes ablation induced by ponded water at the base of a cliff (when present) and reburial by debris. The 3D cliff geometry is updated at regular steps to account for the modifications induced by all these processes. The dynamic backwasting model is initiated with a given cliff outline and glacier surface topography, both derived from observational data. The surface energy balance at the cliff-atmosphere interface is calculated from energy balance equations for every grid cell using as input meteorological data measured at the on-glacier AWS and distributed over the cliff domain. Computation of radiative fluxes accounts for direct- and diffuse components from the sky and the surrounding debris. Reflected shortwave radiation is controlled by (constant) ice and debris albedo values. Longwave radiation emitted from debris, sky and the ice cliff is included in the energy balance calculations. Whereas the radiative fluxes are highly variable in space due to the complex cliff geometry (Buri et al., 2016a,b), the turbulent fluxes (latent and sensible heat) are uniform over the cliff because of the assumption of uniform in space temperature and wind speed. Calculations of the radiative fluxes emitted by the sky and by the surrounding debris surfaces are of high accuracy due to advanced modelling approach, high spatial resolution and detailed representation of the cliff and glacier topography (Steiner et al., 2015; Buri et al., 2016a,b). Fluxes are computed based on sky and terrain horizon angles (local 360°-horizons) calculated for each raster cell based on the geometry of the ice cliff, the glacier surface and the surrounding off-glacier topography. Based on these horizons the shading from solar radiation as well as sky and debris viewing factors are derived and then used for calculation of the single radiative fluxes for every timestep. The calculated melt energy at the ice

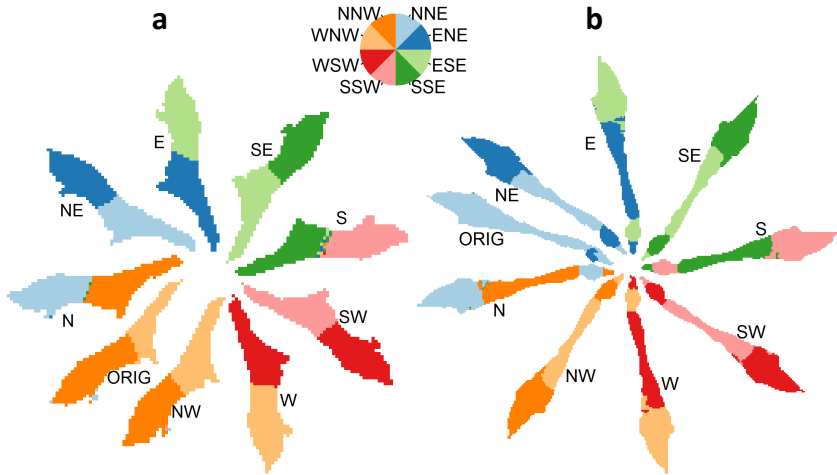


Figure 7.7.: Aspects of cliffs 1 and 2.(a) Aspects derived from UAV-DEM for Cliff 1, as observed (ORIG) and rotated to eight different aspects by increments of 45° . Cliff aspect values are smoothed by applying a 9×9 -cell filter to show a clearer pattern. Aspect labels are placed to indicate the crest of each rotated cliff. (b) Aspects derived for Cliff 2, as observed (ORIG) and rotated to eight different aspects by increments of 45° , as for Cliff 1.

cliff surface is accumulated over a period of two weeks and converted into an ice melt vector. The model accounts for thermo-erosional melt at cliff-water contact zones by adjacent supraglacial ponds, a process that has been suggested to be responsible for maintaining steep sections at the cliff bottom (Brun et al., 2016; Buri et al., 2016b). The melt distance, in combination with the slope and aspect (Fig. S7.6, S7.7) of each cliff cell, is used to update the 3D cliff shape in intervals of two weeks (this time interval was the most appropriate from consideration of model resolution and magnitude of the melt vectors). Subdebris melt of the surrounding glacier surface (a constant value in time and space) is taken into account and subtracted from every off-cliff grid cell on the glacier.

The model allows the cliff to dynamically expand or shrink after every melt update, taking into account the glacier topography adjacent to the ice surface. Based on thresholds for slope and debris view, steep areas at the ice-debris

transition zone become debris-free, and shallow zones along the cliff margin can become debris-covered.

Details of the model can be found in (Buri et al., 2016b), where the model was presented and tested in detail for four cliffs on Lirung Glacier, including the two original Cliff 1 (northwest-facing, 328°) and Cliff 2 (northeast-facing, 30°) of this study. The model was able to accurately reproduce the observed backwasting of the two northern-aspect cliffs. Here we only recall the main modelling steps and the changes we have implemented for this study.

Energy balance

The energy balance at the cliff surface is given by

$$Q_m = I_n + L_n + H + LE \quad (7.1)$$

where Q_m is the energy flux available for melt, I_n and L_n are the net shortwave and longwave radiation fluxes, H is sensible heat, and LE is the latent heat flux (all in Wm^{-2}). The net shortwave radiation flux is equal to the incoming shortwave radiation (I_{in}) minus the shortwave radiation reflected (I_r) by the cliff surface, the latter controlled by the albedo of the cliff surface (α_i). The incoming shortwave radiation consists of a direct component (I_s) and the two diffuse fluxes from the sky (D_s) and the surrounding terrain (D_t). The net longwave radiation flux is equal to the incoming longwave radiation (L_{in}) minus the outgoing longwave flux (L_o) emitted from the cliff surface. The incoming longwave radiation is a combination of longwave radiation emitted from the sky (L_s) and from the surrounding debris surface (L_d). Details of the calculations of each flux can be found in Steiner et al. (2015). The energy balance is driven by hourly meteorological data. These are either assumed uniform over the cliff surface (air and surface temperature, relative humidity of the air and wind speed) or extrapolated to each grid cell (as for the radiation components) using an advanced radiation and shading modelling approach (Buri et al., 2016a,b) (Section 7.6.3). The modelling period is from 19 May to 22 October 2013, which corresponds to the dates of the 2013 UAV-flights (Immerzeel et al., 2014b), and covers an entire ablation season, including part of the pre-monsoon season (May–June), the monsoon season (mid June to mid September) and the post-monsoon season (mid September to October).

Horizon calculation

Radiation inputs to the cliff surface depend on the cliff's slope and orientation and their interaction with the surrounding topography (including shading). The radiation fluxes are calculated as in the original model described in Buri et al. (2016a,b). Here we provide a scheme (Fig. S7.8) that explains the calculation of the horizon angles for both the shortwave- and longwave radiation fluxes from the two DEMs (for close and distal topography). The horizon angles for longwave radiation emitted by the debris ($h_{\phi,d}$) and the sky ($h_{\phi,L}$) are calculated using the high-resolution UAV-DEM within 100m around the cliff. Computation of the solar radiation flux and its shading are based on the ASTER-DEM for a much larger area that includes also distant mountainous terrain starting at the moraine walls of Lirung Glacier.

Aspect filter

To avoid that unrealistic melt directions are generated from noise in the aspect values on the cliff surface a median filter with a window of size 9×9 cell ($51.84m^2$) is applied to the cliff area before every geometry update (Buri et al., 2016b).

Geometry update

Accumulated melt (d_{melt}) derived from Equation 7.1 is applied to all cliff cells at a time interval of two weeks (interval of one month in Buri et al., 2016b):

$$d_{xy} = d_{melt} \sin \beta, \quad d_z = d_{melt} \cos \beta, \quad (7.2)$$

$$d_x = d_{xy} \sin \gamma, \quad d_y = d_{xy} \cos \gamma \quad (7.3)$$

where d_z and d_{xy} (m) are the melt distances in vertical and horizontal direction Buri et al. (2016b). The latter is the resulting vector of the horizontal x- and y-components, d_x and d_y (m), respectively. The angles β and γ indicate slope and backazimuth ($\gamma = \text{azimuth} - 180^\circ$) of the cliff cell (see Fig. 6 in Buri et al. (2016b) for a scheme). Relict topography of former cliff position is removed as in Buri et al. (2016b).

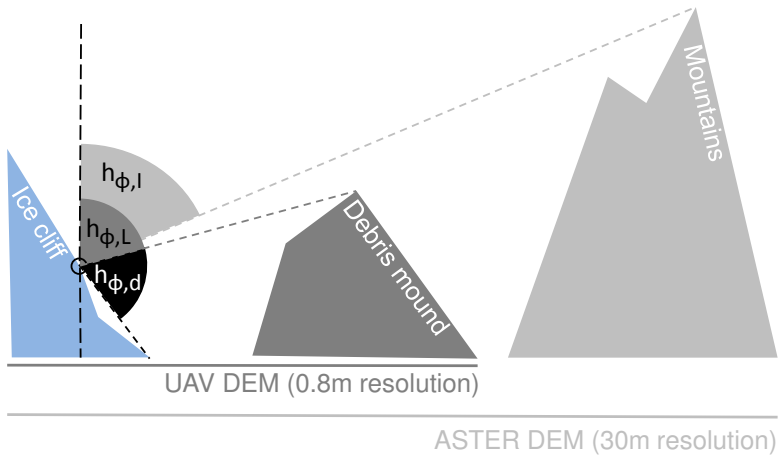


Figure 7.8.: Viewing angles for an ice cliff surface. The horizon angle for long-wave radiation, $h_{\phi,L}$, accounts for debris mounds within the extent of the rotated UAV-DEM (dark grey) and defines the visible sky fraction relevant for emitted radiation (for a specific point on the ice cliff, indicated by a circle, in one azimuth direction). Similarly, the viewing angle for shortwave radiation, $h_{\phi,I}$, accounting for local horizons within the UAV- and ASTER-DEM (light grey), defines the visible sky fraction relevant for solar radiation. Where a debris mound dominates the horizon of a point on the cliff, $h_{\phi,I}$ equals $h_{\phi,L}$. Both horizon angles are normalized by 90° and then summed and divided by 360° (considering all azimuth directions) to determine a single sky view factor for shortwave and longwave radiation ($V_{s,I}$ and $V_{s,L}$, all dimensionless). The debris view angle (black), accounting for the radiation emitted from the surrounding debris mounds is normalized by 90° and then summed and divided by 360° to determine a debris view factor (V_d) for each location on the cliff.

Cliff Outline Derivation

New cliff outlines need to be generated after every geometry update due to the changes in cliff geometry caused by the melt and backwasting of single cells. The single cliff cells can spread apart based on their melt vectors (length and direction defined by accumulated melt, slope and aspect), creating voids within the cliff area. We therefore applied an algorithm that redefines after every backwasting step a continuous ice cliff area. We slightly improved the cliff outline delineation implemented in the original model (Buri et al., 2016b): instead of the numerically more unstable α -shape method using convex hulls (Edelsbrunner et al., 2006) here buffers around cliff cells are applied. In the new algorithm, first a buffer of 1m width ($1.25 \times$ spatial resolution) of additional cliff area is added around all cliff's single coordinates. Second, after unifying all intersecting areas, an additional buffer of cliff area of 0.4m width ($0.5 \times$ spatial resolution) is used to reduce holes within the newly created cliff area. Third, a negative buffer of 0.8m width ($1 \times$ spatial resolution) is applied inside the cliff area to remove newly created area, resulting in a connected cliff polygon roughly covering the raster cells of the updated cliff points. All buffers were optimised to match observations of cliffs evolution. Using buffers instead of a convex hull approach has the main advantage that cliffs can separate in multiple parts and can exist and backwaste in parallel thereafter.

Backwasting model parameters

The model physical parameters which are difficult to measure or were not measured continuously in the field were assumed to be constant for both cliffs and over time in the model. The values for ϵ_i (emissivity of ice, 0.97), ϵ_d (emissivity of debris, 0.95) and z_0 (aerodynamic surface roughness length, 0.003m) were optimised in Steiner et al. (2015) and we use here the same values, while albedo values for ice (α_i , 0.2) and debris (α_d , 0.15) were derived from observations in the field (Steiner et al., 2015).

Reburial based on slope threshold

Reburial by debris of single cliff cells is simulated by prescribing a threshold slope value of 35° . Below this threshold cliff cells are assumed to be debris-covered, above ice free. This allows the cliff to expand or shrink dynamically after every

updating step and is an important implementation to reproduce the observed evolution of the cliffs (Buri et al., 2016b). The slope threshold is lowered by 5° from the value in the original model (Buri et al., 2016b) (from 40 to 35°), because of the different spatial resolution (slightly coarser) of the DEM we use here compared to the one in the original study (Buri et al., 2016b) that shifts the slope distribution towards lower values. To remove unrealistic step changes in the topography within the updated cliff area generated by the reclassification of cells due to the reburial, a median filter with a window of size $3 \times \text{cell}$ ($5.76m^2$) was applied to all elevation values within the cliff area, buffered by additional $3m$.

Debris view factor threshold

To suppress outgrowths of marginal cliff zones cutting unrealistically into adjacent debris slopes, a debris view factor threshold is implemented in the model, optimised against field observations (Buri et al., 2016b). The threshold value was increased from 0.45 as in the original model to 0.5 because of the coarser resolution. Cliff cells with debris view factors above this value are removed from the cliff area after every geometry update. For these cells, sky is visible only in 50% of their view field, hence these cells have a high probability to be exposed to reburial by the surrounding debris.

Glacier surface change

Subdebris melt on Lirung Glacier equal to a rate of $0.0049m d^{-1}$, based on off-cliff DEM-differencing between the May and October 2013 DEMs (Immerzeel et al., 2014b) of Lirung Glacier, is applied in the model to the glacier surface (excluding the cliff area) at every updating step Buri et al. (2016b). No glacier flow is implemented in the model as it is very low on the area of the tongue where the two cliffs are located (Immerzeel et al., 2014b; Buri et al., 2016b).

Pond influence zone

Thermo-erosional melt of supraglacial ponds has been demonstrated to have an important effect on cliffs' ice walls evolution (Driscoll, 1980; Watson, 1980; Pickard, 1983; Miles et al., 2016; Buri et al., 2016a; Brun et al., 2016; Buri et al., 2016b). The presence of ponded water adjacent to a cliff (in this case only

to Cliff 2) is considered in the model by using an enhanced melt rate at the cliff-pond contact. The subaqueous melt is set to $0.033m d^{-1}$, which equals the mean value obtained from energy balance modelling of the pond adjacent to Cliff 2 during the 2013 melt season (Miles et al., 2016). This additional melt rate is applied to the zone where the cliff area intersects the pond outline (and to an additional buffer area of 3m affected by the lake presence).

7.6.4. Extended results

Diurnal cycles of surface energy fluxes for cliffs 1 and 2 are presented in Fig. S7.9 for the original cliff position and aspect and rotated to eight additional aspects by increments of 45° . The diurnal cycles are averaged over the entire modelling period (May to October 2013) and spatially over each cliff area.

Whereas for the direct shortwave radiation component (I_s) large diurnal differences in terms of timing and amount are modelled for the different aspects (Fig. S7.9a), the diffuse shortwave radiation from the sky (D_s) and surrounding terrain (D_t) as well as the longwave radiation flux emitted by debris (L_d) show only very limited variations between aspects at the daily scale (Fig. S7.9b,c,f). The high variability in energy available for melt (Q_m , Fig. S7.9g) is a result of the predominance of I_s on the melt energy. Seasonal variations in the daily patterns of the energy fluxes are best evident in I_s (Fig. S7.10), which shows a strong change in the magnitude and timing of the diurnal maximum from pre- to post-monsoon, with differences depending on the predominant aspect. Cliffs facing northeast (and in less measure east) see a strong reduction in I_s (from more than $500 Wm^{-2}$) to about $300 Wm^{-2}$). Cliffs facing south on the opposite experience an increase in peak radiation from pre- to post-monsoon (Fig. S7.10a-c).

Maps of distributed incoming shortwave radiation (I_{in}) and melt energy (Q_m) at different times of the day for Cliff 1 are shown in Fig. S7.11, indicating large variability as a function of cliff orientation. The aspects that receive the highest amount of I_{in} in total are those between NE and S (Fig. S7.11c), but they shift considerably during the day, with highest receipts in the morning for easterly-facing cliffs and in late afternoon for westerly-facing cliffs (Fig. S7.11a). Again, the spatial pattern of shortwave radiation strongly affects the signal of total energy for melt (Fig. S7.11b). The sums of these fluxes averaged over 24 hours

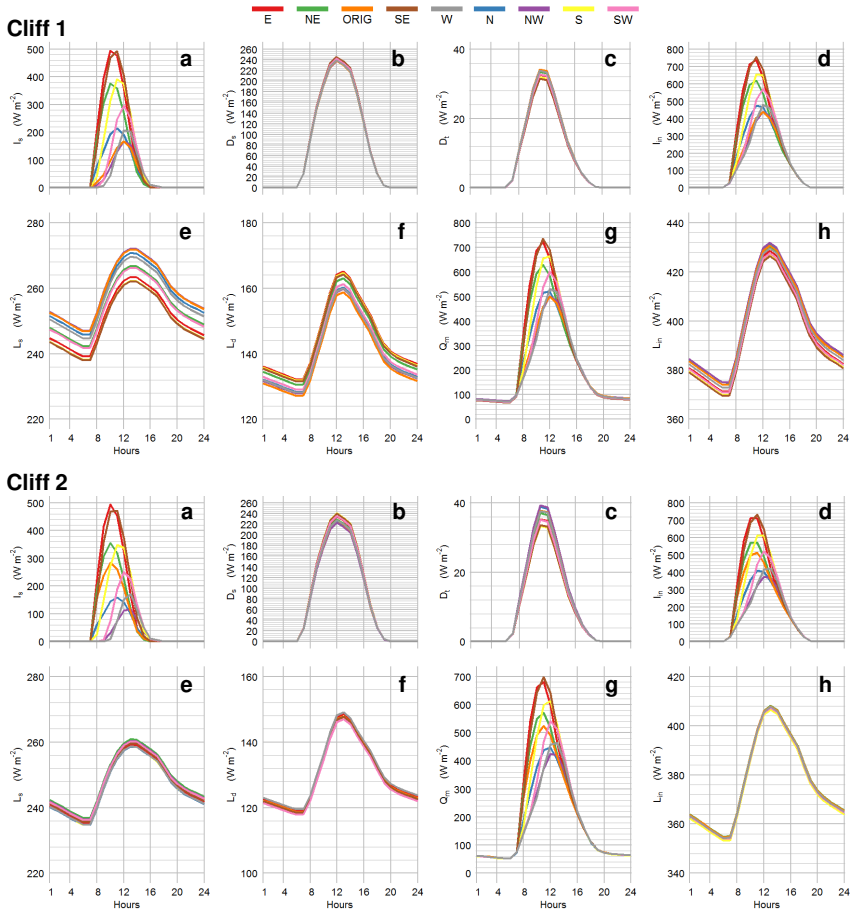


Figure 7.9.: Modelled surface energy fluxes averaged for cliffs 1 and 2 rotated to various aspects. Diurnal cycles (May-October 2013) of energy receipts (Wm^{-2}) averaged for Cliff 1 (top panel) and Cliff 2 (bottom panel) rotated to eight different aspects by increments of 45° . **a**, Direct shortwave radiation, I_s . **b**, Diffuse shortwave radiation from sky, D_s . **c**, Diffuse shortwave radiation from terrain, D_t . **d**, Total incoming shortwave radiation, I_{in} . **e**, Longwave radiation from sky, L_s . **f**, Longwave radiation from debris, L_d , **g**, Total melt energy, Q_m . **h**, Total incoming longwave radiation, L_{in} .

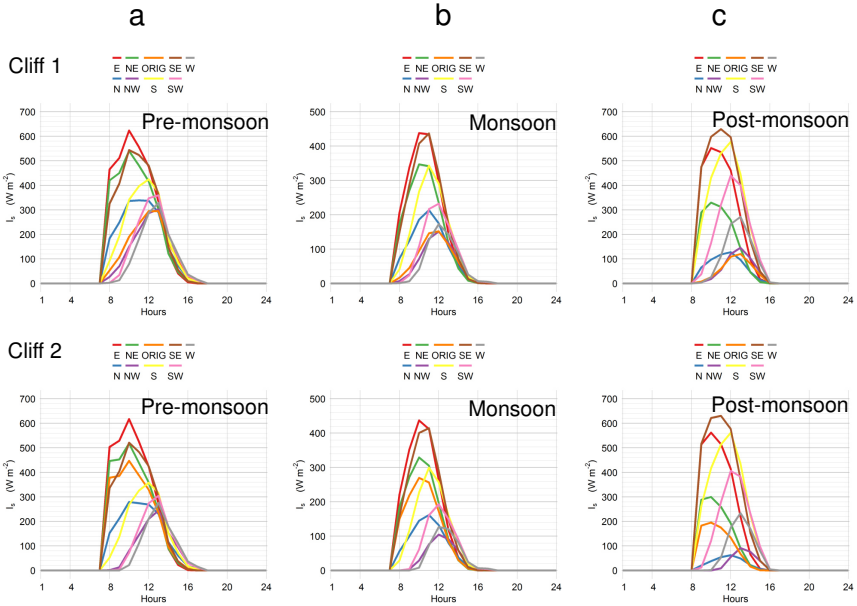


Figure 7.10.: Modelled seasonal direct shortwave radiation averaged for cliffs 1 and 2 rotated to various aspects. (a) Pre-monsoonal diurnal cycle (19 May – 14 June 2013) of direct shortwave radiation receipt (I_s) averaged for cliffs 1 (top) and 2 (bottom) rotated to eight different aspects by increments of 45° . **b**, Monsoonal diurnal cycle (15 June – 19 September 2013) of I_s averaged for cliffs 1 (top) and 2 (bottom) rotated to eight different aspects by increments of 45° . (b,c) Post-monsoonal diurnal cycle (20 September – 22 October 2013) of I_s averaged for cliffs 1 (top) and 2 (bottom) rotated to eight different aspects by increments of 45° .

(Fig. S7.11c–d) indicate that east to southeast aspects have the highest energy incomes throughout the day.

From Fig. S7.12c it is clear that the high amount of melt energy at cliffs with south-easterly orientations is a result of the high amount of I_s affecting these slopes. Whereas the shortwave radiation components show strong spatial variability among different cliff aspects, the spatial patterns of longwave radiation fluxes are basically independent of cliff orientation (Fig. S7.12a–b). Spatial variability of longwave radiation at the cliff scale is evident (Fig. S7.12a,b).

The mean coefficients of variation for I_s are highest for the west-facing cliff (238%, Tab. S7.1) and lowest for the east-facing cliff (146%), which are among the cliff surfaces receiving on average the lowest and highest amount of direct shortwave radiation (Tab. S7.2), respectively. The direct shortwave component is therefore the flux with the highest spatial variability among all fluxes but also shows the highest differences in spatial variability among all aspects.

L_d is strongly influenced by the debris-view factor V_d (Fig. S7.13b), with highest values at the marginal cliff zones (Fig. S7.12a). In contrast, $V_{s,I}$, the factor which defines the incoming diffuse shortwave radiation from the sky (D_s), shows a clear increase along the vertical cliff extent, indicating the highest amount of visible sky at the top sections of the cliff (Fig. S7.13a).

Shortwave radiation is the most important energy flux during the day at the observed northerly-facing cliffs 1 and 2 (Fig. S7.9d). The diffuse and direct components are the main contributors to the total incoming shortwave radiation (Tab. S7.2), and their relative importance varies with different aspects as for some aspects (N, W, SW and NW) the direct component is reduced through self-shading of the cliff (Buri et al., 2016a). Incoming longwave radiation (the sum of radiation emitted by the atmosphere and the debris-covered slopes) is the highest incoming flux to the cliff surface, higher than the total incoming shortwave radiation flux. It is however almost balanced out by the outgoing flux of longwave radiative energy emitted by the cliff surface (equal to $7349Wm^{-2}$ and constant over the cliff and per aspect). In addition, a large majority of that energy is available at night, when melt does not occur because of the total energy flux is negative Hock (2005).

The enhanced energy receipt at cliffs surfaces with aspects that expose them to the sun for most of the day is reflected in the persistence time of cliffs (Tab. S7.3). Cliff 1 disappears for all aspects except the original, a result that is plausible

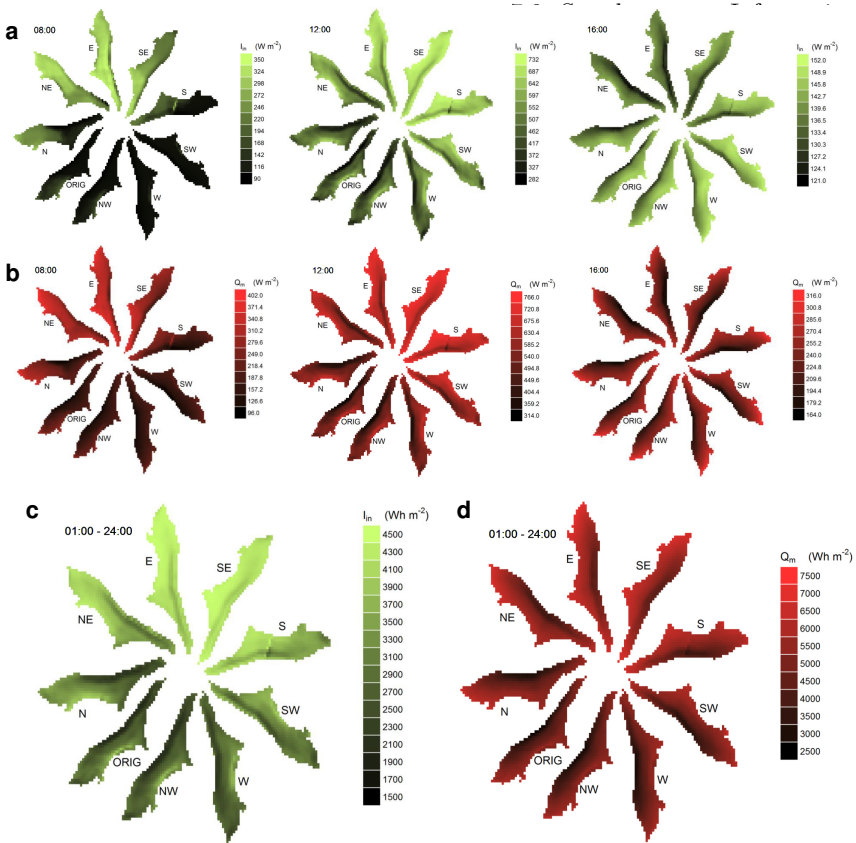


Figure 7.11.: Distributed energy fluxes for Cliff 1 rotated to various aspects. (a) Distributed incoming shortwave radiation averaged over melt season (May-October 2013) rotated to eight different aspects by increments of 45° (indicated by label at crest of each cliff), shown for hours 8 (left), 12 (middle) and 16 (right), respectively. (b) Distributed melt energy averaged over melt season (May-October 2013) rotated to eight different aspects by increments of 45° , shown for hours 8 (left), 12 (middle) and 16 (right), respectively. (c) Distributed daily sum (averaged May-October 2013) of incoming shortwave radiation. (d) Distributed daily sum (averaged May-October 2013) of melt energy.

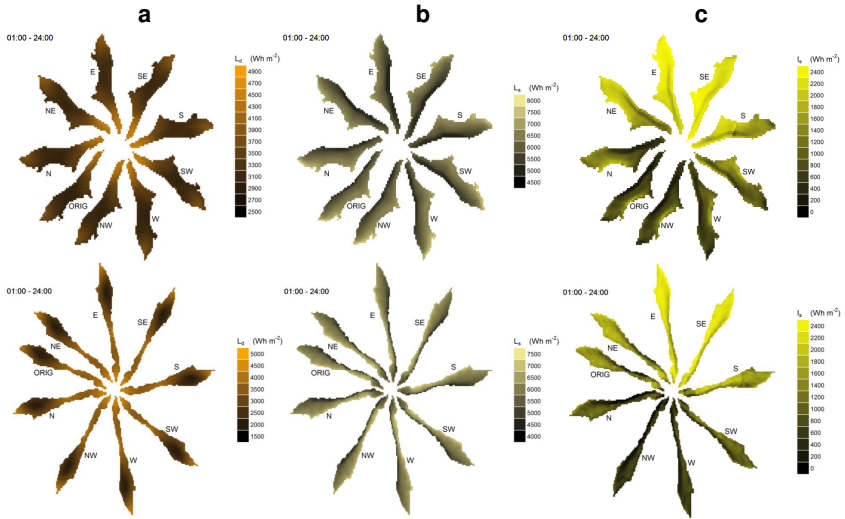


Figure 7.12.: Distributed energy fluxes for cliffs 1 and 2 rotated to various aspects. (a) Distributed longwave radiation from debris averaged over melt season (May-October 2013) at Cliff 1 (top) and Cliff 2 (bottom) rotated to eight different aspects by increments of 45° (indicated by label at crest of each cliff). (b) Distributed longwave radiation from sky averaged over melt season (May-October 2013) at Cliff 1 (top) and Cliff 2 (bottom). (c) Distributed direct shortwave radiation averaged over melt season (May-October 2013) at Cliff 1 (top) and Cliff 2 (bottom).

Table 7.1.: Coefficients of variation for all positive fluxes of entire Cliff 2 per aspect from diurnal cycles averaged from May to October 2013 for direct shortwave radiation (I_s), diffuse shortwave radiation from sky (D_s), diffuse shortwave radiation from terrain (D_t), net shortwave radiation (I_n), total incoming shortwave radiation (I_{in}), longwave radiation from sky (L_s), longwave radiation from debris (L_d), sensible heat flux (H), total melt energy (Q_m), daily melt rate ($Melt$) and total incoming longwave radiation (L_{in}).

Aspect	I_s	D_s	D_t	I_n	I_{in}	L_s	L_d	H	Q_m	Melt	L_{in}
ORIG	1.857	0.359	0.524	0.529	0.529	0.105	0.062	0.629	0.441	0.398	0.073
N	1.871	0.359	0.524	0.517	0.517	0.105	0.062	0.629	0.436	0.390	0.073
E	1.462	0.359	0.524	0.540	0.540	0.105	0.062	0.629	0.450	0.407	0.073
S	1.605	0.359	0.524	0.537	0.537	0.105	0.062	0.629	0.442	0.395	0.073
W	2.382	0.359	0.524	0.480	0.480	0.105	0.062	0.629	0.415	0.372	0.073
NE	1.843	0.359	0.524	0.530	0.530	0.105	0.062	0.629	0.443	0.401	0.073
SE	1.480	0.359	0.524	0.554	0.554	0.105	0.062	0.629	0.453	0.409	0.073
SW	2.252	0.359	0.524	0.501	0.501	0.105	0.062	0.629	0.424	0.380	0.073
NW	1.907	0.359	0.524	0.469	0.469	0.105	0.062	0.629	0.414	0.370	0.073

Table 7.2.: Total positive fluxes of entire Cliff 2 per aspect as sum from diurnal cycles averaged from May to October 2013 for direct shortwave radiation (I_s), diffuse shortwave radiation from sky (D_s), diffuse shortwave radiation from terrain (D_t), net shortwave radiation (I_n), total incoming shortwave radiation from sky (D_s), longwave radiation from sky (L_s), longwave radiation from debris (L_d), sensible heat flux (H), total melt energy (Q_m), daily melt rate ($Melt$) and total incoming longwave radiation (L_{in}), all in $W m^{-2}$ (fluxes) or m (melt).

Aspect	I_s	D_s	D_t	I_n	I_{in}	L_s	L_d	H	Q_m	Melt	L_{in}
ORIG	1293	1679	227	2559	3199	5942	3113	254	4520	0.054	9055
N	780	1656	233	2135	2669	5908	3113	254	4062	0.049	9021
E	2136	1734	212	3265	4082	5919	3126	254	5217	0.063	9046
S	1556	1777	200	2826	3533	5910	3107	254	4749	0.057	9017
W	591	1682	226	2000	2500	5910	3135	254	3951	0.048	9045
NE	1558	1695	223	2780	3476	5960	3098	254	4744	0.057	9058
SE	2158	1771	202	3305	4131	5931	3108	254	5250	0.063	9039
SW	947	1738	211	2317	2896	5945	3092	254	4260	0.051	9037
NW	469	1645	236	1880	2350	5949	3099	254	3834	0.046	9048

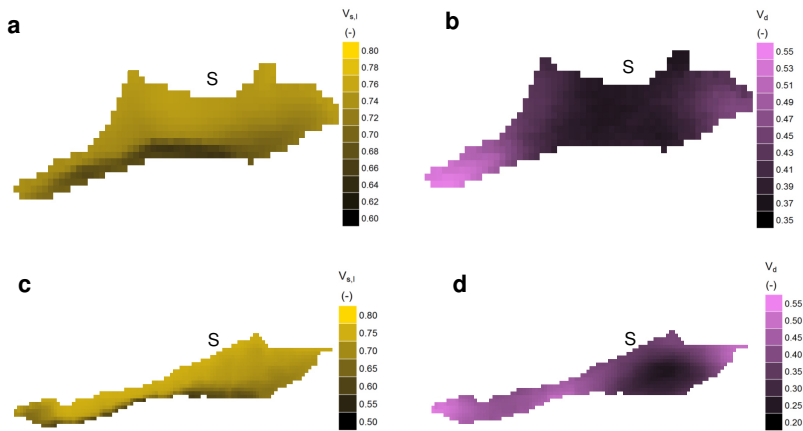


Figure 7.13.: Map of view factors for cliffs 1 and 2 rotated to a southern aspect. (a) Map of sky view factor for shortwave radiation calculated for south-facing Cliff 1. (b) Map of debris view factor for longwave radiation calculated for south-facing Cliff 1. (c) Map of sky view factor for shortwave radiation calculated for south-facing Cliff 2. (d) Map of debris view factor for longwave radiation calculated for south-facing Cliff 2.

Table 7.3.: Survival period of cliffs 1 and 2 rotated to various target aspects. Simulation period is one melt season (3768 hours / 157 days, counted from the start of the simulations, on 19 May 2013). The values show for each aspect until when the cliff was still existing.

Aspect	Cliff 1		Cliff 2	
	(hours)	(days)	(hours)	(days)
ORIG	3768	157	3768	157
N	2712	113	3768	157
NE	2712	113	3768	157
E	2376	99	3384	141
SE	2040	85	3768	157
S	2040	85	3384	141
SW	2712	113	3768	157
W	3384	141	3768	157
NW	3384	141	3768	157

because the original aspect is the one corresponding to the smallest shortwave radiation flux and melt energy (Fig. S7.11c–d) and in reality Cliff 1 shrank and flattened during the melting season (Fig. S7.10a–b), and it disappeared in the next year. Cliff 2 disappears completely before the end of the melt season only for east- to south-facing orientations, which correspond to the largest energy available for melt (Tab. S7.2), and survives the duration of the ablation season for all other aspects, a fact confirmed by the observations in the field (Buri et al., 2016b).

Chapter 8.

Modelling the contribution of supraglacial ice cliffs to the mass-balance of glaciers in Langtang Valley



Figure 8.1.: Heterogeneous debris-covered surface of the lower part of Langtang Glacier, with its lowest tributary in the background. Peak of Gangchempo (6387m a.s.l.) on the right (Oct. 2015).

8.1. Overview

The contribution of supraglacial ice cliffs to the total mass balance of a glacier has never been quantified, and all inference so far has been obtained from upscaling results of point-scale models or observations at selected individual cliffs to the glacier scale (Chapter 1.2.3).

Here we applied the 3D, physically-based cliff backwasting model described in Chapters 6 and 7 to the entire cliff population of each of the four main debris-covered glaciers in Langtang Valley: Lirung, Shalbachum, Langshisha and Langtang Glacier (Fig. 8.2 and Fig. 5.2 in Chapter 2; Tab. C.1 in Appendix C). The model simulates ice cliff backwasting by considering the cliff-atmosphere energy-balance, reburial by debris and the effects of adjacent ponds, and is described in detail in Chapter 7 and has been tested and validated extensively on Lirung Glacier (6 and 7). The model is forced with data from on and off-glacier AWSs extrapolated to each glacier and cliff location.

To estimate the contribution of supraglacial ice cliffs melt to the total glacier melt, a reference total glacier mass balance is needed. For this, we use simulations from a hydrological model (TOPKAPI-ETH (Ragettli et al., 2015, Chapter 1.2.4) applied to the Langtang catchment, which calculates glacier mass balance for each of the catchment glaciers (location of glaciers within catchment Fig. 8.2) in a distributed way. TOPKAPI provides accurate first order estimates of total glacier mass balance. An overview of the model setup used in this study is given in Tab. 8.3, and for details of the model setup, calibration and validation, we refer to Ragettli et al. (2015), where the model was calibrated and validated with an extensive, unique data set of satellite observations, ground glacio-meteorological data and runoff records.

8.2. Data

Topographic data input

Remote-sensing topographic input for the ice cliff model was provided by the high resolution SPOT6-DEM (3m spatial resolution, tri-stereo mode) from 21 April 2014 (Ragettli et al., 2016a), covering the entire Langtang Catchment except the upper part of Langtang Glacier (due to cloud cover). The missing section was replaced by the SPOT7-DEM (3m spatial resolution, tri-stereo mode) from 6 October 2015 (Ragettli et al., 2016a) for the model runs on Langtang Glacier.

Although a product from May 2015 was available as well, this was not used for this study as the surface of most of the higher elevated glacier parts was snow covered and therefore not useful for our mostly visually-based ice cliff delineation approach. For the off-glacier topography, which is relevant for the shading patterns on the cliff surfaces, the ASTER-GDEM2 (ASTER, 2009) with a spatial resolution of 1 arc second (30m) was used. Due to the large amount of raster cells stored when applying the cliff melt model at the glacier scale, the initial DEMs and thus all simulation steps have to be computed separately for smaller glacier sections. Therefore an algorithm partitioning each study glaciers into separate sections was applied (described in Appendix B and Fig. B.1). The high-resolution orthoimages (1.5m spatial resolution, Ragettli et al., 2016a) covering the entire catchment, were combined according to the SPOT-DEM2s used for this study (SPOT6 April 2014 and SPOT7 October 2015) for the same point in time and used to identify ice cliffs and supraglacial ponds manually. To ensure an unbiased manual delineation of cliffs and ponds, we implemented a four-step process including three different persons: One person manually delineated all ice cliffs and ponds, a second person checked the complete inventory visually. The first person then used an algorithm described in Miles et al. (2017b) to identify water surfaces from the thermal band of Landsat images and compared it to the lake inventory to add water bodies that were visually difficult to determine because of similar color as the surrounding terrain. A third person then used the inventory and compared it to slope maps without seeing the orthophotos. Using this the person indicated false positives and false negatives, mainly for cliffs. Using these suggestions the first person rechecked the complete inventory and updated where necessary. Due to the relatively coarse resolution of the orthoimages a confident identification of all ice cliffs, and to a lesser extent also of the ponds, was not always possible. Although e.g. slope patterns at the location of potential ice cliffs often clearly indicated the presence of a steep slope potentially prone to be ice free, sometimes no evidence could be revealed from visual checking of the corresponding locations. In cases where visual verification of assumed ice cliffs failed, we discarded corresponding features. Therefore the dataset of cliff and pond outlines we used can be seen as a conservative inventory, resulting in a rather lower boundary of ice cliff contribution to glacier mass balance. Initial conditions for TOPKAPI-ETH were based on the SPOT6/SPOT7-DEM com-

Table 8.1.: Stations used to force the cliff model with meteorological data (AWSs) and for testing environmental lapse rates (T-Loggers). Short-names: Lirung Glacier (LIR), Shalbachum Glacier (SHA), Langshisha Glacier (LSH) Langtang Glacier (LGT), Kyanjing Gompa (KYA, off-glacier) and Jathang (JAT, off-glacier).

Instr.	Loc.	Elev. (m)	N (°)	E (°)	Data cov. 2014
AWS	KYA	3857	28.21081	85.56948	01/01 – 09/10
T-Logger	JAT	3906	28.19563	85.61321	01/01 – 12/10
AWS	LIR	4076	28.23260	85.56213	04/05 – 03/11
T-Logger	SHA	4305	28.21538	85.66067	10/05 – 27/10
T-Logger	LSH	4450	28.19538	85.69230	01/01 – 31/10
AWS	LGT	4557	28.23891	85.70196	11/05 – 27/10

posite similar to the topographic input for the ice cliff model, but aggregated to a spatial resolution of 30m.

Meteorological data input

Meteorological data used to force the ice cliff model was provided by automatic weather stations on- and off-glacier within Langtang Valley (Figs. 8.2 and 5.2 and Tab. 8.1). The period in which all relevant sensors in Langtang Valley recorded continuous sub-hourly data (5 to 12 minute intervals which are then aggregated to hourly data) during the 2014 melt season starts on 11 May (AWS Langtang initialized) and ends on 9 October 2014 (AWS Kyanjing, KYA, was last read out on that day before the devastating Gorkha Earthquake in 2015; e.g Kargel et al., 2015). During this about 5 month period (150 days) all sensors worked properly without any data gaps, except for 5 consecutive days (18–23 June 2014, Fig.C.2) where AWS Kyanjing was temporally not recording data. The 5-day data gap was filled with air temperature data recorded at the closest off-glacier sensor, Jathang T-Logger (JAT, about 5km linear distance up the valley, see Fig. 8.2 for location and Fig. C.1 for instrument example), applying the environmental lapse rates from Heynen et al. (2016). TOPKAPI-ETH was forced by meteorological data from AWS KYA for the same simulation period (Ragettli et al., 2015).

One important meteorological parameter in terms of ice cliff melt is air temperature. In our ice cliff model approach, a time series of air temperature for each ice cliff according to the cliffs' median elevation as observed in the April 2014 DEM (October 2015 for upper Langtang Glacier) was applied. For cliffs located on Lirung and Langtang Glacier, the time series of hourly air temperature data was

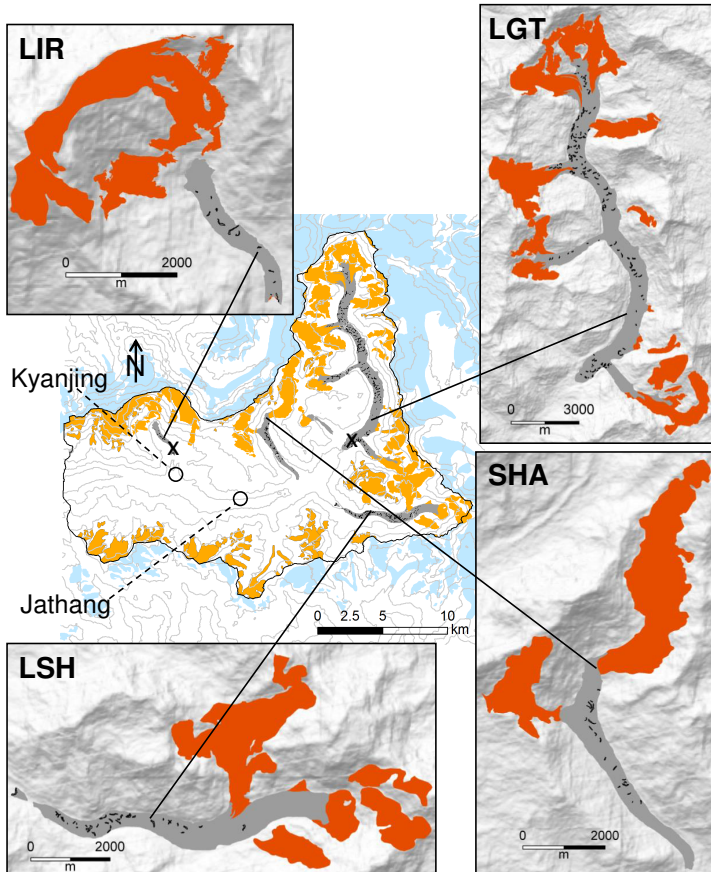


Figure 8.2.: Catchment-scale map of upper Langtang Valley (central map) and glacier-scale maps (marginally aligned) of four debris-covered glaciers as observed in April 2014. Glacierized area is shown in blue and yellow in the central map for glaciers outside and inside the catchment. Debris-cover is drawn in grey, manually delineated ice cliffs are indicated in black. The catchment boundary is indicated in black. The insets show the four study glaciers Langshisha- (LSH), Shalbachum (SHA), Langtang- (LGT) and Lirung Glacier (LIR), with debris-free areas shown in orange and debris-covered tongues in grey. Kyanjing and Jathang indicate the locations of two off-glacier stations used for model testing, crosses on Lirung- and Langtang Glacier indicate sites of on-glacier AWSs. Hillshade rasters in the background are produced from 30m SPOT6-DEMs fro April 2014 (upper Langtang Glacier: SPOT7-DEM).

lapsed directly from their specific on-glacier AWSs (LIR and LGT , Tab. 8.1), using the seasonal environmental lapse rates derived on debris-covered Lirung Glacier for 2014 by Steiner and Pellicciotti (2016) (Tab. C.3, Glacier lapse rates). Air temperatures for ice cliffs modelled on Shalbachum and Langshisha Glacier were lapsed from the off-glacier AWS KYA (Tab. 8.1). To bridge the elevation difference between KYA and the glacier terminus the seasonal environmental off-glacier lapse rates derived for Langtang Valley in 2013 by Heynen et al. (2016) (Tab. C.3, Valley lapse rates) were used and for the on-glacier difference in altitude the lapse rates by Steiner and Pellicciotti (2016) (Tab. C.3, Glacier lapse rates) were applied. Figs. 8.3 and 8.4 show measured and lapsed timeseries and diurnal cycles of air temperature for Langshisha Glacier, compared to AWS KYA (comparisons for the other three glaciers are shown in the Appendix C.1). In this study, two sets of environmental lapse rates for air temperature were used as meteorological forcing for the cliff model: 1) for the elevation difference between KYA and each individual glacier terminus the seasonal environmental off-glacier lapse rates derived for Langtang Valley in 2013 by Heynen et al. (2016) (Tab. C.3, Valley lapse rates) were applied; 2) for the on-glacier difference in altitude seasonal lapse rates by Steiner and Pellicciotti (2016) (Tab. C.3, Glacier lapse rates) were used. An extensive analysis of measured and modelled (lapsed) air temperatures in Langtang Valley, showing time series over the entire melt season and diurnal cycle of all stations is shown in Chapter C.1.

Steiner and Pellicciotti (2016) observed a relation between air and surface temperature exhibiting two segments with distinct slopes, based on distributed long-term measurements on Lirung Glacier in 2012 to 2014. Following Hudson (1966) they fitted piece-wise regression lines to the air and surface temperature observations at each T-Logger location (example in Fig. C.15 from Fig. 12 in Steiner and Pellicciotti, 2016). The median slopes and intercepts derived for the 2014 season on Lirung Glacier (Tab. C.4 from Tab. 3 in Steiner and Pellicciotti, 2016) were applied to all glaciers in our study (except Lirung Glacier, where surface temperature recordings were available for 2014) based on measured on-glacier air temperatures (Langtang Glacier) or lapsed air temperatures from KYA. In Fig. 8.5 the timeseries of surface temperature derived from measured air temperature is shown for all four study glaciers. Time series and diurnal cycles of recorded and modelled surface temperatures are shown in Chapter C.2.

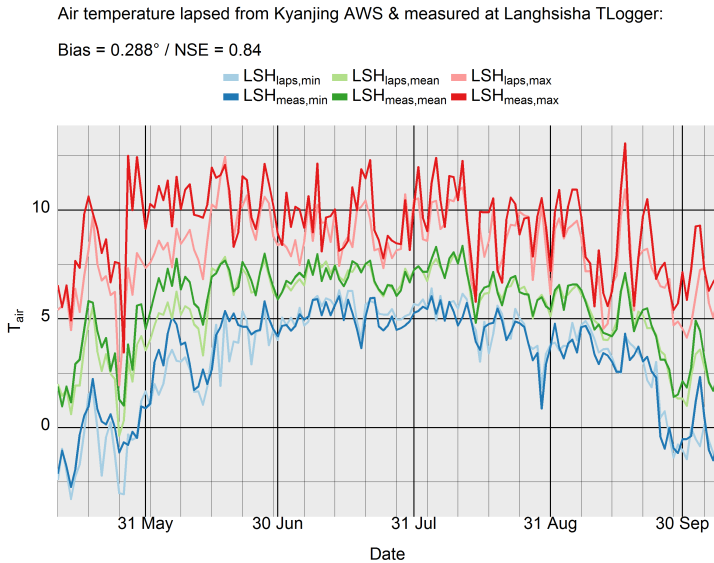
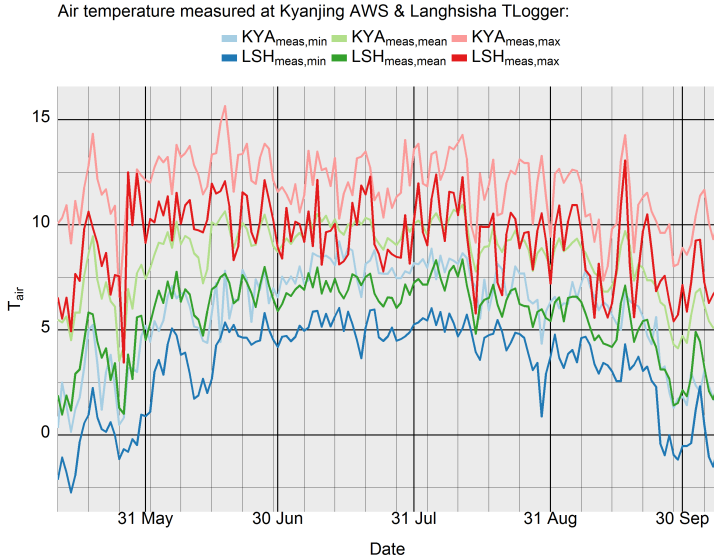


Figure 8.3.: Timeseries of daily minimum, mean and maximum air temperature as measured at Kyanjing AWS (KYA) and Langhsisha T-Logger (LSH) in 2014 (top) and as measured at LSH and lapsed to LSH from KYA (bottom). Gridlines on x-axis indicate weekly (thin) and monthly intervals (thick). ‘Bias’ and ‘NSE’ show the bias of the lapsed values from the measured data and the Nash-Sutcliffe efficiency (Nash and Sutcliffe, 1970), respectively, both based on hourly temperature data.

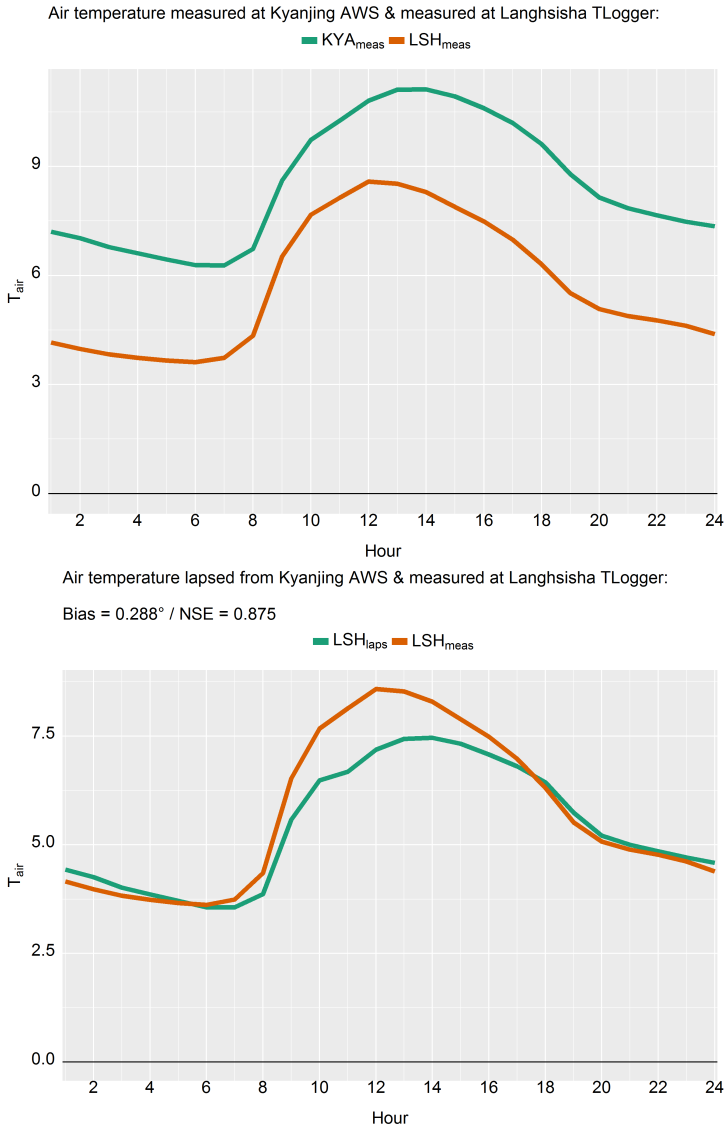


Figure 8.4.: Diurnal cycle of hourly air temperature as measured at Kyanjing AWS (KYA) and Langshisha T-Logger (LSH) in 2014 (top) and as measured at LSH and lapsed to LSH from KYA (bottom). ‘Bias’ and ‘NSE’ show the bias of the lapsed values from the measured data and the Nash-Sutcliffe efficiency (Nash and Sutcliffe, 1970), respectively, both based on hourly temperature data.

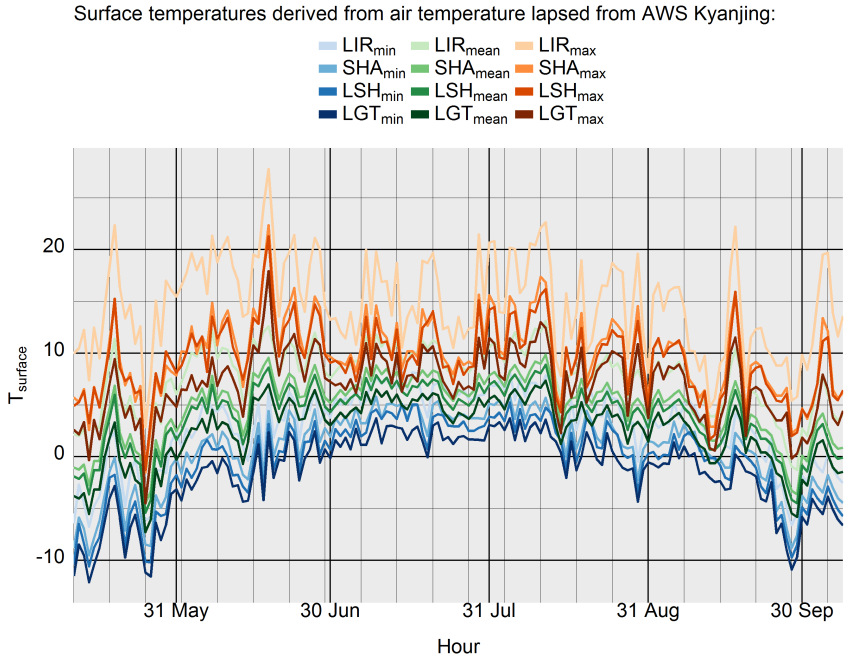


Figure 8.5.: 2014-timeseries of daily minimum, mean and maximum surface temperature as derived from lapsed air temperature from Kyanjing AWS (KYA) to the specific station locations on Lirung-, Shalbachum-, Langshisha- and Langtang Glacier (LIR, SHA, LSH, LGT). Grid-lines on x-axis indicate weekly (thin) and monthly intervals (thick).

Shortwave radiation was measured on-glacier at AWSs Lirung and Langtang. The latter dataset of solar radiation was also applied to the other two study glaciers up-valley, Shalbachum- and Langshisha Glacier without any correction. Diurnal cycles of measured and potential clear-sky incoming shortwave radiation recorded at the two on-glacier stations (LIR and LGT) and at the off-glacier AWS KYA are shown in Fig. 8.6, both for the entire melt season and subset to the three subseasons (pre-monsoon, monsoon and post-monsoon, defined according to Heynen et al., 2016 and Tab. C.2). Comparisons of the timeseries of solar radiation measured at the three stations in the valley, including derivation of cloud factors and comparison to potential clear sky irradiance (relevant for longwave radiation), is shown in Chapter C.3.

Longwave radiation was only measured on-glacier at Lirung AWS in 2014, therefore incoming longwave radiation was modelled as described in Steiner (2014) and Steiner et al. (2015), using the Stefan-Boltzmann relationship as

$$L_{in} = \epsilon_{eff} \sigma T_a^4 \quad (8.1)$$

where ϵ_{eff} is the effective emissivity of the sky, σ the Stefan-Boltzmann constant and T_a the measured air temperature (K). The sky emissivity was determined with distinct parameterizations for clear sky (Dilley and O'Brien, 1998) and cloudy sky (Unsworth and Monteith, 1975), a combination which has been found to provide the best results in a study comparing different models of longwave radiation (Juszak and Pellicciotti, 2013). Steiner (2014) and Steiner et al. (2015) calibrated (2013) and validated (2012) the model with measurements of longwave radiation at AWS Kyanjing for each season separately. The parameters conducted for Lirung Glacier for the 2013 sub-seasons (Steiner (2014); Steiner et al. (2015)) were applied to the study glaciers without longwave radiation records, using either measured (Langtang Glacier) or lapsed T_a and rH_{air} (Shalbachum- and Langshisha Glacier). A comparison of measured and modelled incoming longwave radiation is shown in Fig. 8.7 and in Chapter C.4.

Since the relationship of (rH_{air}) with altitude is poorly documented at present (Miles, 2016), rH is applied in the model without correction to all cliffs on a glacier, as measured at Lirung AWS for cliffs on Lirung Glacier and as measured at Langtang AWS for all the other cliffs. Diurnal cycles of relative air humidity as measured at the three AWSs for the entire melt season and subset to three

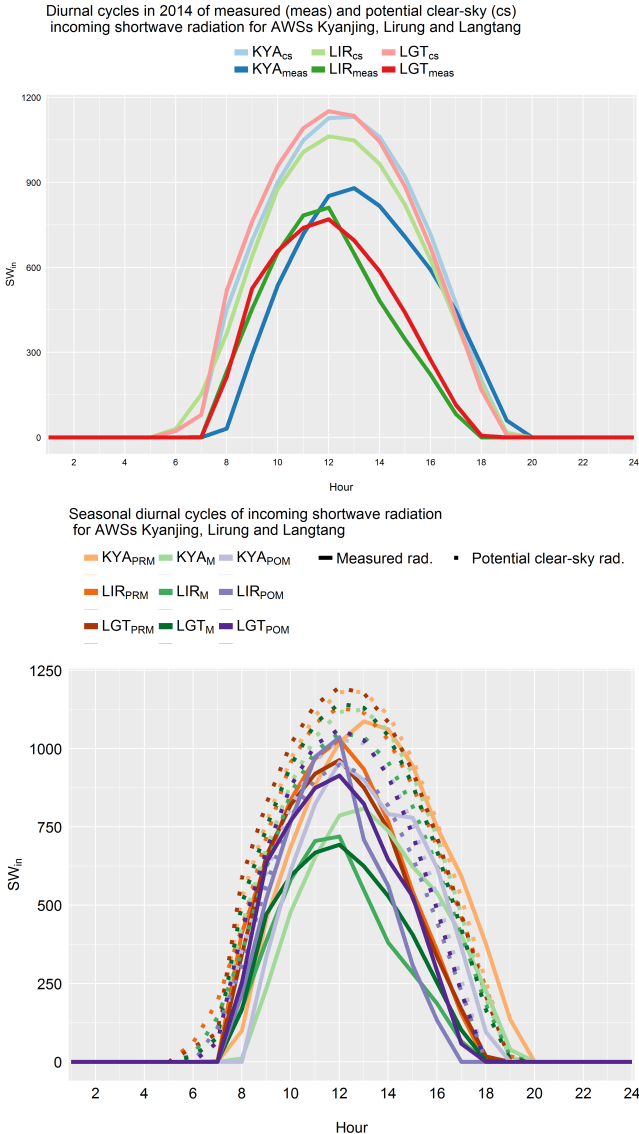


Figure 8.6.: All year (top) and seasonal diurnal cycles (bottom) for pre-monsoon (PRM), monsoon (M) and post-monsoon (POM) of hourly incoming shortwave radiation as measured at AWSs Kyanjing (KYA), Lirung (LIR) and Langtang AWS (LGT) in 2014. Potential clear-sky solar radiation is also indicated (top: pale colours; bottom: dotted lines).

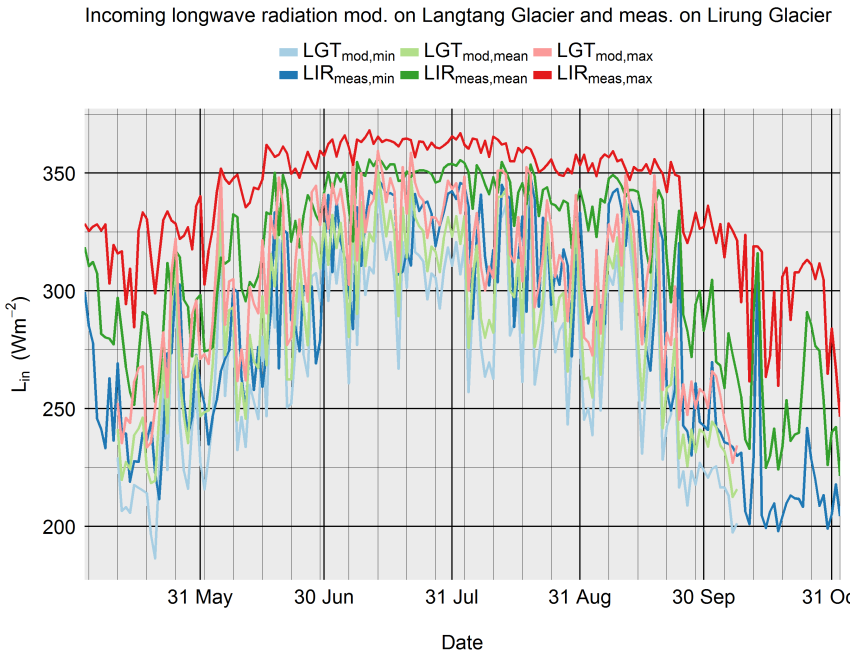


Figure 8.7.: Timeseries of daily minimum, mean and maximum incoming longwave radiation as modelled at Langtang AWS (LGT) and measured at Lirung AWS (LIR). Gridlines on x-axis indicate weekly (thin) and monthly intervals (thick).

subseasons are shown in Fig. 8.8 of relative air humidity and a timeseries is shown in Chapter C.5.

8.2.1. Model application and testing

An overview about the models used in this study, their spatial domain and relevant output is shown in Tab. 8.3. The same model as described in chapter 7 was used to simulate ice cliff melt at the glacier scale, but as the spatial resolution decreased considerably from sub-meter to 3m, few model parameters had to be varied accordingly.

In order to assess the impact of the coarser spatial resolution on the model results, we performed four main test simulations on selected ice cliffs which were within the extent of the UAV-surveys in May 2014 (Kraaijenbrink et al., 2016) and thus covered by submetre-DEM data (Chapter D):

1) Firstly, ice cliff backwasting and associated ice volume losses for one cliff on Lirung Glacier (“Cliff 2” as named in Steiner et al., 2015; Buri et al., 2016a; Brun et al., 2016; Buri et al., 2016b) was simulated by varying the spatial resolution of the UAV-DEM from 0.8m to 3m and 5m (Chapter D.1). We derived ice volume losses and several geometric parameters over time for each spatial resolution. Further we compared the simulated ice cliff outlines (horizontal extent) and vertical cliff profiles with the observed outlines and profiles.

2) Secondly, we tested the effect of different initial DEMs (UAV resampled to 3m spatial resolution and original SPOT6) on the resulting ice cliff volume loss, outline and vertical profile (Chapter).

3) The effect of the (negative) buffer size as part of the automatic ice cliff outline algorithm after geometry updates during the melt season (first scheme in Chapter D.3), was tested on both UAV- and SPOT6-based initial conditions (3m spatial resolution). Resulting ice cliff volume loss, outline and vertical profile were analyzed.

4) Finally, an assessment on how the slope threshold influences the simulated ice cliff backwasting was performed. This model parameter defines below which surface gradient an ice cliff area will be reburied by debris, and therefore influences the expansion or shrinkage of ice cliff shapes. The effect of the critical slope was tested using threshold of 30 and 35° (Chapter D.4).

The test runs helped to select the final parameter set for the simulations at the glacier scale: the negative buffer for the cliff outline algorithm was defined as

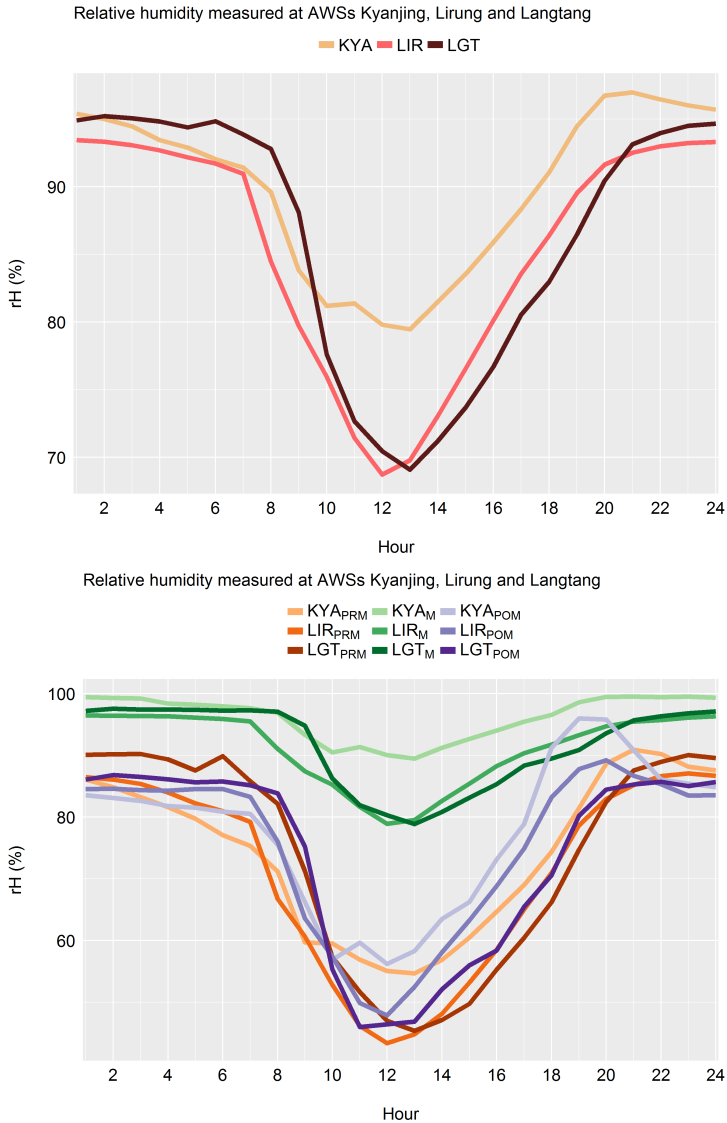


Figure 8.8.: All year (top) and seasonal diurnal cycles (bottom) for pre-monsoon (PRM), monsoon (M) and post-monsoon (POM) of hourly relative air humidity as measured at AWSs Kyanjing (KYA), Lirung (LIR) and Langtang (LGT) in 2014.

Table 8.2.: Buri2017

, resulting in cliff outlines, cliff volume loss and vertical profiles for each test run.] Numerical experiments (Chapter D) using the ice cliff melt model (Buri and Pellicciotti, in revision), resulting in cliff outlines, cliff volume loss and vertical profiles for each test run, in order to test the effects of spatial resolution (a), initial DEMs (b), the buffer size in the cliff delineation algorithm (c; see description of algorithm in Chapter 7.6.3) and the slope threshold to separate debris-free and debris-covered surfaces (d; see description of algorithm in Chapter 7.6.3).

	Numerical experiment	Tested	Appendix
a)	Spatial resolution	0.8m, 3.0m, 5.0m	D.1
b)	DEM-quality	UAV-DEM, SPOT6-DEM	D.2
c)	Buffer size	1.5m, 2.0m, 2.5m, 3.0m	D.3
d)	Slope threshold	30°, 35°	D.4

1.5m (3m the study described in Chapter 7) and the slope threshold remained at 35°.

Not shown are tests on the debris view factor threshold, a parameter to suppress outgrowths of marginal cliff sections cutting unrealistically into adjacent debris slopes. The coarser spatial resolution of the DEM used in the glacier scale approach largely reduces the spatial variability of debris view factors across a single cliff. Therefore the selection of a specific threshold value, used to discard single ice cliff cells at the cliff margin (Chapters 6 and 7), in our test runs affected either none or a large part of all cliff cells. The debris view factor threshold was therefore unable to modify the cliff in a realistic way for the model approach used here and we switched this parameter off.

Accumulated melt derived from energy balance modelling is applied to all cliff cells at a time interval of roughly 3 months (interval of one month in the study described in Chapter 6, interval of two weeks in the study described in Chapter 7). This is an effect of the coarser spatial resolution based on the DEM used in this model approach. A higher update interval would cause numerical instabilities as in general the horizontal melt distance of single ice cliff cells is below the cell size of the grid (3m).

Table 8.3.: Overview of the spatial domain and model outputs for the cliff model used in this Chapter compared to the hydrological model used to estimate the glacier-scale mass balance for the four glaciers in the catchment.

Model domain	Area the model is applied to	Relevant model output
Cliffs <i>(Buri and Pellaciotti, in revision; Chapter 7)</i>	Catchment scale (all cliffs on each glacier)	Melt associated to ice cliffs (spatially distributed)
TOPKAPI-ETH <i>(Ragetti et al., 2015; Chapter 1.2.4)</i>	Glacier scale (entire glacier)	Total glacier mass balance

8.3. Results and discussion

The results of the ice cliff melt simulations from May to October 2014 show the dominant role of Langtang Glacier compared to the other glaciers in the catchment, both in terms of initial (inclined) area and cumulative volume loss (Fig. 8.9, averaged or summed per glacier). This is mainly due to the size of the debris-covered tongues of these glaciers. In the case of Langtang Glacier, its surface covered by a continuous debris mantle is about 14.2 (Lirung Glacier) to about 3.5 times (Langshisha Glacier) bigger than the debris extent of the other study glaciers (Tab. C.1). This difference in size is also reflected in the number of supraglacial ice cliffs per glacier: Langtang Glacier encounters a total number of 138 features distributed on an elevation range from roughly 4485 to 5095 m a.s.l., while on Lirung Glacier the 15 ice cliffs are distributed from 4010 at the glacier terminus to 4265 m a.s.l.. Shalbachum (18 ice cliffs, ranging from 4410 to 4675 m a.s.l.) and Langshisha (35 ice cliffs, ranging from 4380 to 4915 m a.s.l.). Surprisingly the cliff area on all glaciers is reduced dramatically, referring to a potential tendency of the model algorithm to reduce the cliff area after the geometry update in the middle of the melt season too strongly. However, this has no effect on the volume loss- and melt estimates as these are derived based on the cliff geometry as it is before the melt-related geometry adaption. This would need more attention in case the ice cliffs are modelled for more than one melt season. Related to the clear shrinkage signal in terms of ice cliff area, the slope values averaged over all cliffs per glacier follow a fairly similar pattern among each other, with a decrease to 27° after the first geometry update and a tendency towards steeper cliff slopes again at the end of the model period. The model seems to slightly force the initially different shapes towards a more common cliff geometry. Contrastingly, the average cliff on Langtang Glacier shows a different behaviour with a continuous flattening. The cumulative volume loss of the ice cliffs, derived by considering the melt vectors of all single cliffs, show a rather stable increase over the simulated period. Only Langtang Glacier shows a slight break-point at the time when the geometry update is induced. As there is only one geometric correction possible due to the spatial resolution of the DEM the temporal signal of the volume loss caused by ice cliffs can only be separated into two periods, which correspond roughly to pre- and early monsoon (first period) as well as late and post-monsoon seasons (second period). This seasonal separation is visible

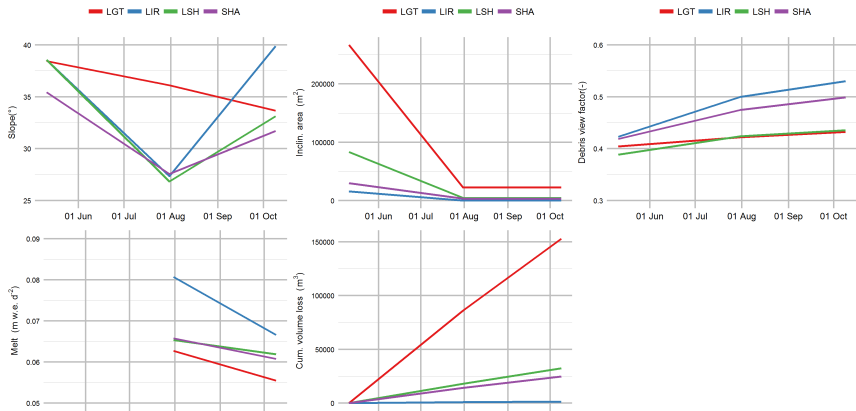


Figure 8.9.: Variables characterising ice cliff variables averaged per glacier for three points in time (initial ice cliff conditions, first- and second cliff geometry correction): slope, inclined area, melt rate and cumulative ice volume loss, separated for Langtang- (LGT), Lirung- (LIR), Langshisha- (LSH) and Shalbachum Glacier (SHA). Model period is 12 May – 9 October 2014 with geometry updates on 1 August and 9 October 2014. The three points in time for each glacier are connected and shown as lines in order to visualize the trends per glacier. Note that simulated melt rates are derived at geomtery updates for the period since the last update.

more clearly in the melt rates separated per glacier, where all melt intensities decrease after 1 August, the date of the geometric adaption of each ice cliff. This corresponds to the clear decrease in air temperature towards post-monsoon. The melt rates, calculated as average ablation for each ice cliff per glacier, are independent of total cliff area and provide therefore no direct information about the amount of ice melt. As expected, they show a clear tendency of higher melt rates towards lower elevated glaciers (ice cliffs), with Lirung Glacier having ice cliff melt rates which are on average 15–20% higher than those simulated for Langtang Glacier, caused by their clearly different altitudinal settings.

The relative contribution of all ice cliffs in terms of area and mass balance (of the debris-covered glacier surface) simulated for each glacier per elevation band (Figs. 8.10 and 8.11) shows the strong discrepancy between the relatively small (projected) area the ice cliffs occupy on the glacier surface (in the order of 0–

5%) and the contrastingly enhanced volume loss they obviously produce (in the order of 0–75%). The detailed results per elevation band are shown in Tab. E. The cliffs' relative contribution to the glacier mass balance is for all four glaciers higher than their corresponding area. This suggests that melt at sloped ice faces is more efficient than melt under debris, as in the potential case of balanced contributions of sub-debris- and ice cliff melt the relative amounts of ice cliff area- and volume loss had to be equal compared to the total glacier area and -mass balance per elevation band. It is obvious that ice cliffs, even only represented by a relatively small number, contribute a lot in terms of glacier area and mass balance especially at the glacier terminus, which coincides with the lowest elevation band shown in Figs. 8.10 and 8.11 per glacier. These steep ice faces at the terminus are not necessarily originating from the same processes as ice cliffs located higher up on the glacier. In the case of Lirung Glacier these ice cliffs are facing south and therefore prone to a large amount of solar radiation during most of the day, implying higher melt rates and volume losses. Shalbachum Glacier has the same all-glacier orientation as Lirung towards south, but no ice cliffs were detected at the terminus, indicating that possibly the debris-thickness is too high to expose ice cliffs. Although not south-facing, the terminal cliffs of Langshisha and Langtang Glacier cover a large part of the total glacier surface in the corresponding lowest elevation band (especially Langshisha Glacier), are numerous (especially Langtang Glacier) and make a major contribution to the total cliff mass balance at the glacier scale (both glaciers). Generally, although at an order of magnitude lower, the cliff area contribution relative to the glacier area follows the altitudinal distribution of the cliff mass balance contribution. Overall, no linear trend of a changing area- or mass balance contribution of ice cliffs with increasing elevation can be detected, both at the glacier- and at the catchment scale. The distribution of both the areal- and volumetric contribution of cliffs roughly follows a normal distribution (although based on a limited sample size due to the elevation-increment and the small amount of ice cliffs) with a peak in the middle of the glacier tongue, especially when the lowest elevation bands with their high mass loss- and area contribution are excluded. Obviously, single ice cliffs have a pronounced effect on a glacier, if the glacier is of small size, as can be observed on Lirung Glacier. Its elevation band from 4200–4250 m a.s.l. shows an areal portion of about 3.5% and loses 44% of the glacier mass at this elevation. The volume loss of the three cliffs at this elevation band

(two very small cliffs and a large ice cliff spanning almost the entire width of the glacier, see also Miles et al., 2017a) represent 68% of the total ice cliff mass loss of Lirung Glacier (Tab. E.1). Corresponding to the mass balance results derived from the simulations with TOPKAPI-ETH, separated for each glacier (Tab. 8.4), Lirung Glacier is relatively well protected from the atmosphere as its mass balance for the debris-covered tongue only (-0.3m w.e.) is the smallest among all four glaciers, although the glacier tongue is the lowest and therefore affected by the highest air temperatures during the melt season.

The inputs from ice cliffs to glacier mass balances, specifically for debris-covered tongues only, range from 9.1% (Shalbachum Glacier) to 36.4% (Lirung Glacier) and are, not surprisingly, reduced when considering the entire glacier area. The impact of simulated ice cliff melt on the all-glacier mass balance ranges from 1.4% (Shalbachum) to 5.5% (Langtang). When considering the simulated mass balances of the entire glaciers, the contribution of ice cliffs is highest on Langtang Glacier and much lower on Lirung Glacier (1.6%), although the latter showed the highest relative cliff melt constrained to the debris-covered area only. Ice cliffs on Lirung Glacier, although small in number, contribute considerably to the overall melt on its debris-mantled glacier tongue, whereas its influence at the glacier scale is largely reduced. This change in ranking among the glaciers is likely a direct result of the ratio between debris-covered- and debris-free area of a glacier. On Langtang Glacier roughly one third is mantled in debris, whereas on Lirung Glacier 83% is clean ice glacier (Tab. C.1), additionally the accumulation zone of Lirung Glacier, ranging from 4500–7200 m a.s.l., is extremely steep and the effective, real inclined area of that zone is even higher, further decreasing the relative areal importance of the debris-covered glacier tongue at the glacier scale.

With the narrow range of areal contributions (relative to total debris-covered glacier parts) of 0.9 (Shalbachum Glacier) to 1.4% (Langshisha Glacier), the impact of ice cliffs on glacier mass balance on the glacier tongue is about 10 (Shalbachum and Langshisha Glacier) to 33 times (Lirung Glacier) higher than the relative area they cover (Tab.) and therefore proofing the exceedance in melt of ice cliffs compared to sub-debris melt. First estimates made on selected cliffs on Lirung Glacier (Chapters 5 and 6) were within this broad range of factors.

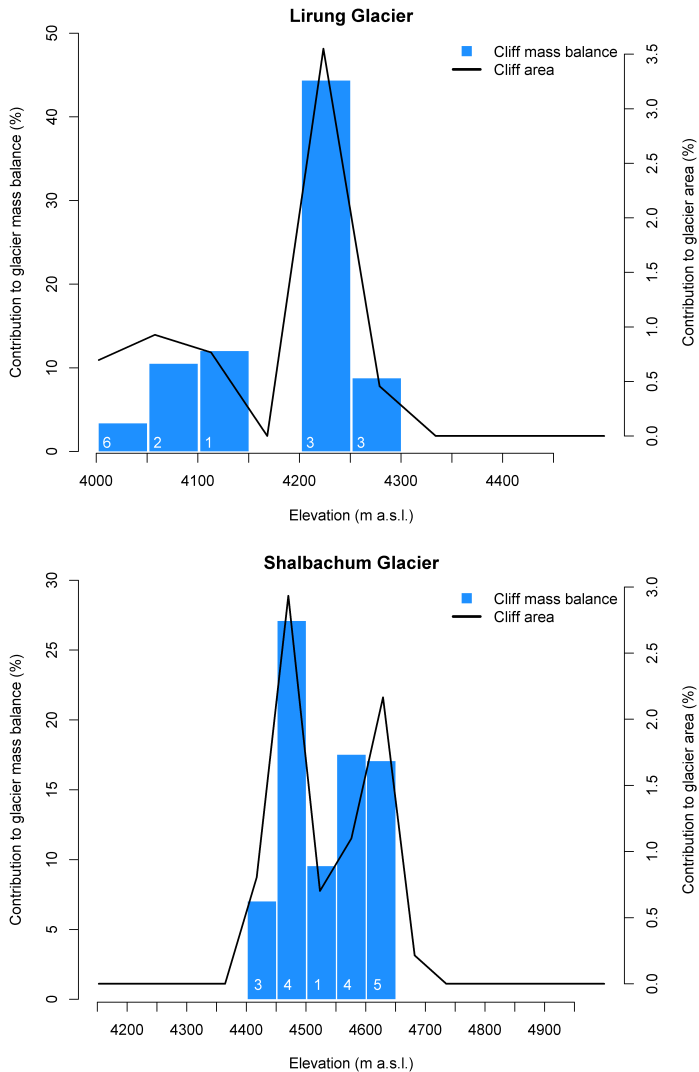


Figure 8.10.: Ice cliff model results showing the contribution in percentages of all ice cliffs per elevation band of the two debris-covered glacier tongues of Lirung- (LIR) and Shalbachum Glacier (SHA; locations within the catchment and detailed maps in Fig. 8.2), in terms of area and mass balance. The number of cliff entities per elevation band is indicated at the bottom of each bar (white number). Only elevation bands in the range of continuous debris on the glacier are shown. Model period is 12 May – 9 October 2014, reference values for total glacier mass balance are from TOPKAPI-ETH simulations.

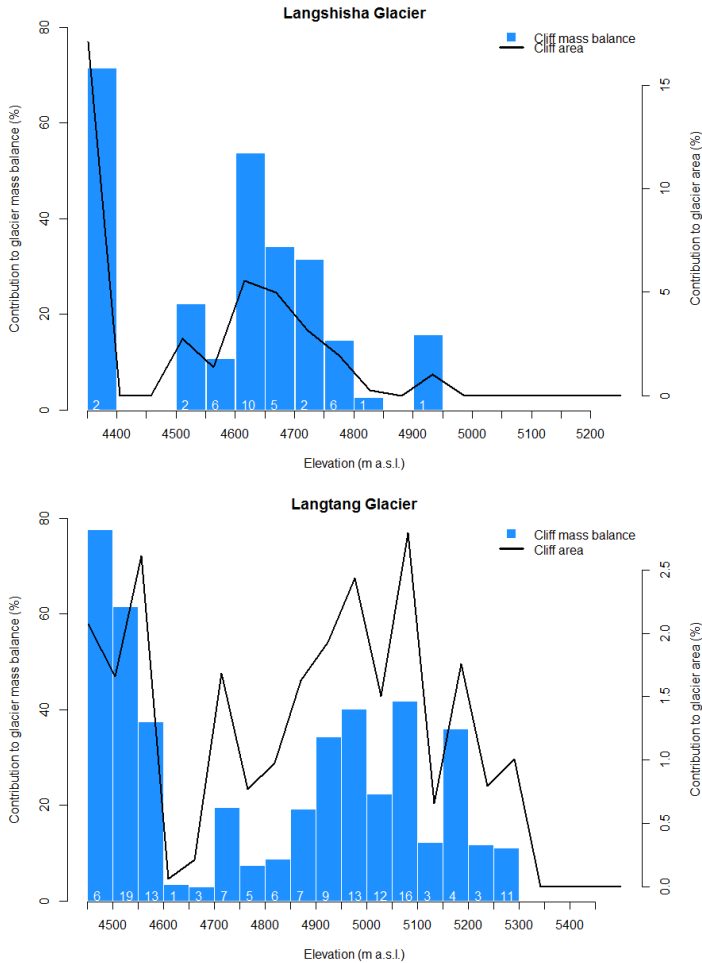


Figure 8.11.: Ice cliff model results showing the contribution in percentages of all ice cliffs per elevation band of the two debris-covered glacier tongues of Langshisha- (LSH) and Langtang Glacier (LGT; locations within the catchment and detailed maps in Fig. 8.2), in terms of area and mass balance. The number of cliff entities per elevation band is indicated at the bottom of each bar (white number). Only elevation bands in the range of continuous debris on the glacier are shown. Model period is 12 May – 9 October 2014, reference values for total glacier mass balance are from TOPKAPI-ETH simulations.

Table 8.4.: Observed and simulated ice cliff area and melt, respectively, related to the glacier scale for each study glacier (*Gla*). $A_{contrib,tot}$ is the contribution of projected cliff area (*Cli* A_{proj} , summed over the entire glacier) relative to the total glacier area (*Gla* A_{tot}); locations of glaciers within the catchment and detailed maps in Fig. 8.2). $A_{contrib,deb}$ is the contribution of *Cli* A_{proj} , relative to the debris-covered glacier area (*Gla* A_{deb}). *Gla* MB_{tot} and *Gla* MB_{deb} show the mass balance results from the hydrological model TOPKAPI-E7H for the entire glacier and the debris-covered tongue only. The MB attributed to ice cliff melt is shown in *Cli* MB_{deb} . The relative contributions of ice cliff melt to the total glacier mass balance and the glacier mass balance for the debris-covered part only are indicated by *Cli* $MB_{contrib,tot}$ and *Cli* $MB_{contrib,deb}$.

<i>Gla</i>	<i>Gla</i> A_{tot} [m^2]	<i>Gla</i> A_{deb} [m^2]	<i>Cli</i> A_{proj} [m^2]	<i>Gla</i> MB_{tot} [m w.e.]	<i>Gla</i> MB_{deb} [m w.e.]	<i>Cli</i> $MB_{contrib,tot}$ [%]	<i>A</i> $_{contrib,tot}$ [%]	<i>A</i> $_{contrib,deb}$ [%]	<i>MB</i> $_{contrib,deb}$ [%]	<i>MB</i> $_{contrib,tot}$ [%]
LGT	40218300	15385108	198117	-0.90	-0.65					
LIR	5783400	1055197	11736	-1.26	-0.30					
LSH	15902100	4402170	62910	-1.00	-0.67					
SHA	10262700	2632886	23355	-1.21	-0.72					
<i>Gla</i>	<i>Cli</i> $-V$ [m^3 w.e.]	<i>Cli</i> MB_{deb} [m w.e.]	<i>Cli</i> MB_{tot} [m w.e.]	<i>A</i> $_{contrib,tot}$ [%]	<i>A</i> $_{contrib,deb}$ [%]	<i>MB</i> $_{contrib,deb}$ [%]	<i>MB</i> $_{contrib,tot}$ [%]			
LGT	-1984003	-0.13	-0.05	0.49	1.29	19.84	5.48			
LIR	-115320	-0.11	-0.02	0.20	1.11	36.43	1.58			
LSH	-454229	-0.10	-0.03	0.40	1.43	15.40	2.86			
SHA	-172879	-0.07	-0.02	0.23	0.89	9.12	1.39			

8.4. Conclusions

By applying a physically-based numerical model, which simulated ice cliff backwasting and associated melt at the glacier scale, and using a physically-based numerical model to estimate total glacier mass balance as reference, we could assess the impact of supraglacial ice cliffs on glacier melt on four debris-covered glaciers in Langtang Valley. The study glaciers varied greatly in terms of initial total number of cliff features, cliffs' areal surface contribution, melt rates and cliffs' volume loss contribution. However, the simulated backwasting amounts of ice cliffs revealed the effectiveness of their melt compared to sub-debris ice loss, a pattern which was modelled for all glaciers.

Langtang Glacier, the largest in size and located at the highest elevation among the glaciers in the catchment, showed also the highest number of ice cliff features. With 5.5% contribution to total glacier mass balance, ice cliffs on Langtang Glacier had the highest impact at the glacier-scale melt, although cliff melt rates are generally lower compared to the other glaciers due to the decreasing air temperature with elevation. Despite the fact that only a reduced population of supraglacial ice cliffs is present on Lirung Glacier, a glacier body which is at a later evolutionary stage in terms of debris-cover and glacier dynamics compared to the other glaciers in the valley, these hotspots of melt largely contribute the ice melt of the debris-covered tongue (36%), exceeding 33 times the relative contribution of their area. Sub-debris melt on Lirung Glacier is considerably damped by a thick debris-mantle (easily reaching >2m in many parts of the glacier, which is more than on the other glaciers here) and therefore ice cliffs are very efficient windows of energy transfer, especially on glaciers with extensive debris layers.

As it is assumed that debris-covered glaciers in general undergo a transition towards a stagnant behaviour with larger debris extents and thicker debris amounts on their surface, as e.g. currently observed on Lirung Glacier, ice cliffs might play a crucial role for an increasing number of debris-covered glaciers in the future, which will be transformed towards more stagnant glaciers with very low sub-debris melt rates such as Lirung Glacier, and ice cliffs may control most of the glacier's downwasting characteristics. It is not clear, however, if supraglacial features as ice cliffs and ponds accelerate glacial decay. Lirung Glacier, the lowest ranging glacier in Langtang Valley also gives a perspective in terms of how

climate change could affect the other glaciers, as air temperatures at the low elevations of Lirung Glacier are already considerably higher on average than for the glaciers located higher up in the valley. The transition of Shalbachum, Langshisha and Langtang Glacier towards a thicker debris layer, which is reducing sub-debris melt, but associated with high melt rates at existing ice cliffs due to eventually higher air temperature, are plausible scenarios for the coming few decades. Yet a better understanding of the sourcing and temporal and spatial (3D) evolution of debris on glaciers, in combination with the appearance, life cycle and decay of supraglacial ice cliffs, is needed to reveal better estimates of the dynamics of debris-covered glaciers.

Some of the inevitable uncertainties in the TOPKAPI simulations of total glacier mass balance might affect the actual range of calculated cliffs contributions. Additional uncertainty in our estimates is due to the quality of the DEM, uncertainties in the cliff delineation and the fact that we use a conservative approach to cliff delineation and discard very small cliffs and those for which uncertainty in topography is high. Despite these uncertainties, our work presents the first estimate of the importance of supraglacial ice-cliffs to total glacier mass-balance. Through the application of a numerical model approach we could advance the understanding of ice cliff melt at the glacier scale by considerably improving previous simplified estimates which were approaches either neglecting the large variability of ice cliff geometries and thus melt patterns (extrapolations from point-scale calculations) and neglecting englacial and supraglacial dynamics (DEM differencing). Our study shows that the volume lost by backwasting of ice cliffs is a non-negligible term in the total glacier mass balance of debris-covered glaciers, contributing by 1.4–5.5% (9.1–36.4% for debris-covered tongues) in a high-elevation catchment in HMA, especially when considering a likely increase in debris-cover extent with climate change on glaciers in HMA and in glaciated areas globally. The results derived with a numerical model provide a partial explanation of the higher-than-expected mass losses of debris-covered glaciers of HMA.

Chapter 9.

Concluding remarks



Figure 9.1.: Lower part of Langtang Glacier and its lowest tributary, peak of Gurkarpo Ri (6889m a.s.l.) in the background. In the foreground the so-called Morimoto Basecamp (Oct. 2015).

9.1. Knowledge advancements

This thesis has analyzed the impact of supraglacial ice cliffs on the mass balance of debris-covered glaciers in the high-elevation Langtang Valley catchment (Central Nepalese Himalaya) through a combination of novel field observations and the development of numerical models. To reach this goal, the processes driving ice cliff melt and -backwasting and the evaluation of their role at the glacier and catchment scale were evaluated through a progression of four main logical steps: First, a grid-based, distributed energy-balance model for the cliff scale that calculates energy fluxes and ablation for every cliff grid cell was developed in Chapter 5. The new grid-based ice cliff melt model considers the surrounding topography, which is relevant for incoming energy fluxes and thus melt rates, in a detailed way, using a high-resolution DEM of the glacier. The model was used to study the spatio-temporal variability of the main energy fluxes at the cliff surface and establish main controls and first order drivers of cliff evolution.

Second, a dynamic ice cliff model simulating the differential melt simulated for the entire ice cliff surface (Chapter 5) was developed from the model in step 1, to model ice cliff backwasting associated with atmospheric melt, sub-aqueous melt at the cliff section in contact with adjacent ponds and reburial by debris.

These findings and the dynamic model of step 2 were then used to simulate how ice cliffs with various orientations evolve over time 7. To investigate the aspect-dependent behaviour of supraglacial ice cliffs, we rotated observed cliffs, including their surrounding glacier surface and ponds, to eight main directions covering the full spectrum of aspect angles, and applied the dynamic ice cliff backwasting model of Chapter 6 to each of them. The simulations showed that southerly-facing cliffs disappear within few weeks or months due to enhanced solar radiation in combination with increasing shadowing towards the bottom, while cliffs with a north and western range do survive the duration of the ablation season, because of reduced solar radiation input.

Finally, in the last synthesis step we addressed the overall goal of the thesis to assess the contribution of ice cliff to total glacier mass balance. We applied the backwasting, 3D cliff model of step 2 and 3 to the entire cliff population of all debris-covered glaciers in the catchment and compared the total mass losses due to cliff backwasting to the estimated glacier mass loss from a hydrological model approach. The impact of the simulated ice cliff melt on the total glacier mass

balance was considerable, with contributions in the dimension of roughly up to 5.5% (up to 36.5% considering the debris-covered area only), despite the rather small areal coverage of these ice cliffs on the glacier scale of <0.5% (<1.5% for the debris-covered area).

The principal conclusions in relation to the research questions described in Chapter 1 can be summarized as follows:

a. The distributed energy-balance and melt pattern of supraglacial ice cliffs

Shortwave radiation is an important contributor to the energy balance of steep ice faces during the day and the diffuse flux from the sky is its dominant component. This is in contrast to flat surfaces, where the direct shortwave radiation is the main source of energy. Modulated by the high spatial variability of the direct shortwave radiation component the net shortwave radiation varies greatly across the ice cliff surface. High local variability was also modelled for the incoming longwave radiation emitted by the debris-covered glacier surface, which represents \sim one quarter of the total incoming longwave flux. Over the 24 hour daily cycle, incoming longwave radiation is the highest positive energy flux modelled for the ice cliff surface. As a result of the high spatial variability in energy fluxes acting on the steep surface, ice cliff melt rates vary considerably in space, with coefficients of variation of 10–40% over the entire season. The two modelled ice cliffs show a more than 13 times higher melt potential than the ice under debris on the tongue of Lirung glacier.

b. The backwasting evolution and associated volume loss of supraglacial ice cliffs

Using the rare dataset collected in the field over two main seasons, we identified distinct patterns of ice cliffs evolution. Ice cliffs only a few hundred meters apart show three main patterns over one melt season: i) reclining geometry leading to disappearance; ii) radial expansion; iii) persistence with a self-similar shape. The main mechanisms controlling the observed evolution patterns are atmospheric melt, pond contact ablation enhancement at the cliff base and reburial by surrounding debris.

A strong dependency of the cliffs' life cycle on ponded water bodies is suggested to keep the cliff geometry constant. Our physically-based 3D dynamic model was able to capture the main cliff dynamics and geometric transformation, simulating the progressive backwasting through interaction with the surrounding topography, and allowing the cliff shape to grow and to shrink over time. Neglecting dynamic cliff geometry changes in the model configuration leads to erroneous results in terms of backwasting patterns and volume losses. Simulated volume losses were in agreement with independent estimates obtained for the same ice cliffs. The contribution of the four selected cliffs to the total sub-debris melt was calculated to be 3.25%, which is more than 17 higher than their contributing area.

c. The controlling factors of ice cliff's persistence and demise

Our model results provided the first evidence that southerly-orientated supraglacial ice cliffs disappear within few weeks to a few months, as conceptually suggested by previous field experience and intuition. This is the first time that this has been proved through numerical modelling including all the concomitant and often contrasting drivers of cliffs changes. This implies that south-facing ice faces are not contributing to glacier mass loss over the long term and it thus improves the understanding of spatial and temporal distribution of ice cliffs on debris-covered glaciers. The key factors controlling the rapid decline of south facing cliffs were found to be the enhanced direct solar radiation received by southerly-oriented cliffs in comparison to northerly-facing ice cliffs, and the increase of the sky-view factor from the cliff's bottom to its top.

At ice cliffs with northerly aspects the longwave radiation from surrounding debris is able to counterbalance the solar radiation at the bottom cliff sections and thus allows maintaining a more self-similar shape and a stable backwasting of the cliff shape, whereas the enhanced shortwave radiation input at the top sections of south-facing cliffs cannot be outweighed by the energy emitted by the debris acting at the cliff's base.

Ponds directly adjacent to ice cliffs are not able to maintain south-facing ice cliffs steep to allow their persistence.

d. The contribution of supraglacial ice cliffs to the total ablation of debris-covered glaciers

We modelled ice cliff melt and backwasting for the entire cliff population of four debris-covered glaciers in the Langtang Valley using initial conditions from high resolution satellite images, and compared it to glacier ablation results derived with a glacio-hydrological model (TOPKAPI-ETH). In this way, we estimated for the first time the impact of ice cliff melt on the mass balance of entire glaciers and catchments using a physically-based approach. This is a key advancement compared to current estimates obtained only indirectly through differencing of DEMs, which cannot separate the mass loss signal from the velocity signal. A high number and relative areal coverage of supraglacial ice cliffs on a glacier tongue is favourable for a high impact of cliffs on glacial melt (e.g. Langtang Glacier). However, already few cliffs, especially on glaciers covered with a thick debris layer, can contribute a large amount of energy to total the mass balance of the debris-covered glacier tongue (e.g. Lirung Glacier), by canceling out the generally effective insulation of the underlying ice through the exposure of ice to the atmosphere. Our results, derived with a numerical model, could show that ice cliffs, acting as hot spots of melt, can partially explain the higher-than-expected mass losses of debris-covered glaciers of HMA.

9.2. Outlook

Three research directions with focus on debris-covered glaciers should be addressed in the future in order to better understand their impact on the cryosphere and hydrology of various mountain regions in the world.

1) Occurrence, evolution and life cycle of supraglacial ice cliffs over time:

Knowledge about the behaviour of ice cliffs at the glacier scale under different climatic and geomorphological conditions is very limited. Investigating the preferential orientation of ice cliffs, glacier surface characteristics which are indicating a high spatial and temporal ice cliff density and assessing where and under which conditions new cliffs form would therefore bridge an existing important knowledge gap. Along with glacier-wide inventories, also the repeated identification of distinct cliffs over several years to record their appearance and decay

would be beneficial for a better understanding of the surface of debris-covered glacier tongues, as nothing is known about how ice cliffs form.

2) Understanding the surface dynamics of debris-covered glaciers:

The transition from treating debris-covered glaciers as different but not important types of glaciers to a hot topic in large-scale studies of glacier mass losses (debris-cover anomaly) took place in the last five years only. Many scientific questions remain unanswered. Beside the investigation of the evolution and relevance of supraglacial ice cliffs for glacier mass balance, which were assessed in this thesis, the knowledge on the mechanisms behind debris' spatial and temporal (3D-) distribution on glaciers has to be advanced. To approach this pressing research task, debris-layer thickness (thermal imagery, profiles), englacial debris transport rates (boreholes, ground penetrating radar) and periglacial debris supply (satellite imagery, avalanche- and permafrost modelling) have to be quantified and rock type and -age have to be determined (exposure dating). It is most likely that debris-cover – not only in HMA but also on glaciers in the Alps – will increase considerably during the next decades of continuous ice volume loss and become an important topic e.g. for water management due to their insulating properties on remaining ice masses, but also in relation to natural hazards and threats to infrastructure, as they provide a constant amount of rock material prone to mass movements triggered by external events.

3) Coupling models describing debris-cover characteristics with glacier dynamic- and hydrological models:

The current implications of debris-cover on glaciers at the catchment and regional scale is not yet fully understood and especially projections into the future are error prone, as our understanding of the evolution of debris-type glaciers is still incomplete. Consequently, the implementation of the findings from research directions (1) and (2) (evolution and life cycle of ice cliffs and surface processes and characteristics of debris-cover), by reducing their complexity or by replacing them by a stochastic approach that incorporates the relevant processes in a representative way, into large-scale models of glacier mass-balance or glacier evolution, should be addressed. The consideration of the processes relevant for debris-covered glaciers in glacier models will be an important advancement in the understanding of the influence of debris-type glaciers in mountainous regions under a changing climate and will be fundamental in terms of global ice masses and sea level rise.

Chapter 10.

Bibliography

- Agisoft (2013) *PhotoScan Professional 0.9.1 User Manual*. Agisoft LLC, St. Petersburg, Russia 1.1, 7.6.2
- Anderson L (2014) *Glacier Response to Climate Change: Modeling the Effects of Weather and Debris-Cover*. Ph.D. thesis, University of Colorado Boulder 1.1, 1.2.3
- Aoki T and Asahi K (1998) Topographical map of the ablation area of the Lirung Glacier in the Langtang Valley, Nepal Himalaya. *Bulletin of Glacier Research*, **16**, 19–31 2.3
- ASTER (2009) *ASTER Global Digital Elevation Model*. NASA Jet Propulsion Laboratory, Pasadena, California, USA (doi: 10.5067/ASTER/ASTGTM.002) 7.6.2, 8.2
- Ayala A (2017) *The role of surface sublimation in the summer mass balance of glaciers in the subtropical semiarid Andes*. Phd thesis, ETH Zurich (doi: 10.3929/ETHZ-B-000000218) 1.2.4
- Ayala A, Pellicciotti F, Macdonell S, Mcphee J, Vivero S, Campos C and Egli P (2016) Modelling the hydrological response of debris-free and debris-covered glaciers to present climatic conditions in the semiarid Andes of central Chile. *Hydrological Processes*, ISSN 10991085 (doi: 10.1002/hyp.10971) 1.2.4
- Bandyopadhyay J and Gyawali D (1994) Himalayan water resources: ecological and political aspects of management. *Mountain Research and Development*, **14**(1), 1–24 1.2.1
- Basnett S, Kulkarni A and Bolch T (2013) The influence of debris cover and glacial lakes on the recession of glaciers in Sikkim Himalaya, India.

- Journal of Glaciology*, **59**(218), 1035–1046, ISSN 00221430 (doi: 10.3189/2013JoG12J184) 1.1, 1.2.2
- Benn D, Wiseman S and Hands K (2001) Growth and drainage of supraglacial lakes on debris-mantled Ngozumpa Glacier, Khumbu Himal, Nepal. *Journal of Glaciology*, **47**(159) 6.6.1
- Benn DI, Bolch T, Hands K, Gulley J, Luckman A, Nicholson LI, Quincey D, Thompson S, Toumi R and Wiseman S (2012) Response of debris-covered glaciers in the Mount Everest region to recent warming, and implications for outburst flood hazards. *Earth-Science Reviews*, **114**(1-2), 156–174 (doi: 10.1016/j.earscirev.2012.03.008) 1.1, 5.1, 6.1, 7.4
- Bernhardt M and Schulz K (2010) Snowslide: A simple routine for calculating gravitational snow transport. *Geophysical Research Letters*, **37**(11), n/a–n/a, ISSN 1944-8007 (doi: 10.1029/2010GL043086), 111502 1.2.4
- Berthier E, Arnaud Y, Kumar R, Ahmad S, Wagnon P and Chevallier P (2007) Remote sensing estimates of glacier mass balances in the Himachal Pradesh (Western Himalaya, India). *Remote Sensing of Environment*, **108**(3), 327–338, ISSN 00344257 (doi: 10.1016/j.rse.2006.11.017) 1.2.1
- Bivand RS, Pebesma E and Gomez-Rubio V (2013) *Applied spatial data analysis with R, Second edition*. Springer, NY 6.7
- Bolch T, Buchroithner M, Pieczonka T and Kunert A (2008) Planimetric and volumetric glacier changes in the Khumbu Himal, Nepal, since 1962 using Corona, Landsat TM and ASTER data. *Journal of Glaciology*, **54**(187), 592–600, ISSN 00221430 (doi: 10.3189/002214308786570782) 1.2.1
- Bolch T, Pieczonka T and Benn DI (2011) Multi-decadal mass loss of glaciers in the Everest area (Nepal Himalaya) derived from stereo imagery. *The Cryosphere*, **5**(2), 349–358, ISSN 1994-0424 (doi: 10.5194/tc-5-349-2011) 1.2.1
- Bolch T, Kulkarni A, Kääb A, Huggel C, Paul F, Cogley JG, Frey H, Kargel JS, Fujita K, Scheel M, Bajracharya S and Stoffel M (2012) The state and fate of Himalayan glaciers. *Science*, **336**(6079), 310–314 (doi: 10.1126/science.1215828) 1.1, 1.2.1, 5.1, 6.1, 7.1
- Brock BW, Willis IC and Sharp MJ (2000) Measurement and parameterization of albedo variations at Haut Glacier d’Arolla, Switzerland. *Journal of Glaciology*, **46**(155), 675–688 1.2.4

-
- Brock BW, Mihalcea C, Kirkbride MP, Diolaiuti G, Cutler MEJ and Smiraglia C (2010) Meteorology and surface energy fluxes in the 2005–2007 ablation seasons at the Miage debris-covered glacier, Mont Blanc Massif, Italian Alps. *Journal of Geophysical Research*, **115**(D9), D09106, ISSN 0148-0227 (doi: 10.1029/2009JD013224) 1.2.2, 6.6.3
- Brun F, Buri P, Miles ES, Wagnon P, Steiner JF, Berthier E, Ragettli S, Kraaijenbrink P, Immerzeel WW and Pellicciotti F (2016) Quantifying volume loss from ice cliffs on debris-covered glaciers using high-resolution terrestrial and aerial photogrammetry. *Journal of Glaciology*, 1–12 (doi: 10.1017/jog.2016.54) 3.1, 3.2, 6.1, 6.2, 6.3.1, 6.3.1, 3, 6.4.1, 6.4.2, 6.5.3, 6.11, 6.2, 6.5.3, 7.1, 7.6.3, 7.6.3, 8.2.1
- Buri P and Pellicciotti F (in revision) Aspect controls the survival of ice cliffs on debris-covered glaciers. *Proceedings of the National Academy of Sciences* 8.2, 8.3
- Buri P, Pellicciotti F, Steiner JF, Miles ES and Immerzeel WW (2016a) A grid-based model of backwasting of supraglacial ice cliffs on debris-covered glaciers. *Annals of Glaciology*, **57**(71), 199–211 (doi: 10.3189/2016AoG71A059) 6.1, 6.2, 6.4, 3, 6.4.1, 6.4.1, 6.6.4, 7.1, 7.2, 7.4, 7.5, 7.6.1, 7.6.2, 7.6.3, 7.6.3, 7.6.3, 7.6.3, 7.6.4, 8.2.1
- Buri P, Miles ES, Steiner JF, Immerzeel WW, Wagnon P and Pellicciotti F (2016b) A physically based 3-D model of ice cliff evolution over debris-covered glaciers. *Journal of Geophysical Research: Earth Surface*, **121**(12), 2471–2493, ISSN 2169-9011 (doi: 10.1002/2016JF004039) 7.1, 7.2, 7.2, 7.3, 7.4, 7.5, 7.6.1, 7.6.2, 7.6.2, 7.6.3, 7.6.3, 7.6.3, 7.6.3, 7.6.3, 7.6.3, 7.6.3, 7.6.3, 7.6.3, 7.6.3, 7.6.3, 7.6.3, 7.6.3, 7.6.3, 8.2.1
- Carenzo M, Pellicciotti F, Mabillard J, Reid T and Brock B (2016) An enhanced temperature index model for debris-covered glaciers accounting for thickness effect. *Advances in Water Resources*, **94**, 457–469 (doi: 10.1016/j.advwatres.2016.05.001) 1.2.4
- Chinn T (1987) Accelerated Ablation at a glacier ice-cliff margin, dry valleys, Antarctica. *Arctic, Antarctic, and Alpine Research*, **19**(1), 71–80 1.2.3
- Cogley JG (2012) Himalayan glaciers in the balance. *Nature*, **488**(7412), 468–469 1.2.1
- Cogley JG (2016) Glacier shrinkage across High Mountain Asia. *Annals of Glaciology* (doi: 10.3189/2016aog71a040) 6.1

- Collier E and Immerzeel WW (2015) High-resolution modeling of atmospheric dynamics in the Nepalese Himalaya. *Journal of Geophysical Research: Atmospheres*, **120**(19), 9882–9896 (doi: 10.1002/2015jd023266) 2.2, 6.6.3
- Collier E, Nicholson LI, Brock BW, Maussion F, Essery R and Bush ABG (2014) Representing moisture fluxes and phase changes in glacier debris cover using a reservoir approach. *The Cryosphere*, **8**(4), 1429–1444, ISSN 1994-0424 (doi: 10.5194/tc-8-1429-2014) 1.2.2
- Cooper P (1969) The Absorption of Radiation in Solar Stills. *Solar Energy*, **12**(3), 333–346 4.1
- Cruz R, Harasawa H, Lal M, Wu S, Anokhin Y, Punsalma B, Honda Y, Jafari M, Li C and Huu Ninh N (2007) Impacts, Adaptation and Vulnerability. Contribution of Working Group II to the Fourth Assessment Report of the Intergovernmental Panel on Climate Change. In M et al Parry (ed.), *Climate Change 2007*, chapter Asia, 469–506, Cambridge Univ. Press, Cambridge, UK 1.2.1
- Dice LR (1945) Measures of the amount of ecologic association between species. *Ecology*, **26**(3), 297–302, ISSN 1939-9170 (doi: 10.2307/1932409) 6.4.2
- Dilley AC and O’Brien DM (1998) Estimating downward clear sky long-wave irradiance at the surface from screen temperature and precipitable water. *Q.J Royal Met. Soc.*, **124**(549), 1391–1401 (doi: 10.1002/qj.49712454903) 5.4.3, 8.2, C.5
- Dong J and Peters-Lidard C (2010) On the relationship between temperature and MODIS snow cover retrieval errors in the western u.s. *IEEE Journal of Selected Topics in Applied Earth Observations and Remote Sensing*, **3**(1), 132–140 (doi: 10.1109/jstars.2009.2039698) 6.4.2
- Driscoll FG (1980) Wastage of the Klutlan ice-cored moraines, Yukon Territory, Canada. *Quaternary Research*, **14**(1), 31–49 6.4, 3, 7.6.3
- Edelsbrunner H, Kirkpatrick D and Seidel R (2006) On the shape of a set of points in the plane. *IEEE Trans. Inf. Theor.*, **29**(4), 551–559, ISSN 0018-9448 (doi: 10.1109/TIT.1983.1056714) 6.4.1, 7.6.3
- Evatt GW, Abrahams ID, Heil M, Mayer C, Kingslake J, Mitchell SL, Fowler AC and Clark CD (2015) Glacial melt under a porous debris layer. *Journal of Glaciology*, **61**(229), 825–836, ISSN 00221430 (doi: 10.3189/2015JöG14J235) 1.2.2, 6.1, 7.1

-
- Foster L (2010) *Utilisation of remote sensing for the study of debris-covered glaciers: development and testing of techniques on Miage Glacier, Italian Alps*. Phd thesis, University of Dundee 2
- Foster L, Brock B, Cutler M and Diotri F (2012) A physically based method for estimating supraglacial debris thickness from thermal band remote-sensing data. *Journal of Glaciology*, **58**(210), 677–691, ISSN 00221430 (doi: 10.3189/2012JoG11J194) 1.2.2
- Fujita K and Sakai A (2014) Modelling runoff from a Himalayan debris-covered glacier. *Hydrology and Earth System Sciences Discussions*, **11**(2), 2441–2482 (doi: 10.5194/hessd-11-2441-2014) 5.1
- Fujita K, Sakai A and Chhetri T (1997) Meteorological observation in Langtang Valley, Nepal Himalayas, 1996. *Bulletin of Glacier Research*, **15**, 71–78, ISSN 09134190 7.3
- Fujita K, Suzuki R, Nuimura T and Sakai A (2008) Performance of ASTER and SRTM DEMs, and their potential for assessing glacial lakes in the Lunana region, Bhutan Himalaya. *Journal of Glaciology*, **54**(185), 220–228 (doi: 10.3189/002214308784886162) 5.5.3
- Fujita K, Inoue H, Izumi T, Yamaguchi S, Sadakane A, Sunako S, Nishimura K, Immerzeel WW, Shea JM, Kayastha RB, Sawagaki T, Breashears DF, Yagi H and Sakai A (2017) Anomalous winter-snow-amplified earthquake-induced disaster of the 2015 Langtang avalanche in Nepal. *Natural Hazards and Earth System Sciences*, **17**(5), 749–764, ISSN 1684-9981 (doi: 10.5194/nhess-17-749-2017) 2.1
- Fushimi H, Yasunari T, Higuchi H, Nagoshi A, Watanabe O, Ikegami K, Higuchi K, Ageta Y, Ohata T and Nakajima C (1980) Preliminary report on flight observations of 1976 and 1978 in the nepal himalayyas. *Journal of the Japanese Society of Snow and Ice*, **41**(Special), 62–66 (doi: 10.5331/seppyo.41.Special_62) 1.2.3
- Fyfe C, Reid T, Brock B, Kirkbride M, Diolaiuti G, Smiraglia C and Diotri F (2014) A distributed energy-balance melt model of an alpine debris-covered glacier. *Journal of Glaciology*, **60**(221), 587–602, ISSN 00221430 (doi: 10.3189/2014JoG13J148) 5.1
- Gardelle J, Berthier E and Arnaud Y (2012) Slight mass gain of Karakoram glaciers in the early twenty-first century. *Nature Geosci*, **5**(5), 322–325 (doi: 10.1038/ngeo1450) 1.1, 1.2.1, 5.1, 6.1, 7.1

- Gardelle J, Berthier E, Arnaud Y and Käab A (2013) Region-wide glacier mass balances over the Pamir-Karakoram-Himalaya during 1999-2011. *The Cryosphere*, **7**(4), 1263–1286 (doi: 10.5194/tc-7-1263-2013) 1.1, 1.2.1, 1.2.2, 5.1, 6.1
- Gardner AS, Moholdt G, Cogley JG, Wouters B, Arendt AA, Wahr J, Berthier E, Hock R, Pfeffer WT, Kaser G, Ligtenberg SRM, Bolch T, Sharp MJ, Hagen JO, van den Broeke MR and Paul F (2013) A reconciled estimate of glacier contributions to sea level rise: 2003 to 2009. *Science (New York, N.Y.)*, **340**(6134), 852–7, ISSN 1095-9203 (doi: 10.1126/science.1234532) 1.2.1, 1.2.2
- Garnier B and Ohmura A (1968) A Method of Calculating the Direct Shortwave Radiation Income of Slopes. *J. Appl. Meteor.*, **7**, 796–800 (doi: [http://dx.doi.org/10.1175/1520-0450\(1968\)007<0796:AMOCTD>2.0.CO;2](http://dx.doi.org/10.1175/1520-0450(1968)007<0796:AMOCTD>2.0.CO;2)) 4.2, A.2, A.3, A.4
- Gilani SZ and Rao NI (2009) A clustering based automated glacier segmentation scheme using digital elevation model. In *Digital Image Computing: Techniques and Applications, 2009. DICTA '09.*, 277–284, IEEE 6.4.2
- Goldthwait RP (1971) Restudy of Red Rock Ice Cliff, Nunatarssuaq, Greenland. In *CRREL Technical Reports*, 224, 1–27, U.S. Army Cold Regions Research and Engineering Laboratory, Hanover, New Hampshire 1.2.3
- Grinsted A (2013) An estimate of global glacier volume. *The Cryosphere*, **7**, 141–151, ISSN 19940416 (doi: 10.5194/tc-7-141-2013) 1.2.1
- Han H, Wang J, Wei J and Liu S (2010) Backwasting rate on debris-covered Koxkar glacier, Tuomuer mountain, China. *Journal of Glaciology*, **56**(196), 287–296 (doi: 10.3189/002214310791968430) (document), 1.1, 1.2.3, 1.2.3, 4.2, 4.2, 5.1, 5.4, 5.4.2, 5.4.4, 5.5.2, 6.1, 6.6.4, A.1, A.2, A.3, A.4
- Herreid S, Pellicciotti F, Ayala A, Chesnokova A, Kienholz C, Shea J and Shrestha A (2015) Satellite observations show no net change in the percentage of supraglacial debris-covered area in northern pakistan from 1977 to 2014. *Journal of Glaciology*, **61**(227), 524–536 (doi: 10.3189/2015jog14j227) 1.2.2, 6.1
- Heuberger H, Masch L, Preuss E and Schrockner A (1984) Quaternary Landslides and Rock Fusion in Central Nepal and in the Tyrolean Alps. *Mountain Research and Development*, **4**(4), 345, ISSN 02764741 (doi: 10.2307/3673238) 2.1

-
- Heynen M, Miles E, Ragettli S, Buri P, Immerzeel WW and Pellicciotti F (2016) Air temperature variability in a high-elevation Himalayan catchment. *Annals of Glaciology*, **57**(71), 212–222 (doi: 10.3189/2016aog71a076) (document), 2.2, 3.1, 3.2, 8.2, 8.2, C.2, C.1, C.3
- Hijmans RJ (2015) *raster: Geographic Data Analysis and Modeling*. R package version 2.4-20 6.7
- Hock R (2005) Glacier melt: a review of processes and their modelling. *Progress in Physical Geography*, **29**(3), 362–391 (doi: 10.1191/0309133305pp453ra) 7.6.4
- Hock R and Noetzi C (1997) Areal melt and discharge modelling of storglaciären, sweden. *Annals of Glaciology*, **24**, 211216 (doi: 10.1017/S0260305500012192) 1.2.4
- Horn BK (1981) Hill shading and the reflectance map. *Proceedings of the IEEE*, **69**(1), 14–47 (doi: 10.1109/PROC.1981.11918) 6.4.1, 7.6.2
- Hudson D (1966) Fitting segmented curves whose join points have to be estimated. *Journal of the American Statistical Association*, **61**(316), 1097–1129 8.2
- Huss M and Hock R (2015) A new model for global glacier change and sea-level rise. *Frontiers in Earth Science*, **3**, ISSN 2296-6463 (doi: 10.3389/feart.2015.00054) 1.2.2
- Huss M, Jouvett G, Farinotti D and Bauder a (2010) Future high-mountain hydrology: a new parameterization of glacier retreat. *Hydrology and Earth System Sciences*, **14**(5), 815–829, ISSN 1607-7938 (doi: 10.5194/hess-14-815-2010) 1.2.4
- Immerzeel W, van Beek L and Bierkens M (2010) Climate change will affect the Asian water towers. *Science (New York, N. Y.)*, **328**(5984), 1382–5, ISSN 1095-9203 (doi: 10.1126/science.1183188) 1.2.1, 7
- Immerzeel W, Beek L, Konz M, Shrestha A and Bierkens M (2011) Hydrological response to climate change in a glacierized catchment in the Himalayas. *Climatic Change*, **110**(3-4), 721–736, ISSN 0165-0009 (doi: 10.1007/s10584-011-0143-4) 2.2
- Immerzeel W, Pellicciotti F and Bierkens M (2013) Rising river flows throughout the twenty-first century in two Himalayan glacierized watersheds. *Nature Geoscience*, **6**(9), 742–745, ISSN 1752-0894 (doi: 10.1038/ngeo1896) 1.2.1

- Immerzeel W, Petersen L, Ragetti S and Pellicciotti F (2014a) The importance of observed gradients of air temperature and precipitation for modeling runoff from a glacierized watershed in the Nepalese Himalayas. *Water Resources Research*, **50**(3), 2212–2226 (doi: 10.1002/2013WR014506.Received) 1.1, 2.3, 3.2, 5.2, 5.3.2, 5.5.2, 7.3, 7.6.1
- Immerzeel W, Kraaijenbrink P, Shea J, Shrestha A, Pellicciotti F, Bierkens M and de Jong S (2014b) High-resolution monitoring of Himalayan glacier dynamics using unmanned aerial vehicles. *Remote Sensing of Environment*, **150**, 93–103, ISSN 00344257 (doi: 10.1016/j.rse.2014.04.025) 1.1, 1.2.3, 2.2, 2.3, 5.3.1, 6.2, 6.4.1, 7.2, 7.5, 7.6.1, 7.6.2, 7.6.3, 7.6.3
- Inoue J and Yoshida M (1980) Ablation and heat exchange over the Khumbu Glacier. *Journal of the Japanese Society of Snow and Ice*, **41**(Special), 26–33 (doi: 10.5331/seppyo.41.Special_26) 1.2.3, 6.1, 3, 7.1
- IPCC (2013) *Climate Change 2013: The Physical Science Basis. Contribution of Working Group I to the Fifth Assessment Report of the Intergovernmental Panel on Climate Change*. Cambridge University Press, Cambridge, United Kingdom and New York, NY, USA, ISBN ISBN 978-1-107-66182-0 (doi: 10.1017/CBO9781107415324) 1.2.1
- Iwata S, Watanabe O and Fushimi H (1980) Surface morphology in the ablation area of the Khumbu Glacier. *Journal of the Japanese Society of Snow and Ice*, **41**(Special), 9–17 (doi: 10.5331/seppyo.41.Special_9) 1.2.3, 6.4
- Juszak I and Pellicciotti F (2013) A comparison of parameterizations of incoming longwave radiation over melting glaciers: Model robustness and seasonal variability. *Journal of Geophysical Research: Atmospheres*, **118**(8), 3066–3084, ISSN 2169897X (doi: 10.1002/jgrd.50277) 5.4.3, 8.2
- Kääb A, Berthier E, Nuth C, Gardelle J and Arnaud Y (2012) Contrasting patterns of early twenty-first-century glacier mass change in the Himalayas. *Nature*, **488**(7412), 495–8, ISSN 1476-4687 (doi: 10.1038/nature11324) 1.1, 1.2.1, 1.2.2, 5.1, 6.1, 7.1
- Kargel JS et al. (2015) Geomorphic and geologic controls of geohazards induced by nepals 2015 gorkha earthquake. *Science*, **351**(6269), aac8353–aac8353 (doi: 10.1126/science.aac8353) 8.2
- Kaser G, Cogley JG, Dyurgerov MB, Meier MF and Ohmura A (2006) Mass balance of glaciers and ice caps: Consensus estimates for 1961–2004. *Geo-*

physical Research Letters, **33**(19), L19501, ISSN 0094-8276 (doi: 10.1029/2006GL027511) 1.2.1, 1.2.2

Kirkbride MP (1993) The temporal significance of transitions from melting to calving termini at glaciers in the central Southern Alps of New Zealand. *The Holocene*, **3**(3), 232–240, ISSN 0959-6836 (doi: 10.1177/095968369300300305) 7.4

Kirkbride MP and Deline P (2013) The formation of supraglacial debris covers by primary dispersal from transverse englacial debris bands. *Earth Surf. Process. Landforms*, **38**(15), 1779–1792 (doi: 10.1002/esp.3416) 1.2.2, 6.1

Kraaijenbrink P, Meijer SW, Shea JM, Pellicciotti F, Jong SMD and Immerzeel WW (2016) Seasonal surface velocities of a Himalayan glacier derived by automated correlation of unmanned aerial vehicle imagery. *Annals of Glaciology*, **57**(71), 103–113 (doi: 10.3189/2016aog71a072) 2.3, 3.2, 7.6.1, 8.2.1

Lambrecht A, Mayer C, Hagg W, Popovnin V, Rezepkin A, Lomidze N and Svanadze D (2011) A comparison of glacier melt on debris-covered glaciers in the northern and southern Caucasus. *The Cryosphere*, **5**(3), 525–538, ISSN 1994-0424 (doi: 10.5194/tc-5-525-2011) 1.2.2

Lejeune Y, Bertrand JM, Wagnon P and Morin S (2013) A physically based model of the year-round surface energy and mass balance of debris-covered glaciers. *Journal of Glaciology*, **59**(214), 327–344, ISSN 00221430 (doi: 10.3189/2013Jog12J149) 1.2.2

Levy J, Fountain A, Dickson J, Head J, Okal M, Marchant D and Watters J (2013) Accelerated thermokarst formation in the McMurdo Dry Valleys, Antarctica. *Scientific reports*, **3** 1.2.3

Lewis K, Fountain A and Dana G (1999) How important is terminus cliff melt?: A study of the Canada Glacier terminus, Taylor Valley, Antarctica. *Global and Planetary Change*, **22**(1), 105–115 1.2.3

Lutz A and Immerzeel W (2013) Water Availability Analysis for the Upper Indus, Ganges, Brahmaputra, Salween and Mekong River Basins FutureWater Report 127. Technical report (doi: Report127) 2.3

Lutz A, Immerzeel W, Shrestha A and Bierkens M (2014) Consistent increase in High Asia's runoff due to increasing glacier melt and precipitation. *Nature Climate Change*, **4**(7), 587–592, ISSN 1758-678X (doi: 10.1038/nclimate2237)

- Marzeion B, Jarosch AH and Hofer M (2012) Past and future sea-level change from the surface mass balance of glaciers. *The Cryosphere*, **6**(6), 1295–1322, ISSN 1994-0424 (doi: 10.5194/tc-6-1295-2012) 1.2.2
- Marzeion B, Jarosch AH and Gregory JM (2014) Feedbacks and mechanisms affecting the global sensitivity of glaciers to climate change. *The Cryosphere*, **8**(1), 59–71 (doi: 10.5194/tc-8-59-2014) 1.2.2
- Mattson LE and Gardner JS (1993) Ablation on Debris Covered Glaciers : an Example from the Rakhiot Glacier , Punjab , Himalaya. *Snow and Glacier Hydrology*, **218**, 289–296 1.2.2
- Meier MFMF, Dyurgerov MB, Rick UK, O’Neel S, Pfeffer WT, Anderson RS, Anderson SP and Glazovsky AF (2007) Glaciers Dominate Eustatic Sea-Level Rise in the 21st Century. *Science* 1.2.1, 1.2.2
- Miles E (2016) *Spatio-temporal variability and energy-balance implications of surface ponds on Himalayan debris-covered glaciers*. Phd thesis, University of Cambridge 2.2, 2.3, 8.2
- Miles ES, Willis I, Pellicciotti F, Steiner JF, Buri P and Arnold N (2016) Refined energy-balance modelling of a supraglacial pond, Langtang Khola, Nepal. *Annals of Glaciology*, **57**(71), 29–40 (doi: 10.3189/2016AoG71A421) 2.3, 3.1, 5.2, 5.5.3, 6.1, 6.4, 3, 7.1, 7.2, 7.5, 7.6.1, 7.6.3
- Miles ES, Steiner JF and Brun F (2017a) Highly variable aerodynamic roughness length (z_0) for a hummocky debris-covered glacier. *Journal of Geophysical Research: Atmospheres*, ISSN 2169897X (doi: 10.1002/2017JD026510) 1.2.2, 2.3, 3.1, 8.3
- Miles ES, Willis IC, Arnold NS, Steiner JF and Pellicciotti F (2017b) Spatial, seasonal and interannual variability of supraglacial ponds in the langtang valley of nepal, 19992013. *Journal of Glaciology*, **63**(237), 88105 (doi: 10.1017/jog.2016.120) 8.2
- Miles ES, Steiner J, Willis I, Buri P, Immerzeel WW, Chesnokova A and Pellicciotti F (2017c) Pond dynamics and supraglacial-englacial connectivity on debris-covered lirung glacier, nepal. *Frontiers in Earth Science*, **5**(69), ISSN 2296-6463 (doi: 10.3389/feart.2017.00069) 3.1
- Mölg T (2003) Solar-radiation-maintained glacier recession on Kilimanjaro drawn from combined ice-radiation geometry modeling. *Journal of Geophysi-*

-
- cal Research*, **108**(D23), 4731, ISSN 0148-0227 (doi: 10.1029/2003JD003546)
1.2.3
- Naito N, Kadota T, Fujita K, Sakai A and Nakawo M (2002) Surface lowering over the ablation area of Lirung Glacier, Nepal Himalayas. *Bulletin of Glacier Research*, **19**, 41–4 2.3
- Nash J and Sutcliffe J (1970) River flow forecasting through conceptual models part I – A discussion of principles. *Journal of Hydrology*, **10**(3), 282–290, ISSN 00221694 (doi: 10.1016/0022-1694(70)90255-6) 8.3, 8.4, C.2, C.3, C.4, C.5, C.6, C.7, C.8, C.9, C.10, C.11, C.12, C.13, C.14, C.18, C.19, C.20, C.21, C.22, C.23
- Nicholson L and Benn DI (2006) Calculating ice melt beneath a debris layer using meteorological data. *Journal of Glaciology*, **52**(178), 463–470 1.2.2, 6.1
- Nicholson L and Benn DI (2013) Properties of natural supraglacial debris in relation to modelling sub-debris ice ablation. *Earth Surface Processes and Landforms*, **38**(5), 490–501, ISSN 01979337 (doi: 10.1002/esp.3299) 1.2.2
- Numura T, Fujita K, Yamaguchi S and Sharma R (2012) Elevation changes of glaciers revealed by multitemporal digital elevation models calibrated by GPS survey in the Khumbu region, Nepal Himalaya, 1992–2008. *Journal of Glaciology*, **58**(210), 648–656, ISSN 00221430 (doi: 10.3189/2012JoG11J061) 1.1, 5.1, 5.5.3
- Numura T, Fujita K and Sakai A (2017) Downwasting of the debris-covered area of Lirung Glacier in Langtang Valley, Nepal Himalaya, from 1974 to 2010. *Quaternary International*, ISSN 10406182 (doi: 10.1016/j.quaint.2017.06.066) 7.6.1
- Ohmura A (1968) The Computation of Direct Insolation on a Slope. *Climatological Bulletin*, **3**(1963), 42–53 5.4.2
- Olson DL and Delen D (2008) *Advanced Data Mining Techniques*. Springer Science + Business Media (doi: 10.1007/978-3-540-76917-0) 6.4.2
- Østrem G (1959) Ice melting under a thin layer of moraine, and the existence of ice cores in moraine ridges. *Geografiska Annaler*, **41**(4), 228–230 1.1, 1.2.2, 6.1, 7.1
- Pellicciotti F, Brock B, Strasser U, Burlando P, Funk M and Corripio J (2005) An enhanced temperature-index glacier melt model including the short-wave radiation balance: development and testing for Haut Glacier d’Arolla,

- Switzerland. *Journal of Glaciology*, **51**(175), 573–587, ISSN 00221430 (doi: 10.3189/172756505781829124) 1.2.4
- Pellicciotti F, Stephan C, Miles E, Herreid S, Immerzeel W and Bolch T (2015) Mass-balance changes of the debris-covered glaciers in the Langtang Himal, Nepal, 1974–99. *Journal of Glaciology*, **61**(226), 373–386 (doi: 10.3189/2015JoG13J237) 1.1, 1.2.2, 2.3, 5.1, 5.2, 6.1
- Pepin N, Bradley RS, Diaz HF, Baraer M, Caceres EB, Forsythe N, Fowler H, Greenwood G, Hashmi MZ, Liu XD, Miller JR, Ning L, Ohmura A, Palazzi E, Rangwala I, Schöner W, Severson I, Shahgedanova M, Wang MB, Williamson SN and Yang DQ (2015) Elevation-dependent warming in mountain regions of the world. *Nature Climate Change*, **5**(5), 424–430 (doi: 10.1038/nclimate2563) 1.2.1
- Petersen L and Pellicciotti F (2011) Spatial and temporal variability of air temperature on a melting glacier: Atmospheric controls, extrapolation methods and their effect on melt modeling, Juncal Norte Glacier, Chile. *Journal of Geophysical Research*, **116**(D23), D23109, ISSN 0148-0227 (doi: 10.1029/2011JD015842) 3.2, 5.3.1, C.1
- Pickard J (1983) Short notes: Surface lowering of ice-cored moraine by wandering lakes. *Journal of Glaciology*, **29**(102), 338–342 6.4, 3, 7.6.3
- Plüss C and Ohmura A (1997) Longwave radiation on snow-covered mountainous surfaces. *J. Appl. Meteor.*, **36**(6), 818–824 (doi: 10.1175/1520-0450-36.6.818) 5.4.3
- Pritchard HD (2017) Asia’s glaciers are a regionally important buffer against drought. *Nature*, **545**(7653), 169–174, ISSN 0028-0836 (doi: 10.1038/nature22062) 1.2.1, 7
- Purdie J and Fitzharris B (1999) Processes and rates of ice loss at the terminus of Tasman Glacier, New Zealand. *Global and Planetary Change*, **22**(1-4), 79–91, ISSN 09218181 (doi: 10.1016/S0921-8181(99)00027-2) 1.2.3, 6.1
- R Core Team (2015) *R: A Language and Environment for Statistical Computing*. R Foundation for Statistical Computing, Vienna, Austria 6.4.1, 6.7, 7.6.3
- Radić V and Hock R (2011) Regionally differentiated contribution of mountain glaciers and ice caps to future sea-level rise. *Nature Geoscience*, **4**(2), 91–94, ISSN 1752-0894 (doi: 10.1038/ngeo1052) 1.2.2

-
- Ragetli SG (2014) *Modeling the response of high-elevation, glacierized watersheds to climate change: A new methodological framework applied to the Andes and the Himalaya*. Phd thesis, ETH Zurich (doi: 10.3929/ETHZ-A-010394813) 1.2.4
- Ragetli S and Pellicciotti F (2012) Calibration of a physically based, spatially distributed hydrological model in a glacierized basin: On the use of knowledge from glaciometeorological processes to constrain model parameters. *Water Resources Research*, **48**(3), n/a–n/a, ISSN 00431397 (doi: 10.1029/2011WR010559) 1.2.4
- Ragetli S, Cortés G, McPhee J and Pellicciotti F (2013a) An evaluation of approaches for modelling hydrological processes in high-elevation, glacierized Andean watersheds. *Hydrological Processes*, n/a–n/a, ISSN 08856087 (doi: 10.1002/hyp.10055) 1.2.4
- Ragetli S, Pellicciotti F, Bordoy R and Immerzeel W (2013b) Sources of uncertainty in modeling the glaciohydrological response of a Karakoram watershed to climate change. *Water Resources Research*, **49**(9), 6048–6066, ISSN 00431397 (doi: 10.1002/wrcr.20450) 1.2.4
- Ragetli S, Pellicciotti F, Immerzeel WW, Miles ES, Petersen L, Heynen M, Shea JM, Stumm D, Joshi S and Shrestha A (2015) Unraveling the hydrology of a Himalayan catchment through integration of high resolution in situ data and remote sensing with an advanced simulation model. *Advances in Water Resources*, **78**, 94–111 (doi: 10.1016/j.advwatres.2015.01.013) 1.1, 1.2.1, 1.2.4, 2.2, 2.3, 5.2, 5.5.2, 6.6.4, 8.1, 8.2, 8.3
- Ragetli S, Bolch T and Pellicciotti F (2016a) Heterogeneous glacier thinning patterns over the last 40 years in Langtang Himal, Nepal. *The Cryosphere*, **10**(5), 2075–2097 (doi: 10.5194/tc-10-2075-2016) 1.1, 1.1, 1.2.2, 1.2.3, 2.3, 3.2, 6.1, 7.1, 8.2, C.1
- Ragetli S, Immerzeel WW and Pellicciotti F (2016b) Contrasting climate change impact on river flows from high-altitude catchments in the himalayan and andes mountains. *Proceedings of the National Academy of Sciences*, **113**(33), 9222–9227 (doi: 10.1073/pnas.1606526113) 1.2.4
- Rana B (1997) Application of a conceptual precipitation-runoff model (HYCY-MODEL) in a debris-covered glacierized basin in the Langtang Valley, Nepal Himalaya. *Annals of Glaciology*, **25**, 226–231 5.5.2

- Raper SCB and Braithwaite RJ (2006) Low sea level rise projections from mountain glaciers and icecaps under global warming. *Nature*, **439**(7074), 311–313, ISSN 0028-0836 (doi: 10.1038/nature04448) 1.2.2
- Reid T and Brock B (2014) Assessing ice-cliff backwasting and its contribution to total ablation of debris-covered Miage glacier, Mont Blanc massif, Italy. *Journal of Glaciology*, **60**(219), 3–13, ISSN 00221430 (doi: 10.3189/2014JoG13J045) (document), 1.1, 1.2.3, 1.2.3, 4.2, 4.2, 5.1, 5.4, 5.4, 5.4.4, 5.5.2, 5.5.3, 6.1, 2, 6.4.1, 6.6.4, A.1
- Reid TD, Carenzo M, Pellicciotti F and Brock BW (2012) Including debris cover effects in a distributed model of glacier ablation. *J. Geophys. Res.*, **117**(D18) (doi: 10.1029/2012jd017795) 1.2.2, 5.1
- Reindl D, Beckman W and Duffie J (1990) Diffuse fraction correlations. *Solar Energy*, **45**(1), 1–7 4.2, 5.4.2, 5.4.2
- Rittger K, Painter TH and Dozier J (2013) Assessment of methods for mapping snow cover from MODIS. *Advances in Water Resources*, **51**, 367–380 (doi: 10.1016/j.advwatres.2012.03.002) 6.4.2, 6.4.2
- Roehl K (2008) Characteristics and evolution of supraglacial ponds on debris-covered Tasman Glacier, New Zealand. *Journal of Glaciology*, **54**(188), 867–880 6.4
- Rounce DR, Quincey DJ and McKinney DC (2015) Debris-covered glacier energy balance model for Imja–Lhotse Shar Glacier in the Everest region of Nepal. *The Cryosphere*, **9**(6), 2295–2310 (doi: 10.5194/tc-9-2295-2015) 1.2.2, 6.6.3
- Rowan AV, Egholm DL, Quincey DJ and Glasser NF (2015) Modelling the feedbacks between mass balance, ice flow and debris transport to predict the response to climate change of debris-covered glaciers in the Himalaya. *Earth and Planetary Science Letters*, **430**, 427–438 1.2.2, 7.1
- Sakai A, Nakawo M and Fujita K (1998) Melt rate of ice cliffs on the Lirung glacier, Nepal Himalayas, 1996. *Bull. Glacier Res*, **16**, 57–66 1.1, 1.2.3, 1.2.3, 2.3, 5.1, 5.2, 5.5.2, 6.1, 6.4, 6.6.4, 7.1, 7.3, 7.6.1
- Sakai A, Takeuchi N, Fujita K and Nakawo M (2000) Role of supraglacial ponds in the ablation process of a debris-covered glacier in the Nepal Himalayas. *IAHS Publ. 265*, 119–132 1.1, 2.3, 5.2, 6.1, 7.1
- Sakai A, Nakawo M and Fujita K (2002) Distribution characteristics and energy balance of ice cliffs on debris-covered glaciers, Nepal Himalaya. *Arctic*,

-
- Antarctic, and Alpine Research*, 12–19 1.1, 1.1, 1.2.3, 2.3, 5.1, 5.5.2, 7.1, 7.4, 7.6.1
- Sakai A, Fujita K and Kubota J (2004) Evaporation and percolation effect on melting at debris-covered Lirung Glacier, Nepal Himalayas, 1996. *Bulletin of Glacier Research*, **21**, 9–15 7.6.1
- Sakai A, Nishimura K, Kadota T and Takeuchi N (2009) Onset of calving at supraglacial lakes on debris-covered glaciers of the Nepal Himalaya. *Journal of Glaciology*, **55**(193), 909–917, ISSN 00221430 (doi: 10.3189/002214309790152555) 3
- Schauwecker S, Rohrer M, Huggel C, Kulkarni A, Ramanathan AL, Salzmann N, Stoffel M and Brock B (2015) Remotely sensed debris thickness mapping of Bara Shigri Glacier, Indian Himalaya. *Journal of Glaciology*, **61**(228), 675–688, ISSN 00221430 (doi: 10.3189/2015JoG14J102) 1.2.2
- Scherler D, Bookhagen B and Strecker M (2011) Spatially variable response of Himalayan glaciers to climate change affected by debris cover. *Nature Geoscience*, **4**(3), 156–159, ISSN 1752-0894 (doi: 10.1038/ngeo1068) 1.2.2, 6.1, 7.1
- Seko K (1987) Seasonal variation of altitudinal dependence of precipitation in Langtang Valley, Nepal Himalayas. *Bulletin of Glaciological Research*, **5**, 41–47 2.2
- Shangguan D, Liu S, Ding Y, Wu L, Deng W, Guo W, Wang Y, Xu J, Yao X, Guo Z and Zhu W (2014) Glacier changes in the Koshi River basin, central Himalaya, from 1976 to 2009, derived from remote-sensing imagery. *Annals of Glaciology*, **55**(66), 61–68, ISSN 02603055 (doi: 10.3189/2014AoG66A057) 1.2.1
- Sharp RP (1947) The Wolf Creek Glaciers, St. Elias Range, Yukon Territory. *Geographical Review*, **37**(1), 26–52, ISSN 00167428 (doi: 10.2307/211360) 1.2.3
- Sharp RP (1949) Studies of superglacial debris on valley glaciers. *American Journal of Science*, **247**(5), 289–315 (doi: 10.2475/ajs.247.5.289) 1.2.3
- Shiraiwa T and Yamada T (1992) Glacier Inventory of the Langtang Valley, Nepal Himalayas. *Low Temperature Science, Series A, Physical sciences. Data report*, **50**, 47–72 5.2

- Steinegger U, Braun LN, Kappenberger G and Tartari G (1993) Assessment of Annual Snow Accumulation over the Past 10 Years at High Elevations in the Langtang Region. In *Snow and Glacier Hydrology*, 218, 155–166 2.2
- Steiner J (2014) *Modeling Ice Cliff Backwasting on a debris-covered Glacier*. Master thesis, ETH Zurich 8.2, 8.2, C.4, C.5
- Steiner JF and Pellicciotti F (2016) Variability of air temperature over a debris-covered glacier in the Nepalese Himalaya. *Annals of Glaciology*, **57**(71), 295–307 (doi: 10.3189/2016aog71a066) (document), 2.2, 3.1, 6.2, 6.6.3, 7.6.2, 8.2, 8.2, C.1, C.1, C.3, C.2, C.4, C.15
- Steiner J, Pellicciotti F, Buri P, Miles E, Immerzeel W and Reid T (2015) Modeling ice cliff backwasting on a debris covered glacier in the Nepalese Himalayas. *Journal of Glaciology*, **61**(229), 889–907 (doi: 10.3189/2015JoG14J194) 1.1, 2.3, 3.1, 3.2, 5.1, 5.2, 5.3.1, 5.3.3, 5.4, 5.4.3, 5.4.3, 5.4.4, 5.4.5, 5.2, 5.5.1, 6.1, 6.2, 2, 6.4.1, 6.6.3, 7.2, 7.4, 7.6.1, 7.6.2, 7.6.3, 7.6.3, 7.6.3, 8.2, 8.2, 8.2.1
- Suzuki R, Fujita K and Ageta Y (2007) Spatial distribution of thermal properties on debris-covered glaciers in the Himalayas derived from ASTER data. *Bulletin of Glacier Research*, **24**, 13–22 1.2.2
- Tachikawa T, Hato M, Kaku M and Iwasaki A (2011) Characteristics of ASTER GDEM version 2. In *2011 IEEE International Geoscience and Remote Sensing Symposium*, IEEE (doi: 10.1109/igarss.2011.6050017) 3.2, 5.3.2, 6.4.1
- Takeuchi Y, Kayastha RB and Nakawo M (2000) Characteristics of ablation and heat balance in debris-free and debris-covered areas on Khumbu Glacier, Nepal Himalayas, in the pre-monsoon season. *IAHS Publication*, **264**(2), 53–61, ISSN 0144-7815 1.2.2
- Takeuchi N, Sakai A, Kohshima S, Fujita K and Nakawo M (2012) Variation in Suspended Sediment Concentration of Supraglacial Lakes on Debris-covered Area of the Lirung Glacier in the Nepal Himalayas. *Global Environmental Research*, **16**, 95–104 2.3
- Thompson S, Benn DI, Mertes J and Luckman A (2016) Stagnation and mass loss on a Himalayan debris-covered glacier: processes, patterns and rates. *Journal of Glaciology*, **62**(233), 467–485 (doi: 10.1017/jog.2016.37) 1.2.3, 1.2.3, 6.1, 6.4, 6.6.4, 7.1

-
- Unsworth M and Monteith J (1975) Long-wave radiation at the ground I. Angular distribution of incoming radiation. *Quart. J. R. Met. SOC*, **101**, 13–24
5.4.3, 8.2, C.5
- Uppala SM et al. (2005) The era-40 re-analysis. *Quarterly Journal of the Royal Meteorological Society*, **131**(612), 2961–3012, ISSN 1477-870X (doi: 10.1256/qj.04.176) 2.2
- Vincent C, Wagnon P, Shea JM, Immerzeel WW, Kraaijenbrink P, Shrestha D, Soruco A, Arnaud Y, Brun F, Berthier E and Sherpa SF (2016) Reduced melt on debris-covered glaciers: investigations from Changri Nup Glacier, Nepal. *The Cryosphere*, **10**(4), 1845–1858, ISSN 1994-0424 (doi: 10.5194/tc-10-1845-2016) 7.1
- Watanabe O, Fushimi H, Inoue J, Iwata S, Ikegami K, Tanaka Y, Yoshida M and Upadhyay BP (1980) Outline of Debris Cover Project in Khumbu Glacier. *Journal of the Japanese Society of Snow and Ice*, **41**(Special), 5–8 (doi: 10.5331/seppyo.41.Special_5) 1.2.3
- Watson R (1980) Landform development on moraines of the Klutlan Glacier, Yukon Territory, Canada. *Quaternary Research*, **14**(1), 50 – 59, ISSN 0033-5894 (doi: [http://dx.doi.org/10.1016/0033-5894\(80\)90006-X](http://dx.doi.org/10.1016/0033-5894(80)90006-X)) 6.4, 3, 7.6.3
- Watson CS, Quincey DJ, Carrivick JL and Smith MW (2016) The dynamics of supraglacial ponds in the Everest region, central Himalaya. *Global and Planetary Change*, **142**, 14–27 (doi: 10.1016/j.gloplacha.2016.04.008) 6.6.3
- Watson CS, Quincey DJ, Carrivick JL and Smith MW (2017) Ice cliff dynamics in the Everest region of the Central Himalaya. *Geomorphology*, **278**, 238–251 (doi: 10.1016/j.geomorph.2016.11.017) 1.1, 1.2.3, 1.2.3, 7.1
- Weidinger JT, Schramm JM and Nuschej F (2002) Ore mineralization causing slope failure in a high-altitude mountain crest - On the collapse of an 8000 m peak in Nepal. *Journal of Asian Earth Sciences*, **21**(3), 295–306, ISSN 13679120 (doi: 10.1016/S1367-9120(02)00080-9) 2.1
- Wickham H (2009) *ggplot2: elegant graphics for data analysis*. Springer New York, ISBN 978-0-387-98140-6 6.7
- Winkler M, Kaser G, Cullen NJ, Mölg T, Hardy DR and Pfeffer WT (2010) Land-based marginal ice cliffs: Focus on Kilimanjaro. *Erdkunde*, **64**(2), 179–193, ISSN 00140015 (doi: 10.3112/erdkunde.2010.02.05) (document), 1.2.3, 1.3

- Winkler M, Pfeffer WT and Hanke K (2012) Kilimanjaro ice cliff monitoring with close range photogrammetry (doi: 10.5194/isprsarchives-xxxix-b5-441-2012) 1.2.3
- Wong L and Chow W (2001) Solar radiation model. *Applied Energy*, **69**(3), 191–224, ISSN 03062619 (doi: 10.1016/S0306-2619(01)00012-5) 4.1, 4.1
- Zhang Y, Fujita K, Liu S, Liu Q and Nuimura T (2011) Distribution of debris thickness and its effect on ice melt at Hailuogou glacier, southeastern Tibetan Plateau, using in situ surveys and ASTER imagery. *Journal of Glaciology*, **57**(206), 1147–1157, ISSN 00221430 (doi: 10.3189/002214311798843331) 1.2.2
- Zou KH, Warfield SK, Bharatha A, Tempany CM, Kaus MR, Haker SJ, Wells WM, Jolesz FA and Kikinis R (2004) Statistical validation of image segmentation quality based on a spatial overlap index. *Academic Radiology*, **11**(2), 178–189 (doi: 10.1016/s1076-6332(03)00671-8) 6.4.2

Appendix A.

Modelling radiative fluxes over complex cliff geometries: Results

In Fig. A.4 the modelled components of the incoming shortwave radiation for a slope are presented for three subsequent days. At the same time the incoming solar radiation was measured at the AWS (brown) close to the cliff as well as directly at the cliff slope (yellow). These measurements are also shown in the same figure for comparison. On the first day of the observed period (8 May) the peak of the modelled solar radiation income at the slope (orange) is clearly overestimated, whereas the magnitude fits better at the two following days. It can be seen that in the afternoon hours, when direct solar radiation is absent, the modelled and the observed curves fit quite well, as the diffuse component (mostly the one from the sky) is the main or even only contributor to the total income. The main source of error seems to lie in the morning data before noon. There is a distinct overestimation of total shortwave income in the morning in all three example days.

In Figs. A.5 to A.7 the incoming radiation is modelled along the cliff profiles. The three profiles which provide the topographical information (slope, aspect, skyview factor and debrisview factor) for the modelling are derived from the UAV-DEM from October 2013. A high variability can be seen from the top to the bottom of the cliffs, therefore it seems that the topographical characteristics (of the surrounded area or the one of the cliff itself) have a high influence on the solar radiation budget at the cliff.

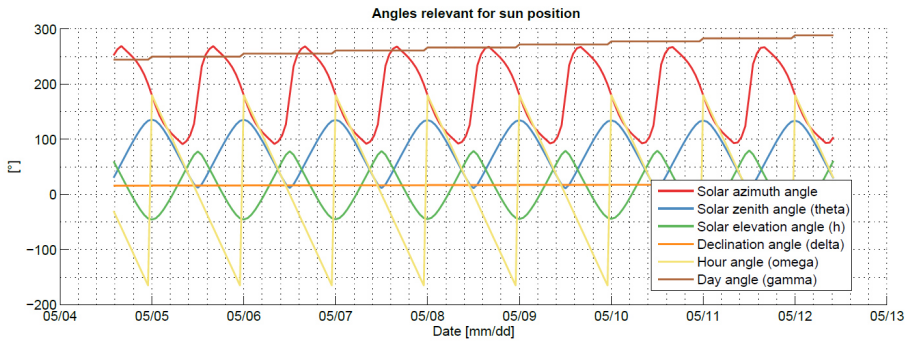


Figure A.1.: Time series of calculated sun-relevant angles according to Han et al. (2010) and Reid and Brock (2014) for Cliff 1 on Lirung Glacier at the position of the CNR1-instrument. With these angles the position of the sun can be determined for every timestep at a certain point. Note that the solar zenith and elevation angle (blue and green, respectively) sum up to 90° . The hour angle (yellow) decreases during the day and starts again at its highest daily level at midnight.

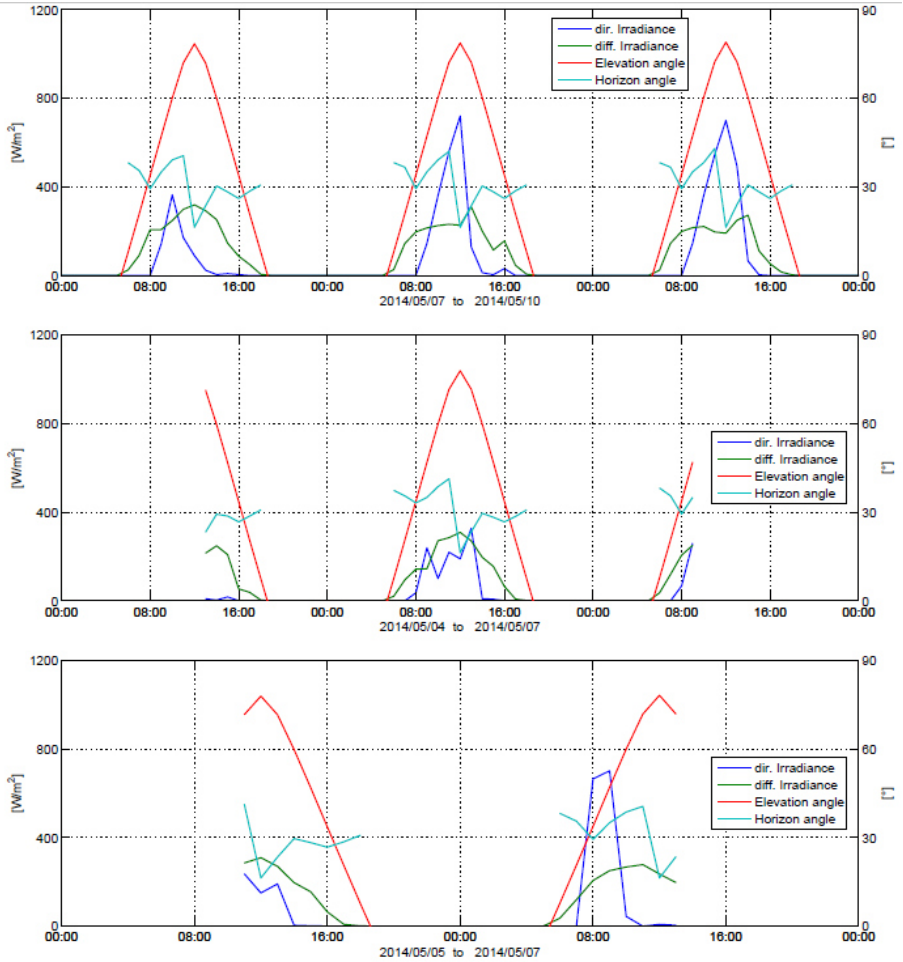


Figure A.2.: Time series of calculated direct and diffuse irradiance and two relevant angles for the direct solar radiation. The irradiances were calculated for three locations on Cliff 1 (centre: top panel, east profile: middle panel) as well as on the “south cliff” (bottom panel), each with a certain slope and aspect, according to Garnier and Ohmura (1968) and Han et al. (2010). The point in time where the solar elevation angle (red) exceeds the local horizon angle (light blue, derived from UAV DEM from October 2013) direct solar radiation (dark blue) on the cliff is possible if weather conditions are appropriate.

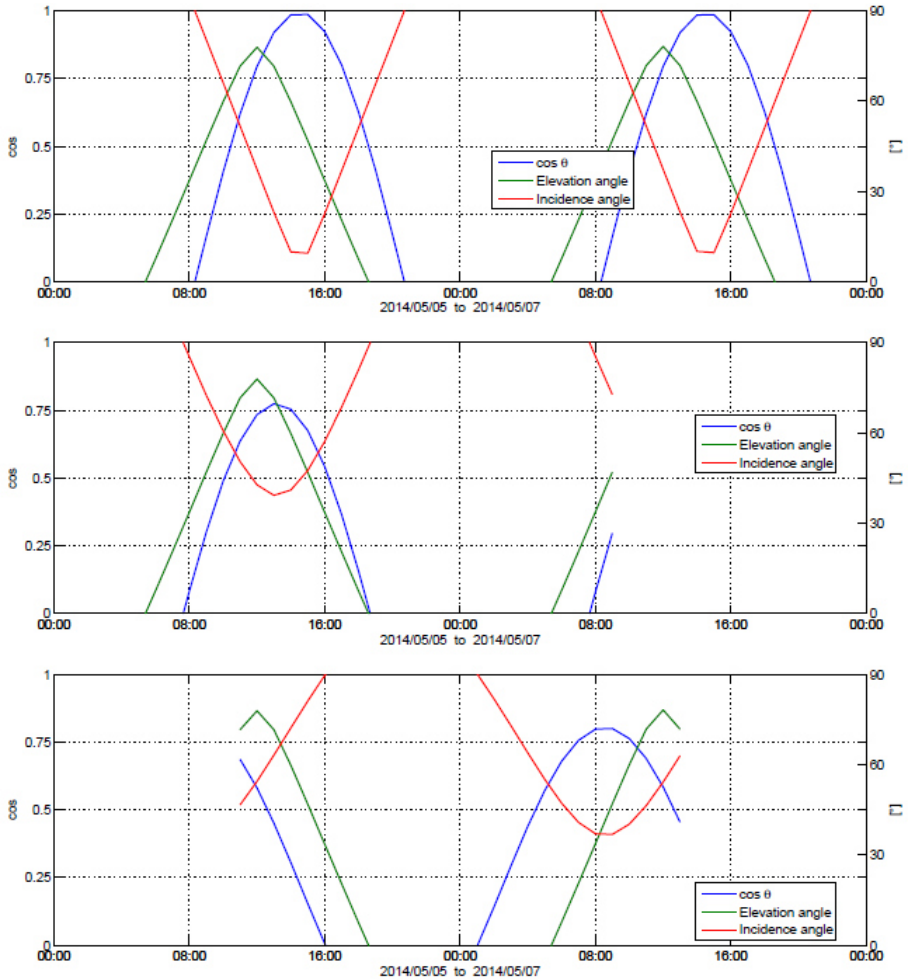


Figure A.3.: Time series of the elevation angle (green), incidence angle (red) as well as the cosine of the latter. The angles were calculated for three locations on Cliff 1 (centre: top panel, eastprofile: middle panel) and on the “south cliff” (bottom panel), each with a certain slope and aspect, according to Garnier and Ohmura (1968) and Han et al. (2010). It can be seen that the incidence angle is e.g. at the south cliff very low around noon due to the southern position of the sun at the same time. Accordingly the cosine is high at midday, as this factor reduces the normal direct irradiance I_b only slightly to the slope (Eq. 4.14).

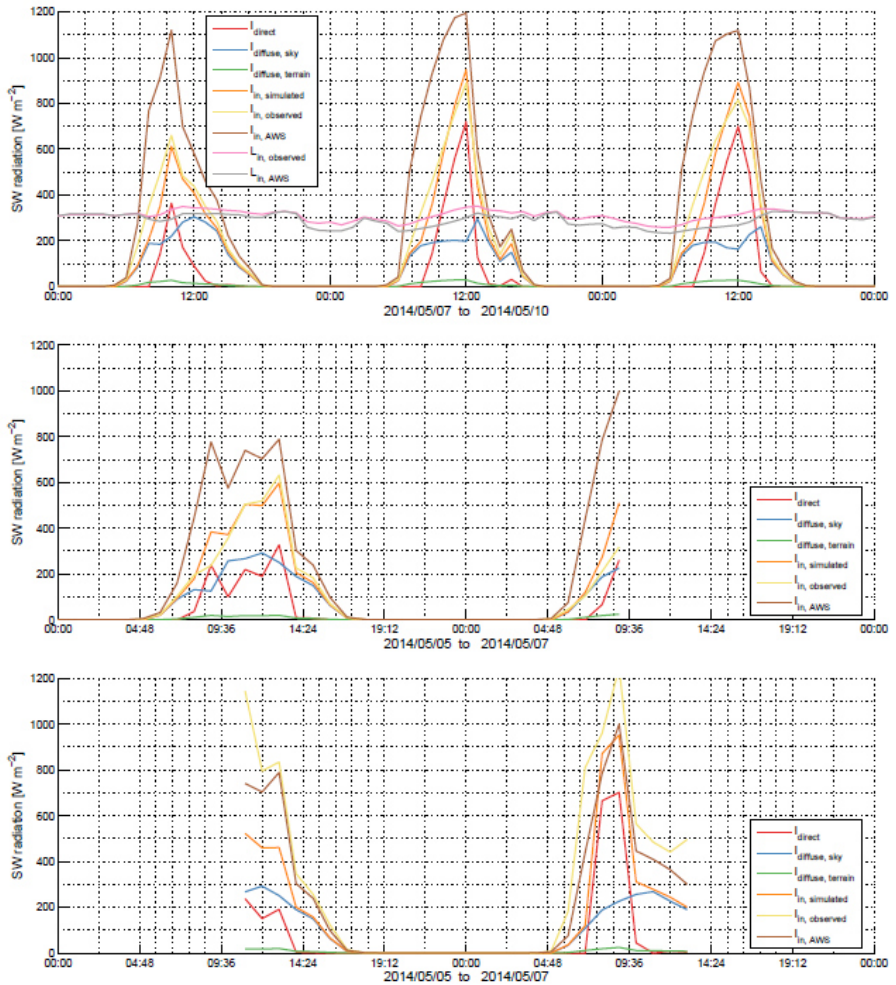


Figure A.4.: Time series of calculated direct and diffuse irradiance for a cliff slope as well as measured incoming and longwave radiation at the AWS and directly on the cliff. The values were calculated for three locations on Cliff 1 (centre: top panel, eastprofile: middle panel) and on the “south cliff” (bottom panel), each with a certain slope and aspect, according to Garnier and Ohmura (1968) and Han et al. (2010). The simulated slope radiation (diffuse and direct) is shown in orange, the actually measured solar radiation on the cliff can be seen in yellow. In brown the observations at the AWS, which provides the data for the simulations.

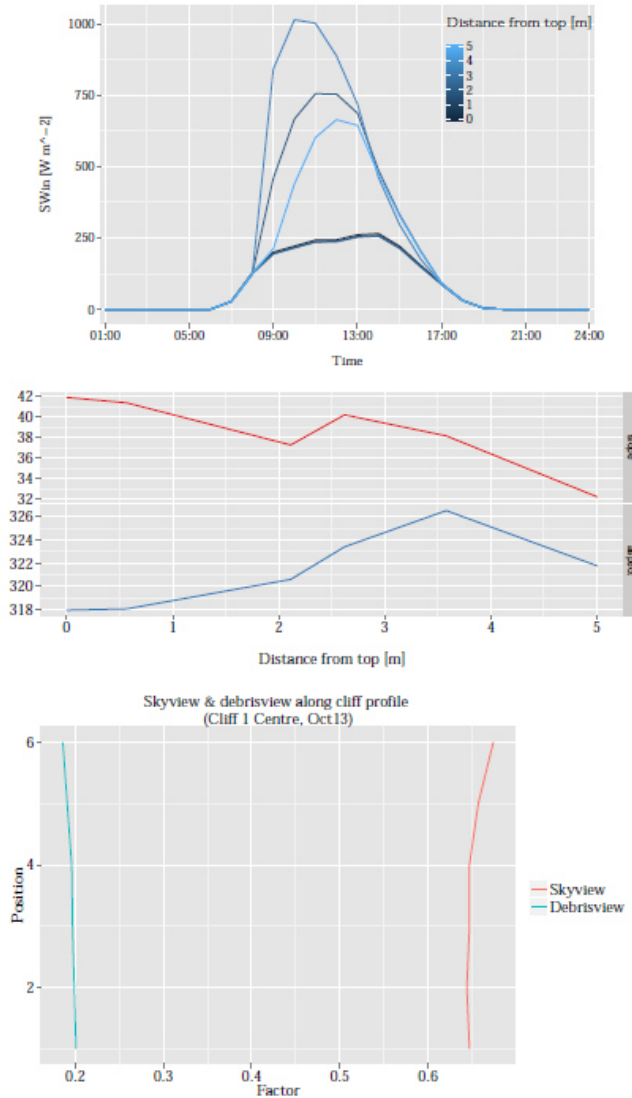


Figure A.5.: Top: diurnal cycle of modelled shortwave radiation along the central profile at Cliff 1 for a period of nine days in May 2014 (DEM from October 2013). Middle: topographical characteristics from profile derived from UAV-DEM. Bottom: Skyview and debrisview factors along the cliff profile.

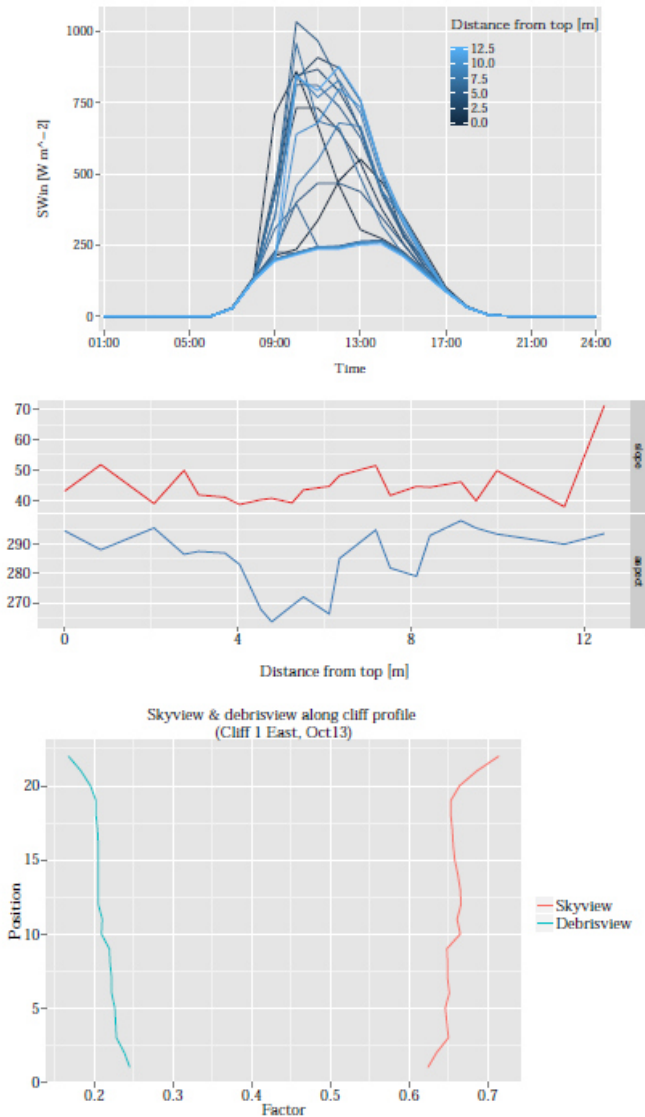


Figure A.6.: Top: diurnal cycle of modelled shortwave radiation along the east profile at Cliff 1 for a period of nine days in May 2014 (DEM from October 2013). Middle: topographical characteristics from profile derived from UAV-DEM. Bottom: Skyview and debrisview factors along the cliff profile.

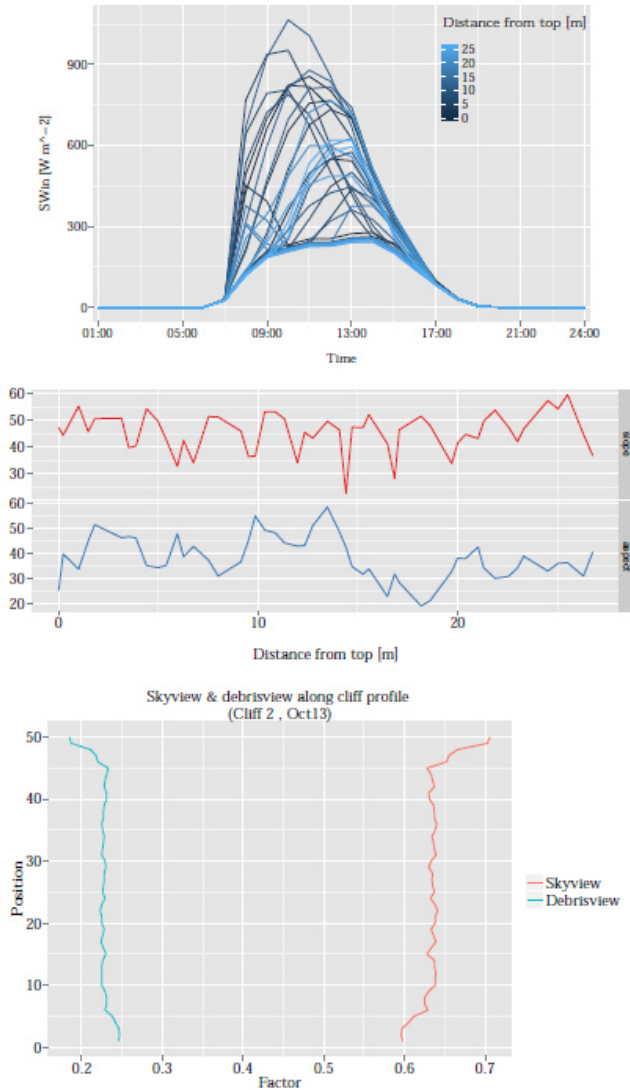


Figure A.7.: Top: diurnal cycle of modelled shortwave radiation along the central profile at Cliff 2 for a period of nine days in May 2014 (DEM from October 2013). Middle: topographical characteristics from profile derived from UAV-DEM. Bottom: Skyview and debrisview factors along the cliff profile.

Appendix B.

Ice cliff modelling at the glacier scale: Partitioning

Due to the big amount of cliff pixels (in the range of 10-100k per glacier), the glacier i.e. the cliff population has to be divided into multiple parts in order to distribute the computational costs in several model runs. This partitioning is done using an algorithm, which separates the glacier into sections according to the number of pixels. For our machine (Xeon 3.4GHz/31.9GB RAM) used for the simulation runs usually a cliff pixel number of about 3000 was feasible in terms of computation speed and memory. An example for the automatic partitioning can be found in Fig. B.1 (left). If cliffs or ponds are cut by a sector boundary line, affected polygons (shown in Fig. B.1, right) are always transferred to and evaluated in the next glacier sector downglacier within the simulation runs. To avoid discontinuities in the surrounding topography of ice cliffs located close to a boundary line, the above applied partitioning algorithm is only applied to the ice cliff entities, whereas the DEM is cropped 100m to the extent of ice each cliff individually in the ice cliff model code. Therefore each ice cliff, although close to a glacier sector line, is evaluated in the model incorporating its intended surrounding topography.

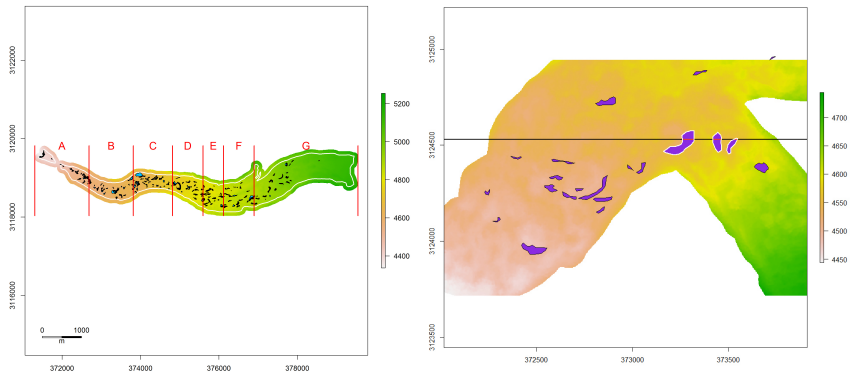


Figure B.1.: Left: Partitioning (red lines and labels) of Langshisha Glacier using an algorithm following cliff pixel distribution on the glacier. Cliffs and ponds are shown in black and blue, respectively. Right: Fine-scale partitioning on Langtang Glacier of cliffs (violet) or lakes (not shown) if cut by a sector boundary line (black). Affected cliffs, indicated here by a white outline, are always transferred to and evaluated in the next glacier sector downglacier within the simulation runs. The same procedure is valid for ponds.

Appendix C.

Ice cliff modelling at the glacier scale: Meteorological forcing

Table C.1.: Characteristics of the studied upper Langtang catchment. The measures are based on the SRTM 1 arcsec Global DEM and glacier outlines of 2006 (Tab. 1 from Ragettli et al. (2016a)).

	Name	Area (km ²)	Debris cover (km ²)	Mean slope (%)	Mean slope glacier tongue* (%)	AAR**	Elevation range m a.s.l.
1	Langtang	46.5	15.5	17.1	7.2	52 %	4479–6615
2	Langshisha	16.3	4.5	17.7	7.5	55 %	4415–6771
3	Shalbachum	10.2	2.6	16.9	9.1	52 %	4231–6458
4	Lirung	6.5	1.1	34.0	9.9	49 %	4044–7120
5	Ghanna	1.4	0.7	20.9	15.5	15 %	4721–5881
6	Kimoshung	4.4	–	24.4	32.1	86 %	4385–6648
7	Yala	1.9	–	22.7	20.3	40 %	5122–5676

* Here we consider the debris-covered area for glaciers with debris-covered tongues and all glacier area below 5400 m a.s.l. for debris-free glaciers.

** Assuming an equilibrium line altitude of 5400 m a.s.l. (Sugiyama et al., 2013; Ragettli et al., 2015).

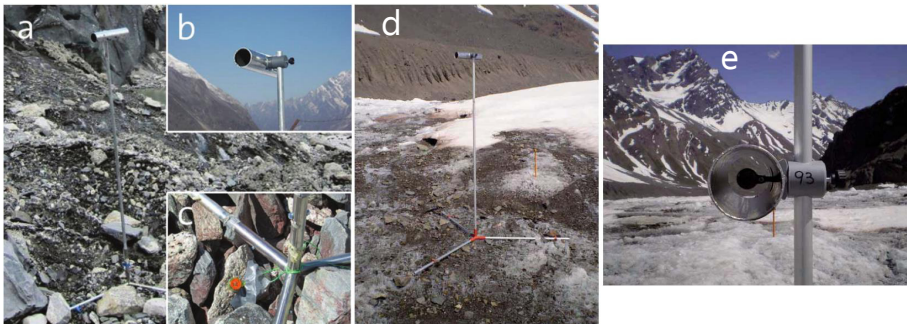


Figure C.1.: T-Logger structure (a and d), consisting of air temperature measurements 2m above glacier surface, where the sensor is placed in a cylinder shielded from solar radiation with aluminium foil and aligned in the direction of the valley (b and e), and a surface sensor taped to a rock and roped to the base structure (shown here without shielding; c) (Fig. 2 from Steiner and Pellicciotti (2016), a–c, and Fig. 2 from Petersen and Pellicciotti (2011), d–e). Example images from Lirung Glacier, Nepal (a–c) and Juncal Norte Glacier, Chile (d and e).

Table C.2.: Definition of seasons used in this study, based on Heynen et al. (2016).

Season	Short name	Start	End
Pre-monsoon	PRM	1 Mar	14 Jun
Monsoon	M	15 Jun	30 Sep
Post-monsoon	POM	1 Oct	30 Nov

C.1. Air temperature

This section presents timeseries of air temperature measured in the valley used for the meteorological forcing of the ice cliff model as described in Chapter 7 and applied to the glacier scale 8. Tab. C.3 shows the hour-specific valley- and glacier-lapse rates from Heynen et al. (2016) (valley) and Steiner and Pellicciotti (2016) (on-glacier). In Figs. C.2–C.14 daily values from May to October 2014 and diurnal cycles of measured and lapsed air temperature are visualized.

Table C.3.: Air temperature lapse rates derived for Langtang Valley for the 2013 season (Heynen et al., 2016) and for debris-covered Lirung Glacier for the 2014 season (Steiner and Pellicciotti, 2016), all subdivided into subseasons pre-monsoon (PRM), monsoon (M) and post-monsoon (POM).

Valley lapse rates 2013				Glacier lapse rates 2014			
Hour	PRM	M	POM	Hour	PRM	M	POM
0	-0.00601	-0.00429	-0.00516	0	-0.0051	-0.0037	-0.0044
1	-0.00601	-0.00430	-0.00509	1	-0.0048	-0.0036	-0.0046
2	-0.00597	-0.00430	-0.00508	2	-0.0047	-0.0036	-0.0051
3	-0.00593	-0.00427	-0.00501	3	-0.0049	-0.0035	-0.0053
4	-0.00588	-0.00425	-0.00491	4	-0.0042	-0.0036	-0.0054
5	-0.00581	-0.00425	-0.00482	5	-0.0050	-0.0036	-0.0053
6	-0.00576	-0.00421	-0.00485	6	-0.0064	-0.0036	-0.0060
7	-0.00555	-0.00429	-0.00487	7	-0.0177	-0.0079	0.0217
8	-0.00495	-0.00412	-0.00458	8	-0.0255	-0.0161	-0.0063
9	-0.00514	-0.00407	-0.00456	9	-0.0284	-0.0222	-0.0260
10	-0.00533	-0.00457	-0.00565	10	-0.0331	-0.0231	-0.0279
11	-0.00557	-0.00456	-0.00578	11	-0.0380	-0.0218	-0.0301
12	-0.00592	-0.00465	-0.00597	12	-0.0379	-0.0205	-0.0317
13	-0.00624	-0.00472	-0.00598	13	-0.0371	-0.0175	-0.0294
14	-0.00655	-0.00478	-0.00616	14	-0.0309	-0.0149	-0.0249
15	-0.00675	-0.00481	-0.00639	15	-0.0257	-0.0124	-0.0167
16	-0.00670	-0.00478	-0.00619	16	-0.0201	-0.0101	-0.0116
17	-0.00661	-0.00471	-0.00573	17	-0.0116	-0.0065	-0.0082
18	-0.00655	-0.00461	-0.00559	18	-0.0082	-0.0048	-0.0071
19	-0.00634	-0.00448	-0.00546	19	-0.0072	-0.0041	-0.0060
20	-0.00619	-0.00436	-0.00538	20	-0.0062	-0.0038	-0.0053
21	-0.00609	-0.00430	-0.00531	21	-0.0049	-0.0038	-0.0050
22	-0.00600	-0.00425	-0.00529	22	-0.0050	-0.0039	-0.0046
23	-0.00599	-0.00425	-0.00524	23	-0.0051	-0.0038	-0.0044

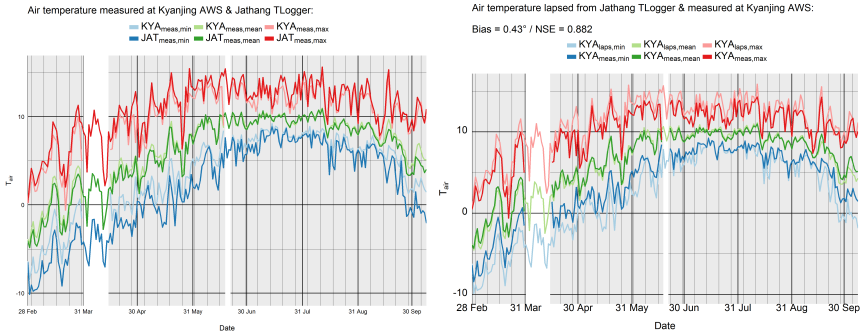


Figure C.2.: Timeseries of daily minimum, mean and maximum air temperature as measured at Kyanjing AWS (KYA) and Jathang T-Logger (JAT) in 2014 (left) and as measured at KYA and lapsed to KYA from JAT (right). The time period shown in white indicates the data gap in the KYA data. ‘Bias’ and ‘NSE’ show the bias of the lapsed values from the measured data and the Nash-Sutcliffe efficiency (Nash and Sutcliffe, 1970), respectively, both based on hourly temperature data.

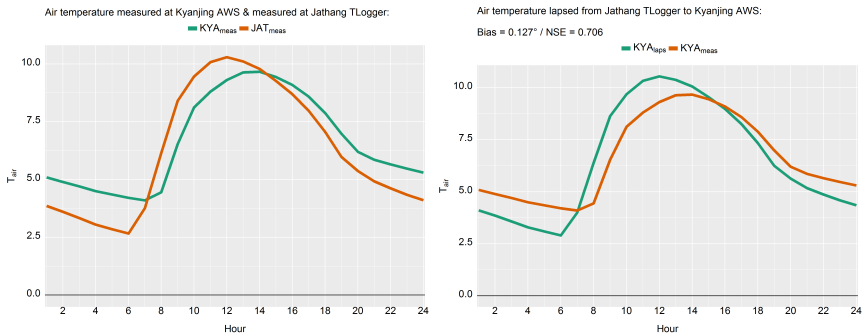


Figure C.3.: Diurnal cycle of hourly air temperature as measured at Kyanjing AWS (KYA) and Jathang T-Logger (JAT) in 2014 (left) and as measured at KYA and lapsed to KYS from JAT (right). ‘Bias’ and ‘NSE’ show the bias of the lapsed values from the measured data and the Nash-Sutcliffe efficiency (Nash and Sutcliffe, 1970), respectively, both based on hourly temperature data.

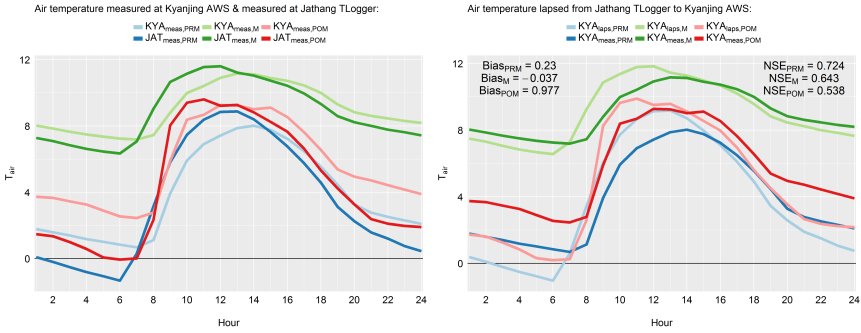


Figure C.4.: Seasonal diurnal cycles (pre-monsoon, monsoon and post-monsoon) of hourly air temperature as measured at Kyanjing AWS (KYA) and Jathang T-Logger (JAT) in 2014 (left) and as measured at KYA and lapsed to KYA from JAT from JAT (right). ‘Bias’ and ‘NSE’ show the seasonal bias of the lapsed values from the measured data and the seasonal Nash-Sutcliffe efficiency (Nash and Sutcliffe, 1970), respectively, both based on hourly temperature data.

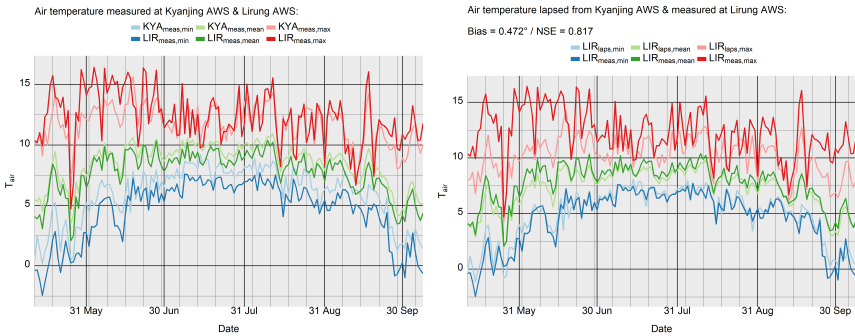


Figure C.5.: Timeseries of daily minimum, mean and maximum air temperature as measured at Kyanjing AWS (KYA) and Lirung AWS (LIR) in 2014 (left) and as measured at LGT and lapsed to LIR from KYA (right). ‘Bias’ and ‘NSE’ show the bias of the lapsed values from the measured data and the Nash-Sutcliffe efficiency (Nash and Sutcliffe, 1970), respectively, both based on hourly temperature data.

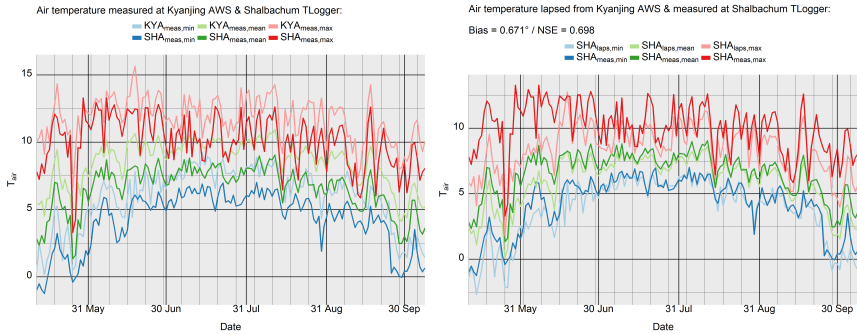


Figure C.6.: Timeseries of daily minimum, mean and maximum air temperature as measured at Kyanjing AWS (KYA) and Shalbachum T-Logger (SHA) in 2014 (left) and as measured at SHA and lapsed to SHA from KYA (right). ‘Bias’ and ‘NSE’ show the bias of the lapsed values from the measured data and the Nash-Sutcliffe efficiency (Nash and Sutcliffe, 1970), respectively, both based on hourly temperature data.

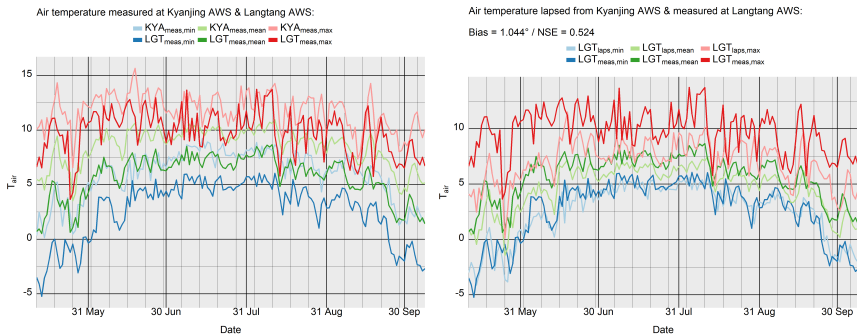


Figure C.7.: Timeseries of daily minimum, mean and maximum air temperature as measured at Kyanjing AWS (KYA) and Langtang AWS (LGT) in 2014 (left) and as measured at LGT and lapsed to LGT from KYA (right). ‘Bias’ and ‘NSE’ show the bias of the lapsed values from the measured data and the Nash-Sutcliffe efficiency (Nash and Sutcliffe, 1970), respectively, both based on hourly temperature data.

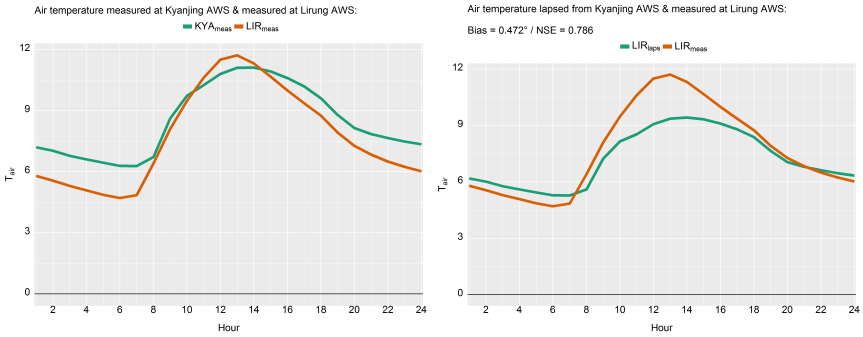


Figure C.8.: Diurnal cycle of hourly air temperature as measured at Kyanjing AWS (KYA) and Lirung AWS (LIR) in 2014 (left) and as measured at LIR and lapsed to LIR from KYA (right). ‘Bias’ and ‘NSE’ show the bias of the lapsed values from the measured data and the Nash-Sutcliffe efficiency (Nash and Sutcliffe, 1970), respectively, both based on hourly temperature data.

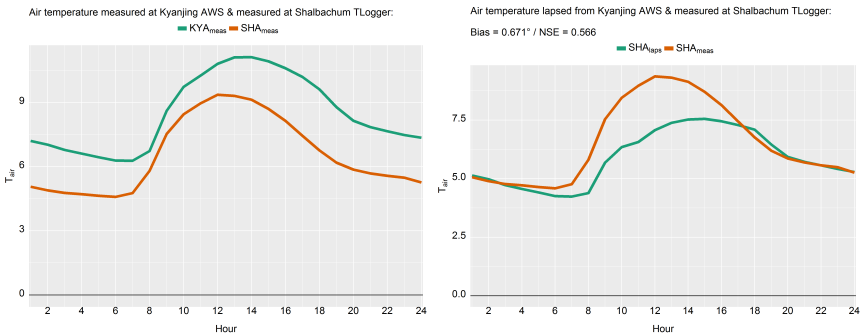


Figure C.9.: Diurnal cycle of hourly air temperature as measured at Kyanjing AWS (KYA) and Shalbachum T-Logger (SHA) in 2014 (left) and as measured at SHA and lapsed to SHA from KYA (right). ‘Bias’ and ‘NSE’ show the bias of the lapsed values from the measured data and the Nash-Sutcliffe efficiency (Nash and Sutcliffe, 1970), respectively, both based on hourly temperature data.



Figure C.10.: Diurnal cycle of hourly air temperature as measured at Kyanjing AWS (KYA) and Langtang AWS (LGT) in 2014 (left) and as measured at LGT and lapsed to LGT from KYA (right). ‘Bias’ and ‘NSE’ show the bias of the lapsed values from the measured data and the Nash-Sutcliffe efficiency (Nash and Sutcliffe, 1970), respectively, both based on hourly temperature data.

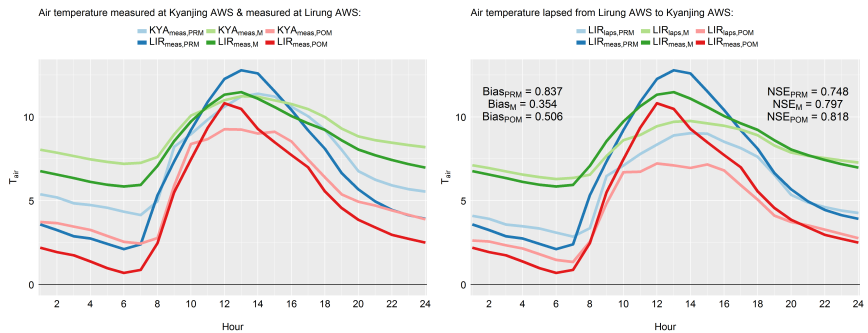


Figure C.11.: Seasonal diurnal cycles (pre-monsoon, monsoon and post-monsoon) of hourly air temperature as measured at Kyanjing AWS (KYA) and Lirung AWS (LIR) in 2014 (left) and as measured at LIR and lapsed to LIR from KYA (right). ‘Bias’ and ‘NSE’ show the seasonal bias of the lapsed values from the measured data and the seasonal Nash-Sutcliffe efficiency (Nash and Sutcliffe, 1970), respectively, both based on hourly temperature data.

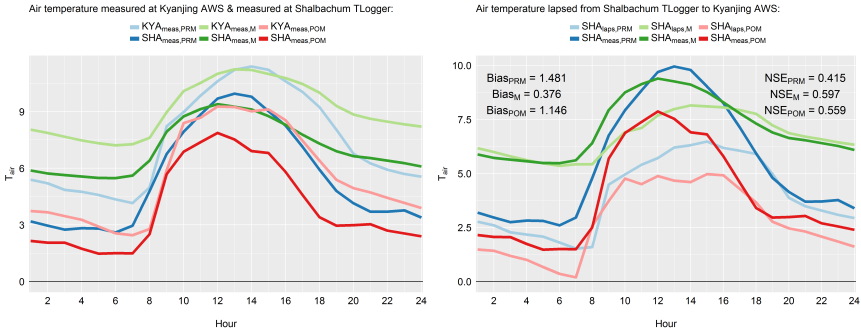


Figure C.12.: Seasonal diurnal cycles (pre-monsoon, monsoon and post-monsoon) of hourly air temperature as measured at Kyanjing AWS (KYA) and Shalbachum T-Logger (SHA) in 2014 (left) and as measured at SHA and lapsed to SHA from KYA (right). ‘Bias’ and ‘NSE’ show the seasonal bias of the lapsed values from the measured data and the seasonal Nash-Sutcliffe efficiency (Nash and Sutcliffe, 1970), respectively, both based on hourly temperature data.

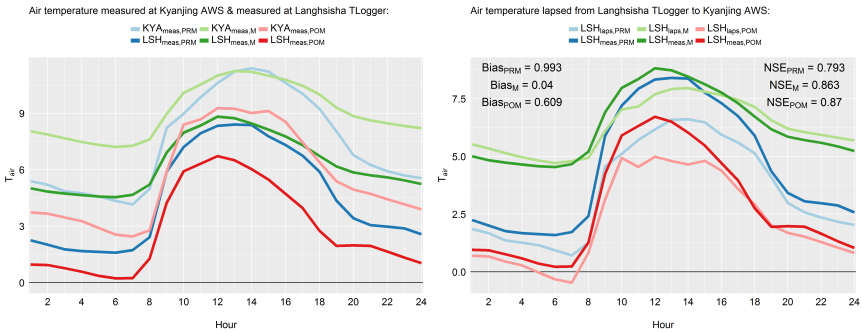


Figure C.13.: Seasonal diurnal cycles (pre-monsoon, monsoon and post-monsoon) of hourly air temperature as measured at Kyanjing AWS (KYA) and Langshisha T-Logger (LSH) in 2014 (left) and as measured at LSH and lapsed to LSH from KYA (right). ‘Bias’ and ‘NSE’ show the seasonal bias of the lapsed values from the measured data and the seasonal Nash-Sutcliffe efficiency (Nash and Sutcliffe, 1970), respectively, both based on hourly temperature data.

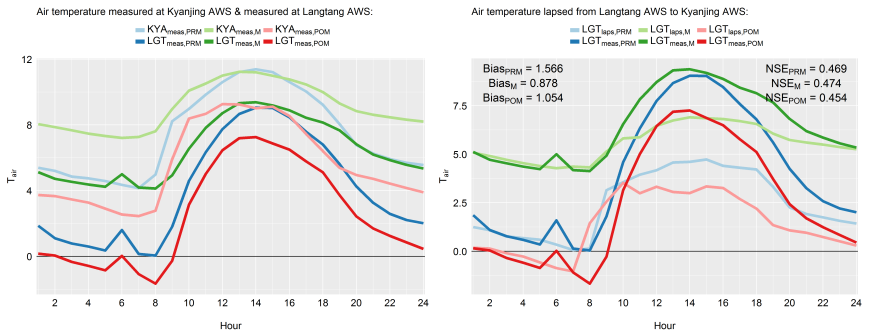


Figure C.14.: Seasonal diurnal cycles (pre-monsoon, monsoon and post-monsoon) of hourly air temperature as measured at Kyanjing AWS (KYA) and Langshisha AWS (LGT) in 2014 (left) and as measured at LGT and lapsed to LGT from KYA (right). ‘Bias’ and ‘NSE’ show the seasonal bias of the lapsed values from the measured data and the seasonal Nash-Sutcliffe efficiency (Nash and Sutcliffe, 1970), respectively, both based on hourly temperature data.

C.2. Surface temperature

This section presents timeseries of surface temperature measured in the valley used for the meteorological forcing of the ice cliff model as described in Chapter 7 and applied to the glacier scale 8. Tab. C.3 shows the season-specific parameter pairs for the relation between air- and surface temperature from Steiner and Pellicciotti (2016). Fig. C.4 presents an example of the relation between air- and surface temperature (Steiner and Pellicciotti, 2016) In Figs. C.16–C.24 daily values from May to October 2014 and diurnal cycles of measured and modelled surface temperature are visualized.

Table C.4.: Median slopes (a_1 and a_2) and intercepts (b_1 and b_2) of the piecewise regression for the $T_{air}-T_{surf}$ -relation in all three seasons in 2014 from Steiner and Pellicciotti (2016) (Tab. 3). The parameter pairs are for the lower and upper segment respectively, which are red and blue in Fig. C.15. $T_{c,surf}$ is the threshold surface temperature ($^{\circ}\text{C}$), $T_{c,air}$ is the threshold air temperature ($=T_{c,surf} \cdot a_2 + b_2$, $^{\circ}\text{C}$).

Season	a_1	b_1	a_2	b_2	$T_{c,surf}$	$T_{c,air}$
PRM	0.56	2.65	0.33	4.67	7.76	7.23
M	0.52	3.67	0.28	6.50	11.41	9.69
POM	0.59	1.84	0.29	4.00	5.83	5.69

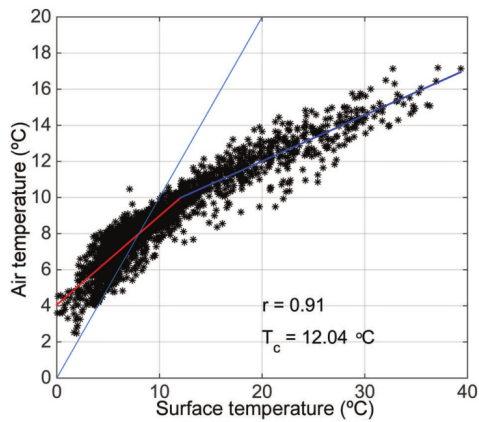


Figure C.15.: Example of determination of the piece-wise regressions for T-Logger 5 on Lirung Glacier in pre-monsoon 2013 from Steiner and Pellicciotti (2016) (Fig. 12). T_c is the threshold surface temperature where the two regression lines meet.

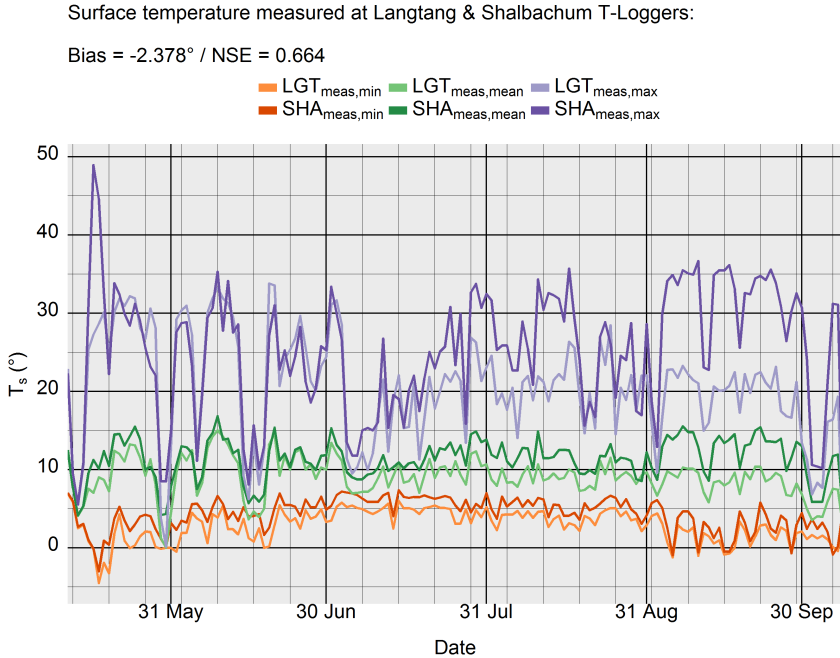


Figure C.16.: Timeseries of daily minimum, mean and maximum surface temperature as measured at Langtang (LGT) and Shalbachum (SHA) T-Loggers in 2013.

C.2.1. Comparison of surface temperatures on Langtang- and Shalbachum Glaciers

Because surface temperatures were not measured on Langtang Glacier in 2014 but in the year before, we compared the T-Logger data from Langtang Glacier measured in 2013 to the temporally consistent records on Shalbachum Glacier. The Shalbachum surface temperatures observed during the 2014 season could be possibly extrapolated to Langtang Glacier, using a lapse rate or a constant shift. More likely, the surface temperatures for Langtang Glacier could be derived from the $T_{air}-T_{surf}$ -relation, as T_{air} -records are available from the AWS Langtang during 2014.

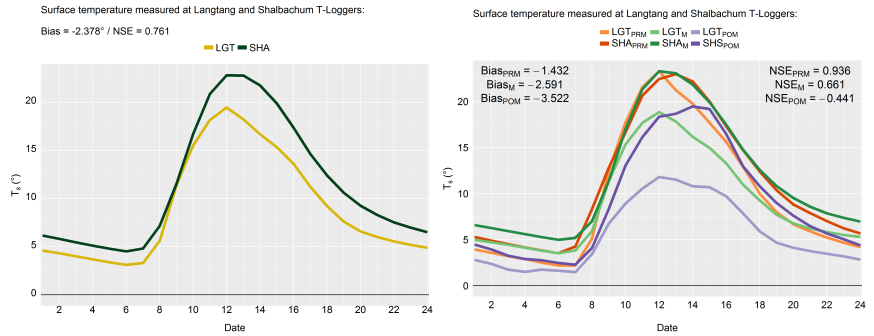


Figure C.17.: All year (left) and seasonal diurnal cycles (right) for pre-monsoon (PRM), monsoon (M) and post-monsoon (POM) of hourly surface temperature as measured at Langtang (LGT) and Shalbachum (SHA) T-Loggers in 2013.

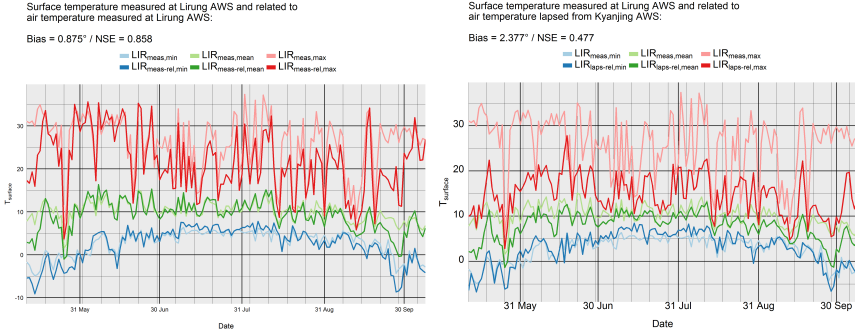


Figure C.18.: Timeseries of daily minimum, mean and maximum surface temperature as measured at Lirung AWS (LIR) in 2014 and related to measured air temperature (left), and surface temperature as measured at LIR and related to lapsed air temperature (right). ‘Bias’ and ‘NSE’ show the bias of the modelled values from the measured data and the Nash-Sutcliffe efficiency (Nash and Sutcliffe, 1970), respectively, both based on hourly temperature data.

C.2.2. Surface temperature measured and related to measured or lapsed air temperatures on Lirung- and Shalbachum Glacier

The only continuous on-glacier surface temperature measurements in 2014 were available for Lirung- (AWS) and Shalbachum Glacier (T-Logger). In the following plots we therefore show, first for Lirung- and then Shalbachum Glacier, a comparison of measured surface temperatures measured on-glacier (‘meas’) to either a) surface temperature derived from air temperatures directly measured on-glacier (‘meas-rel’) or b) surface temperature derived from air temperatures measured at Kyanjing AWS and then lapsed to the specific glacier (‘laps-rel’).

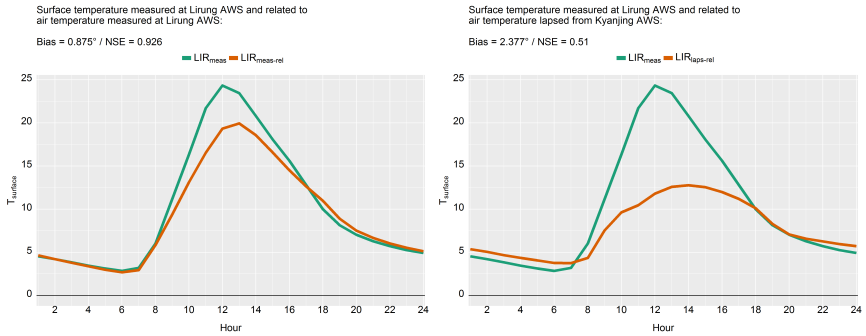


Figure C.19.: Diurnal cycle of hourly surface temperature as measured at Lirung AWS (LIR) in 2014 and related to measured air temperature (left), and surface temperature as measured at LIR and related to lapsed air temperature (right). ‘Bias’ and ‘NSE’ show the bias of the modelled values from the measured data and the Nash-Sutcliffe efficiency (Nash and Sutcliffe, 1970), respectively, both based on hourly temperature data.

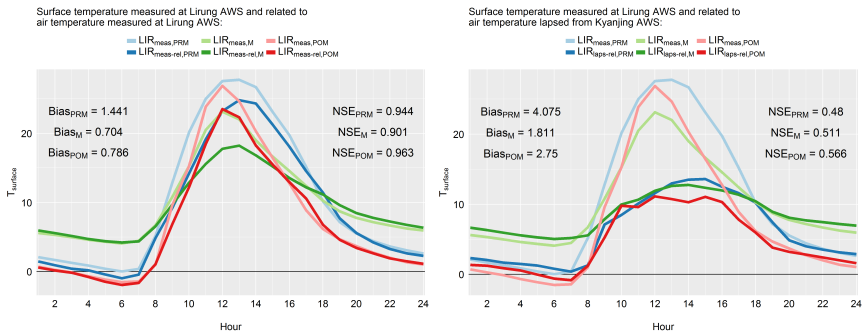


Figure C.20.: Seasonal diurnal cycle of hourly surface temperature as measured at Lirung AWS (LIR) in 2014 and related to measured air temperature (left), and surface temperature as measured at LIR and related to lapsed air temperature (right). ‘Bias’ and ‘NSE’ show the bias of the modelled values from the measured data and the Nash-Sutcliffe efficiency (Nash and Sutcliffe, 1970), respectively, both based on hourly temperature data.

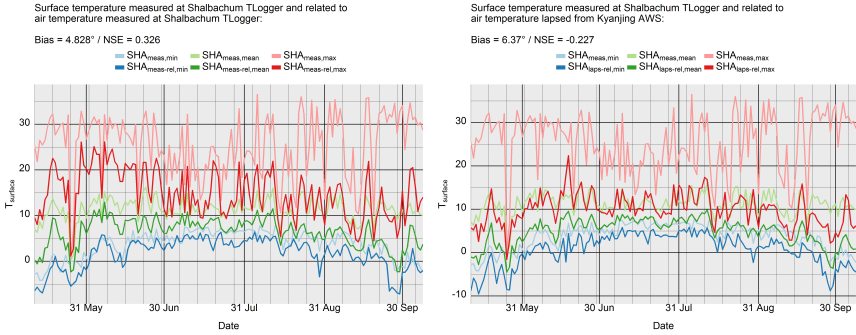


Figure C.21.: Timeseries of daily minimum, mean and maximum surface temperature as measured at Shalbachum T-Logger (SHA) in 2014 and related to measured air temperature (left), and surface temperature as measured at SHA and related to lapsed air temperature (right). ‘Bias’ and ‘NSE’ show the bias of the modelled values from the measured data and the Nash-Sutcliffe efficiency (Nash and Sutcliffe, 1970), respectively, both based on hourly temperature data.

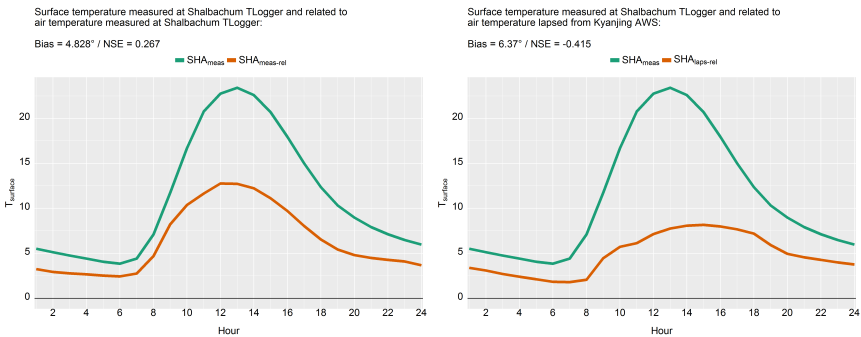


Figure C.22.: Diurnal cycle of hourly surface temperature as measured at Shalbachum T-Logger (SHA) in 2014 and related to measured air temperature (left), and surface temperature as measured at SHA and related to lapsed air temperature (right). ‘Bias’ and ‘NSE’ show the bias of the modelled values from the measured data and the Nash-Sutcliffe efficiency (Nash and Sutcliffe, 1970), respectively, both based on hourly temperature data.

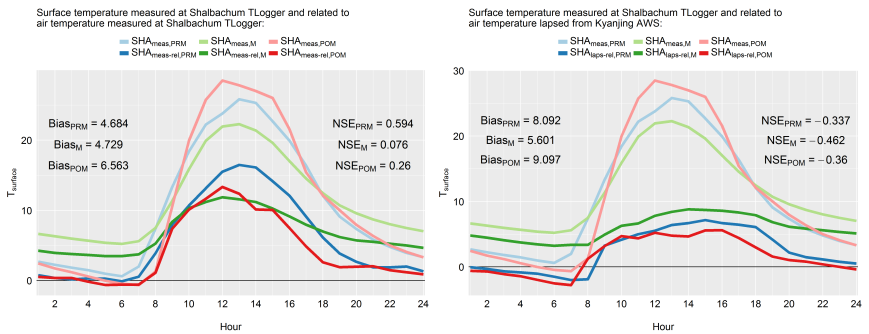


Figure C.23.: Seasonal diurnal cycle of hourly surface temperature as measured at Shalbachum T-Logger (SHA) in 2014 and related to measured air temperature (left), and surface temperature as measured at SHA and related to lapsed air temperature (right). ‘Bias’ and ‘NSE’ show the bias of the modelled values from the measured data and the Nash-Sutcliffe efficiency (Nash and Sutcliffe, 1970), respectively, both based on hourly temperature data.

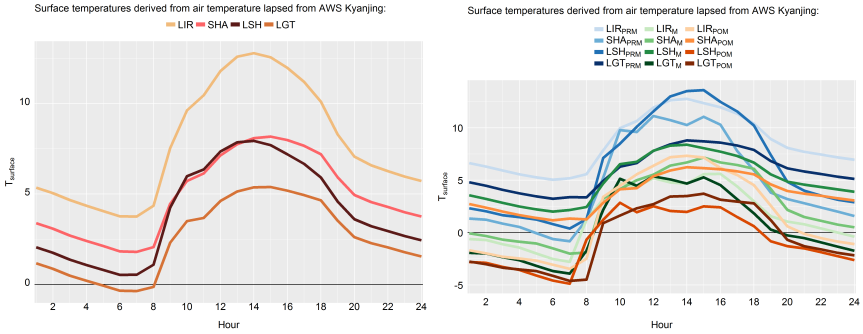


Figure C.24.: Diurnal cycles of hourly surface temperature during 2014 (left) and separated into subseasons (right) as derived from lapsed air temperature from Kyanjing AWS (KYA) to the specific station locations on Lirung-, Shalbachum-, Langhshisha- and Langtang Glacier (LIR, SHA, LSH, LGT).

C.2.3. Surface temperature related to lapsed air temperatures on all four study glaciers

In the following plots we show, for all four study glaciers, modelled surface temperatures derived from air temperatures measured at Kyanjing AWS and then lapsed to the specific glacier.

C.3. Shortwave radiation

In this section shortwave radiation measured at Kyanjing (KYA; off-glacier), Lirung- and Langtang Glacier (LIR, LGT; both on-glacier) during the 2014 melt season is presented. First a timeseries of daily mean- and maximum incoming shortwave radiation, compared to theoretical potential clear-sky solar radiation, is shown in Fig. C.25. Derived from this dataset, daily mean cloud-factors are shown in Fig. C.26.

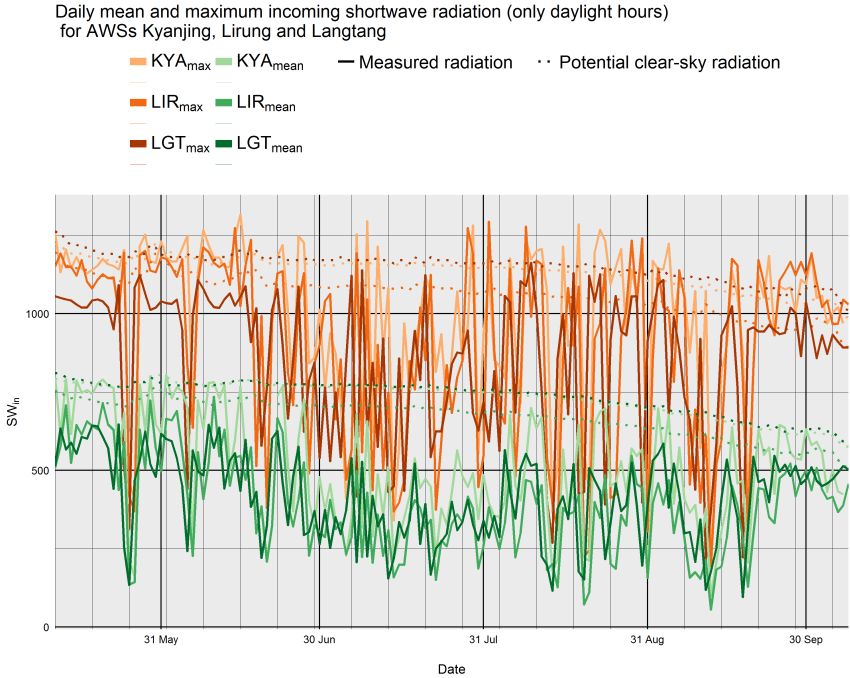


Figure C.25.: Timeseries of daily mean and maximum incoming shortwave radiation as measured at AWSs Kyanjing (KYA), Lirung (LIR) and Langtang AWS (LGT) in 2014. Potential clear-sky solar radiation is also indicated (dotted lines).

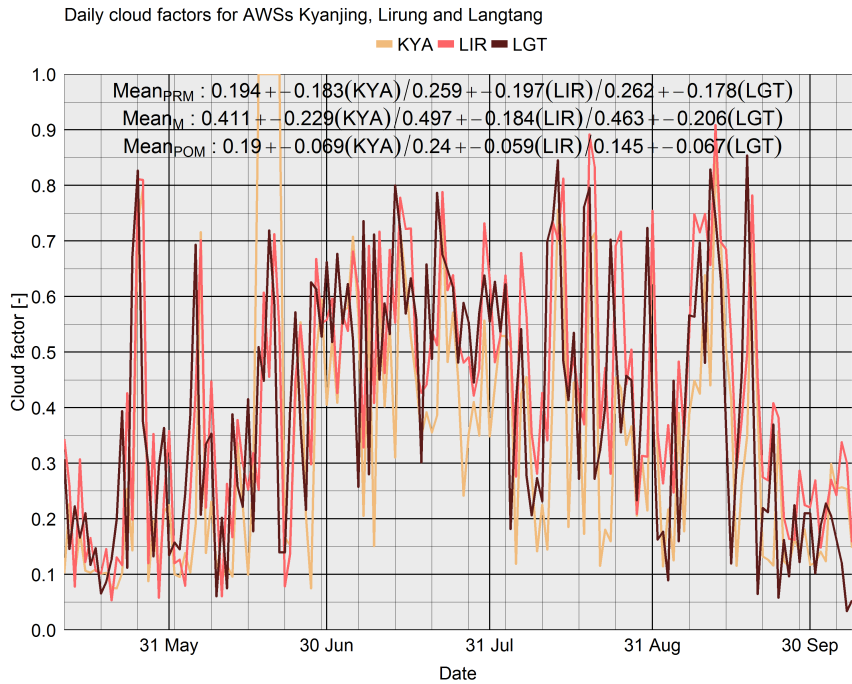


Figure C.26.: Timeseries of daily mean cloud-factors derived for AWSs Kyanjing (KYA), Lirung (LIR) and Langtang AWS (LGT) in 2014. Seasonal means and standard deviations per station are also indicated.

C.4. Longwave radiation

Parameter sets for modelling longwave radiation derived from air temperature as described in Steiner (2014) are shown in Tab. C.5. Fig. C.27 compares measured and modelled longwave radiation for Lirung- and Langtang Glacier.

Table C.5.: [

]Steiner2014.] Parameter sets for alternatives ‘A’ and ‘B’ (Table 7 from Steiner, 2014). Modelling clear sky emissivity (Dilley and O’Brien, 1998) requires three parameters (a–c) to be calibrated on clear sky days, while clouded sky emissivity (Unsworth and Monteith, 1975) requires an additional two (d and e). In our study the parameters of alternative A are used throughout.

Season	a	b	c	d	e	adj
Pre-Monsoon (A)	28.01	115.55	115.83	0.70	-0.12	-
Monsoon (A)	26.64	133.54	80.50	-0.11	0.45	-
Post-Monsoon (A)	33.60	118.06	96.93	0.76	-0.18	-
Pre-Monsoon (B)	8.39e-07	99.34	119.95	0.75	-0.27	1.36
Monsoon (B)	8.39e-07	78.41	83.36	-1.47	0.73	1.85
Post-Monsoon (B)	8.39e-07	94.56	101.18	1.70	-0.71	1.46

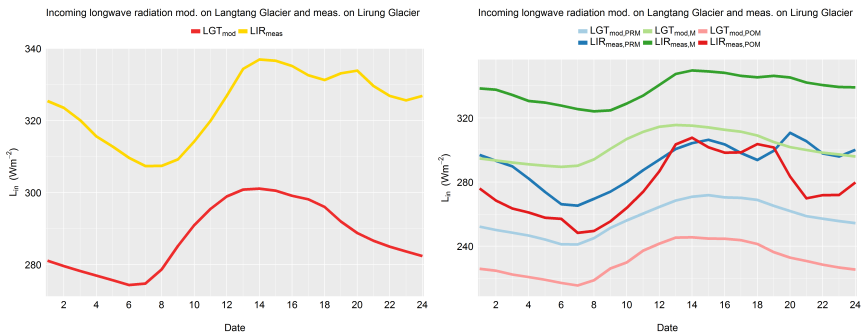


Figure C.27.: All year (left) and seasonal diurnal cycles (right) for pre-monsoon (PRM), monsoon (M) and post-monsoon (POM) of hourly incoming longwave radiation as modelled at Langtang AWS (LGT) and measured at Lirung AWS (LIR) in 2014.

C.5. Relative humidity of the air

A timeseries for 2014 of measured relative humidity at three different stations is shown in Fig. C.28, indicating daily mean, minimum and maximum values per station.

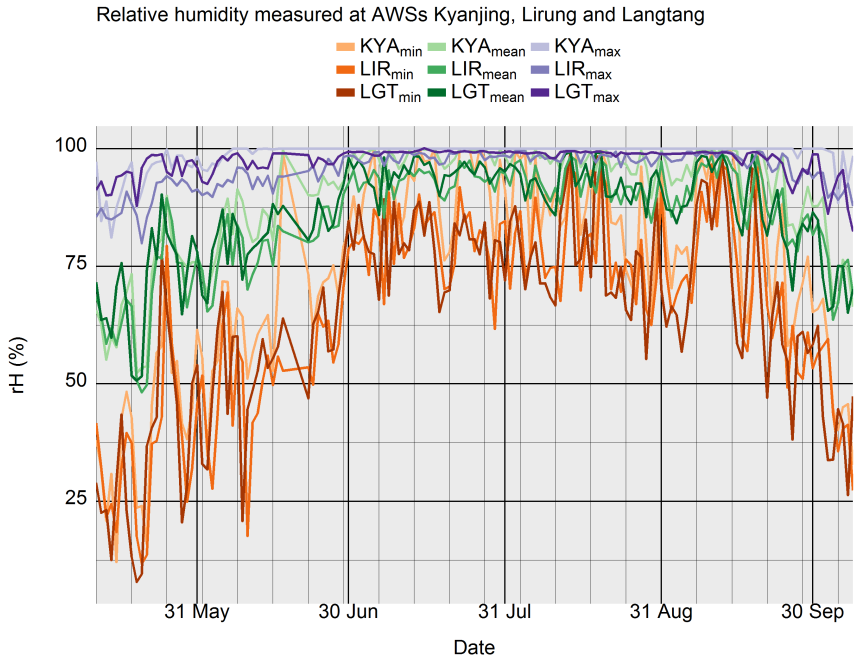


Figure C.28.: Timeseries of daily minimum, mean and maximum relative air humidity as measured at AWSs Kyanjing (KYA), Lirung (LIR) and Langtang (LGT) in 2014.

Appendix D.

Ice cliff modelling at the glacier scale: Testing of model parameters

D.1. Test on spatial resolution

In this section test results on ice cliff backwasting and volume losses, using the ice cliff melt model (as described in Chapters 7 and 8) with varying spatial resolution varying from 0.8m to 3m and 5m, are presented. Ice volume losses and the evolution of several geometric parameters over time were tested for each spatial resolution. Further the simulated ice cliff outlines (horizontal extent) and vertical cliff profiles were compared with the observed outlines and profiles.

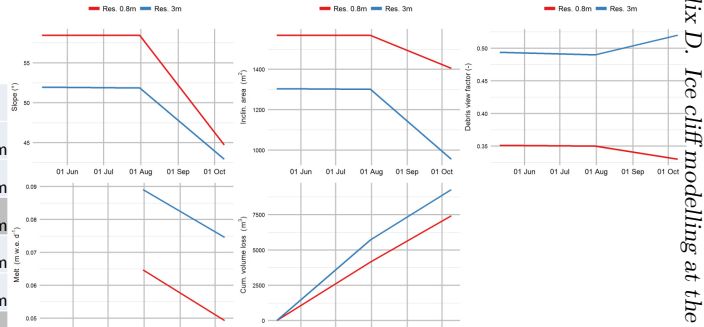
Summary statistics: Test on spatial resolution

Cliff 2, Lirung Glacier

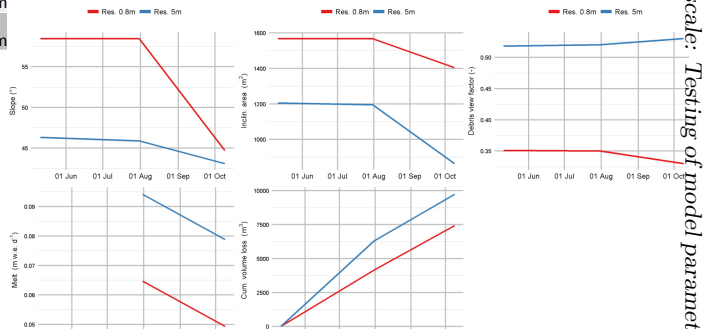
Date	inclA	VolLoss	Slope	Aspect	Vsl	VsL	Vd	MPD	Version
12.05.2014 00:00	1'568	0	59	27	0.67	0.8	0.35	NA	Res. 0.8m
01.08.2014 00:00	1'567	4'150	59	27	0.67	0.8	0.35	0.065	Res. 0.8m
09.10.2014 23:00	1'404	7'427	45	35	0.66	0.79	0.33	0.049	Res. 0.8m
12.05.2014 00:00	1'304	0	52	29	0.73	0.89	0.49	NA	Res. 3m
01.08.2014 00:00	1'301	5'711	52	29	0.73	0.89	0.49	0.089	Res. 3m
09.10.2014 23:00	955	9'281	43	42	0.7	0.86	0.52	0.075	Res. 3m
12.05.2014 00:00	1'205	0	46.3	30.7	0.74	0.91	0.52	NA	Res. 5m
01.08.2014 00:00	1'195	6'292	45.9	30	0.74	0.91	0.52	0.094	Res. 5m
09.10.2014 23:00	864	9'738	43.1	41	0.71	0.89	0.53	0.079	Res. 5m

Test on spatial resolution

Cliff 2, Lirung Glacier: 0.8m vs. 3m

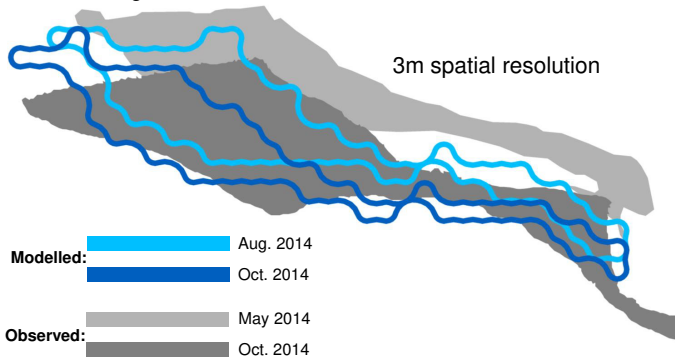


Cliff 2, Lirung Glacier: 0.8m vs. 5m



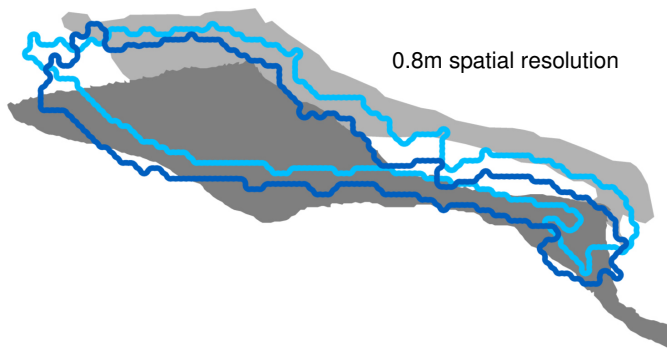
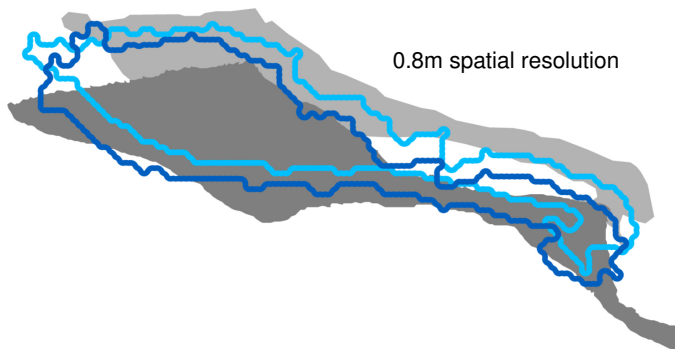
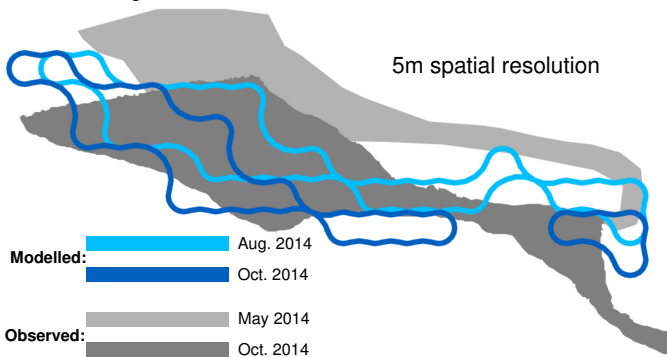
Test on spatial resolution

Cliff 2, Lirung Glacier: 0.8m vs. 3m



Test on spatial resolution

Cliff 2, Lirung Glacier: 0.8m vs. 5m

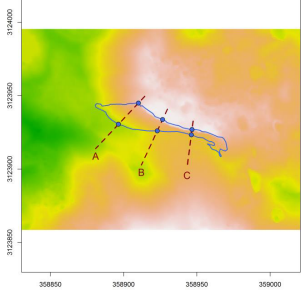


D.1. Test on spatial resolution

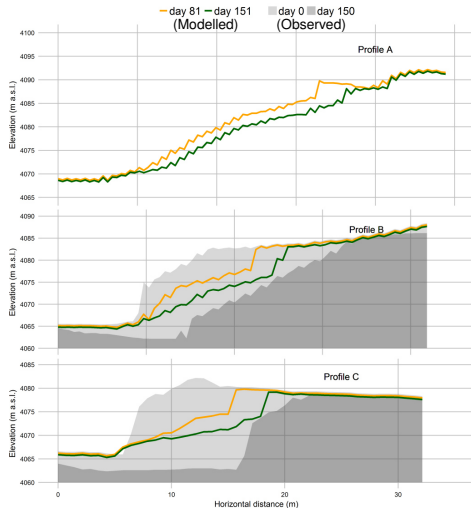
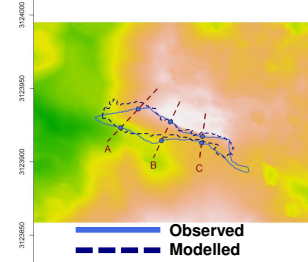
Test on spatial resolution

Cliff 2, Lirung Glacier, 0.8m spatial resolution

May 2014



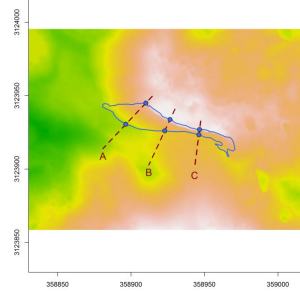
Oct. 2014



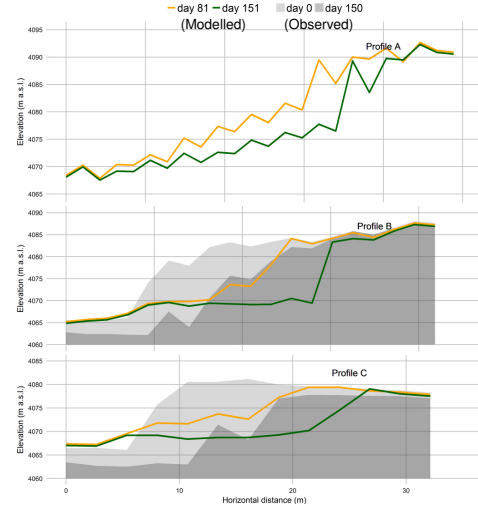
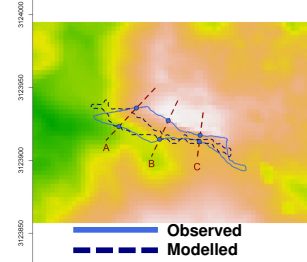
Test on spatial resolution

Cliff 2, Lirung Glacier, 3m spatial resolution

May 2014



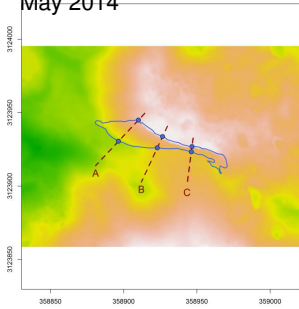
Oct. 2014



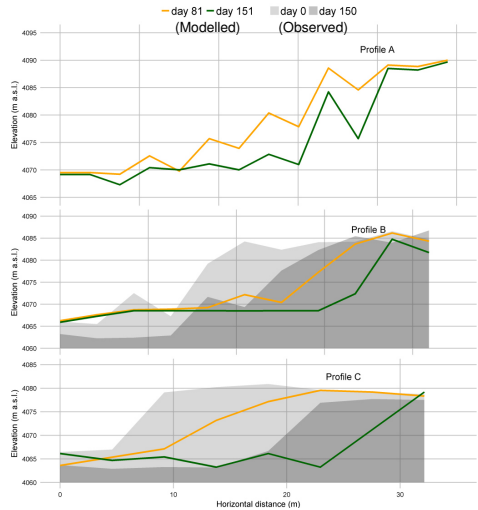
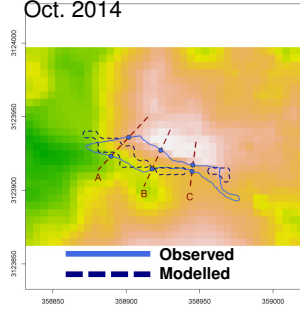
Test on spatial resolution

Cliff 2, Lirung Glacier, 5m spatial resolution

May 2014



Oct. 2014



D.2. Test on DEMs

Simulations on single cliffs using UAV- and SPOT6 DEMs (3m spatial resolution, Cliff 2, Lirung Glacier).

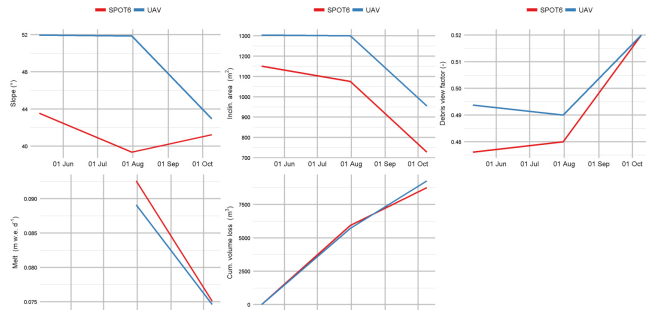
Summary statistics: Test on DEMs

Cliff 2, Lirung Glacier

Date	inclA	VolLoss	Slope	Aspect	Vsl	VsL	Vd	MPD	Version	Glacier
12.05.2014 00:00	1'151	0	44	32	0.74	0.92	0.48	NA	SPOT6	Lirung
01.08.2014 00:00	1'075	5'940	39	33	0.74	0.92	0.48	0.093	SPOT6	Lirung
09.10.2014 23:00	728	8'775	41	38	0.70	0.86	0.52	0.075	SPOT6	Lirung
12.05.2014 00:00	1'304	0	52	29	0.73	0.89	0.49	NA	UAV	Lirung
01.08.2014 00:00	1'301	5'711	52	29	0.73	0.89	0.49	0.089	UAV	Lirung
09.10.2014 23:00	955	9'281	43	42	0.70	0.86	0.52	0.075	UAV	Lirung

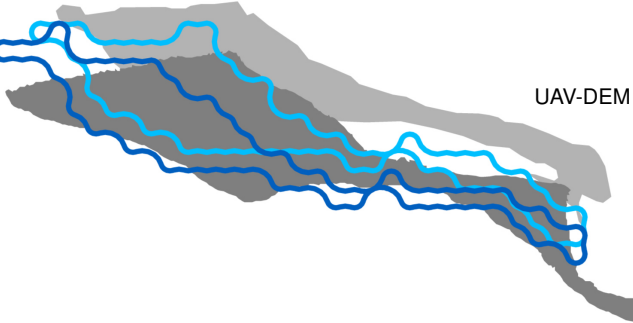
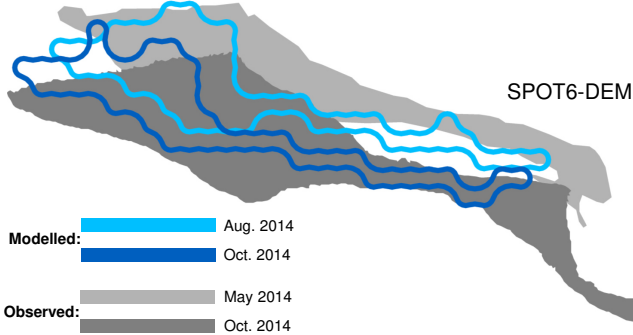
Test on DEMs

Cliff 2, Lirung Glacier



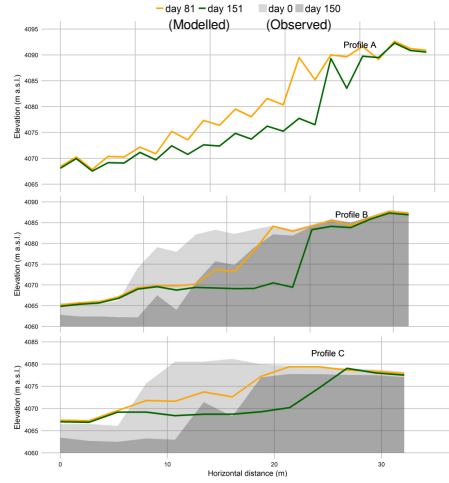
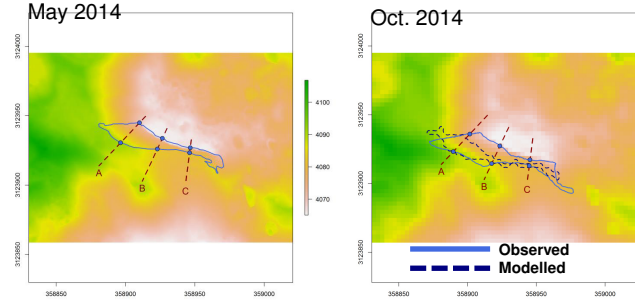
Test on DEMs

Cliff 2, Lirung Glacier



Test on DEMs

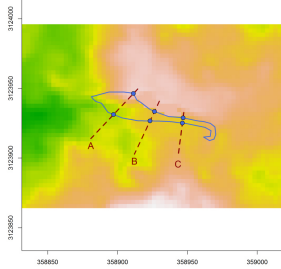
Cliff 2, Lirung Glacier, UAV-DEM (3m)



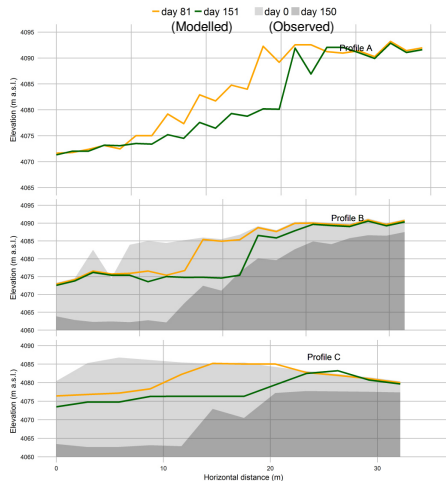
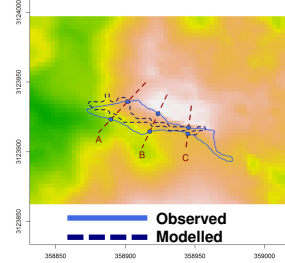
Test on DEMs

Cliff 2, Lirung Glacier, SPOT6-DEM (3m)

May 2014



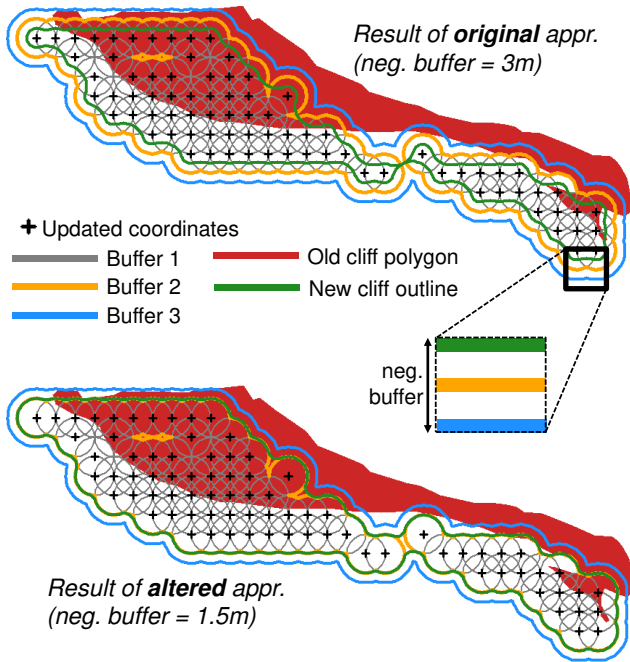
Oct. 2014



D.3. Test on negative buffers

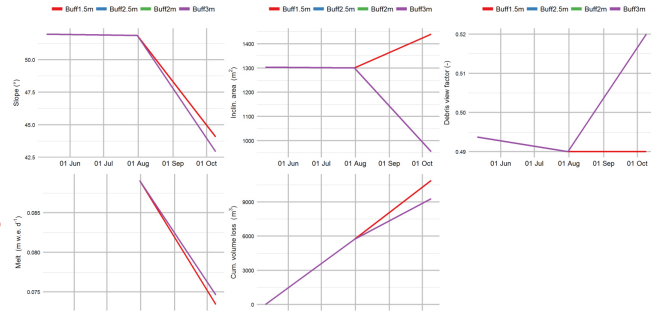
Simulations on single cliffs using UAV- and SPOT6 DEMs with different negative buffer sizes between 1.5 and 3m (3m spatial resolution, Cliff 2, Lirung Glacier).

Test on negative buffers
Examples:

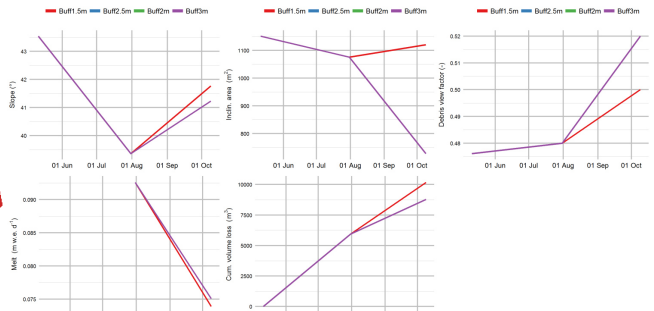


Test on negative buffers

Cliff 2, Lirung Glacier, UAV-DEM (3m) and -outlines (May 2014)

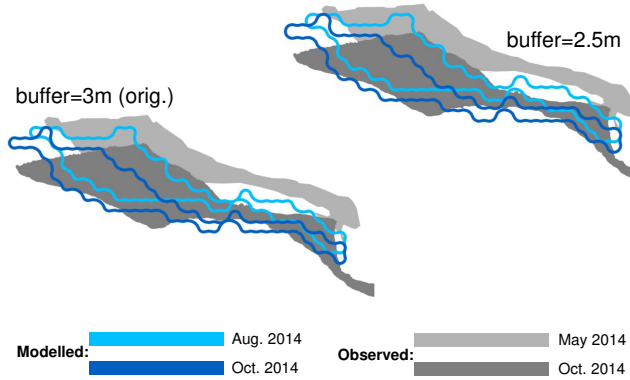


Cliff 2, Lirung Glacier, SPOT6-DEM (3m) and -outlines (Apr. 2014)



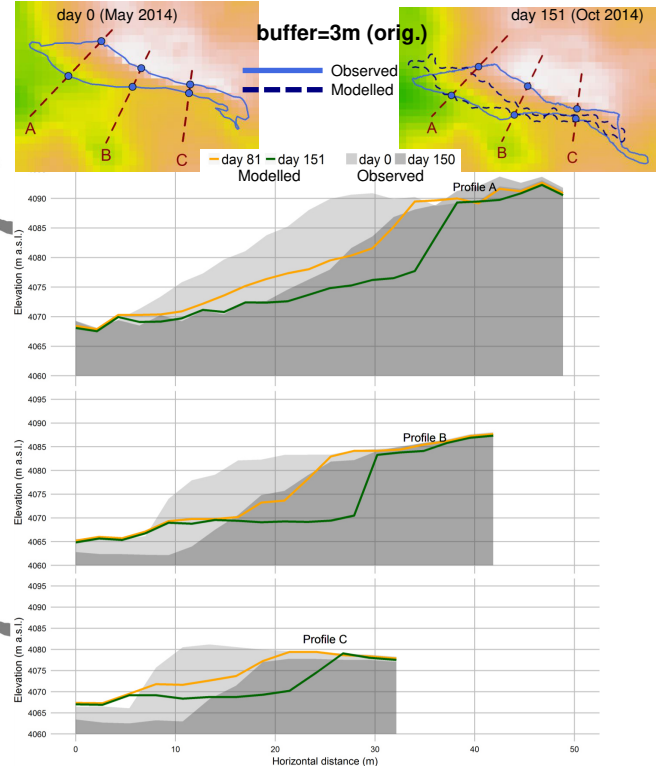
Test on negative buffers

Cliff 2, Lirung Glacier, UAV-DEM (3m) and -outlines (May 2014)



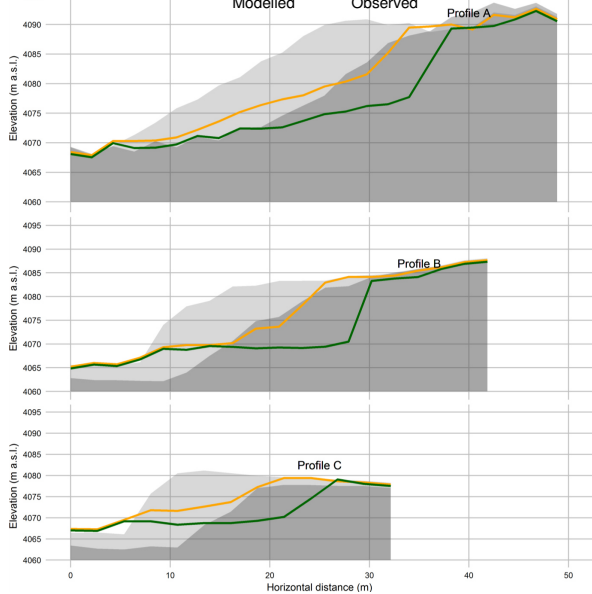
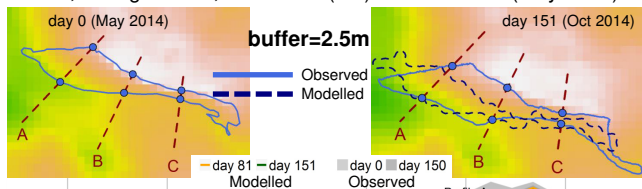
Test on negative buffers

Cliff 2, Lirung Glacier, UAV-DEM (3m) and -outlines (May 2014)



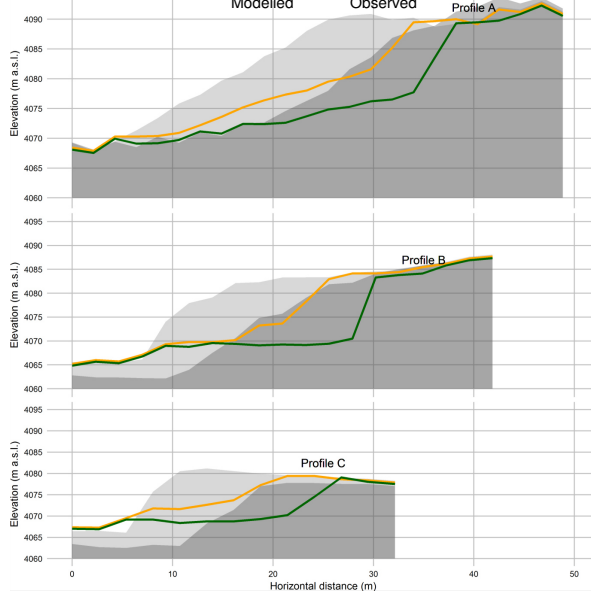
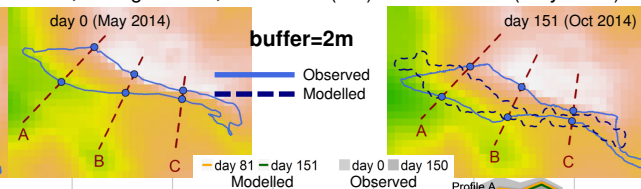
Test on negative buffers

Cliff 2, Lirung Glacier, UAV-DEM (3m) and -outlines (May 2014)



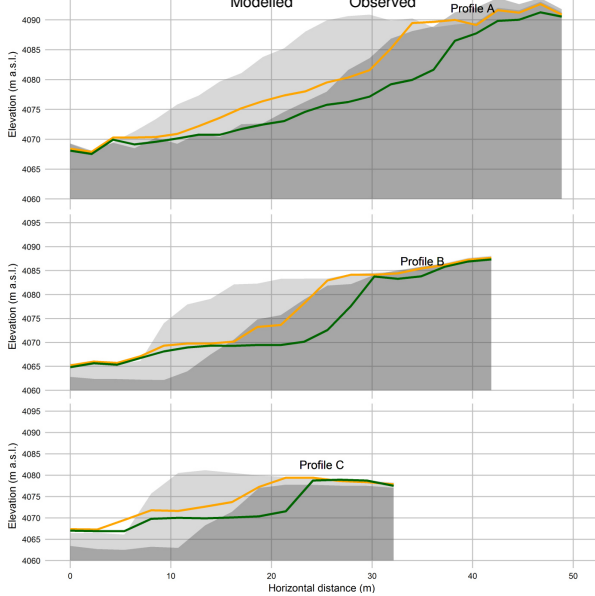
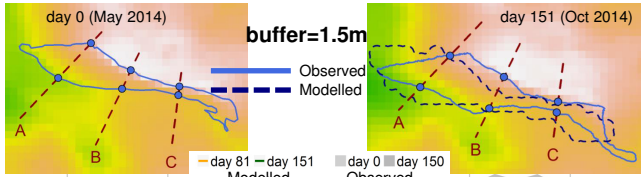
Test on negative buffers

Cliff 2, Lirung Glacier, UAV-DEM (3m) and -outlines (May 2014)



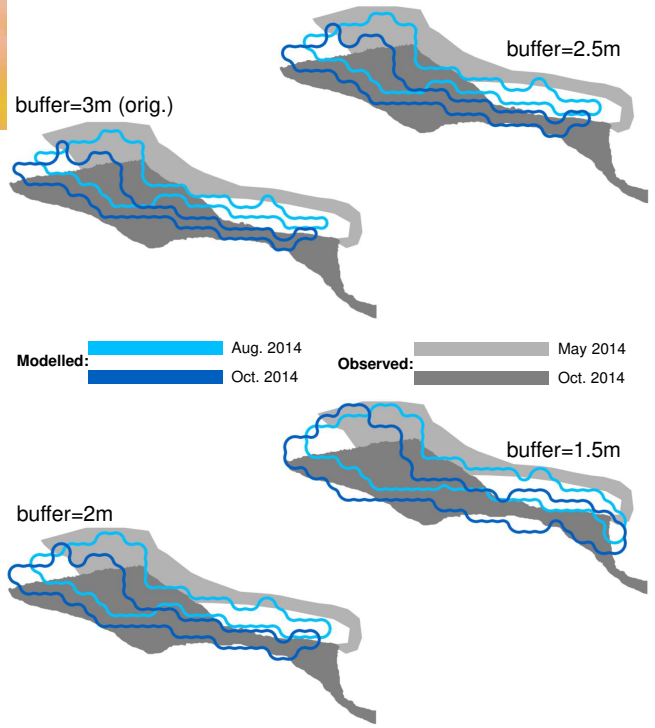
Test on negative buffers

Cliff 2, Lirung Glacier, UAV-DEM (3m) and -outlines (May 2014)



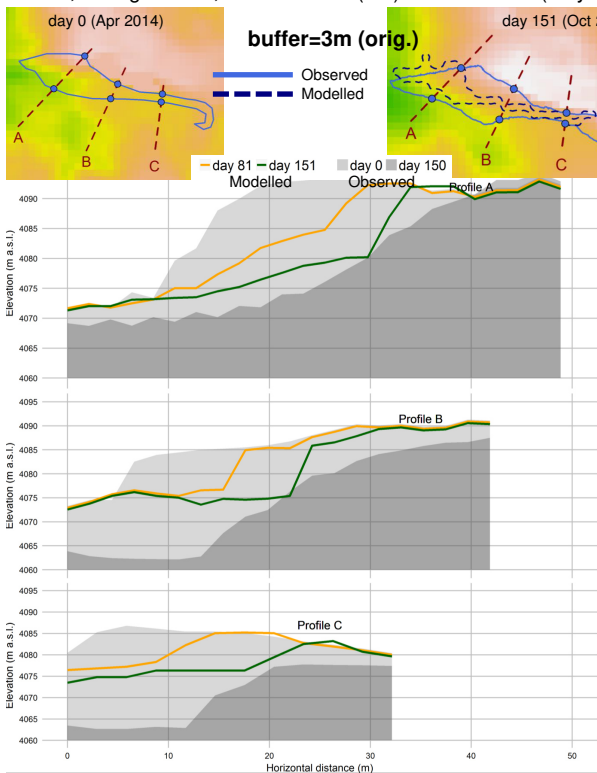
Test on negative buffers

Cliff 2, Lirung Glacier, SPOT6-DEM (3m) and -outlines (Apr. 2014)



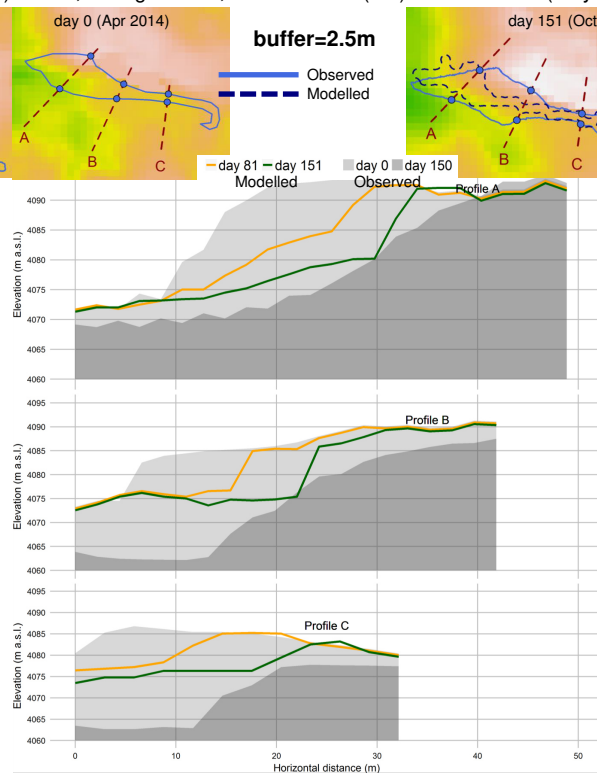
Test on negative buffers

Cliff 2, Lirung Glacier, SPOT6-DEM (3m) and -outlines (May 2014)



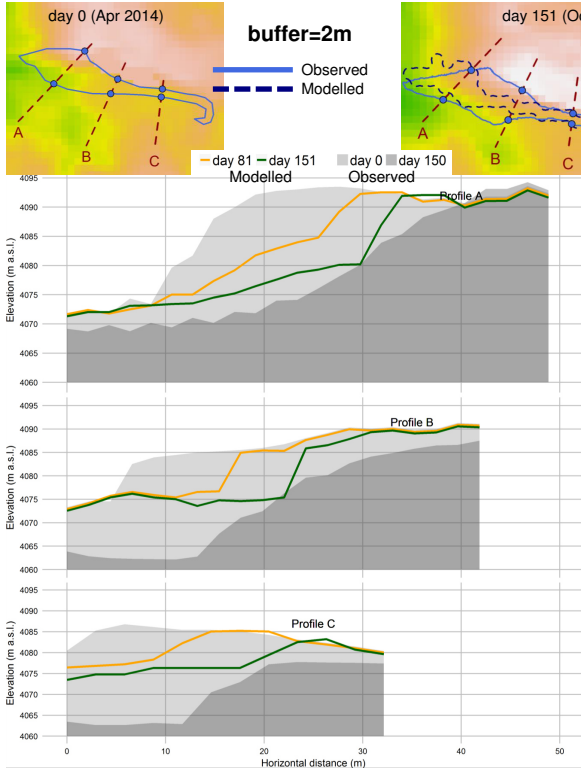
Test on negative buffers

Cliff 2, Lirung Glacier, SPOT6-DEM (3m) and -outlines (May 2014)



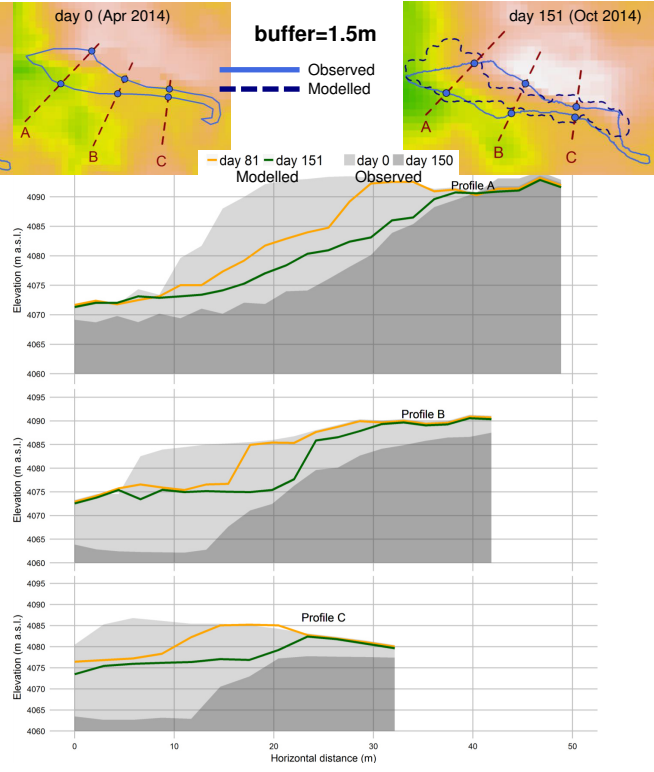
Test on negative buffers

Cliff 2, Lirung Glacier, SPOT6-DEM (3m) and –outlines (May 2014)



Test on negative buffers

Cliff 2, Lirung Glacier, SPOT6-DEM (3m) and –outlines (May 2014)

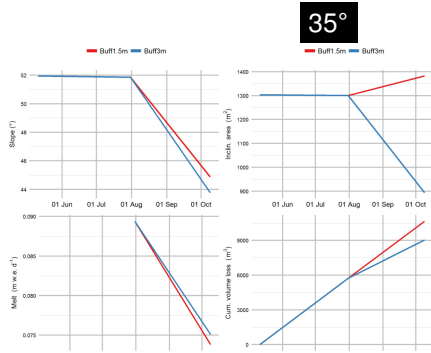
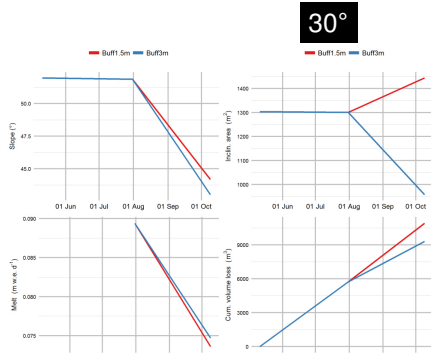


D.4. Test on slope thresholds

Simulations on single cliffs using UAV- and SPOT6-DEMs with slope thresholds of 30° and 35° (3m spatial resolution, Cliff 2, Lirung Glacier).

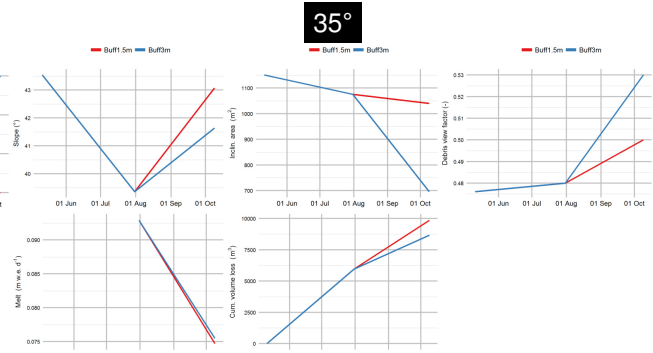
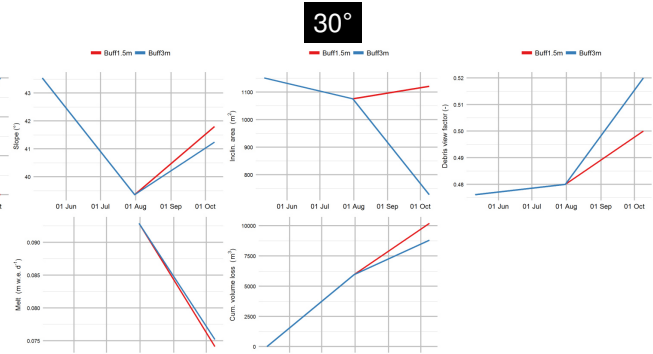
Test on slope thresholds

Cliff 2, Lirung Glacier, UAV-DEM (3m) and –outlines (May 2014)



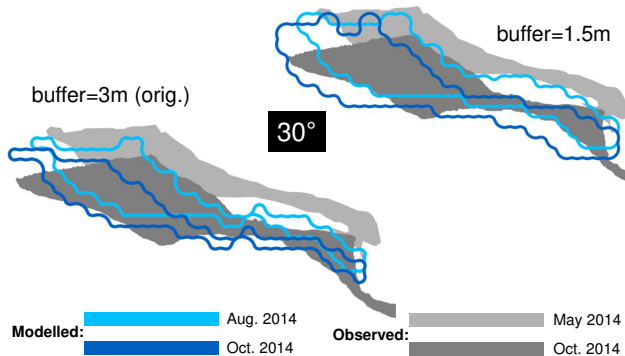
Test on slope thresholds

Cliff 2, Lirung Glacier, SPOT6-DEM (3m) and –outlines (Apr 2014)



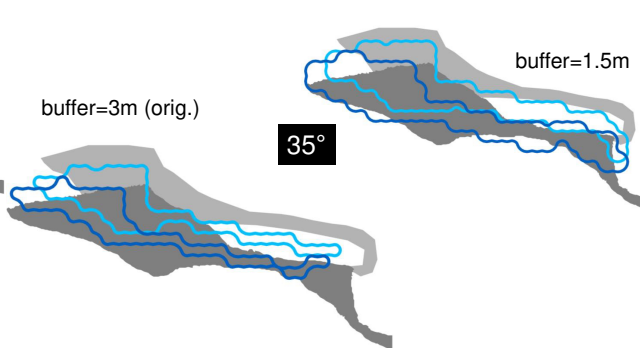
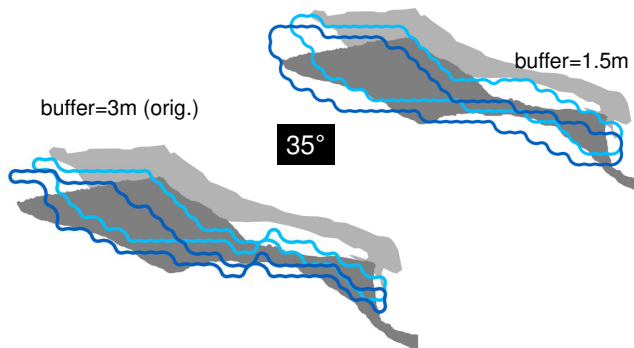
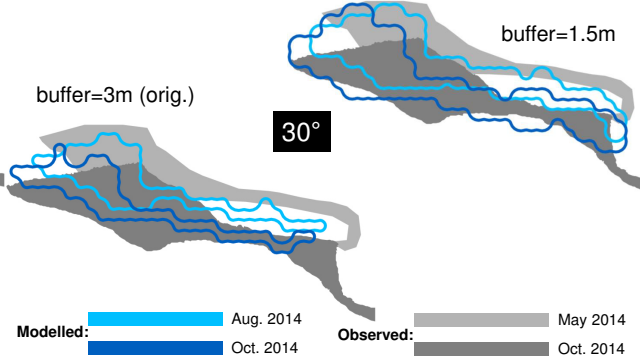
Test on slope thresholds

Cliff 2, Lirung Glacier, UAV-DEM (3m) and -outlines (May 2014)



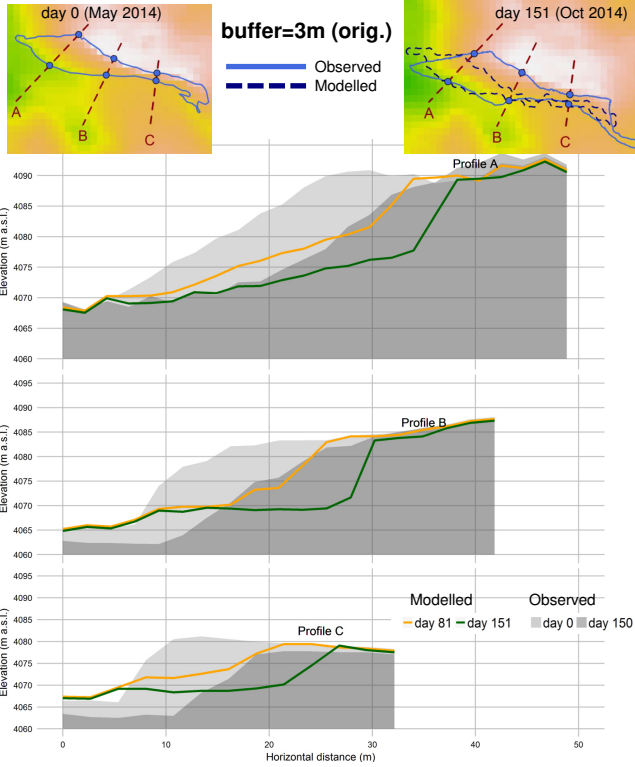
Test on slope thresholds

Cliff 2, Lirung Glacier, SPOT6-DEM (3m) and -outlines (Apr 2014)



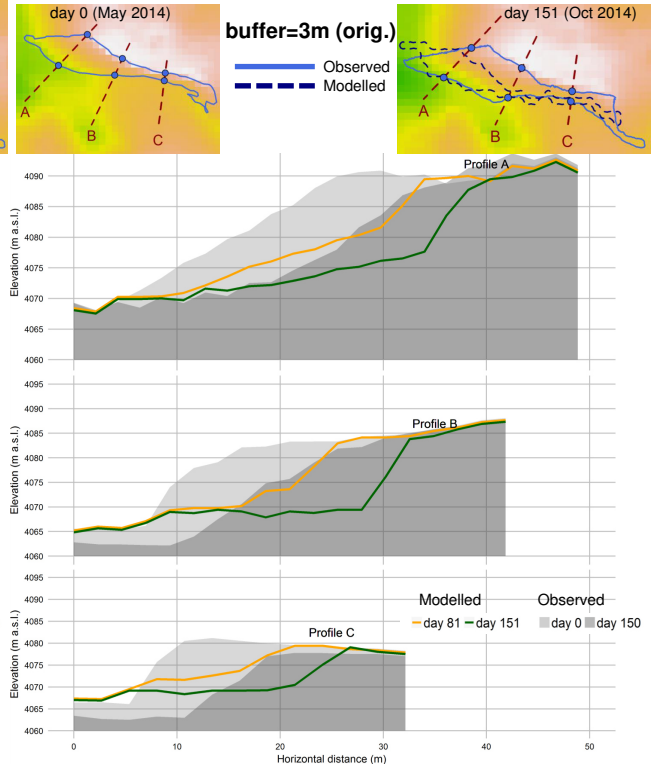
Test on slope thresholds: 30°

Cliff 2, Lirung Glacier, UAV-DEM (3m) and –outlines (May 2014)



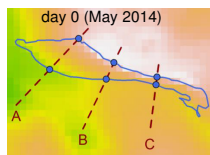
Test on slope thresholds: 35°

Cliff 2, Lirung Glacier, UAV-DEM (3m) and –outlines (May 2014)



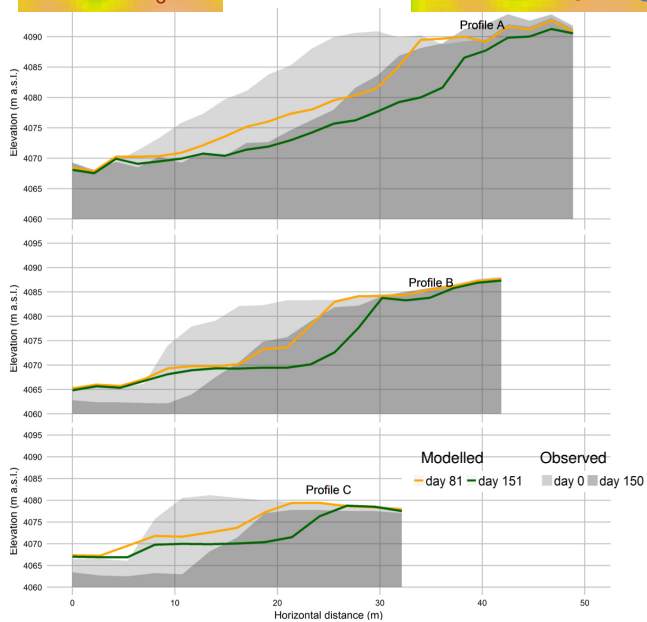
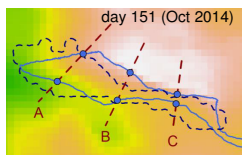
Test on slope thresholds: **30°**

Cliff 2, Lirung Glacier, UAV-DEM (3m) and -outlines (May 2014)



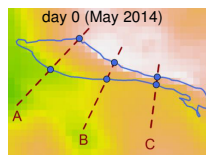
buffer=1.5m

— Observed
- - - Modelled



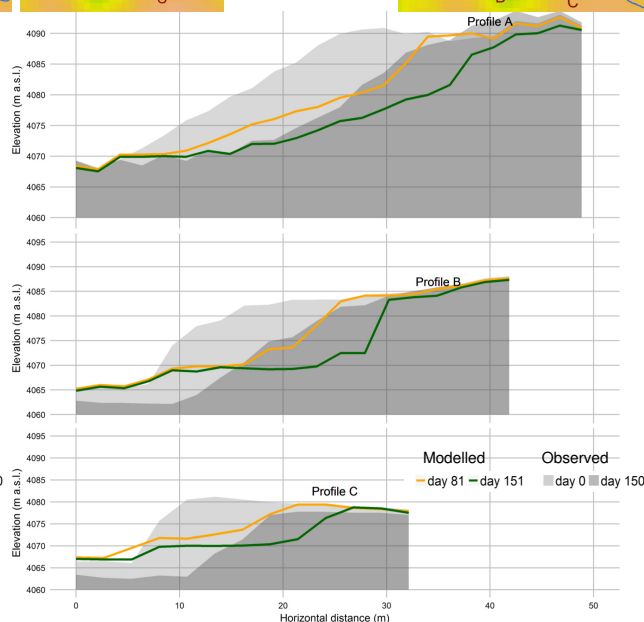
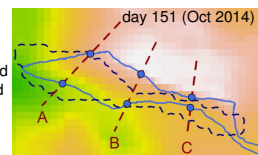
Test on slope thresholds: **35°**

Cliff 2, Lirung Glacier, UAV-DEM (3m) and -outlines (May 2014)



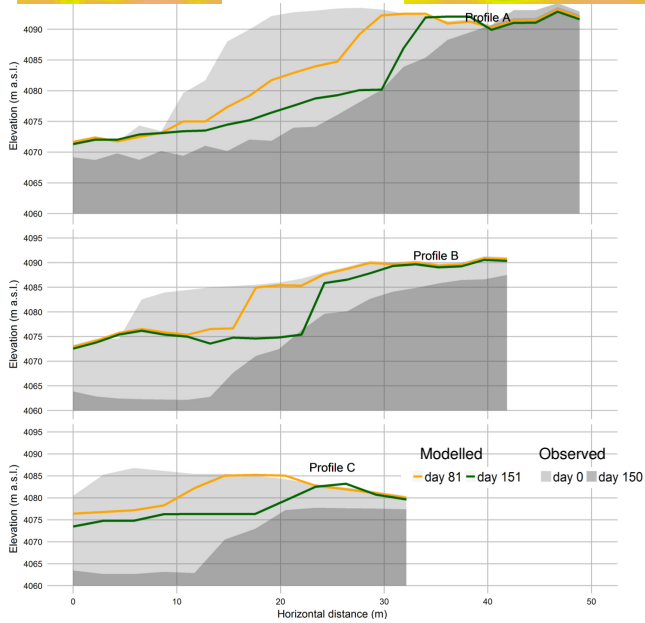
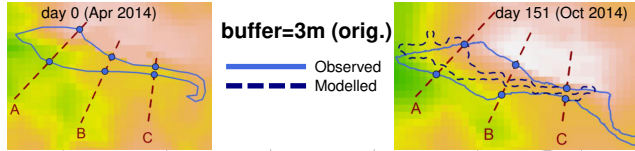
buffer=1.5m

— Observed
- - - Modelled



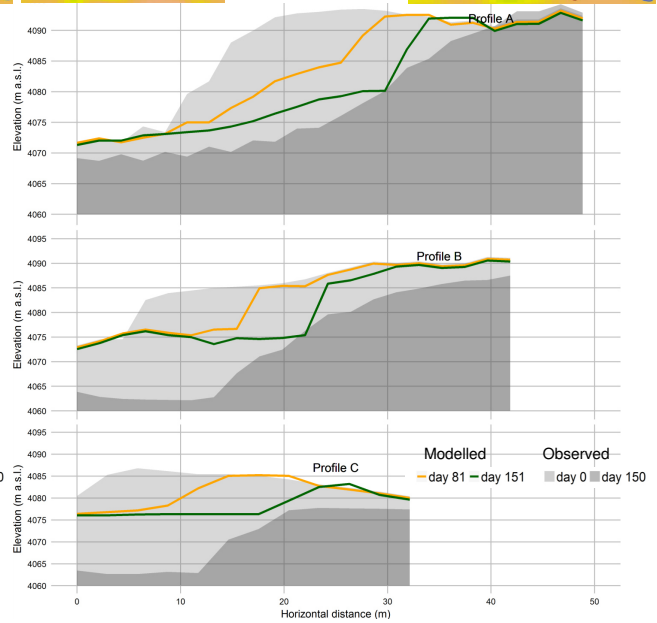
Test on slope thresholds: 30°

Cliff 2, Lirung Glacier, SPOT6-DEM (3m) and –outlines (Apr 2014)



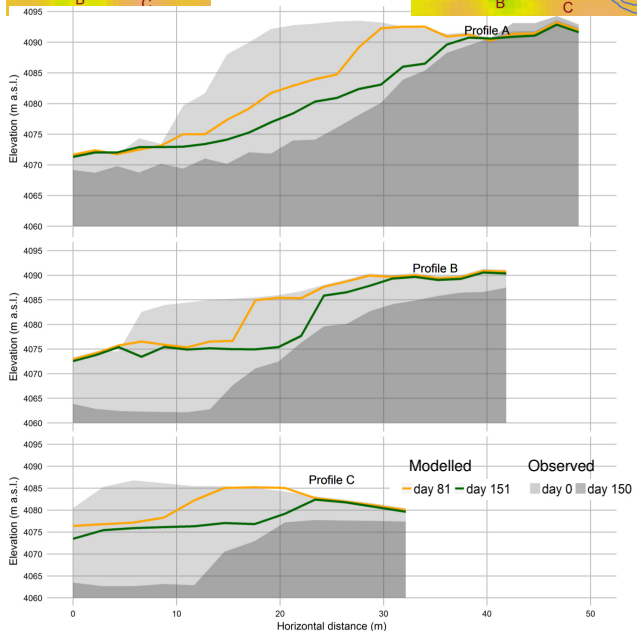
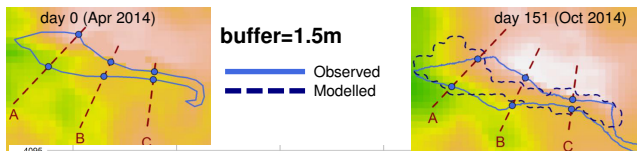
Test on slope thresholds: 35°

Cliff 2, Lirung Glacier, SPOT6-DEM (3m) and –outlines (Apr 2014)



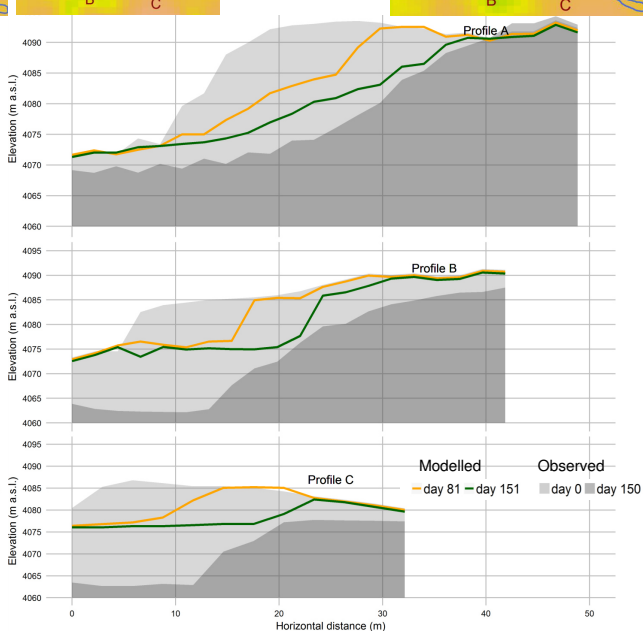
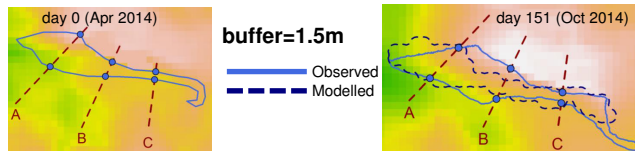
Test on slope thresholds: **30°**

Cliff 2, Lirung Glacier, SPOT6-DEM (3m) and -outlines (Apr 2014)



Test on slope thresholds: **35°**

Cliff 2, Lirung Glacier, SPOT6-DEM (3m) and -outlines (Apr 2014)



Appendix E.

Ice cliff modelling at the glacier scale: Results

Table E.1.: Model results for melt of supraglacial ice cliffs (ice cliff model) only and total melt glacier melt (TOPKAPL-ETH), including cliffs and ponds, for the debris-covered glacier tongue of Lirung Glacier, aggregated to 50m-elevation bands (*EB*). Model period was 12 May – 9 October 2014. *Gla MB* (mass balance) indicates simulated glacier melt per *EB*. Further the glacier surface- (*Gla A*) and cliff areas (inclined and projected: *Cli A_{incl}*, *Cli A_{proj}*) of the corresponding glacier-*EB* are indicated. *Cli MB* shows the simulated *MB* of all cliffs per *EB*, but distributed over the entire glacier surface of the corresponding band. *Gla - V* and *Cli - V* indicate glaciers' and cliffs' ice volume losses. *A_{con}* and *MB_{con}* show how much of the total glacier melt can be attributed to ice cliff melt.

	<i>EB</i>	<i>Gla</i>	<i>Gla MB</i>	<i>Gla A</i>	<i>Gla - V</i>	<i>Cli - V</i>	<i>Cli A_{incl}</i>	<i>Cli A_{proj}</i>	<i>Cli MB</i>	<i>A_{con}</i>	<i>MB_{con}</i>
	[m a.s.l.]		[m w.e.]	[m ²]	[m ³ w.e.]	[m ³ w.e.]	[m ²]	[m ²]	[m w.e.]	[%]	[%]
4000	LIR		-1.43	71100	-101669	3402	606	495	-0.05	0.70	-3.35
4050	LIR		-0.88	111600	-98280	10295	1348	1035	-0.09	0.93	-10.48
4100	LIR		-0.63	108000	-68287	8187	1032	828	-0.08	0.77	-11.99
4150	LIR		-0.95	110700	-105235	NA	NA	NA	NA	NA	NA
4200	LIR		-0.79	222300	-175870	77945	10574	7893	-0.35	3.55	-44.32
4250	LIR		0.54	325800	177341	15492	1886	1485	-0.05	0.46	8.74
4300	LIR		1.16	73800	85695	NA	NA	NA	NA	NA	NA
4350	LIR		-0.59	21600	-12703	NA	NA	NA	NA	NA	NA
4400	LIR		-0.57	900	-509	NA	NA	NA	NA	NA	NA

Table E.2.: Model results for melt of supraglacial ice cliffs (ice cliff model) only and total melt glacier melt (TOPKAPI-ETH), including cliffs and ponds, for the debris-covered glacier tongue of Shalbachum Glacier, aggregated to 50m-elevation bands (*EB*). Model period was 12 May – 9 October 2014. *Gla MB* (mass balance) indicates simulated glacier melt per *EB*. Further the glacier surface- (*Gla A*) and cliff areas (inclined and projected; *Cli A_{incl}*, *Cli A_{proj}*) of the corresponding glacier-*EB* are indicated. *Cli MB* shows the simulated *MB* of all cliffs per *EB*, but distributed over the entire glacier surface of the corresponding band. *Gla -V* and *Cli -V* indicate glaciers' and cliffs' ice volume losses. *A_{con}* and *MB_{con}* show how much of the total glacier melt can be attributed to ice cliff melt.

<i>EB</i> [m a.s.l.]	<i>Gla</i>	<i>Gla MB</i> [m w.e.]	<i>Gla A</i> [m ²]	<i>Gla -V</i> [m ³ w.e.]	<i>Cli -V</i> [m ³ w.e.]	<i>Cli A_{incl}</i> [m ²]	<i>Cli A_{proj}</i> [m ²]	<i>Cli MB</i> [m w.e.]	<i>A_{con}</i> [%]	<i>MB_{con}</i> [%]
4150	SHA	-0.58	900	-522	NA	NA	NA	NA	NA	NA
4200	SHA	-0.90	59400	-53254	NA	NA	NA	NA	NA	NA
4250	SHA	-0.55	196200	-107798	NA	NA	NA	NA	NA	NA
4300	SHA	-0.65	122400	-79358	NA	NA	NA	NA	NA	NA
4350	SHA	-0.53	165600	-87729	NA	NA	NA	NA	NA	NA
4400	SHA	-0.69	226800	-157257	11008	2352	1827	-0.05	0.81	-7.00
4450	SHA	-0.84	162000	-135419	36662	5601	4752	-0.23	2.93	-27.07
4500	SHA	-0.63	265500	-167046	15911	2221	1863	-0.06	0.70	-9.52
4550	SHA	-0.83	387000	-319690	55936	5834	4257	-0.14	1.10	-17.50
4600	SHA	-0.68	460800	-312949	53362	12941	9981	-0.12	2.17	-17.05
4650	SHA	-0.51	315000	-160635	0	786	675	0.00	0.21	0.00
4700	SHA	-0.96	136800	-131317	NA	NA	NA	NA	NA	NA
4750	SHA	-1.35	855000	-115014	NA	NA	NA	NA	NA	NA
4800	SHA	-1.48	432000	-63875	NA	NA	NA	NA	NA	NA
4850	SHA	-0.47	3600	-1689	NA	NA	NA	NA	NA	NA
4900	SHA	-0.26	900	-236	NA	NA	NA	NA	NA	NA

Table E.3.: Model results for melt of supraglacial ice cliffs (ice cliff model) only and total melt glacier melt (TOPKAPL-ETH), including cliffs and ponds, for the debris-covered glacier tongue of Langshisha Glacier, aggregated to 50m-elevation bands (*EB*). Model period was 12 May – 9 October 2014. *Gla MB* (mass balance) indicates simulated glacier melt per *EB*. Further the glacier surface- (*Gla A*) and cliff areas (inclined and projected; *Cli A_{mcl}*, *Cli A_{proj}*) of the corresponding glacier-*EB* are indicated. *Cli MB* shows the simulated *MB* of all cliffs per *EB*, but distributed over the entire glacier surface of the corresponding band. *Gla - V* and *Cli - V* indicate glaciers' and cliffs' ice volume losses. *A_{con}* and *MB_{con}* show how much of the total glacier melt can be attributed to ice cliff melt.

<i>EB</i>	<i>Gla</i>	<i>Gla MB</i>	<i>Gla A</i>	<i>Gla - V</i>	<i>Cli - V</i>	<i>Cli A_{mcl}</i>	<i>Cli A_{proj}</i>	<i>Cli MB</i>	<i>A_{con}</i>	<i>MB_{con}</i>
[m a.s.l.]		[m w.e.]	[m ²]	[m ³ w.e.]	[m ³ w.e.]	[m ²]	[m ²]	[m w.e.]	[%]	[%]
4350	LSH	-1.58	36900	-58351	41598	8839	6318	-1.13	17.12	-71.29
4400	LSH	-0.96	32400	-31020	NA	NA	NA	NA	NA	NA
4450	LSH	-0.61	36900	-22334	NA	NA	NA	NA	NA	NA
4500	LSH	-1.04	140400	-145691	32040	5152	3852	-0.23	2.74	-21.99
4550	LSH	-0.92	258300	-237664	25188	4689	3528	-0.10	1.37	-10.60
4600	LSH	-0.79	396900	-314486	168718	29413	22059	-0.43	5.56	-53.65
4650	LSH	-0.92	167400	-154154	52285	10885	8325	-0.31	4.97	-33.92
4700	LSH	-0.76	215100	-163607	51247	9385	6867	-0.24	3.19	-31.32
4750	LSH	-0.91	362700	-330995	47324	8529	7011	-0.13	1.93	-14.30
4800	LSH	-0.65	486000	-314093	7823	1484	1206	-0.02	0.25	-2.49
4850	LSH	-0.54	525600	-281469	NA	NA	NA	NA	NA	NA
4900	LSH	-0.49	366300	-180738	28007	4688	3744	-0.08	1.02	-15.50
4950	LSH	-0.54	324000	-175009	NA	NA	NA	NA	NA	NA
5000	LSH	-0.48	320400	-152982	NA	NA	NA	NA	NA	NA
5050	LSH	-0.44	355500	-157189	NA	NA	NA	NA	NA	NA
5100	LSH	-0.60	380700	-226652	NA	NA	NA	NA	NA	NA
5150	LSH	-0.52	12600	-6523	NA	NA	NA	NA	NA	NA

Table E.4.: Model results for melt of supraglacial ice cliffs (ice cliff model) only and total melt glacier melt (TOPKAPI-ETH), including cliffs and ponds, for the debris-covered glacier tongue of Langtang Glacier, aggregated to 50m-elevation bands (*EB*). Model period was 12 May – 9 October 2014. *Gla MB* (mass balance) indicates simulated glacier melt per *EB*. Further the glacier surface- (*Gla A*) and cliff areas (inclined and projected; *Cli A_{incl}*, *Cli A_{proj}*) of the corresponding glacier-*EB* are indicated. *Cli MB* shows the simulated *MB* of all cliffs per *EB*, but distributed over the entire glacier surface of the corresponding band. *Gla - V* and *Cli - V* indicate glaciers' and cliffs' ice volume losses. *A_{con}* and *MB_{con}* show how much of the total glacier melt can be attributed to ice cliff melt.

<i>EB</i> [m a.s.l.]	<i>Gla</i>	<i>Gla MB</i> [m w.e.]	<i>Gla A</i> [m ²]	<i>Gla - V</i> [m ³ w.e.]	<i>Cli - V</i> [m ³ w.e.]	<i>Cli A_{incl}</i> [m ²]	<i>Cli A_{proj}</i> [m ²]	<i>Cli MB</i> [m w.e.]	<i>A_{con}</i> [%]	<i>MB_{con}</i> [%]
4450	LGT	-0.69	200700	-139435	108051	5074	4158	-0.54	2.07	-77.49
4500	LGT	-0.70	534600	-376824	231317	10812	8856	-0.43	1.66	-61.39
4550	LGT	-0.65	784800	-506419	189265	27143	20502	-0.24	2.61	-37.37
4600	LGT	-0.62	1530900	-943433	30967	1412	936	-0.02	0.06	-3.28
4650	LGT	-0.68	1158300	-783807	22061	3279	2448	-0.02	0.21	-2.81
4700	LGT	-0.69	1274400	-881421	171190	28964	21474	-0.13	1.69	-19.42
4750	LGT	-0.67	1524600	-1025487	74909	16324	11727	-0.05	0.77	-7.30
4800	LGT	-0.72	1033200	-747689	63364	14531	10089	-0.06	0.98	-8.47
4850	LGT	-0.58	947700	-552973	105619	23870	15417	-0.11	1.63	-19.10
4900	LGT	-0.61	859500	-520655	177510	23199	16551	-0.21	1.93	-34.09
4950	LGT	-0.56	968400	-539635	215636	32868	23589	-0.22	2.44	-39.96
5000	LGT	-0.66	915300	-606626	134769	18146	13734	-0.15	1.50	-22.22
5050	LGT	-0.59	780300	-459876	191224	27263	21807	-0.25	2.79	-41.58
5100	LGT	-0.58	724500	-421751	50919	5680	4761	-0.07	0.66	-12.07
5150	LGT	-0.59	663300	-388803	139205	14436	11664	-0.21	1.76	-35.80
5200	LGT	-0.58	572400	-330854	38001	5638	4554	-0.07	0.80	-11.49
5250	LGT	-0.64	579600	-368079	39997	6906	5850	-0.07	1.01	-10.87
5300	LGT	-0.67	249300	-167336	NA	NA	NA	NA	NA	NA
5350	LGT	-0.90	75600	-68130	NA	NA	NA	NA	NA	NA
5400	LGT	-0.60	900	-539	NA	NA	NA	NA	NA	NA

About the author



Pascal Buri

Born : 12 February 1988 in Winterthur, Switzerland
Nationality : Swiss
Address : Stefano Franscini Platz 3
HIF CO 46.4, ETH Hönggerberg
Institute of Environmental Engineering (IfU)
ETH-Zurich, Swiss Federal Institute of Technology
8093 Zurich, Switzerland
Phone : +41 (0) 44 633 42 07
Email : buri@ifu.baug.ethz.ch
pascalburi@gmail.com

Education

Dec 2013 - : PhD candidate, Institute of Environmental Engineering, ETH Zurich
Nov 2017 : Supervisors: Prof. Dr. Francesca Pellicciotti and Prof. Dr. Paolo Burlando,
Hydrology and Water Resources Management Group

Sep 2011 - : Master of Science in Physical Geography (Minor in Glaciology)
May 2013 : Department of Geography, University of Zurich
Thesis: *Simulation of cold-firn-temperatures at an Alpine site using the model GEOTop*
Supervisors: Prof. Dr. Stephan Gruber and Prof. Dr. Andreas Vieli,
Glaciology and Geomorphodynamics Group

Sep 2008 - : Bachelor of Science in Geography
Jun 2011 : Department of Geography, University of Zurich
Thesis: *Methoden zur Messung und Modellierung der Winter-Massenbilanz von alpinen Gletschern*
Supervisor: Dr. Philip Jörg, Remote Sensing Laboratories

Aug 2003 - : Matura, Linguistic Profile
Aug 2007 : Kantonsschule Im Lee, Winterthur

Peer-reviewed publications

Miles ES, Steiner JF, Willis I, **Buri P**, Immerzeel WW, Chesnokova A and Pellicciotti F (2017b) Pond dynamics and supraglacial-englacial connectivity on debris-covered Lirung Glacier, Nepal. *Frontiers in Earth Science*, 69 (5), 1-19 (doi:10.3389/feart.2017.00069)

Buri P, Miles ES, Steiner JF, Immerzeel WW, Wagnon P, Pellicciotti F (2016b) A physically-based 3D-model of ice cliff evolution over debris-covered glaciers. *Journal of Geophysical Research: Earth Surface*, 12 (121), 2471--2493 (doi:10.1002/2016JF004039)

Brun F, **Buri P**, Miles ES, Wagnon P, Steiner JF, Berthier E, Ragetti S, Kraaijenbrink P, Immerzeel WW, Pellicciotti F, Quantifying volume loss from ice cliffs on debris-covered glaciers using high resolution terrestrial and aerial photogrammetry. *Journal of Glaciology*, 62 (234), 684-695 (doi:10.1017/jog.2016.54)

Heynen M, Miles ES, Ragetti S, **Buri P**, Immerzeel WW, Pellicciotti F (2016) Air temperature variability in a high-elevation Himalayan catchment. *Annals of Glaciology*, 57 (71), 212-222 (doi:10.3189/2016AoG71A076)

Buri P, Pellicciotti F, Steiner JF, Miles ES, Immerzeel WW (2016a) A grid-based model of backwasting of supraglacial ice cliffs on debris-covered glaciers. *Annals of Glaciology*, 57 (71), 199-211 (doi:10.3189/2016AoG71A059)

Miles ES, Pellicciotti F, Willis IC, Steiner JF, **Buri P**, Arnold NS (2016) Refined energy-balance modelling of a supraglacial pond, Langtang Khola, Nepal. *Annals of Glaciology*, 57 (71), 29-40 (doi:10.3189/2016AoG71A421)

Steiner JF, Pellicciotti F, **Buri P**, Miles ES, Immerzeel WW, Reid TD (2015) Modelling ice-cliff backwasting on a debris-covered glacier in the Nepalese Himalaya. *Journal of Glaciology*, 61 (229), 889-907 (doi: 10.3189/2015Jog14J194)

Selected presentations in conferences

Buri P, Miles E, Steiner J, Ragetti S and Pellicciotti F (Dec. 2017) Modelling the contribution of supraglacial ice cliffs to the mass-balance of glaciers in the Langtang catchment, Nepalese Himalaya. *AGU Fall Meeting*, New Orleans, USA (**Poster**)

Buri P and Pellicciotti F (Dec. 2017) What controls the survival of ice cliffs on debris-covered glaciers? An investigation into the aspect-dependent evolution of supraglacial cliffs in the Nepalese Himalaya. *AGU Fall Meeting*, New Orleans, USA (**Poster**)

Buri P, Miles E, Steiner J, Immerzeel W, Wagnon P and Pellicciotti F (Dec. 2016) Modeling the evolution of supraglacial ice cliffs on Himalayan debris-covered glaciers. *AGU Fall Meeting*, San Francisco, USA (**Talk**)

Buri P, Steiner J, Miles E and Pellicciotti F (Nov. 2016) Modelling backwasting of supraglacial ice cliffs over a debris-covered glacier, Nepalese Himalayas. *14th Swiss Geoscience Meeting*, Geneva, Switzerland (**Talk**)

Buri P, Miles E, Steiner J and Pellicciotti F (Oct. 2016) Physically-based modelling of ice cliff melt on a debris-covered glacier, Nepalese Himalayas. *2nd Annual INARCH Workshop*, Grenoble, France (**Poster**)

Buri P, Steiner J, Miles E, Immerzeel W and Pellicciotti F (Apr. 2016) Investigating ice cliff evolution and contribution to glacier mass-balance using a physically-based dynamic model. *EGU General Assembly*, Vienna, Austria (**Poster**)

Buri P, Miles E, Steiner J and Pellicciotti F (Feb. 2016) 3D-modelling of ice cliff evolution on a debris-covered glacier, Nepalese Himalayas. *20th Alpine Glaciology Meeting*, Munich, Germany (**Talk**)

Buri P, Pellicciotti F, Ragetti S, Steiner J, Egli P and Miles E (Feb. 2016) Debris-covered glaciers in High Mountain Asia: their dynamics, surface processes, contribution to mass balance - what we know and what we do not. *International Conference on Climate and Environment Change Impact on the Indus Basin Waters*, Kathmandu, Nepal (**Talk**)

Buri P, Brun F, Miles E, and Pellicciotti F (Sep. 2015) Physical modelling of ice cliff dynamics on a debris-covered glacier in the Nepalese Himalaya. *IGS British Branch Meeting*, Durham, UK (**Talk**)

Buri P, Pellicciotti F, Steiner J, Miles E and Immerzeel W (Mar. 2015) A grid-based model of backwasting of supraglacial ice cliffs over debris-covered glaciers. *IGS International Symposium on Glaciology in High-Mountain Asia*, Kathmandu, Nepal (**Talk**)

Buri P, Steiner J, Pellicciotti F, Miles E, Immerzeel W and Reid T (Dec. 2014) A grid-based model for backwasting at supraglacial ice cliffs on a debris-covered glacier. *AGU Fall Meeting*, San Francisco, USA (**Poster**)

Buri P, Steiner J, Pellicciotti F, Miles E, Immerzeel W and Reid T (Feb. 2014) Modelling ice cliff-backwasting on a debris-covered glacier in the Nepalese Himalayas. *18th Alpine Glaciology Meeting*, Innsbruck, Austria (**Poster**)

Reviewer for

The Cryosphere, Earth and Planetary Science Letters, Journal of Glaciology